

THÈSE

Pour obtenir le grade de

**DOCTEUR DE LA COMMUNAUTE UNIVERSITE
GRENOBLE ALPES**

Spécialité : **Nano électronique et Nano technologies**

Arrêté ministériel : 7 août 2006

Présentée par

Aikaterini VALALAKI

Thèse dirigée par **Philippe BENECH** et
codirigée par **Androula G NASSIOPOULOU**

préparée au sein des Laboratoires **INN-Nano4NPS** et
IMEP-LaHC
dans l'École Doctorale d'Electronique, Electrotechnique,
Automatique & Traitement du signal (EEATS)

Etude des propriétés thermoélectriques et d'isolation thermique du Si poreux et Si nanocristallin

Thèse soutenue publiquement le **25 mai 2016**,
devant le jury composé de :

Prof. Philippe BENECH

Professeur, Université Grenoble-Alpes, Grenoble, Directeur de thèse

Dr. Isabelle BERBEZIER

Directrice de Recherche, IM2NP, CNRS, Marseille, Membre

Prof. Gaël GAUTIER

Professeur INSA-CVL, Tours, Rapporteur

Dr. Vladimir LYSENKO

Chargé de Recherche, INL, CNRS, Lyon, Rapporteur

Dr. Mireille MOUIS

Directrice de Recherche, IMEP-LAHC, CNRS, Grenoble, Président du
jury

Dr. Androula G NASSIOPOULOU

Directrice de Recherche, INN, NCSR Demokritos, Athènes, co-Directrice
de thèse



Acknowledgements

First and foremost, I would like to give my sincere thanks to my thesis supervisor, Dr. Androula Nassiopoulou, for her valuable guidance and constant encouragement throughout this study. She gave me the opportunity to do this thesis and she is always supporting and motivating me in every step of this effort. Except for supervising my study in this academic role, she was also supportive and full of understanding in special moments for me and I am deeply thankful for that.

I would also like to thank my supervisor, Prof. Philippe Benech, for trusting me all these years. I am really grateful for his cooperation and his beneficial comments. Apart from his help in research matters, he also helped me with all the administrative procedures and this is highly appreciated.

Many thanks also go to all the members of the thesis committee for accepting the invitation to be members of the jury of this thesis and enriching this dissertation with their valuable suggestions and constructive comments. I also really appreciate their patience and their support during the defense despite the unexpected technical problems.

I would like to express my thanks to all my officemates, although finally we were not at the same office! Manolis, Violetta, Irini, Giannis and Panagiotis always help me with their scientific opinions and fruitful conversations but mainly with their friendship and valuable support. Laurent should not be left out of this team. Despite his short stay, our discussions were stimulating while his willingness to help is exemplary.

I would also like to thank all the people in the Department of Microelectronics of the Institute of Nanoscience and Nanotechnology of NCSR “Demokritos”, and especially the clean-room staff and SEM operators for our excellent collaboration.

Special thanks are due to my teacher, Ioannis Patis for being a real teacher in school and life. Without his advice, encouragement and selfless support my life would undoubtedly be constructed in a very different motif.

My sincere gratitude goes to my friends. Everyone is special and is next to me in an invaluable and unique way. I could write pages for each one of them, but briefly, I thank: Vasso, Eleni and Evelina for being always there for me in every single moment of my life, Lena and Giorgos because they are the best even at papers, Thanos for his screen and not only, Nicolas for motivating me with his own way, Andreas because he likes thunderbolts, Ermina because she was exceptional from school, Nikoleta for her touching messages, Eleni, Nota, Leonidas and Giorgos because the distance is unable to delete memories, Panagiotis and Giannis for being referred again and Dimitris because he drives me to exceed myself.

Most of all, I would like to thank my family, and especially my mother, for their and especially her unconditional love and unwavering support throughout my life. The words are just poor to express my infinite gratitude. Thank you for everything!!

To those who left..

Abstract

This thesis is devoted to the thermal conductivity and other thermoelectric properties of porous silicon (PSi) and thin polycrystalline Si films (thickness: 100-500 nm).

PSi is a complex material composed of a Si skeleton of interconnected nanowires and dots, separated by voids. When it is highly porous, its thermal conductivity is very low, even below that of the amorphous Si. This makes it a good material for use as a thermal isolation platform on the Si wafer. In addition, its Seebeck coefficient is much higher than that of bulk c-Si.

We studied k of PSi layers with different morphologies and porosities, in the temperature range 4.2-350K. The measurements below 20K are the first reported in the literature. A plateau-like dependence on temperature was observed for T below 20K, while above this temperature a monotonic increase with T is observed. The observed behaviour was interpreted using known theoretical models, based mainly on the fractal nature of PSi. PSi was characterized as a fractal material by calculating its fractal dimension using SEM images and the box counting algorithm.

Two different methods were used to determine porous Si thermal conductivity: the DC method combined with FEM analysis and the 3ω method. Concerning the 3ω method, two improved approaches were proposed for extracting k from the 3ω voltage as a function of frequency: the first uses a fitting of the experimental data to the asymptotic solution of the Cahill's integral formula, and the second is based on the analysis of the experimental data by combining them with a solution of the transient heat transfer equation using FEM analysis. The results in this second case were more accurate and in very good agreement with the DC method.

We also measured the Seebeck coefficient (S) of PSi membranes with porosities 40-84% using a home-built setup, which was fabricated, calibrated and tested within this thesis. A value as high as 1mV/K was obtained for the 51% porosity sample. An anomalous porosity dependence of S was obtained, which was attributed to the interplay between energy filtering, phonon scattering and phonon drag effects. The results were explained by combining them with PL and TEM measurements, used for the determination of nanocrystal sizes. We concluded that, despite of the extremely low k and the high S of PSi, the material with the studied high porosities is not adequate for use as a "good thermoelectric" material, because of its significantly low electrical conductivity, which decreases with increasing porosity, resulting from carrier depletion during formation.

We also studied the thermoelectric properties of thin, boron-doped, polycrystalline silicon films, which are much more attractive for use as Si-based thermoelectrics than porous Si. Their thermoelectric performance is improved by decreasing film thickness, due to a decrease in polysilicon grain size. Thin films with thickness between 100-500nm were investigated. We measured their thermal conductivity, resistivity and Seebeck coefficient and extracted their thermoelectric figure of merit, which showed threefold increase by reducing film thickness down to 100nm. A value as high as 0.033 was achieved, which is the highest reported in the literature so far for boron-doped polysilicon films at room temperature. This increase is attributed to a decrease in the grain size of the material. The obtained value shows the interest of nanocrystalline Si films for integration in efficient Si-based thermoelectric generators, compatible with CMOS processing.

Résumé

Cette thèse a été consacrée à l'étude du Si poreux comme matériaux à faible conductivité thermique (k) pour application aux dispositifs thermoélectriques à base de Si. D'autres paramètres thermoélectriques, comme par exemple le coefficient Seebeck de ce matériau, ont été également étudiés.

Si poreux est un matériau complexe composé de nanostructures de Si séparées de vide. Quand la porosité est élevée, sa conductivité thermique est bien inférieure à celle de Si cristallin. Nous avons étudié la conductivité thermique de Si poreux de différentes morphologies et porosités dans la gamme de températures 4.2-350K. Les mesures à $T < 20K$ sont les premières dans la bibliographie et ont montré une saturation de k en fonction de T pour ces températures. A des températures supérieures à 20K, k augmente régulièrement avec la température. La dépendance de température de k de Si poreux a été interprétée en considérant des modèles théoriques, basées sur la nature "fractal" de Si poreux. Nous avons calculé la dimension fractale de Si poreux par des images de microscopie électronique à balayage (SEM) et l'algorithme de "box counting".

Deux méthodes différentes ont été utilisées pour mesurer k : la méthode à courant direct (dc) combinée avec une analyse FEM et la méthode 3ω . Nous avons proposé deux approches améliorées pour extraire k du signal de potentiel 3ω en fonction de la fréquence. La première considère l'accord des résultats expérimentaux avec la solution asymptotique intégrale de la formule de Cahill, et la seconde fait une analyse des résultats expérimentaux en solvant l'équation temporelle de transfert de chaleur par des éléments finis. Plus précise est la méthode 3ω combinée avec des éléments finis. Les résultats correspondants sont en bon accord avec ceux obtenus par la méthode dc.

Nous avons aussi étudié le Si poreux comme matériau thermoélectrique. Dans ce cas, le Si poreux peut être intéressant si il a une faible porosité, car le matériau à haute porosité est très résistive. Dans ce but, nous avons déterminé le coefficient Seebeck (S) des membranes de Si poreux de différentes porosités dans la gamme 40-84%, en utilisant un dispositif de mesure spécialement développé à cet effet. Pour des échantillons de porosité 51%, la valeur de coefficient S est de 1mV/K, bien supérieure à celle le Si cristallin. La dépendance de S de la porosité n'est pas monotone, et ceci est attribué à une combinaison des effets de filtrage d'énergie, des collisions des phonons et interactions phonon-porteurs électriques. Les résultats obtenus sont basées sur des mesures de photoluminescence (PL) et observations microscopiques à transmission (TEM). Nous avons enfin conclue que, malgré le coefficient S très élevé, le Si poreux n'est pas adéquat comme matériau thermoélectrique à cause de sa faible conductivité électrique, qui diminue en augmentant la porosité à cause de la résultante déplétion de porteurs.

Nous avons aussi étudié des films minces polycristallins dopés avec du Bore. Ces films sont très intéressants comme matériaux thermoélectrique, car ils sont compatibles avec les procédés de fabrication des circuits intégrés de Si. Leur performance thermoélectrique est améliorée par diminution de la taille des grains. Des films minces polycristallins d'épaisseur entre 100 et 500nm ont été étudiés. Tous leurs paramètres thermoélectriques ont été mesurés et nous avons trouvé que le facteur de performance thermoélectrique zT augmente d'un facteur 3 en diminuant l'épaisseur de 500 à 100nm ceci étant attribué à la diminution de la taille des grains dans les films, conduisant à $zT = 0.033$, qui est la meilleure valeur reporté dans la littérature. Ce résultat compétitif augmente le potentiel d'utilisation des films polycristallins dans des dispositifs thermoélectriques efficaces, compatibles à la technologie de Si.

Table of Contents

Acknowledgements.....	3
Abstract	7
Résumé	9
Table of Contents	11
Introduction	17
Chapter 1 Thermoelectric materials and devices.....	19
1.1 Introduction	20
1.2 Thermoelectric effect.....	22
1.2.1 Seebeck effect	22
1.2.2 Peltier effect	23
1.2.3 Thomson effect.....	23
1.3 Thermoelectric figure of merit	24
1.3.1 Seebeck Coefficient.....	24
1.3.1.1 Seebeck coefficient measurement methods	25
1.3.2 Thermal conductivity	27
1.3.2.1 Thermal conductivity measurement methods	27
1.3.3 Electrical conductivity.....	32
1.3.3.1 Electrical conductivity measurement methods	32
1.4 Optimization of the thermoelectric performance of a material	34
1.4.1 State-of-the-art thermoelectric materials.....	35
1.5 Si-based thermoelectrics.....	36
1.5.1 State-of-the-art Si-based thermoelectric materials.....	37
1.6 Thermoelectric applications	38
1.6.1 Thermoelectric generator	39
1.6.2 Thermoelectric cooling	39
1.6.3 Sensing	40
1.7 Conclusions	40
Chapter 2 Formation and Properties of Porous Silicon	41
2.1 Introduction	42
2.2 Porous Si formation	43
2.2.1 Porous Si formation by electrochemical etching of bulk c-Si.....	43
2.2.1.1 Fundamentals of electrochemical etching of c-Si.....	43

2.2.1.2	I-V Curves and formation conditions	45
2.2.1.3	Anodization cells	45
2.2.2	Porous Silicon formation by electroless etching	47
2.2.2.1	Stain etching.....	47
2.2.2.2	Galvanic etching	47
2.2.2.3	Metal-Assisted Chemical Etching (MACE)	47
2.2.3	Local porous Si formation.....	48
2.2.3.1	Local anodization through mask	48
2.2.3.2	Local anodization using etch stops	49
2.2.4	Free standing porous Si membranes (FSPSi)	50
2.3	Porous Si morphology and structure	50
2.4	Porosity and thickness measurements	51
2.5	Conclusions	52
Chapter 3 Porous Si thermal conductivity in the temperature range 4.2-350K		53
3.1	Introduction	54
3.2	Thermal transport at the nanoscale	56
3.3	Temperature dependence of thermal conductivity	56
3.3.1	Crystalline materials.....	56
3.3.2	Amorphous materials and glasses	57
3.4	Porous Si layers studied in this thesis.....	57
3.4.1	Isotropic Porous Si	57
3.4.2	Anisotropic Porous Si.....	58
3.4.3	Test structure	59
3.5	DC method with consequent FEM analysis	59
3.5.1	Finite Element Method (FEM) simulations – General considerations.....	60
3.5.1.1	Heat transfer.....	60
3.5.2	Implementation of the method	63
3.5.3	Experimental results – Temperature dependence of porous Si Thermal resistance.....	67
3.5.4	Experimental results - Temperature dependence of Porous Si thermal conductivity.....	70
3.5.5	Comparison with other materials and theory	72
3.6	3 ω method.....	75
3.6.1	General assumptions and considerations.....	75
3.6.1.1	One - dimensional Line heater	76
3.6.1.2	Infinite heat source at the surface	79

3.6.1.3	Effect of finite thickness of the substrate.....	80
3.6.1.4	Finite width of the heater	81
3.6.1.5	Approximate solution to the exact equation	82
3.6.2	Experimental setup.....	83
3.6.3	Data analysis	84
3.6.3.1	The slope method.....	84
3.6.3.2	Extracting thermal conductivity using Cahill's integral form – Approach1...	85
3.6.3.3	3 ω method with consequent FEM analysis – Approach 2.....	85
3.6.4	Experimental results.....	87
3.6.4.1	Bulk c-Si covered with a thin TEOS oxide.....	87
3.6.4.2	Anisotropic porous Si - 70% porosity.....	89
3.6.4.3	Isotropic porous Si - 63% porosity	93
3.7	Conclusions	95
Chapter 4 Thermal conductivity of PSi in the temperature range 4.2-20K – Interpretation of the plateau		97
4.1	Introduction	98
4.2	Fractals and their physical properties	98
4.2.1	Fractal dimension	99
4.2.2	Methods of measuring fractal dimension	100
4.2.2.1	Scattering experiment	100
4.2.2.2	Image analysis.....	100
4.3	Fractons	101
4.4	Fractal nature of porous Si.....	102
4.4.1	Porous Si fractal dimension.....	102
4.4.1.1	Isotropic Porous Si.....	102
4.4.1.2	Anisotropic porous Si	104
4.5	Plateau-like behavior of porous Si thermal conductivity at cryogenic temperatures – Interpretation based on its fractal geometry	106
4.6	Conclusions	110
Chapter 5 Effectiveness of porous Si as a thermal insulating platform on the Si wafer		111
5.1	Introduction	112
5.2	Temperature distribution in a test device incorporating a thermal insulating porous Si layer	113
5.3	Effect of applied power	114
5.4	Effect of porous Si layer thickness	115

5.5	Comparison to bulk c-Si and other CMOS compatible thermal insulators	116
5.6	Conclusions	117
Chapter 6 Seebeck coefficient of porous Si as a function of porosity.....		119
6.1	Introduction	120
6.2	Study of porous Si free standing membranes	121
6.2.1	Fabrication process.....	121
6.2.2	SEM and TEM characterization.....	122
6.2.3	PL measurements	122
6.3	Seebeck coefficient measurements	123
6.3.1	Home-built setup description	124
6.3.2	Data analysis	124
6.3.3	Validity of the measurements.....	125
6.3.3.1	Seebeck coefficient of highly doped p-type Si	125
6.3.3.2	Diagnostic test measurements for hysteretic behavior.....	126
6.3.3.3	Comparison with simulations	127
6.4	Experimental results – Porosity dependence of porous Si Seebeck coefficient	128
6.5	Conclusions	130
Chapter 7 Thermoelectric performance of LPCVD polycrystalline Si thin films		131
7.1	Introduction	132
7.2	Polycrystalline Silicon.....	133
7.2.1	Low Pressure Chemical Vapor Deposition (LPCVD)	133
7.2.2	Microstructure of undoped polysilicon films deposited by LPCVD.....	133
7.2.3	Microstructure of doped polysilicon films deposited by LPCVD.....	134
7.2.4	Polysilicon grain growth	134
7.3	Polycrystalline Si thin films studied in this thesis	135
7.3.1	Structural characterization.....	135
7.4	Electrical resistivity and TCR.....	138
7.4.1	Test structure	138
7.4.2	Measurement method	138
7.4.3	Experimental results	138
7.4.3.1	Electrical resistivity	138
7.4.3.2	TCR.....	139
7.4.3.3	Comparison with theory.....	140
7.5	Seebeck coefficient.....	140
7.5.1	Test structure	140

7.5.2	Measurement method	141
7.5.3	Experimental results	141
7.5.3.1	Comparison with theory	142
7.6	Thermal conductivity	143
7.6.1	Test structure	143
7.6.2	Measurement method	143
7.6.3	Experimental results	144
7.6.4	Comparison with theory	145
7.7	Power factor & Figure of merit	146
7.8	Comparison with other works on polysilicon films found in the literature	147
7.9	Conclusions	148
Conclusions		149
Perspectives		151
 Résumé Long		 153
	Introduction	155
	Matériaux et dispositifs thermoélectriques (Chapitre 1)	157
	Formation et propriétés du Si poreux (Chapitre 2)	158
	Conductivité thermique du Si poreux dans la gamme de température 4.2-350K (Chapitre 3)	158
	Conductivité thermique du Si poreux dans la gamme de températures 4.2-20K - Interprétation du plateau (Chapitre 4)	161
	Efficacité du Si poreux utilisé comme plateforme d'isolation thermique du Si (Chapitre 5)	162
	Coefficient Seebeck du Si poreux en fonction de la porosité (Chapitre 6)	162
	La performance thermoélectrique des films minces de Si nanocristallin (Chapitre 7)	163
	Conclusions	165
	Perspectives	166
 References		 167

Introduction

Thermoelectrics is a fast growing research field the last years because of the urgent need to find environmentally friendly alternative energy sources. The scenario of producing energy from existing temperature differences is stimulating the research community to find ways to enhance the efficiency of thermoelectric devices. Although such devices have still relatively low efficiency, the vision of being able to utilize the global waste heat to produce energy was an important incentive towards this thesis.

Regarding availability and sustainability for the large scale application of thermoelectrics, Si nanostructures are now among the most preferential solutions. Apart from the advantages of incorporating Si in large scale thermoelectric devices, due to its abundance, the improvement of the thermoelectric performance of Si-based devices is expected to have a huge impact on the modern technological world, because Si is the basic material of integrated circuits and semiconductor electronics. Thus, this dissertation focused on the study of Si-based thermoelectrics.

Porous silicon (PSi) is a type of nanostructured Si, which can be formed by a massive, low cost and CMOS compatible technique, which is the electrochemical dissolution of bulk crystalline Si. Its properties can be tuned and adjusted by changing the electrochemical conditions used. PSi has been studied and used so far as a low thermal conductivity material, which provides an excellent platform for the integration on it of thermal devices, including thermoelectrics.

The previous knowledge of the Nano4NPS group at NCSR “Demokritos” (<http://nano4nps.imel.demokritos.gr/>) on thermal sensors and thermoelectric devices using porous Si thermal isolation technology, was used as the initial background and was extended further in this thesis with the objective to improve the performance of the existing devices and fully understand the properties of the materials used. Nano4NPS group have successfully integrated thermal sensors and thermoelectric generators on the Si wafer for a number of different applications. The principle of operation of thermal sensors is based on the effective thermal isolation on Si by a thick porous Si layer. Thus, a temperature difference can be produced on porous Si compared to that on the bulk. Thermocouples made of p-type polycrystalline Si in contact with Aluminum are integrated on the surface of the wafer with their “hot” contact lying on the porous Si areas and their “cold” contact lying on Si. This way, at the two last ends of thermocouples a potential difference is created, due to Seebeck effect, and the changes on this signal due to changes in the temperature difference is calibrated to sense air and generally gas flow, microfluidic flow etc. On the other hand, by exploiting an existing temperature difference and using a similar configuration, power can be produced at the output of this device, which, in this case, is called “thermoelectric generator”.

There are two critical parameters that define the sensitivity and the efficiency of the thermoelectric devices: 1) the effectiveness of porous Si as a thermally insulating substrate and 2) the effectiveness of the thermoelectric materials composing the thermocouples. Thus, by considering the same design and configuration of the device, an improvement of one or of both of the above parameters is directly translated in an improved overall device performance. This was the objective of this thesis and was successfully reached. We investigated the thermal conductivity of porous Si with different structure and morphology in a wide temperature range and also fully characterized polycrystalline Si as a thermoelectric material. By combining the proved effectiveness of porous Si as a local thermal isolation platform on the Si wafer and the improved thermoelectric figure of merit of polycrystalline Si, improved Si-based devices can be fabricated with increased efficiency and sensitivity.

In this framework, the present thesis is constructed as follows:

In chapter 1, the basics and fundamentals of thermoelectric materials and devices are introduced. All three parameters used to characterize a thermoelectric material are described, along with the known methods, which are frequently used for their experimental determination. Before describing the possible applications of thermoelectrics, the state-of-the-art thermoelectric materials, with record performances so far, are reviewed.

In chapter 2, there is an introduction to porous Si technology, its fabrication processes and the resulting material morphology and structure. This chapter focuses on PSi formation by electrochemical etching, which is the method used for the preparation of the samples studied in this thesis.

Chapter 3 concentrates on the experimental results of PSi thermal conductivity (k) in the temperature range 4.2-350K. The two methods used, namely the DC and the 3ω method, are presented in detail, while alternative approaches for the latter are introduced. The test structures and the exact way of implementing each method are presented. The validity of the methods is also assessed. All the obtained experimental results are compared to each other, to bulk c-Si and to other CMOS compatible, low thermal conductivity materials. The temperature dependence of PSi thermal conductivity is explained based on known theoretical models, which, however, were proved to be inadequate to describe the k (T) trend at cryogenic temperatures. This is the subject of interest of chapter 4.

Following the observed discrepancy between thermal conductivity experimental results and theory at low temperatures, chapter 4 interprets the obtained results based on the fractal nature of PSi. To this aim, after a brief introduction to fractals and their physical properties, the fracton model is presented and discussed. PSi is then characterized as a fractal object by extracting its fractal dimension using SEM images and the box counting algorithm. Fracton model is proved to interpret nicely well our experimental results.

In chapter 5, the effectiveness of PSi as a thermal insulator is evaluated, based on the k (T) experimental results and FEM simulations. A detailed study is presented, which demonstrates the advantages of using PSi as a local thermal isolation platform on the Si wafer, on which Si-based thermoelectrics can be effectively integrated for improved operation.

In chapter 6, after presenting the home-built setup, which was fabricated, calibrated and tested within this thesis, the porosity dependence of PSi Seebeck coefficient is presented and the possible mechanisms involved are analysed, based mainly on photoluminescence measurements, as well as on SEM and TEM images, which reveal the structure and morphology of the studied porous Si membranes.

Finally, in chapter 7, thin polycrystalline silicon films are measured as promising Si-based thermoelectric materials. A systematic study of the thermoelectric figure of merit of boron-doped LPCVD polysilicon thin films is presented, which is primarily based on the significant reduction of material's grain size, resulting in consequent strong reduction of material's thermal conductivity. A threefold increase of the thermoelectric figure of merit of polysilicon films by reducing film thickness down to 100nm was achieved, reaching a competitive value of 0.033.

In overall, this Ph.D. thesis demonstrated the effectiveness of PSi as a local thermal isolation platform on the Si wafer, for the on-chip integration of thermoelectric and generally thermal devices. Compared to the literature, the thermal characterization of porous Si layers was extended to temperatures below 20K, thus completing its study in a wide temperature range. The dominant thermal transport mechanisms involved were investigated, paving the way towards full understanding of the thermal conductivity behaviour of PSi, so as to be able to adjust this property by adjusting material's structure and morphology.

In parallel, polysilicon thin films with different thickness were characterized. An enhancement of their thermoelectric figure of merit was achieved by reducing the grain size of the films through reduction of film thickness. These layers constitute a low cost, fully CMOS compatible solution for the development of efficient Si-based thermoelectrics.

Chapter 1

Thermoelectric materials and devices

Thermoelectrics is defined as the science and technology associated with thermoelectric generation and refrigeration. The technology of thermoelectricity began during the World War II, when the Soviet Union, under Academician Ioffe's inspiration, produced 1-4 watt thermoelectric generators to be included in a "partisan mess kit" and capable of powering a small radio from a small cooking fire.

Rowe DM (2006) Thermoelectrics handbook : macro to nano. CRC/Taylor & Francis, Boca Raton

1.1 Introduction

It is a common consensus that climate change is the biggest environmental and humanitarian crisis of our time. Thus, it is urgent to find alternatives on energy generation and its global utilization. Figure 1.1 shows the energy flow diagram of United States in 2012, indicating the major energy sources and the energy distribution among the final consumers.

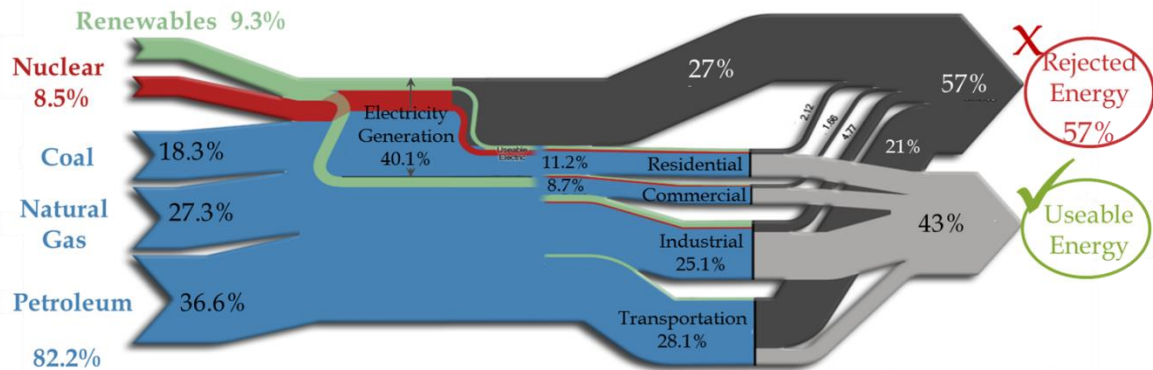


Figure 1.1: Sankey diagram of United States in 2012 showing the contribution of the major energy sources [1].

As it can be seen in the Sankey diagram above, only 43% of total generated energy is useable. The remaining percentage is rejected to the environment as waste heat. Thus, if we achieve to convert even a ~10% of this energy to useful forms, this could have a huge impact on overall energy utilization. In this respect, thermoelectric generators and coolers are highly promising devices, because they can tap into this rejected energy by the direct conversion of temperature difference in voltage and vice versa. It is, thus, common sense that the benefits of increasing the efficiency of such materials/devices are tremendous.

Until recently, thermoelectrics found only limited applications due to their low efficiency. A resurgence of interest in this field [2] came about 20 years ago, when thermoelectrics reached the nanoscale [3]. Then, Hicks and Dresselhaus [2] showed theoretically that by decreasing dimensionality, thermoelectric efficiency can be enhanced beyond initial expectations. This observation, inspired research community and now the interest in thermoelectrics is continuously grown. This short flashback is adequate to explain the Figure 1.2a which shows the number of publications using the word “thermoelectric” during time from 1955 to 2015 (recognizing the fact that neither all publications are relevant nor that such statistics include all relevant activity on the field).

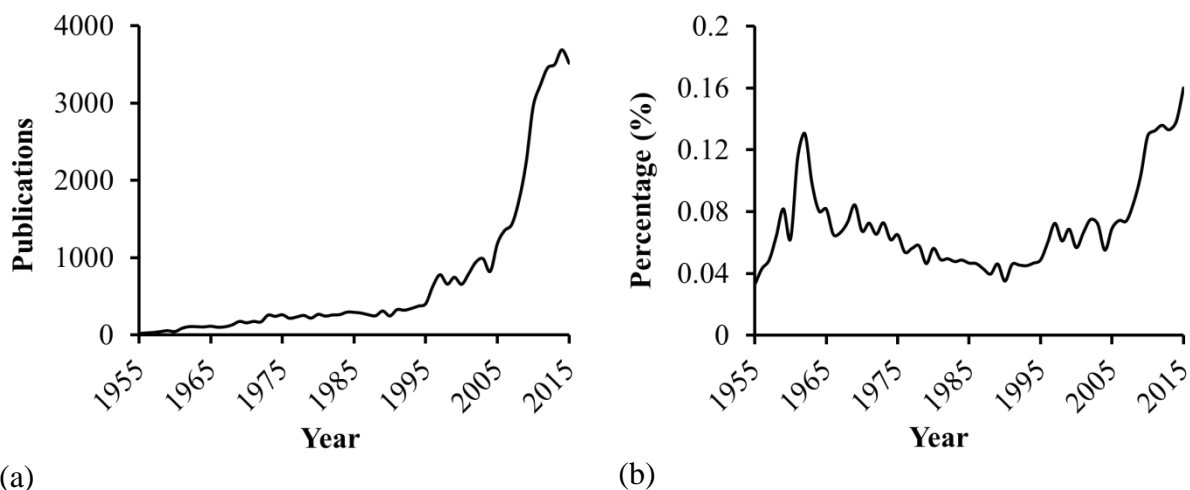


Figure 1.2: a) Number of publications using the word “thermoelectric” during time (1955-2015) and b) as a percentage of all publications for the same period as they can be found in the Scopus database (<https://www.scopus.com/>).

Figure 1.2b depicts the same statistics but as a percentage of all works that have been published in every research field during this period. It is worth noting that in 2015, publications concerning thermoelectrics were 0.16% of all published studies. This is the greatest percentage reached at this field so far. The presented statistics were taken from Scopus database.

In this chapter, the basic principles and theoretical considerations regarding thermoelectric materials and devices will be presented along with applications and examples in different fields of interest, from macro to nanoscale. The requirements that a material should fulfil in order to be a “good” thermoelectric material will be presented. All the thermoelectric parameters that are needed in order to fully characterize a thermoelectric material will be analyzed, while the methods that are commonly used in this respect will be described. Finally, the materials with record performances so far will be reviewed and Si-based thermoelectrics will be introduced, considering that Silicon nanostructures are among the most preferential solutions for such applications, in the frame of feasibility and sustainability.

1.2 Thermoelectric effect

Thermoelectrics is defined as the science and technology associated with thermoelectric generation and refrigeration [4]. **Thermoelectric effect** is the direct conversion of temperature differences to electric voltage and vice versa. The term “thermoelectric effect” encompasses three separately identified effects: Seebeck effect, Peltier effect and Thomson effect. All of them are described below.

1.2.1 Seebeck effect

An electric potential is generated within any isolated conducting material that is subjected to a temperature gradient; this is the **absolute Seebeck effect** [5].

Relative Seebeck effect is the electromotive force production and consequently an electric current in a loop of material consisting of at least two dissimilar conductors, when the two junctions are maintained at different temperatures. This is depicted in Figure 1.3.

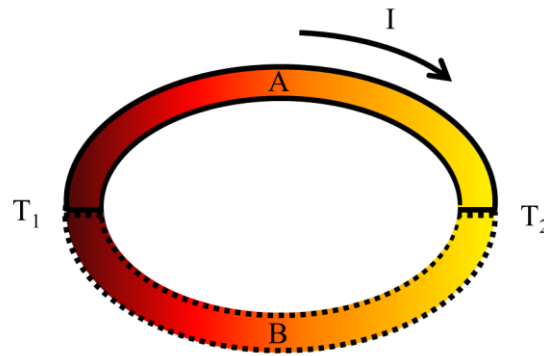


Figure 1.3: Relative Seebeck effect in a closed circuit with A, B two dissimilar conductors, and T_1 , T_2 the temperatures at the two junctions with $T_1 > T_2$ and $S_{AB} > 0$, where S_{AB} is the relative Seebeck coefficient of the two thermoelectric materials A and B in contact.

At the atomic scale, an applied temperature gradient at the two ends of a thermoelectric material causes carriers to diffuse from the hot to the cold side. Mobile charge carriers transport to the cold side, while oppositely charged carriers and immobile nuclei remain at the hot side, giving rise to a thermoelectric voltage. This voltage urges charge carriers to move back to the hot side. When these two transport mechanisms come to equilibrium, steady state condition in the material is reached. Thus, if we have two different thermoelectric materials in contact, voltage is generated due to temperature difference, the so called electromotive (emf) force. In the case of closed circuit (see Figure 1.3), current flows through the conductors, if their junctions are maintained at different temperatures.

We define the **Seebeck coefficient** (S), which is a measure of the magnitude of an induced thermoelectric voltage in response to an applied temperature difference at the two ends of a thermoelectric material. In the case of two materials in contact, the **relative Seebeck coefficient** is defined as $S_{AB} = S_B - S_A$. More details concerning Seebeck Coefficient can be found in the corresponding section.

In general, the Seebeck effect is described by the following equation:

$$\nabla V = -S \cdot \nabla T \quad (1.1)$$

where ∇V is the voltage gradient (V) between two points of a material with temperature gradient ∇T (K) and S is the Seebeck coefficient (V/K).

1.2.2 Peltier effect

The **Peltier effect** is the reverse phenomenon of Seebeck effect and it is assumed to be the origin of the foundation of thermoelectric cooling. Opposed to Seebeck, **relative Peltier effect** is the reversible change in the heat content at an interface between dissimilar conductors that results from the flow of current across it [5]. The rate of heat absorption (or liberation) at the junction (\dot{Q}) between two conductors A and B is given by the following equation:

$$\dot{Q} = \Pi_{AB} \cdot I \quad (1.2)$$

where Π_{AB} is the relative Peltier coefficient ($\Pi_{AB} = \Pi_A - \Pi_B$, where Π_A, Π_B are the **absolute Peltier coefficients** of conductor A and B respectively (V)) and I the applied electric current (A) (from A to B, as shown schematically in Figure 1.4). The **Peltier coefficient** is a measure of the amount of heat carried per unit charge and its sign depends on which junction is heated and which is cooled.

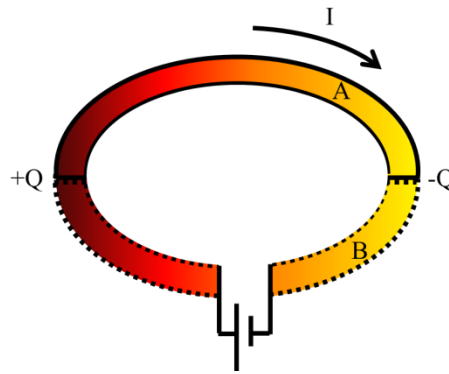


Figure 1.4: Peltier effect when current is applied between two different conductors. One junction is heated up and the other is cooled down by the same amount of heat Q ($\Pi_{AB} > 0$).

As it can be deduced from the previous analysis, if a simple thermoelectric circuit is closed and a temperature gradient exists, then a current will flow in the circuit, due to Seebeck effect. This current, however, in its turn, will transfer heat from one side to the other, due to Peltier effect. Thus, there is a close relationship between these two effects, which is represented with the following equation:

$$\Pi_{AB} = T \cdot S_{AB} \quad (1.3)$$

Both the magnitude and the direction of the heat flow in a thermoelectric circuit do not depend on the junction (neither on its dimensions nor on the contact potential) between the two materials, but only on the type of the materials used. This is applicable both in Seebeck and in Peltier effects. Each material, depending only on its thermoelectric properties, contributes with a specific way in the resulting heat flow in the circuit.

It is worth noting that **Peltier effect** should not be correlated to **Joule heating**. Joule heating does depend on dimensions, it has a quadratic behavior with current and it is an irreversible process, contrary to Peltier effect which is thermodynamically reversible [5].

1.2.3 Thomson effect

The **Thomson effect** is the reversible change of heat content within any single homogeneous conductor in a temperature gradient, when an electric current passes through it [5]. It, practically, describes the heating or cooling of a current-carrying conductor with a temperature gradient, as it is schematically shown in Figure 1.5. The measured rate of Thomson heat conduction is proportional to the current intensity and to the temperature difference, according to the equation:

$$\dot{Q} = -\mu \cdot I \cdot \nabla T \quad (1.4)$$

where μ is the **Thomson coefficient** (V/K), I is the current intensity (A) and ∇T is the resulting temperature gradient (K). Thomson effect can be either positive or negative. If heat is evolved, when current flows from the hotter to the colder side, a positive Thomson effect occurs (Figure 1.5). Oppositely, for the same conditions heat is absorbed and a negative Thomson effect takes place.

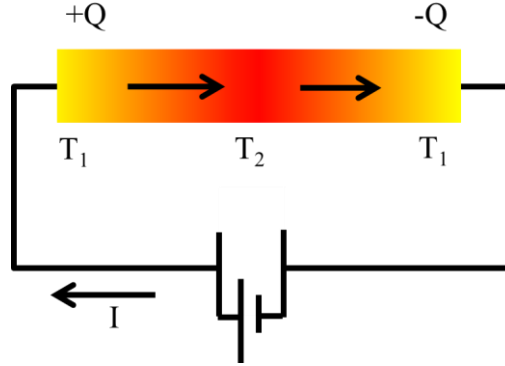


Figure 1.5: Positive Thomson effect in a current-carrying conductor with a temperature difference ($T_1 < T_2$).

1.3 Thermoelectric figure of merit

The thermoelectric performance of a material is characterized by its dimensionless **figure of merit**:

$$zT = \sigma S^2 T / (k_e + k_l), \quad (1.5)$$

where σ is the electrical conductivity (S/m), S the Seebeck Coefficient (V/K), T the absolute temperature (K), k_e and k_l the electronic and lattice components of thermal conductivity (W/m.K) respectively. The factor σS^2 is the well-known **power factor**. The need of improving the overall performance of thermoelectric materials was pointed out in the introduction of this chapter. It is highly demanding to find thermoelectric materials with high zT values. In this respect, high Seebeck coefficient and high electrical conductivity are needed while thermal conductivity should be low. Each one of these parameters is described below along with the most frequently used techniques for their measurement.

1.3.1 Seebeck Coefficient

Absolute Seebeck Coefficient (S), also known as **thermopower** or **thermoelectric power**, is a measure of the magnitude of an induced thermoelectric voltage in response to an applied temperature difference at the two ends of a thermoelectric material. It is a fundamental electronic transport property of a material and is defined as the ratio of thermoelectric voltage (ΔV) to the temperature difference (ΔT):

$$S = -\frac{\Delta V}{\Delta T} \quad (1.6)$$

Practically, Seebeck coefficient is a measure of the entropy that is transferred with a charge carrier as it moves in the volume of a thermoelectric material, divided by the charge itself [4]. Consequently, Seebeck coefficient is determined by the interaction of charge carriers with each other and with phonons.

From the above analysis it is deduced that the thermoelectric power S is the sum of a **diffusion part** S_d and a **phonon drag part** S_{ph} , such that: $S = S_d + S_{ph}$.

The diffusion part results from the spatial variation of the occupation probability of the

charge carriers, which is caused by the temperature gradient along the sample. The phonon drag part is due to momentum that is transferred from lattice vibrations to electrons by electron-phonon scattering [6]. The separation of Seebeck coefficient in these two components is useful later for the interpretation of the measurements carried out on porous Silicon samples.

1.3.1.1 Seebeck coefficient measurement methods

In Seebeck Coefficient metrology, the diversity in apparatus designs, data acquisition and contact geometry has resulted in conflict materials data [7]. Practically, it was just very recently when Lowhorn et al. from National Institute of Standards and Technology (NIST) reported the development of a certified Seebeck coefficient Standard Reference Material from 10 to 390K [8]. This is a bar-shaped piece of nonstoichiometric telluride.

In order to extract S of a thermoelectric material, a temperature difference must be applied and measured at two points of the sample under test with simultaneous measurement of the resulting thermovoltage. Then S is extracted straightforward from Equation (1.6). The basic requirements for obtaining an accurate Seebeck coefficient measurement are:

- ✓ Good thermal and electrical contacts
- ✓ Synchronous measurement of voltage and temperature
- ✓ Accurate measurement of small voltages and temperatures with eliminating external parasitic contributions

Extracting reliably the Seebeck coefficient of a material and, especially when it is in thin film form, is not an easy task. In the following section, the relevant measurement methods and possible arrangements are summarized [9, 10].

Although the dimensions of a sample do not affect its S , the accuracy of the measurement depends on the used configuration. There are two possible such arrangements; two and four-point probe.

- *Two point-probe configuration*

In two-point probe configuration, the temperature difference and the thermoelectric voltage are measured on the probes (hot and cold sinks), which are in direct contact with the ends of the sample, as it is shown in Figure 1.6. Such arrangement is preferred since it is simpler and avoids contacts problems [9].

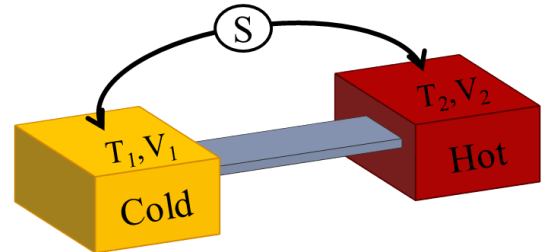


Figure 1.6: Two-point probe arrangement for Seebeck coefficient measurements

- *Four-point probe configuration*

In four-point probe configuration, the temperature and thermoelectric potential are measured at two points of the sample and separately from the hot and cold sinks, as Figure 1.7 depicts. This arrangement is convenient when the same platform is used for the electrical conductivity measurements, because with the four-point probe this measurement is far more accurate, as it will be described in the relevant section.

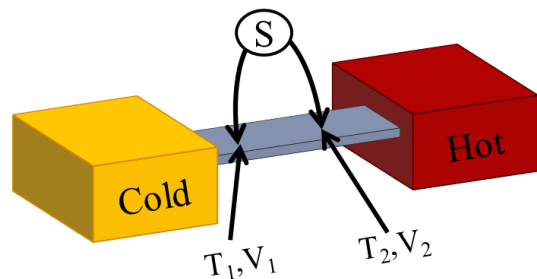


Figure 1.7: Four-point probe configuration for Seebeck coefficient measurements

Each configuration described above can be used in either integral or differential Seebeck coefficient measurement mode [9]. Both of them are reviewed below.

- *Integral method*

In the integral mode, large temperature differences are applied at the two ends of the sample under test and the corresponding thermovoltage is measured. An analytic approximation is then used to fit the experimental data. The Seebeck coefficient is obtained by differentiating these data. This method minimizes the influence of voltage offsets due to large temperature gradients; corresponding errors are thus minimized. However, due to the complex temperature dependence of S , there is no simple analytical expression to be used for fitting the experimental data. Moreover, there are not objective criteria to evaluate the accuracy of the obtained derivative. To overcome the drawbacks of this method, the differential one can be used instead.

- *Differential method*

In this method, a small temperature gradient is applied between the two ends of the thermoelectric material under test and the induced potential is simultaneously measured. Limiting the measurements in a short enough temperature range, the Seebeck coefficient is just the ratio of voltage difference to the temperature gradient (considering linear dependence of Seebeck coefficient with temperature at this specific range). Even though the differential method solves the problems related to the integral method, it demands much more sensitive instrumentation because the gradients measured could be very small.

The differential method is distinguished in three categories: steady-state, quasi-steady-state and transient. A brief description of each of these categories is given in the following paragraphs.

- *Steady-state condition*

As its name indicates, measurements are recorded after the steady-state condition in the thermoelectric system is reached. Then, multiple measurements are taken and the Seebeck coefficient is extracted from the linear fit of thermovoltage vs temperature difference data points. This way, the possible voltage offsets are eliminated. Although the method applying steady-state conditions is proved to be accurate enough, it is time consuming and thus impractical and inefficient. An improved alternative is the use of quasi-steady state condition.

- *Quasi-steady-state condition*

In this case, multiple measurements are recorded before a steady-state condition is reached. Heat flux increases continuously during data recording. It is essential that instrumentation and data acquisition are carefully designed and used because thermal offsets could be introduced. A common solution to diminish such effects is to use interpolated data for the time dependence of temperature and voltage [11].

- *Transient condition*

When the transient method is used, a sinusoidal temperature difference is applied between the two ends of the thermoelectric sample. Then lock-in amplifiers are used to extract the voltage and temperature difference and consequently Seebeck coefficient. While faster, this technique has some limitations concerning the thickness of the samples. In addition, there are no objective criteria on the appropriate frequency range for an accurate measurement. Moreover, the requirement of lock in amplifiers increases the cost and adds complexity to data acquisition.

1.3.2 Thermal conductivity

Thermal conductivity k is the property of a material to conduct heat. Heat energy is transmitted through solids via electrical carriers, phonons, electromagnetic waves, spin waves or other excitations. The total thermal conductivity of a material is the sum of all the components representing the different excitations that occur in the solid [12]. However, the main heat carrying entities in solids are charge carriers and phonons, with other excitations contributing much less to the total thermal conductivity. Thus, in most cases other contributions are considered to be negligible. This assumption leads to the simplification that thermal conductivity of a solid is composed of two independent terms: the **electronic** (k_e) and the **lattice** (k_l) parts, such that:

$$k = k_e + k_l \quad (1.7)$$

According to **Fourier's law** of conduction, thermal conductivity is defined as the rate of heat flow through a square meter of a solid where a temperature gradient exists in the direction of heat flow and it is given by the following equation:

$$k = -\frac{\vec{q}}{\vec{\nabla}T} \quad (1.8)$$

where \vec{q} is the heat flux vector (W/m^2) across a unit cross section perpendicular to \vec{q} and T is the absolute temperature (K).

Thermal conductivity, and particularly its temperature dependence, is related to the structure and morphology of solids. Furthermore, thermal conductivity is a key parameter in the characterization of thermoelectric materials. Thus, its accurate measurement is necessary for the estimation of the overall thermoelectric performance of a material.

1.3.2.1 Thermal conductivity measurement methods

The accurate measurement of this parameter can pose many challenges. The structure of the sample, its dimensions and the thermal conductivity value itself should be taken into account in order to minimize measurement errors. Particularly, when sizes go down to nanometer scale and/or thermal conductivity values go to extremes, practical and other issues may be arise.

This section provides a review of the more typical measurement methods for thermal conductivity characterization, along with their advantages and drawbacks. Thermal conductivity measurement techniques can be categorized according to the diagram of Figure 1.8 and are comprehensively reviewed in Ref. [12]. The general principle of all the measurement techniques is heating of the sample (either electrically or optically) and then measuring heat transport through the material under test.

As it can be seen in Figure 1.8 there are electrical and optical heating and sensing methods with the former being direct and the latter indirect. Generally, using direct methods, the amount of heat transfer into the sample can be precisely controlled and the temperature increase due to the heat pulse can be accurately determined. Thus, electrical methods are more frequently used for such measurements.

The electrical direct methods can be distinguished in steady-state and transient methods. Both of them were used and compared in this thesis. In the following, a brief description of each method will be given.

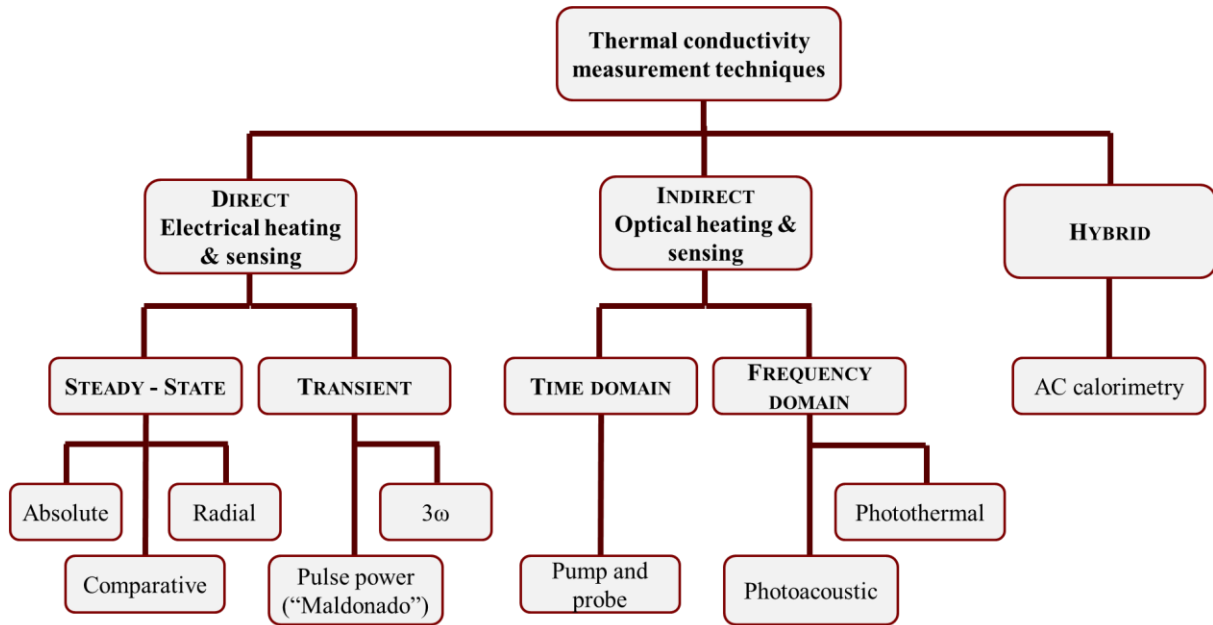


Figure 1.8: Diagram showing the most typical measurement techniques to obtain thermal conductivity.

- *Steady state direct current (dc) method*

This method is based on the measurement of thermal conductance from sensing an induced temperature difference at two points of the sample under test in response to an applied heating power. Then taking into account the dimensions of the sample, thermal conductivity is obtained using the following relation:

$$k = \frac{\dot{Q} \cdot L}{A \cdot \Delta T} \quad (1.9)$$

where L is the distance between the two points under test (m), A is the cross sectional area of the sample perpendicular to heat flow (m^2), \dot{Q} is the heating power (W) and ΔT the measured temperature difference (K). Practically, the above equation is the Fourier's law of heat conduction assuming one-dimensional (1-D) geometry of a homogeneous material.

- *Steady state dc method combined with FEM analysis*

There are cases for which the one-dimensional heat conduction model does not give a good approximation and thus should not be applied. In these cases, a modification of the method can be used, in which the experimental data of heating power and induced temperature differences are combined with **Finite Element Method (FEM)** analysis to obtain thermal conductivity of the sample under test [13–15]. This method was used for temperature dependence thermal conductivity measurements of porous Silicon and it is explained in detail in the experimental part of the thesis.

Depending on the configuration used, the steady state method can be either comparative or radial.

- *Comparative technique*

In the comparative approach, a standard material with known thermal conductivity is placed in series between the heater and the sample. This method is best suited when the thermal conductivity of the standard is comparable to that of the sample. Then, Equation (1.9) should be modified to incorporate the total thermal conductance as the sum of the two materials. Taking into account the specific dimensions of each material, the thermal conductivity of the sample under test is extracted using the following equation:

$$k = k_s \left(\frac{A_s \cdot \Delta T_s \cdot L}{A \cdot \Delta T \cdot L_s} \right) \quad (1.10)$$

where the subscript s stands for the “standard” material. This method adds more thermal contact points and thus is less accurate.

- *Radial flow technique*

Finally, in the radial flow configuration [16], heat is applied internally in cylindrical shaped samples. To provide accuracy, the length of the sample should be much larger than its radius to obtain a uniform radial heat flow at the mid-section of the sample.

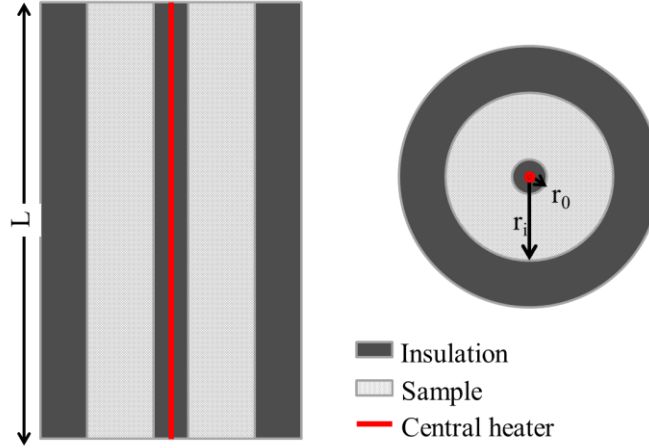


Figure 1.9: Cross sectional and to view schematic representation of the radial heat flow configuration

Then again Equation (1.9) is modified to:

$$k = \frac{\dot{Q} \cdot \ln(r_o/r_i)}{2 \cdot \pi \cdot L \cdot (T_i - T_o)} \quad (1.11)$$

where r_o and r_i are the inside and outside radius (m) where the corresponding T_o and T_i temperatures (K) are measured (see Figure 1.9). However, this method is much more difficult to apply and it requires cylindrical samples, thus is rarely used.

Summarizing, in all the aforementioned configurations of steady state method the choice of the specimen geometry is dictated by the conductivity to be measured, by thermometer sensitivity, and by the maximum and minimum values of heating power that can be tolerated [5]. Special care should be given in estimating the possible heat losses during measurements in order to obtain the best accuracy. Finally, as it was also pointed out for Seebeck coefficient measurements, depending on the sample and the conditions used this method can be impractical due to long waiting times until steady state condition to be reached.

- *Transient electrical methods*

An alternative to the steady state methods that solves the impractical and inefficient long times involved in the steady state methods is the transient ones. The most frequently used such techniques are summarized below.

- *Pulse power “Maldonado” technique*

The experimental set-up for this technique is the same as in steady-state method, except that the heating current is modulated by a square wave of constant current. Thus, small thermal gradients are induced [17]. Maldonado used this method to extract both thermal conductivity and thermopower of the samples.

- *3 ω method*

3 ω method is a widely implemented approach for measuring thermal conductivity of bulk materials and thin films and was first introduced by Cahill [18].

In the 3 ω method a thin metallic strip lying on the surface of the sample under test acts both as a heater and thermometer. 3 ω can be used in both two and four point probe configurations as it is shown in Figure 1.10. If the sample is electrically conductive, a thin insulating film must be grown before the deposition of the resistor.

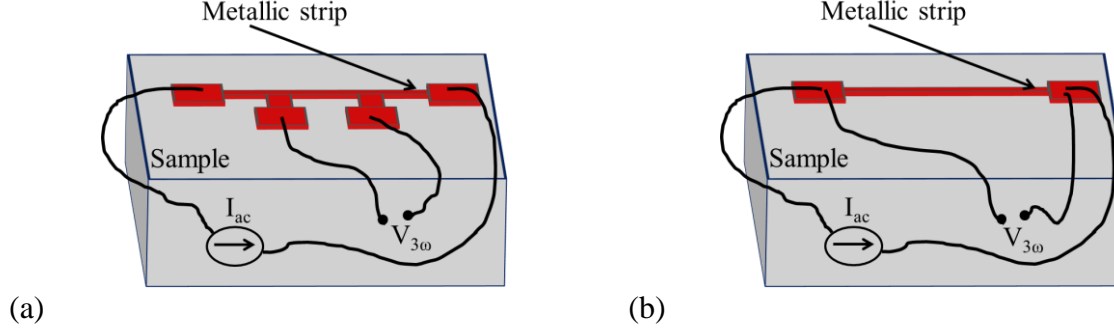


Figure 1.10: 3D schematic representation of the test structures used for 3 ω measurements in (a) four-point probe and in (b) two-point probe configuration respectively.

An alternative current (ac) $I_h(t) = I_{ho} \cos(\omega t)$ with angular frequency ω (rad/s) and amplitude I_{ho} (A) is applied to the strip. Due to Joule heating, this current creates an oscillating heat source $\dot{Q}(t) = \frac{1}{2} I_{ho}^2 R_{ho} (1 + \cos(2\omega t))$, where R_{ho} is the resistance of the metallic resistor (Ω) at the reference temperature. The corresponding temperature rise is composed of a dc part (ΔT_{DC}) and a 2ω modulated part ($|\Delta T_{AC}| \cos(2\omega t + \varphi)$), where φ is the phase shift between the temperature oscillations and the excitation current. Considering linear dependence of the resistance of the metallic strip on temperature, the steady-state harmonic oscillations in the heater produce harmonic variations in the resistance given by:

$$R_h(t) = R_{ho} (1 + \beta_h (\Delta T_{DC} + |\Delta T_{AC}| \cos(2\omega t + \varphi))) \quad (1.12)$$

Consequently the voltage drop across the heater can be calculated from Ohm's law as:

$$V_h(t) = I_{ho} R_{ho} \left[(1 + \beta_h \Delta T_{DC}) \cos(\omega t) + \frac{1}{2} \beta_h |\Delta T_{AC}| \cos(\omega t + \varphi) + \frac{1}{2} \beta_h |\Delta T_{AC}| \cos(3\omega t + \varphi) \right] \quad (1.13)$$

In the above equation β_h is the **temperature coefficient of resistance (TCR)** of the heater.

The 3 ω voltage components are measured with a lock-in amplifier and used to calculate corresponding in-phase and out-of-phase temperature oscillations, from which the thermal conductivity of the sample is extracted.

Different ways to extract thermal conductivity from measured 3 ω voltages have been proposed in the literature, either analytically or using complex equations. A different approach using FEM simulations is also proposed in this thesis. A detail discussion and comparison with proposed models taken from the literature can be found in Chapter 3.

- *Optical methods*

Optical indirect techniques have also been reported for thermal conductivity measurements. It should be noted that, in general, optical methods require much more expensive equipment and, in addition, some properties of the samples should be known for determining thermal conductivity. Thus, the electrical methods are generally preferred. However, optical methods are non-destructive and they do not require special sample preparation. Thus, they can be useful when the samples are fragile and cannot withstand the microfabrication process used for sample preparation for the electrical measurements. The most typical optical measurement

methods are the pump and probe, the photoacoustic and the photothermal methods, which are briefly discussed below.

- *Pump and probe method*

This technique is well suited for measurements on very thin layers because of the very short effective penetration depth. A metallic film is usually deposited on the layer under test (in the case of dielectric or semiconducting films). The metallic coating must be thicker than the absorption depth of the layer and thin enough, so as to assume uniform temperature of the coating.

A pump light pulse is focused on the sample and induces a temperature increase on the metallic film. This temperature rise results in a proportional change in the optical reflectivity [19]. The temporal temperature response can be measured with fast radiation detectors in the case of nanoscale laser heating or using time-delayed probe light pulse for femtosecond and picosecond laser heating, respectively [12]. Using these data, thermal conductivity is extracted. However, proper considerations should be made in order to obtain an accurate value, taking into account all the experimental parameters in the data analysis.

- *Photoacoustic method*

Photoacoustic spectroscopy is a powerful tool in the optical and thermal characterization of semiconductors [12] and thereby it can be also applied for thermal conductivity measurements.

A modulated monochromatic light beam is used to thermally excite the surface of the sample, which is placed inside a sealed photoacoustic cell with an optically transparent window. The resulting modulated thermal gradients on the surface of the sample induce acoustic waves in the gas inside the cell, which can be detected by a commercial microphone. The resulting signal depends on both the amount of heat that is generated on the sample and on how the heat diffuses through the sample [20]. Of course, the photoacoustic signal is also affected by the thermal properties of the gas inside the cell. However, these parameters are usually known and, thus, thermal diffusivity and thermal conductivity of the sample can be both obtained using the acquired data.

- *Photothermal method*

In all photothermal methods, the sample is heated using a modulated continuous-wave laser. The induced temperature rise on the surface of the sample can be monitored by changes in reflected beam or thermal emission and expansion signals. Depending on the detected signal, the corresponding photothermal method is developed and named differently [12]. In each case, different equipment and considerations are needed.

- *Hybrid methods*

As the diagram in Figure 1.8 displays, it is possible to measure thermal conductivity using a combination of electrical heating and optical sensing and vice versa. These are commonly known as hybrid methods and the well-developed AC calorimetry method is described below.

- *AC calorimetry*

In this method the heating of the sample is applied using a laser, while the induced temperature increment is measured with thermometers lying on the surface of the sample. The distance between the laser and the sensors must be taken into account. As an alternative approach, the sample can be heated using a resistor on its surface and the thermal response can be obtained by reflectance change or thermal emission from the sample. A comprehensive

review in ac calorimetry can be found in Ref. [21], where all the possible heating and sensing methods are presented and discussed.

1.3.3 Electrical conductivity

Electrical conductivity σ is one of the most important electrical parameters of semiconductors. It measures the ability of a material to conduct an electrical current. It is an intrinsic property of a material and it is the reciprocal of electrical resistivity. **Electrical resistivity** ρ is a property related to carrier drift in materials such as metals and semiconductors [22]. Macroscopically, it is the normalized resistance of the material by its dimensions and for a uniform current flow in a resistor, like the one shown in Figure 1.11, is given by the following equation:

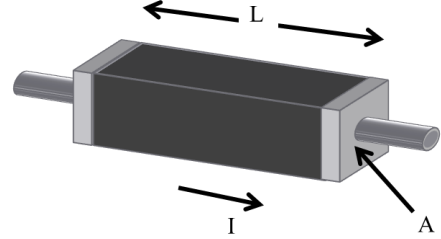


Figure 1.11: Resistive material with metal contacts in which equation 1.14 can be applied.

$$\rho = \frac{R \cdot A}{L} \quad (1.14)$$

where R is the resistance of the material (Ω), A is the cross sectional area perpendicular to current flow (m^2) and L is the length of the material (m). The electrical resistivity is measured in ($\Omega \cdot m$).

In case of thin semiconducting layers, **sheet resistivity** ρ_s (Ω/\square) can be used instead of ρ , which is the resistivity divided by the **thickness** t of the layer.

Microscopically, from solid state theory, electrical resistivity of a homogeneous semiconductor is given by the following relation:

$$\rho = \frac{1}{q \cdot (n \cdot \mu_n + p \cdot \mu_p)} \quad (1.15)$$

where q is the electronic charge (C), n and p are the free electron and hole concentrations (m^{-3}) respectively and μ_n and μ_p their drift mobilities ($m^2 V^{-1} s^{-1}$).

1.3.3.1 Electrical conductivity measurement methods

The most frequently used measurement techniques to obtain the electrical resistivity of bulk materials and thin films are: the two and four point probe methods and the Van der Pauw technique. All of them are described in the following paragraphs.

- *Two point probe method*

The simplest way to measure electrical resistivity is by measuring the resistance of a uniform strip with specific dimensions. This can be easily implemented by applying a dc current at its ends and measuring the resulting voltage. Then, using the dimensions of the sample, electrical resistivity is extracted from Equation (1.14). The main drawback of this measurement technique is the contact resistances. Particularly, the measured resistance incorporates the contact resistances, a fact that introduces significant errors when specific care is not taken to reduce them. Additionally, if probes are used for the measurement, instead of large metallic contacts, the spreading resistances are also part of the total resistance measured [22]. Thus the obtained resistivity value is much less accurate. All these uncertainties can be surmounted using the four point probe method.

- *Four point probe method*

In this case, the measurement is made using four contacts. The dc current is applied at the outer ones, while the voltage is measured at the inner ones, as Figure 1.12 schematically

shows. The most usual geometry is the in-line probe arrangement and particularly with equal probe spacing s . For a bulk material of semi-infinite thickness and probes far away from any boundary (see Figure 1.12a), resistivity is simply calculated by [22]:

$$\rho = 2 \cdot \pi \cdot s \cdot \frac{\Delta V}{I} \quad (1.16)$$

where s is the probe spacing (m), I is the applied current (A) and ΔV the measured voltage (V).

For thin semiconducting film on an insulating substrate (see Figure 1.12b) the above relationship is replaced by:

$$\rho = 4.532 \cdot t \cdot \frac{\Delta V}{I} \quad (1.17)$$

For the above equation to be valid the thickness t of the film must be much smaller than the half of the probe spacing s (i.e. $t < s/2$).

This method eliminates errors from contact and spreading resistances and thus it was applied for all the electrical conductivity measurements throughout the present study.

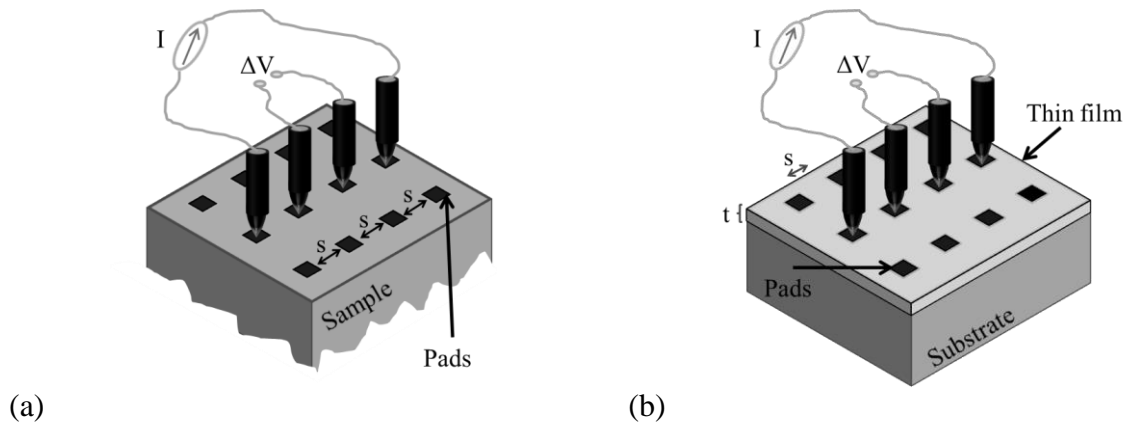


Figure 1.12: Four point probe configuration for electrical resistivity measurement of (a) bulk semi-infinite material and (b) thin semiconducting film on an insulating substrate

- *Van der Pauw method*

Another commonly used technique to measure electrical resistivity is the Van der Pauw method [23]. Its basic advantage is that it can accurately measure the electrical resistivity of a sample with arbitrary shape (Figure 1.13). Apart from electrical resistivity, it can be used for mobility and sheet carrier density measurements and for determining the type of the semiconductor (n- or p- type). Four contacts are used again, which are placed in the periphery of the sample. Current is applied at two adjacent contacts and the voltage is measured in the remaining ones. Then, the resistivity of a uniform sample with thickness t is given by [22]:

$$\rho = \frac{\pi \cdot t}{\ln 2} \cdot \frac{(R_A + R_B)}{2} \cdot f \quad (1.18)$$

where $R_A = \frac{V_3 - V_4}{I_{1,2}}$ and $R_B = \frac{V_4 - V_1}{I_{2,3}}$ and f is a correction factor. In the case of symmetrical geometries the above equation is simplified to:

$$\rho = \frac{\pi \cdot t}{\ln 2} \cdot R_A \quad (1.19)$$

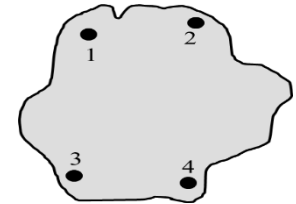


Figure 1.13: Sample arbitrary shaped with contacts for Van der Pauw method

An important note should be made here. The electrical resistivity measurements are carried out in order to characterize thermoelectric materials, thus the thermoelectric effects should be taken into account during the measurements. Peltier effect can be significant during the electrical measurement, introducing temperature gradients along the sample. This fact induces

an additional thermoelectric potential at the contacts where the voltage is measured (V_{measured}) such that [4]:

$$V_{\text{measured}} = V_{\text{IR}} + S \cdot \Delta T \quad (1.20)$$

where V_{IR} is the resistive voltage (V) and $S \cdot \Delta T$ is the thermovoltage induced by the temperature difference that Peltier effect creates. In order to eliminate such errors, relatively fast measurements should be acquired (~ 2 - 3 sec) or switching the current direction during the measurement, either using a fast-switching DC or AC current source. In this way the Seebeck voltage is practically subtracted if we get the average of measurements in two opposite directions..

1.4 Optimization of the thermoelectric performance of a material

As it was mentioned in section 1.3, the thermoelectric performance of a material is characterized by its dimensionless **figure of merit** (zT). Thus, materials with high zT values are needed for optimum thermoelectric devices. As follows from Equation (1.5), to obtain a

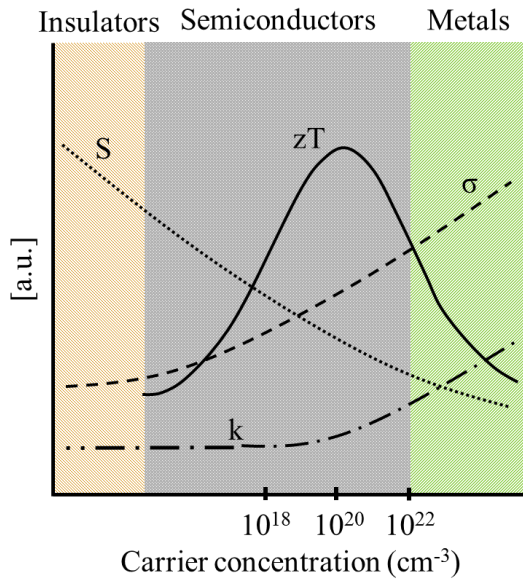


Figure 1.14: Seebeck coefficient (S), electrical conductivity (σ), thermal conductivity (k) and figure of merit (zT) of materials with respect to their carrier concentration [24].

high zT , the material should show increased power factor ($\sigma^2 S$) and reduced thermal conductivity ($k_e + k_l$). However, all these thermoelectric properties are somehow correlated and their interdependency makes the enhancement of zT very challenging. The interplay between the conflicting parameters is illustrated in the graph shown in Figure 1.14, where S , σ , k and zT are plotted as a function of carrier concentration [24].

As Figure 1.14 shows, the best zT is obtained for heavily doped semiconductors. Insulators have very poor electrical conductivity that leads practically to inefficient thermoelectric performance, independently of their giant Seebeck coefficient. On the other hand, metals show higher zT , even higher than that of lightly doped semiconductors. However, their high thermal conductivity and relatively low Seebeck coefficient result in lower zT compared to semiconductors with high carrier concentration ($\sim 10^{20} \text{ cm}^{-3}$), where the zT peak is observed.

The high thermal conductivity of metals is attributed to its dominant electronic part k_e , which is proportional to electrical conductivity as **Wiedemann-Franz law** [25] predicts:

$$k_e = L \cdot \sigma \cdot T \quad (1.21)$$

where L is the Lorenz factor $= 2.4 \cdot 10^{-8} \text{ W} \cdot \Omega \cdot \text{K}^{-2}$ for free electrons. By substituting Equation (1.21) to the equation that defines zT , the following relation is obtained:

$$zT = \frac{S^2 / L}{1 + k_l / k_e} \quad (1.22)$$

Thus, for metals with very high electrical conductivity, where $k_l / k_e \ll 1$, the figure of merit is practically determined by only the Seebeck coefficient [26], as it is also shown in Figure 1.14.

Contrary to metals, in semiconductors both electronic and lattice components affect the total thermal conductivity. Particularly in the doping range of interest, where the zT peak occurs, the latter one is dominating. This is the reason why a common strategy to obtain a material with high zT is to make its lattice thermal conductivity vanish.

The idea of improving zT by reducing the lattice contribution to thermal conductivity, while keeping relatively high electrical conductivity and Seebeck coefficient, provides a useful strategy, known as ***electron crystal – phonon glass*** approach [5]. The idea is a material that could conduct the electrical current like a long-range ordered crystalline material and on the other hand to inhibit heat flow like an amorphous one. In this respect different approaches have been proposed to introduce scattering sites in a material with the aim to impede the phonon propagation and thus reduce the lattice thermal conductivity without significant reduction in power factor. The most typical of those are [27]:

- *Alloying solids with good electronic properties (point defect approaches), with most efficient case so far that involving heavy atoms (i.e. BiSb, ZnSb and SiGe)*
- *Filling complex lattice structures (like skutterudites and clathrates) with nanoparticles or “rattling” atoms*
- ***Nanostructuring of semiconductors and generally use of low dimensional systems.*** *This strategy includes among the others the study of thin films and nanograin and porous materials. Such examples are nanograin Si and porous Si which were both studied in this thesis. These materials can potentially be embodied in the family of “good Si-based thermoelectrics”. For more information concerning Si-based thermoelectrics see section 1.5.*

Another approach to increase zT apart from reducing thermal conductivity is to increase power factor by manipulating electronic density of states (DOS). This can be achieved using quantum confinement phenomena in low dimensional systems [28].

1.4.1 State-of-the-art thermoelectric materials

All the concepts described above aim at enhancing the zT of a thermoelectric material. According to their zT , thermoelectric materials are distinguished in three categories [29]:

- ✓ Materials with average zT of about 1.0 are the first generation thermoelectrics
- ✓ Materials with average zT from 1.0-1.7 are known as the second generation thermoelectrics
- ✓ Materials with zT from 1.8 to 2.2 are called “the third generation thermoelectrics”

Figure 1.15 summarizes the state-of-the-art zT values of thermoelectric materials that have been reported so far as a function of temperature. For simplicity reasons only the highest values are presented and not the temperature dependence of zT of each material. Moreover, the graph is limited to reviewing p-type bulk materials because they used to have, in general, better performance, while only p-type materials were studied in this work. As it can be extracted from the figure, the zT value of ~2.6 for SnSe at 923K is the highest published so far.

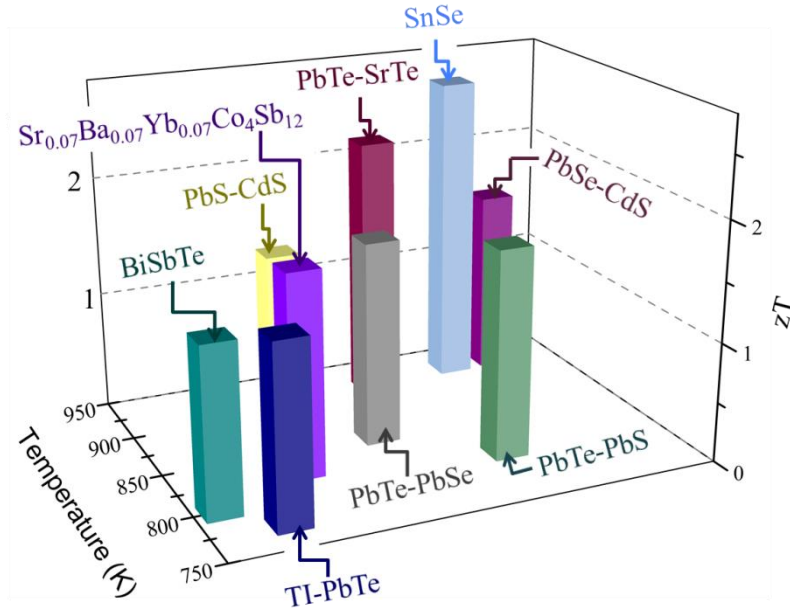


Figure 1.15: State-of-the-art bulk p-type thermoelectric materials. The graph shows the thermoelectric figure of merit (zT) as a function of temperature for the record p-type thermoelectric materials so far: BiSbTe [30], $\text{Sr}_{0.07}\text{Ba}_{0.07}\text{Yb}_{0.07}\text{Co}_4\text{Sb}_{12}$ [31], TI-PbTe [32], PbTe-PbS [33], PbTe-PbSe [34], PbTe-SrTe [35], PbS-CdS [36], PbSe-CdS [37] and SnSe[38].

1.5 Si-based thermoelectrics

Conventionally, the aforementioned state-of-the-art thermoelectric materials achieve high zT values with bismuth telluride and lead telluride finding already commercial applications at different operating temperatures. Their high zT is mainly attributed to the low thermal conductivity because of the heavy elements in these materials, which, however, do not deteriorate their electrical properties.

Notwithstanding, the above materials include rare or toxic elements, while they have exotic properties and low stability. Among the others, telluride, due to its limited availability in the earth's crust, is too expensive. It is worth noting here that material's sustainability should be also evaluated in order for a material to be considered for use in a product. Yadav et al. [39] recently studied the feasibility and sustainability of thermoelectric materials with high zT for large scale deployment. They concluded that the most expensive materials are the ones that contain rare earth elements. Even though some of them show very good thermoelectric performance, this does not necessarily mean that they are feasible to be used in large-scale applications. Thus, what should the research community look for, is to establish economical, scalable and environmentally friendly thermoelectric solutions.

Silicon is the second most abundant element on earth crust and thus its availability is nearly inexhaustible! This fact makes Si a very cheap material. Among the others, Silicon is the basic material of modern semiconductor electronics and therefore there is huge infrastructure and know-how available for its production and processing. Monocrystalline Si is very poor thermoelectric material due to its high thermal conductivity; however this can be improved through nanostructuring, thus making it promising. Apart from the advantages of incorporating Si in large scale thermoelectric devices due to its abundance, the enhancement of its zT can potentially have a huge impact in the modern technological world. This is because it is highly beneficial to combine Silicon with other CMOS (Complementary Metal Oxide Semiconductor) devices towards both lowering fabrication cost and more importantly adding more functionality to Si by combining logic and memories with other functions

(system – on – chip : SoC). Thus, we can imagine that an efficient thermoelectric generator or cooling device on chip would be of great technological interest. It is now more than obvious why the community is “desperately seeking silicon” as a thermoelectric material [40]. A brief sum up of the best Si-based thermoelectric materials is given in the following section.

In this respect, the present study focused on characterizing Si-based and Si-compatible materials for use in integrated thermoelectric devices. Apart from measurements of their thermoelectric performance, a comprehensive study on using porous Si as an integrated thermal insulating platform on which thermoelectrics could be integrated is presented.

1.5.1 State-of-the-art Si-based thermoelectric materials

Having the motivation to study Si-based and Si-compatible thermoelectric materials, the development that has been already achieved in this field is briefly summarized here. Figure 1.16 shows the temperature dependence of the record zT values of different Si-based materials. Both experimental and theoretical results taken from the literature are depicted in the Figure. 20nm width Si nanowires that have been reported by Boukai et al. [41] are since 2008 the champion in Si-based thermoelectrics, showing their best performance at 200K with a zT of ~ 1 . On the other hand, the nanoporous silicone-based nanoribbons was proved to be very promising alternatives with calculated zT reaching 3.1, a value that is insensitive to temperature from 100K up to 400K, as Sadeghi et al. [42] very recently reported, based on theoretical studies. In the majority of the materials shown in the following graph, the high zT was obtained by exploiting the advantage of phonon confinement in Si nanostructures to both decrease thermal conductivity and enhance or not deteriorate significantly power factor.

Although Si nanowires and nanomeshes (i.e. holey Si) exhibit such high zT values, it is a great challenge to incorporate them in the mainstream planar CMOS configuration so far. Thus, nanocrystalline and porous Si were studied in this thesis as promising alternatives for the on-chip integration of thermoelectric devices.

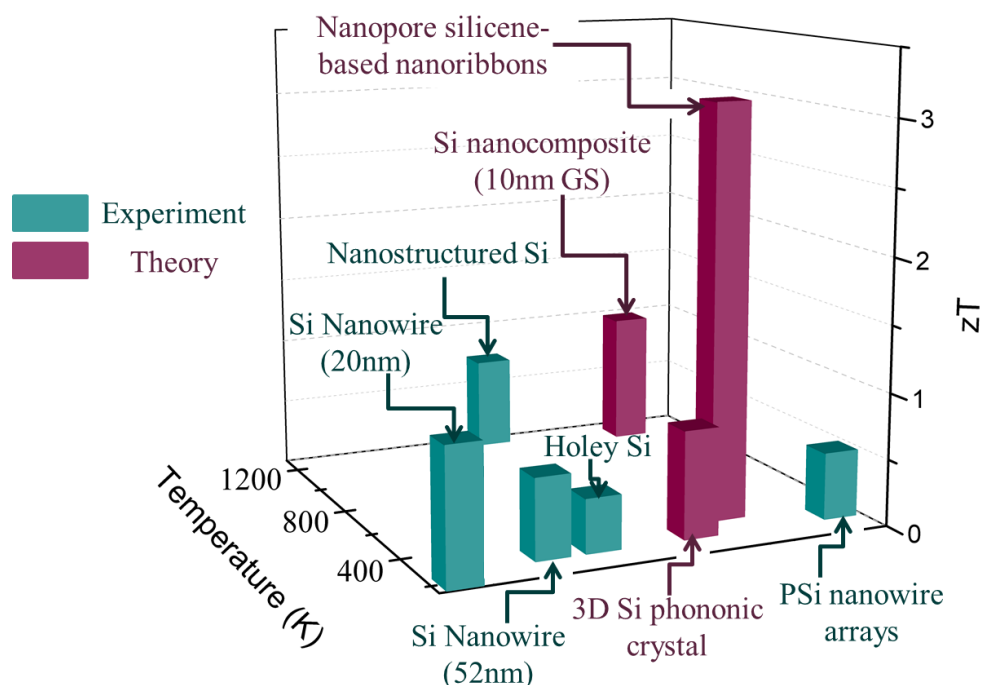


Figure 1.16: State-of-the-art Si-based and Si-compatible thermoelectric materials taken from the literature. The experimental values concern: 20nm width Si nanowire [41], nanostructured bulk Si [43], 52nm width Si nanowire [44], holey Si [45], porous Si nanowire arrays [46] and theoretical studies are for: 3D Si phononic crystals [47], Si nanocomposites with 10nm average grain size [48] and nanopores silicone-based nanoribbons [42].

1.6 Thermoelectric applications

Until this point, thermoelectric materials and their figure of merit were the focal point of the literature review as an introduction to the subject of the thesis. In this section, the use of thermoelectric materials in thermoelectric applications will be presented. According to the configuration and working mode, thermoelectric applications can be divided into three categories: *power generators*, *coolers* and *thermal sensors*.

All the thermoelectric devices, independently of their working mode gather a number of advantages which are:

- ✓ they are solid state reliable devices with no moving parts
- ✓ they operate with low noise and vibration
- ✓ they have long lifetimes without the need of any maintenance
- ✓ they can be easily controlled with electronics and they are scalable
- ✓ their operation does not involve any harmful working fluid

It should be mentioned here that the efficiency of a thermoelectric device depends on many other parameters apart from the zT of the materials involved. Operating temperature, thermoelectric compatibility issues, thermal contacts and other thermal losses are some of them. Thus, undoubtedly the ZT of a thermoelectric device is much smaller than the zT of the thermoelectric materials that incorporates (ZT (upper case) is to distinguish the figure of merit of a device for the specific material zT (lower case)). For a Peltier cooler the *device* ZT_c is defined from [26] equation:

$$\Delta T_{\max} = \frac{ZT_c^2}{2} \quad (1.23)$$

where ΔT_{\max} is the maximum temperature drop that can be achieved. For a thermoelectric generator on the other hand, ZT_G is obtained from the *maximum efficiency* (η_G) such that:

$$\eta_G = \frac{(T_h - T_c)}{T_h} \cdot \frac{\sqrt{1 + ZT_G} - 1}{\sqrt{1 + ZT_G + \frac{T_c}{T_h}}} \quad (1.24)$$

where T_h and T_c are the temperatures at the hot and cold site of the device, respectively. Like all heat engines, the maximum power-generation efficiency of a thermoelectric generator is thermodynamically limited by the *Carnot efficiency* η_c .

Figure 1.17 shows for comparison the ratio of thermoelectric power *generator efficiency* (η_G) to the Carnot efficiency (η_c) as a function of device ZT . The data shown in the Figure were obtained considering $T_c = 300K$ and $T_h = 500K$, $\eta_c = 40\%$. From the graph of Figure 1.17 we can deduce that a realistic scenario with a device thermoelectric figure of merit of approximately 1 predicts efficiency of 20% that of the Carnot limiting efficiency at these operating temperatures. In the following sections, the operation principles and basic considerations concerning the three thermoelectric applications mentioned before are summarized.

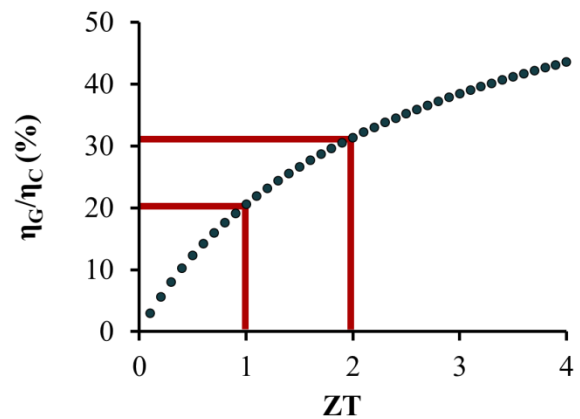


Figure 1.17: Ratio of thermoelectric generator efficiency to Carnot efficiency for $\Delta T=200K$ and $T_c=300K$.

1.6.1 Thermoelectric generator

A thermoelectric generator contains a large number of thermocouples of n-type and p-type materials that are connected electrically in series and thermally in parallel (see Figure 1.18).

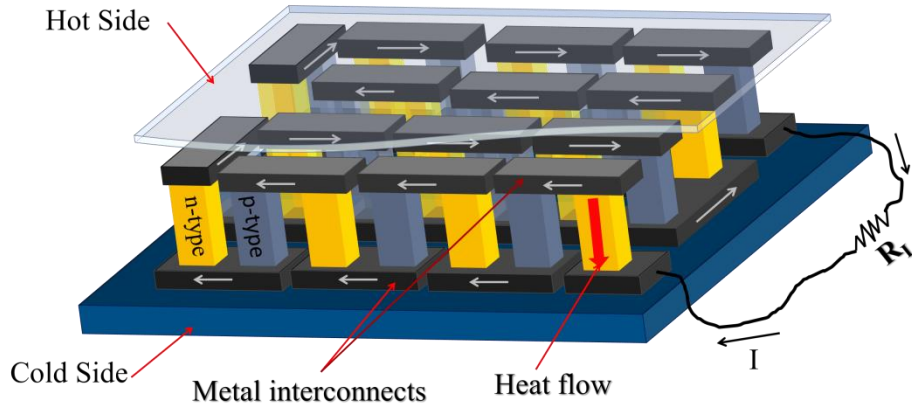


Figure 1.18: Schematic representation of a thermoelectric generator. P-type and n-type thermoelectric materials are connected electrically in series and thermally in parallel and thus a net thermovoltage is created at the final two ends. If the circuit is closed, current flows in the direction shown above.

Heat is pumped into one side (hot side in Figure 1.18) and rejected from the opposite (cold side). Due to the applied temperature difference, a thermovoltage is induced between the two ends of each element. Adjacent elements show thermovoltage of opposite sign because the materials have opposite majority carriers. Thus, practically, what is achieved is to get a net potential difference at the final two ends of the device which is just the sum of all the induced thermovoltages. The thermocouples are connected to an electrical load of resistance R_L and thus the produced electrical current I is given by:

$$I = \frac{\sum(S_p - S_n) \cdot \Delta T}{R + R_L} \quad (1.25)$$

where S_p and S_n are the Seebeck coefficients (V/K) of p-type and n-type elements respectively and R is the total electrical resistance (Ω) of the device.

Consequently, the heat flow drives the resulting electrical current, which therefore determines the output useful power:

$$W = I^2 \cdot R_L \quad (1.26)$$

Thermoelectric generators' operation is based on Seebeck effect and find different important applications like waste-heat recovery in automobiles [49] and other combustion-engine-powered vehicles [50, 51], power space systems [4], remote power along oil pipelines and body temperature powered watches [52] etc. Apart from all these large scale devices, a very good progress has already been achieved on on-chip thermoelectric generators [53–55].

1.6.2 Thermoelectric cooling

The same device, as the one described before, can be used for thermoelectric cooling, if an electrical current is applied at the two ends of the device. A heat sink, for the heat to be rejected, is needed. Thermoelectric cooling devices are also known as Peltier coolers and as their name denotes, their principle of operation is based on Peltier effect.

Solid-state Peltier coolers provide precise thermal management for optoelectronics and passenger seat cooling in automobiles [26]. Peltier coolers for cooling instrumentation,

laboratory apparatus and consumer appliances are commercially available, while thermoelectric cooling has been also used for on-chip hot spot remediation in microelectronics [56, 57].

1.6.3 Sensing

Thermoelements can be assumed as “active” or “self-generating” transducers converting temperature differences into electrical signals. They are, thus, usually used for sensing applications.

The open circuit arrangement of two thermoelectric materials in contact is called thermocouple and is widely used as temperature sensor. To increase the sensitivity of such measurements many thermocouples can be connected electrically in series and form a thermopile. *Thermopiles* are used for small temperature difference detection. Both thermocouples and thermopiles are commercially available and are widely used as temperature sensors. They are inexpensive and can measure a wide range of temperatures.

Thermocouples can also be integrated on-chip using standard CMOS processing. A plenty of modern microsensors base their function on Seebeck effect. Depending on the design, such devices can be used not only as temperature sensors, but also as gas and microfluidic flow sensors [58–60], accelerometers [61], power sensors [62], infrared detectors [63, 64] etc. The key parameter in such applications is to create a thermal insulating platform locally on the Si wafer. Porous Si has been widely used in this respect as an effective substrate on which thermocouples can be integrated. In this respect, a comprehensive study of the effectiveness of porous Si as a thermal insulating platform in a wide temperature range was carried out in this work and will be analyzed in Chapter 5 of the thesis.

1.7 Conclusions

In this chapter, the basic principles and considerations regarding thermoelectrics were discussed. Each thermoelectric effect was presented, while the possible applications exploiting them were reviewed. A detailed analysis concerning thermoelectric materials and their performance was made, based on their dimensionless figure of merit zT . All the parameters that are taken into account in zT calculations were analyzed, along with the possible ways to measure them. All the measurement techniques were evaluated according to their advantages and drawbacks, while the methods used for thermoelectric characterization in this thesis were reported.

The enhancement of the overall thermoelectric performance of a material is a challenging task because of the interdependence of the different thermoelectric parameters, which are: the Seebeck coefficient, the electrical and the thermal conductivity. However, nanostructuring has been proved both experimentally and theoretically to improve the figure of merit of a thermoelectric material. Si-based thermoelectrics were introduced and the motivation of using them instead of other more efficient thermoelectric materials was analyzed. Finally, the state-of-the-art thermoelectric materials that have been reported so far were reviewed. The record zT values were 2.6 for SnSe at 923K and ~ 1 for Si-based thermoelectric materials (20nm width Si nanowires).

Chapter 2

Formation and Properties of Porous Silicon

“The semiconductor silicon has often been referred to as the most studied and most influential material made by mankind. The stone, bronze and iron “ages” became the “silicon age” with the emergence of integrated circuits. Micromachining it enabled complex microdevices with moving parts to be realized. Nanostructuring it via porosification has yielded some amazing phenomena...”

Handbook of Porous Silicon, edited by Leigh Canham, Springer 2014

2.1 Introduction

Porous Silicon (PSi) is a complex material that is formed by electrochemical etching of bulk crystalline Silicon in solutions containing Hydrofluoric Acid (HF). It is composed of a Si skeleton and voids. It was accidentally discovered by the Uhlirs, a husband and wife team working at Bell Laboratories in the 1950s in their try to find an electrochemical technique to machine Silicon (Si) for use in the fabrication process of microelectronic devices. Uhlir found that under specific electrochemical conditions, Si wafer does not dissolve uniformly, as it was expected, but pores are formed instead [65].

Until the early 1990s, the studies concerning PSi are limited and basically focused in its use for dielectric isolation in microelectronics [66, 67]. Then, PSi attracted the interest of the research community for its efficient, bright, red-orange photoluminescence at room temperature that was reported by Leigh Canham [68]. From that time on, the material's properties, its formation mechanisms and morphology have been deeply studied by many authors. A ballpark measure of research activity concerning PSi can be obtained by the number of publications that use the word “porous Si” during time, according to Scopus data base (recognizing the fact that neither all publications are relevant nor that such statistics include all relevant activity in the field). This synopsis from 1956 is presented in Figure 2.1a, while statistics concerning the subject areas of publications are summarized in Figure 2.1b.

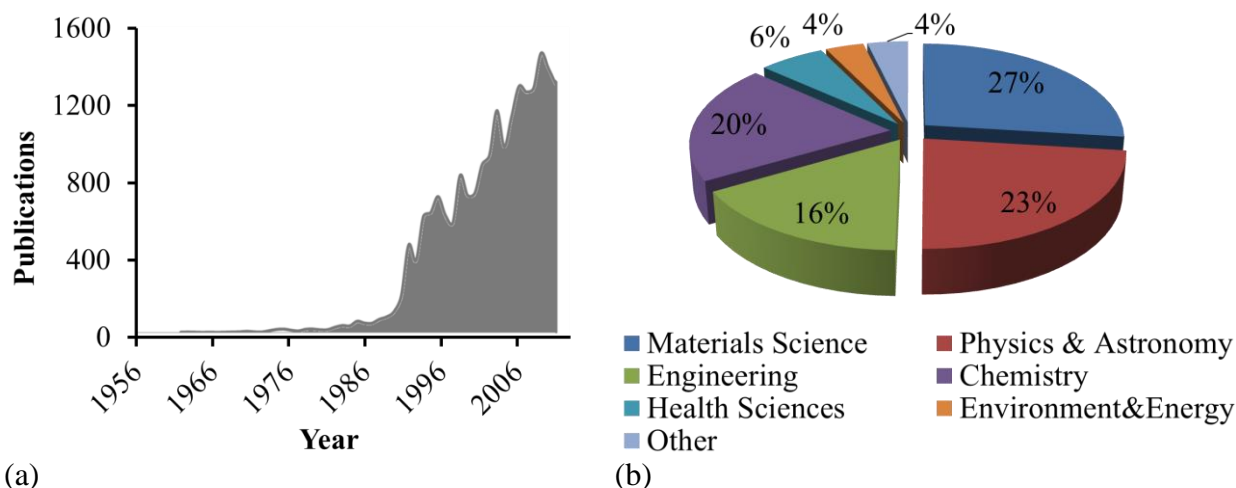


Figure 2.1: a) Number of publications concerning “porous Si” during time (1956-2013) and b) statistics of the corresponding subject areas of the publications for the same period as they can be found in the Scopus database (<https://www.scopus.com/>).

The first studies on PSi were published in the field of integrated optoelectronics for applications in light-emitting diodes [68–70]. Although these studies did not show competitive results compared to other efficient technologies in this field, they demonstrated that PSi has very different properties than that of bulk crystalline Si. This outcome triggered researchers to examine its potential use in different applications. Thus, apart from the field of optics [71, 72], porous Si has been used in thermal [58, 73, 74] and chemical sensors [75], as a sacrificial layer for MEMS technology [76, 77], biosensors [78], nanomedicine [79], Radio Frequency (RF) devices [80–82], microfluidics [83] and thermoelectrics [53].

Detailed reviews on studies that have been carried out all these years on porous Si and applications can be found in the books [84–86].

The present chapter gives an overview of fundamentals governing porous Silicon formation mechanisms and the electrochemical conditions that must be fulfilled to form PSi layers with specific morphology and structure. The most frequently used methods to measure porosity and thickness of PSi layers are discussed, while the processes to fabricate PSi layers locally on the Si wafer, as well as PSi free standing membranes, are presented.

2.2 Porous Si formation

The porosification of the surface of a silicon wafer is generally referred to as “*anodization*” and occurs when the wafer is anodically biased in a fluoric-based electrolyte solution. Although HF is the most frequently used electrolyte for PSi formation, anodization of Si can also occur in organic solvents like dimethylformamide (DMF) and dimethylsulfoxide (DMSO).

The anodic behavior of Si as an electrode has been extensively studied in the literature, because the phenomena that take place during its anodization can potentially be used for many applications in different technological fields. Electrochemical etching of Si is the most frequently used method to form PSi [84, 87]. It can be achieved by applying either constant current or constant voltage between the electrolyte and the Si electrode. Constant current is preferable, as it allows a better control of both the porosity and thickness of the porous Si layer and a good reproducibility [88]. Consequently, this method was used in the present study and a comprehensive review of its basic principles is analyzed in the following section.

However, it has also been found that PSi can be formed without the application of external electrical field. This technique is well known as “stain-etching” [89] due to the color change it imparts. Galvanic etching and Metal-Assisted Chemical Etching (MACE) are also electroless techniques to fabricate porous Si and are briefly summarized in this chapter.

2.2.1 Porous Si formation by electrochemical etching of bulk c-Si

2.2.1.1 Fundamentals of electrochemical etching of c-Si

Concerning electrochemical etching of c-Si, the most acceptable explanation about the formation mechanism itself and the reason why the walls between the pores are so remarkably resistant against further chemical attack, is that proposed by Lehmann and Gösele in 1991[90]. Generally, for the dissolution of Si the presence of holes is necessary. This fact can be further understood by considering that n-type Si cannot be anodized without the injection of holes, which is usually achieved by illumination (photo-assisted etching). There are two basic reactions that take place during anodization. That is, direct dissolution of Silicon via reaction (I) and indirect dissolution through the formation and dissolution of SiO_2 via reaction (II)[91], as it is shown in Figure 2.2.

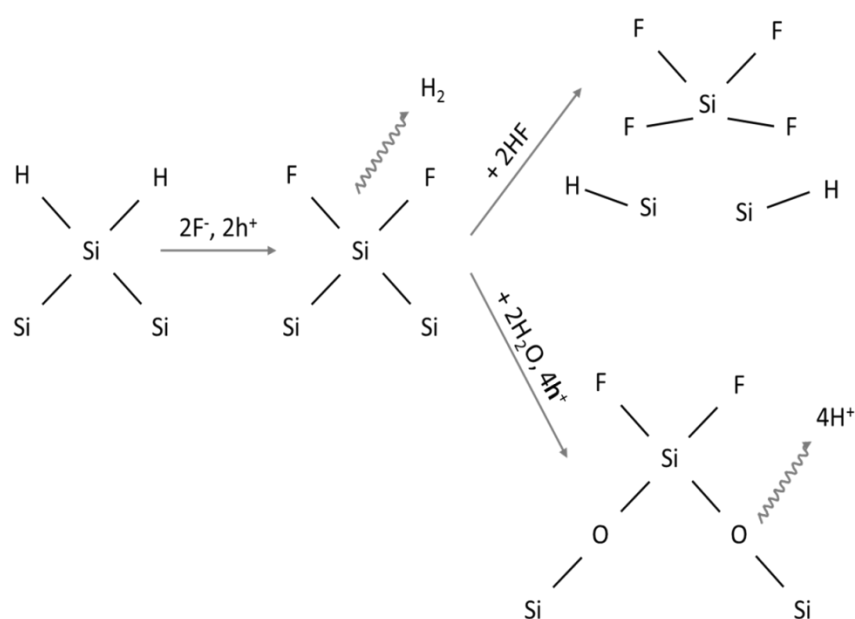


Figure 2.2: Two different reaction paths for a Silicon electrode in HF solution [91].

At low current densities, reaction (I) is dominant. The process is limited by the existence

and distribution of holes on the surface of Si. This happens because Si atoms removal occurs locally, at points where the concentration of holes is high (e.g. curvatures) and thus pores are formed. When current density reaches a critical value, J_{ep} , reaction (II) governs. Then, electropolishing of Si takes place and pores do not form. Practically, what happens at this case is that the concentration of holes is high and uniform on the Si surface, thus the process is limited by F^- ions. Then, a SiO_2 film is formed on the whole Si surface. Further increasing of the current density results in increasing oxide thickness, while by increasing HF concentration the oxide dissolution rate also increases and leads to electropolishing of the Si wafer. Consequently, pores can be formed on the Si wafer when the surface is not oxidized or it is partially covered by oxide. Figure 2.3 shows schematically a representation of the distribution of holes and F^- ions on Si – electrolyte interface, at current densities below (Figure 2.3a) and above (Figure 2.3b) critical current density J_{ep} .

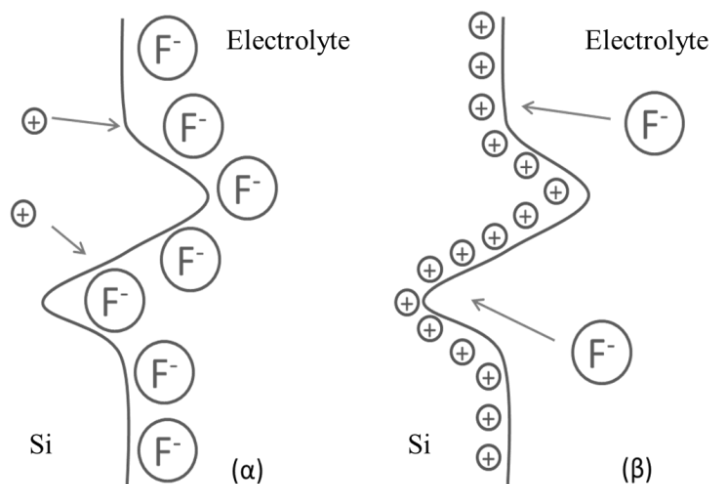


Figure 2.3: Schematic representation of the Si – electrolyte interface when the applied current density J is a) $J < J_{ep}$ and b) $J > J_{ep}$.

It must be mentioned at this point that the specific pore structure, which can be obtained with the above described process, is determined by the spatial and temporal distribution of the reactions and their rates. The electrochemical parameters depend also on geometric factors of the system. Thus, porous Si structure and morphology greatly vary with the electrochemical conditions used in anodization [84, 91].

The most important factor that influences the resulting porous Si films during galvanostatic electrochemical etching of c-Si, are summarized below [84]:

- *Anodization current density*

An increase in the applied current density results in porous Si layers with higher porosity and larger pores.

- *Electrolyte composition and HF*

A decrease in the concentration of HF in the electrolyte leads to higher porosities of the resulting porous Si layers.

- *Type of the c-Si wafer (n or p)*

Depending on the type of the initial c-Si wafer, different porous Si morphology and structure can be obtained. As it was mentioned before, for the anodization of n-type c-Si, the sample must be illuminated in order to be etched. The first n-type Silicon layers were macroporous (diameter of the pores $>50nm$).

- *Resistivity of the c-Si wafer*

The resistivity of the c-Si substrate plays a very important role in the structure and morphology of the resulting porous Si layer. More specifically, by anodizing highly doped Si substrates (p^+ , n^+), vertical pores with dendritic – like morphology are formed. The PSi in this case acts as a highly anisotropic material with its in-plane thermal and electrical conductivity

being very different from the corresponding cross-plane ones. On the other hand, if the starting c-Si is a lightly doped wafer, the porous Si that is formed has a sponge-like morphology. The latter material is homogeneous and isotropic in structure and morphology. This difference has a significant effect on all the properties of the material.

2.2.1.2 I-V Curves and formation conditions

As it was explained before, porous Si formation takes place only within a specific window of applied current density. There is a critical value J_{ep} , above which electropolishing occurs and pores do not form. For values much less than J_{ps} (which is the first peak shown in Figure 2.4) porous Si is formed. For current densities J between these two values, there is a transition region in which part of c-Si is polished and part of it becomes porous Si. The two mechanisms compete in the determination of the surface morphology. All these, are summarized in Figure 2.4, where typical anodic I-V curves presented; one corresponding to anodization in the dark and the other under illumination. The first peak is the J_{ps1} and J_{ps2} for n-type Silicon under illumination and p-type Silicon in the dark respectively and the second is J_{ep1} and J_{ep2} [92].

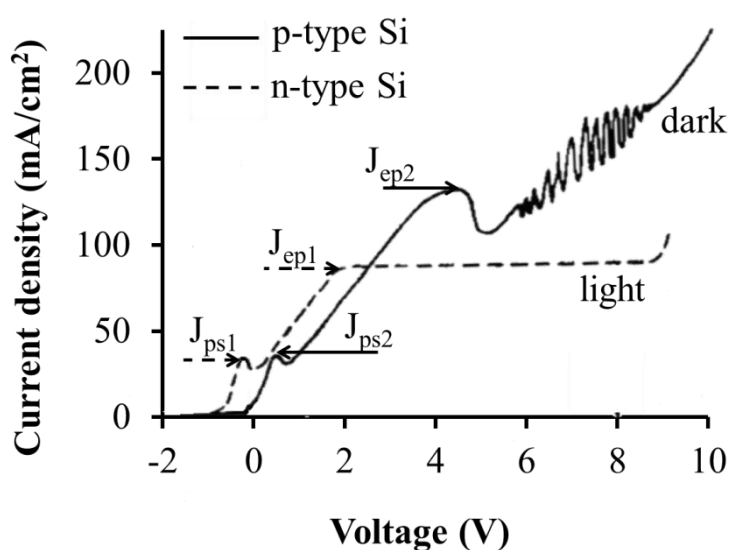


Figure 2.4: Typical anodic I-V curve measured on p-type Si in the dark (continuous line) and on n-type Si under illumination (dashed line) in a 2.5% HF electrolyte [92].

As it is shown in Figure 2.4, at small anodic potentials the current increases exponentially with electrode potential until the first peak J_{ps} is reached. At anodic overpotentials, in excess of the second peak J_{ps} , Si electropolishing takes place. Between these regions there is the transition one, which was mentioned before.

2.2.1.3 Anodization cells

Many anodization cells have been reported in the literature, with some of them being commercialized. Two types of anodization cells are most frequently used: single and double tank configurations. The single tank cells can be either in vertical (Figure 2.5a) or horizontal (Figure 2.5b) arrangement [84, 85].

In the single tank case the main cell body itself is made of an HF/organic solvent resistant polymer such as Teflon®, in which the electrolyte is placed. An HF resistant and electrically conductive material (commonly Pt) is immersed in the electrolyte and serves as the cathode. In this configuration a back side contact is used. Practically, the surface of the Si wafer, that will be anodized, is the one that is in contact with the electrolyte, while the opposite one is placed in contact with a metallic plate (commonly Al). This is the anode and thus the electrical circuit is closed. The two sides are isolated with an O-ring and thus the electrolyte cannot reach the metallic back-side contact. The O-ring should be composed of either Kalrez® or Viton® in order to be resistant both in HF and organic solvents, primarily ethanol.

As it was mentioned before the cell can be either in vertical or in horizontal arrangement. The vertical one, which is the most frequently used, ensures the uniformity of the resulting porous Si layers and offers good control of both thickness and porosity. In addition, it can be used in photo-assisted electrochemical etching (for anodization of n-type Si wafers) as well, without any change in the experimental setup. On the other hand, the horizontal configuration induces porosity and thickness gradients due to lateral potential drop. Thus, the single tank vertical arrangement is the one that was used for the preparation of porous Si samples in this thesis.

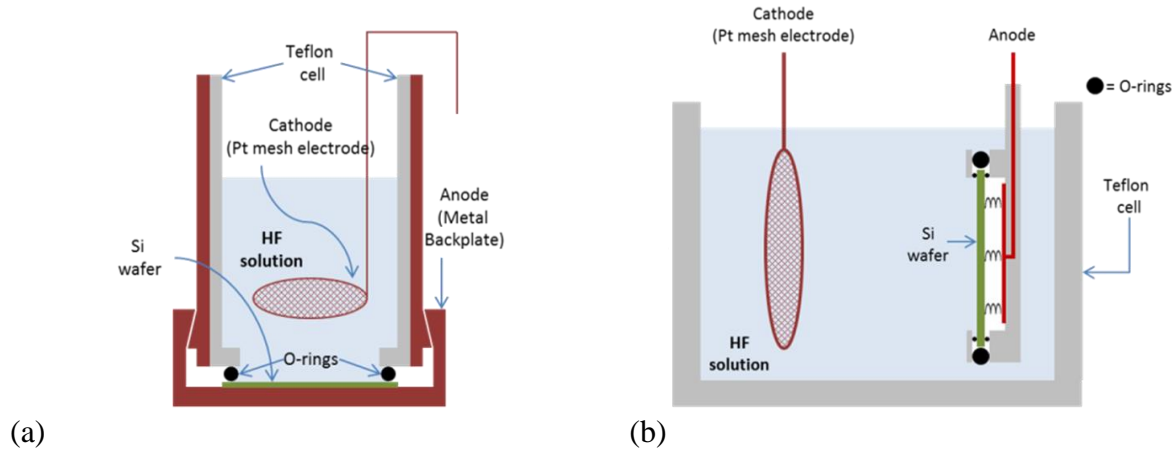


Figure 2.5: Single tank anodization cell in a) vertical and b) horizontal arrangement

Another type of anodization cell is the double-tank cell using electrolytic back-side contact (Figure 2.6). It is also composed of a Teflon® cell with two tanks clamped together with the wafer to be anodized. Both tanks are filled with HF solution and a mesh electrode (commonly Pt) is immersed in each one, serving as anode or cathode respectively. The two tanks composing the cell are separated by the wafer to be anodized. The current flows from one tank to the other through the Si wafer.

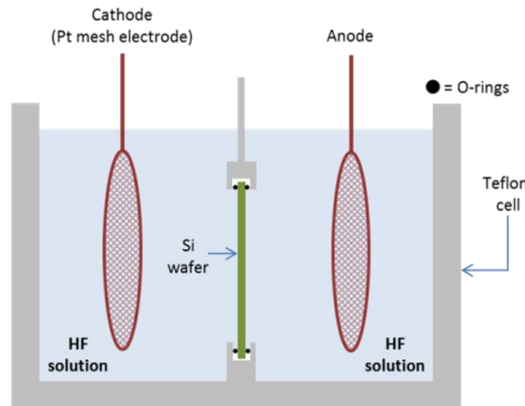


Figure 2.6: Double-tank anodization cell, the most commonly used cell for industrial applications.

It should be noted here that uniform porous Si layers can be obtained by anodizing highly doped Si substrates without any treatment of the initial wafer. However, for lightly doped Si, an ohmic back-contact is needed for good porous Si_n layer uniformity. More details about ohmic contacts formation in our samples thesis can be found in Chapter 3.

Another source of structural and morphology inhomogeneities in porous Si layers is the existence of chemical concentration gradients and hydrogen gas bubbles at the anodized surface of the Si wafer. These are typical problems encountered in all cell configurations described before. To eliminate both phenomena, the circulation of the electrolyte by chemical pumping is used. Double-tank anodization cells with chemical pumps for electrolyte circulation are the most commonly used cells in industrial applications.

2.2.2 Porous Silicon formation by electroless etching

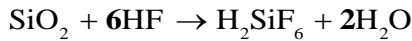
2.2.2.1 Stain etching

Porous Si can also be formed without applying external electric field using the stain etching technique. Aqueous or ethanoic solution with HF and HNO₃ is used in this case. The reactions that take place for porous Si formation with stain etching are [93]:

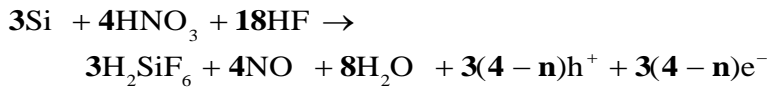
Cathode:



Anode:



Overall:



From the above reactions, it is obvious, that at the beginning NO and holes are produced at the cathode, which are used for the reactions that take place at the anode. This fact results in porous Si formation both in p and n-type c-Si wafer without the need of hole injection via illumination. The morphology and structure of porous Si, as well as its etching rate, depend on the concentrations of HF and HNO₃ in the solution and the type and resistivity of the initial c-Si substrate.

This is a very easy and low cost method to fabricate porous Si layers. However, it induces uniformity problems and the formed porous Si layers cannot be very thick.

2.2.2.2 Galvanic etching

This is a type of anodic etching at open circuit that results from exposure of a metal contact on a silicon wafer to an appropriate solution. Galvanic etching can be performed in either acidic or alkaline solutions and it can be used to form porous layers or complete etching of the Si wafer [85]. This method is based on the deposition of noble metal (especially gold or platinum) on the surface of the c-Si wafer. Then, by dipping the wafer into an HF solution, a galvanic element is formed into the electrolyte by the metal/Si junction. Silicon has a lower standard potential compared to noble metal and thus this potential difference induces a current into silicon, which results in porous Si formation [94]. This is a quick and low cost method and it can be used for the fabrication of thick porous Si layers. However, it is not compatible with CMOS processing due to the metallization step used.

2.2.2.3 Metal-Assisted Chemical Etching (MACE)

This method is based on a localized oxidation and dissolution of Si in HF in the presence of an oxidizing agent, whereas the metal (generally noble metal) enhances the etching process [85]. Microscopically, Si acts as a local anode and metal as a local cathode, producing a local current flow between these sites during etching [95]. Thus, this method is based on the same electrochemical mechanism as galvanic etching.

The noble metal (Au, Pt, or Au/Pd) can be deposited on the Si wafer or dissolved in the HF solution and it is used to increase the Si dissolution rate. The metal choice and its morphology have a strong impact on the resulting porous Si layer, thus different structures can be obtained (porous Si, nanowires), their diameter being tunable by adjusting the experimental parameters [96]. The method is simple and low cost and much quicker than stain etching for porous Si formation.

2.2.3 Local porous Si formation

Silicon is the basic material of semiconductor electronics and therefore there is huge infrastructure and know-how available for its production and processing. It is thus highly advantageous to combine Silicon with other devices towards both lowering fabrication cost and more importantly adding more functionality to Si by combining logic and memories with other functions (system – on – chip : SoC). Thus, for most device applications in micro and nanoelectronics it is essential to be able to form porous Si in predefined areas. Local anodization of patterned areas through a mask is the most commonly used technique while selective anodization using etch stops has also been reported [97].

2.2.3.1 Local anodization through mask

In this section, the most commonly used mask materials for local porous Si formation on the Si wafer are reviewed [97, 98]. A mask material can be placed on the wafer either before or after the porous Si formation, procedures known as “before etching” and “after etching” respectively. Both of them are schematically shown in Figure 2.7. However, this section is focused in the “before etching” patterning because it is the process used in this work. More details about “after etching” patterning can be found elsewhere [99, 100].

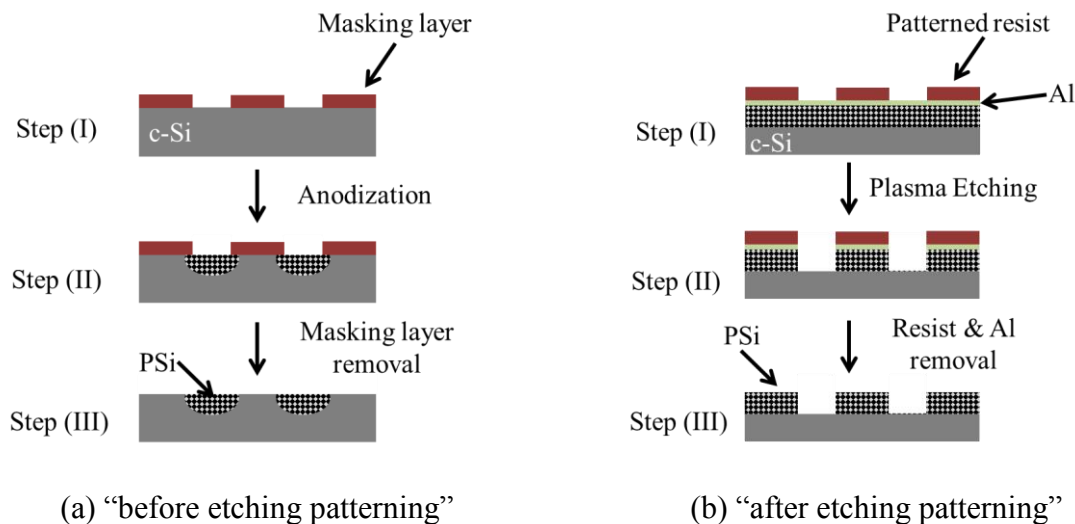


Figure 2.7: Schematic representation of (a) “before etching” and (b) “after etching” patterning of porous Si in predefined areas.

One of the basic requirements of the “before etching” patterning is that the mask material should not be etched by the HF-containing electrochemical solution. The direct use of AZ photoresist as a mask for the local porous Si formation would be of great technological interest, as it is also used in standard photolithography process and it can be easily removed. However, the AZ 5214 photoresist withstands the HF-containing solution only for 2-5min and is then dissolved. So, it can be used only for thin porous Si layers. To solve this restriction Starkov et al. [101] showed that a thick SU-8 photoresist coating with an additional heating stage can successfully be used for 75min of electrochemical etching in ethanoic HF solution. More recently, Hourdakakis and Nassiopoulou [102] reported that photoresist AZ 9260 can withstand the HF attack for times as long as 60min. Thus, it is possible to fabricate local porous Si layers up to 50-60 μ m using the AZ 9260 photoresist.

Silicon dioxide was also studied as a potential masking layer for local porous Si formation and proved to be effective only for short anodization times (few minutes) because of its high dissolution rate in HF (~250nm/min)[98].

It is known that Silicon nitride (Si_3N_4) withstands HF attack for much longer times. Consequently, it was also examined as possible masking material. Nevertheless, it was experimentally shown that it induces stresses in the porous Si films, causing cracking [103]. On the contrary, non-stoichiometric Silicon Nitride, deposited by Low Pressure Chemical

Vapor Deposition (LPCVD), has been proved to be an adequate mask [97]. Silicon Carbide (SiC) was also studied as a masking material for local porous Si formation. In crystalline form, it becomes porous in HF and thus it is inappropriate for use as a mask [104]. On the other hand, the amorphous SiC deposited by CVD could be an option but it shows some patterning and removal issues [103].

Recently, Defforge et al. [105] reported the use of plasma-deposited fluoropolymer (FP) as a masking layer for porous Si localization. For the patterning of the FP film, a hard mask of silicon dioxide must be first fabricated on the surface of the film. Apart from this extra step, FP seems to be a promising material for local porous Si formation, although some issues concerning the whole process are still under investigation.

Undoped polycrystalline Si (polysilicon) has been tested for local anodization because of its known resistance in HF solutions. However, Kaltsas & Nassiopoulou [98] demonstrated that if it used directly on the Si substrate, there is a small current flow through the mask to the c-Si substrate during electrochemical etching. Thus, the surface below the mask is affected by the electrochemical solution and becomes rough, because porous Si formation is initiated under the polycrystalline layer. This problem was overcome by adding a SiO₂ layer between the Si substrate and the mask. Thus, the best mask for local porous Si formation was reported by Kaltsas and Nassiopoulou [98], which is a bilayer of polysilicon/SiO₂ on Si. It was proved to be adequate for more than 5-6 hours of anodization without any change in its structure. This double-layer mask was used for the fabrication of porous Si layers locally on the Si wafer in this thesis. Figure 2.8, depicts selective Scanning Electron Microscopy (SEM) image of locally formed porous Si samples that were prepared in the frame of the present study. More details about the exact process flow are given in Chapter 6.

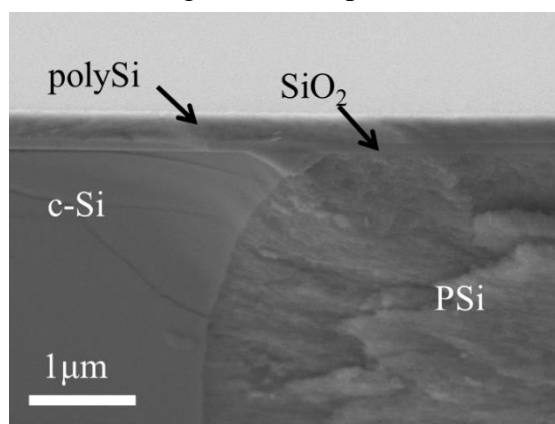


Figure 2.8: Cross sectional SEM image of a locally formed porous Si layer in a predefined square structure. In the image the double layer polysilicon /SiO₂ that was used as a mask is indicated (step II of figure 2.7a)

As mentioned above, the poly Si/SiO₂ mask is an excellent anodization masking material for porous Si formation. However, its removal after anodization involves a number of process steps, which increase fabrication complexity. A more appropriate masking material for the case of devices integrated on the same Si wafer with electronics is the use of a thick photoresist mask, as in the process developed by Hourdakos and Nassiopoulou [102], or the use of fluoropolymer, as in the process developed by Defforge et al. [105]. In this thesis, since our objective was to develop discrete structures for characterization, we did not take into account the above drawback, but we adopted the more robust mask for very thick porous Si layers.

2.2.3.2 Local anodization using etch stops

Instead of using a deposited coating as a mask, the creation of etch stops in predefined regions is an alternative for local anodization. This method is based on the amorphization of specific patterning regions of the Si substrate by ion implantation. Porosified layers can be

then created with anodization only in non-implanted areas because the amorphised regions act as etch stops (masking for anodization) [106, 107]. N-type implanted areas in a p-type silicon substrate is a common etch stop example [108]. Under the same electrochemical conditions in the dark, the n-type areas remain unaffected during anodization while porous Si is formed in the p-type areas of the wafer.

2.2.4 Free standing porous Si membranes (FSPSi)

Free standing porous Silicon membranes have been extensively studied in the literature because of their potential use in a variety of applications, such as medical implants, microfluidic reservoirs, fuel cells, different types of sensors, drug delivery, micro pumps etc. Free standing porous Si membranes can be fabricated by either right through anodization or two-step electrochemical etching [109]. Both techniques are described below.

- *Anodization right through the entire Si wafer thickness*

The whole thickness of the Si wafer can be anodized to form a free standing membrane. In the case of standard thickness Si wafers, there are two main drawbacks. Depending on the electrochemical conditions used, the anodization process could last several hours making the process inefficient and time-consuming, while in such thick porous Si layers, porosity gradients in their depth are observed. On the other hand, if thin Si wafers are used for right through anodization, apart from the difficulties to handle them, the cost is significantly increased. This makes the process expensive and thus not preferable.

- *Formation of free standing porous Si membranes by two step electrochemical etching*

PSi layer of chosen thickness is initially formed with anodization either on the whole wafer or on predefined areas through a masking layer. At this step, current densities below the critical value J_{ps} (which corresponds to the first peak in the current-potential curve as it was mentioned in section 2.2.1.2), are applied. After PSi formation, the membranes are detached from the substrate by electropolishing, using current densities much higher than J_{ps} . In both steps, the same HF ethanoic electrolyte is used. This method is known as “lift-off” technique and it can be used to fabricate free standing porous Si (FSPSi) membranes with a wide range of thicknesses and porosities in short time and without the need of expensive equipment.

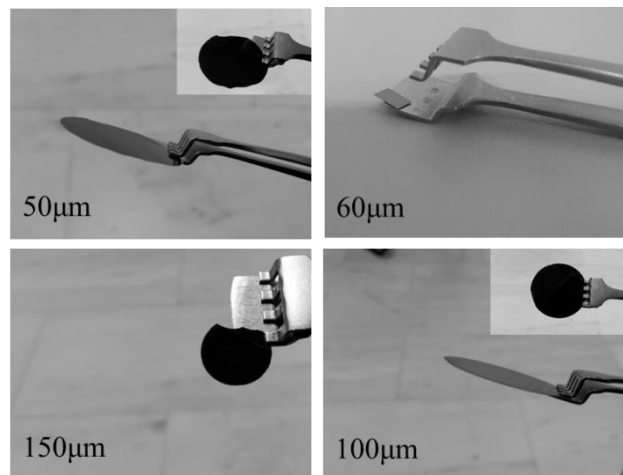


Figure 2.9: Examples of circular & rectangular FSPSi membranes with different thicknesses prepared by two step anodization process on p+ Si wafer.

The two step anodization process was used in this thesis for FSPSi membranes formation. Particularly, as it will be described in detail later, FSPSi membranes with different porosities and specific dimensions were fabricated and their thermoelectric properties were investigated. Figure 2.9 shows some examples of free standing porous Si membranes fabricated in this work with thicknesses ranging from 50-150µm in circular and rectangular shapes. All the membranes were prepared by anodization of p⁺ type Si substrate.

2.3 Porous Si morphology and structure

As it was mentioned before, depending on the electrochemical conditions used, as well as the doping type and level of the initial c-Si wafer, porous Si layers with different structure and

morphology can be formed. The morphological parameters that determine the porous Si layers are the shape of the pores, the pore diameter and the inter-pore distance.

According to IUPAC classification [110], porous Si is distinguished considering the pore diameter in three categories:

- **Microporous** with pore diameter $\leq 2\text{nm}$
- **Mesoporous** with pore diameter between $2\text{-}50\text{nm}$
- **Macroporous** with pore diameter $\geq 50\text{nm}$

Another parameter that characterizes porous Si is the porosity. **Porosity** is a measure of pore/Si ratio and is calculated as a fraction of the volume of voids over its total volume. Depending on the porosity, porous Si is categorized in:

- **Low porosity** (0-30%)
- **Medium porosity** (30-70%)
- **High porosity** (70-95%)

Figure 2.10 illustrates typical porous Si morphologies that can be formed by anodization of both n and p-type Si substrates (from reference [84]). The crystallographic orientation of the initial Si wafer is also a very important factor that determines the orientation or size of the pores of the resulting material.

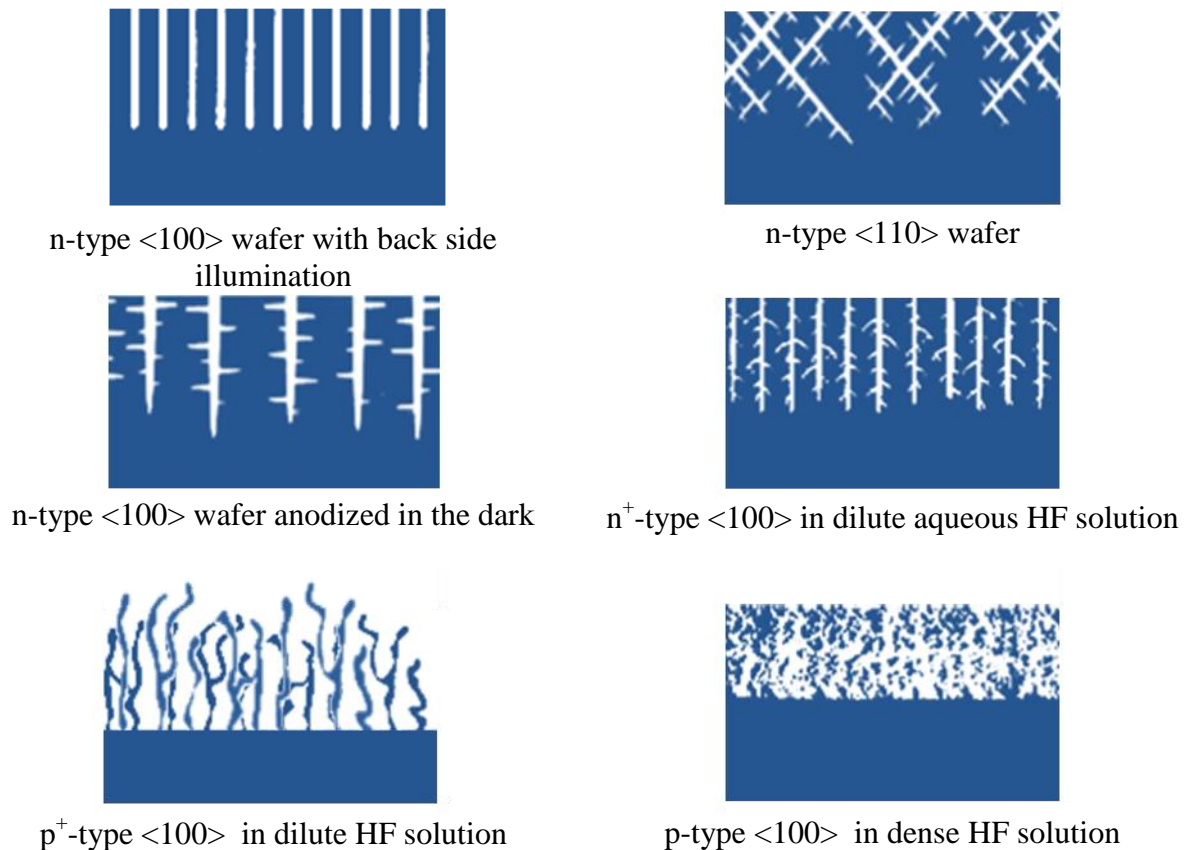


Figure 2.10: Schematic representation of typical porous Si morphologies [84]

2.4 Porosity and thickness measurements

As it was indicated in the previous section, porosity is one of the basic parameters that characterize a porous Si layer. Thus, its value should be accurately measured. The most frequently used method to measure porosity of porous Si is the three weight measurement or gravimetric technique [111]. Using this method, the porosity P is simply calculated by the

following equation:

$$P = \frac{m_1 - m_2}{m_1 - m_3} \quad (2.1)$$

where m_1 the initial mass of the sample, m_2 the mass after anodization and m_3 the mass of the sample after removing the formed PSi layer. Porous Si can be easily removed in diluted hydroxide solutions (KOH, NaOH, NH_4OH etc). Because of its high specific surface area (ranges between $1\text{-}1000\text{m}^2/\text{cm}^3$ [112]), it dissolves very quickly in such solutions even at room temperature [113]. In this work a diluted KOH solution at room temperature was used for PSi dissolution and porosity measurements. Single-crystal substrate is also etched by this solution but at room temperature its etch rate is very small (less than $25\text{nm}/\text{min}$ in diluted KOH solutions [114]).

From the above measurements, it is also possible to extract the thickness of the layer according to the following relation [84]:

$$t = \frac{m_1 - m_3}{S \cdot d} \quad (2.2)$$

where d is the density of bulk Si and S the area that was anodized to form porous Si.

Apart from the above method, porous Si membrane thickness can be measured by SEM or by step measurements after the dissolution of the porous Si layer. These methods are direct and accurate. All the aforementioned measurement techniques were used and compared in this study and the results are presented in the experimental part of the thesis.

Ellipsometry and other optical and acoustic methods have been proposed in the literature as non-destructive techniques to measure both porosity and thickness of porous Si layers with relatively good accuracy. A comprehensive review of these methods can be found in [86]. However, all these techniques are indirect, based on mathematical models and assumptions, while their implementation requires special and expensive equipment.

2.5 Conclusions

This chapter is an introduction to the basics of porous Si. The variety of reported applications and the increased research activity considering porous Si, as it was presented in this chapter, denote its significance in different scientific fields and particularly modern micro and nanoelectronics.

The main PSi formation techniques were described with emphasis on the electrochemical etching of Si in solutions that containing HF, the so-called “anodization”. Using this method under galvanostatic conditions, it is possible to fabricate thick porous Si layers, with homogeneity and reproducibility in a controllable way. The advantages of this method compared to electroless techniques were demonstrated. The mechanisms that are involved in porous Si formation in each case were analyzed, while the parameters that determine porous Si morphology and structure were discussed. The possible ways to form local porous Si in predefined areas on the Si wafer and free standing porous Si membranes were presented with examples of fabricated samples in the frame of the current study. Finally, the methods used for measuring the most important characteristics of porous Si layers, i.e. porosity and thickness, were reported.

Chapter 3

Porous Si thermal conductivity in the temperature range 4.2- 350K

The concept of thermal conductivity required nearly three hundred years for its development and involved the expenditure of an immense amount of mental energy and experimental effort. Galileo, Hooke, Newton, Bobrhaave, Franklin, Black, Rumford, Fourier – giants in the scientific world – contributed to the development of this concept...

Burr AC (1933) Notes on the History of the Concept of Thermal Conductivity. University of Chicago Press on behalf of History of Science Society

3.1 Introduction

Thermal conductivity is a fundamental thermal property of materials. Besides being integral part of the characterization of thermoelectric materials, as it was indicated in a previous chapter, its determination and accurate measurement is necessary for many other reasons.

Thermal conductivity measures the ability of a material to conduct heat. Materials with very high or very low thermal conductivities, i.e. “good” thermal conductors or insulators, are of great technological importance and are used accordingly in plenty of applications from the macro to the nanoscale. Their value, denoting their effectiveness in conducting or inhibiting thermal transport through their volume, could enhance or deteriorate the efficiency of the final device. Consequently, it is a critical parameter that should be known in a wide range of temperatures in order for new devices with improved efficiencies to be designed and fabricated.

On the other hand, the temperature dependence of thermal conductivity of a solid is a powerful tool to investigate its structure and morphology, possible lattice defects and imperfections or other interesting and exciting phenomena. Thus, the understanding of thermal transport mechanisms in complex materials, such as porous Si, is an indispensable step before their integration in efficient thermoelectric applications.

This thesis focuses on thermally insulating materials, and particularly on porous Si, for its use both as a substrate and as a thermoelement for thermoelectric applications. Porous Si, at high porosities, is composed of nanowires and nanodots separated by air and thus, due to its morphology itself, it is expected to have much lower thermal conductivity than that of bulk crystalline Si. This is demonstrated experimentally in the present chapter.

Room temperature porous Si thermal conductivity has been extensively studied by many authors using different measurement techniques: photoacoustic method [115, 116], Micro-Raman [117, 118], 3ω [119], steady state with FEM analysis [14, 15], etc. The thermal conductivity of porous Si depends strongly on its porosity and structure. The values of room temperature thermal conductivity of porous silicon with ~70% porosity range from 0.17 – 0.74W/m.K. This discrepancy is originated from the different structure and morphology of the samples, depending on the type and resistivity of the Si substrate and the electrochemical conditions used. Although there is a large number of references concerning the room temperature thermal conductivity of porous Si, its temperature dependence has been measured only by few authors [119, 120].

In this thesis, a systematic study of the temperature dependence of porous Si layers, down to liquid helium temperatures, was made. This chapter starts with an introduction on nanoscale thermal transport and a short description of the possible mechanisms that determine the temperature dependence of thermal conductivity in crystalline and amorphous materials follows. This brief theoretical background is necessary for the consequent analysis of low temperature thermal conductivity of porous Si. Finally, we report on the results concerning samples fabricated and studied in this thesis.

As it was already mentioned, two methods were used for porous Si thermal conductivity measurements, namely the steady state dc method and the 3ω method. Both of them with the corresponding test structures, experimental set up and basic assumptions used in their general implementation in our lab are described in the following paragraphs. Finite Element Method (FEM) simulations were systematically used in the two characterization methods used and thus some basic notes concerning this numerical technique and how it solves the partial differential equations of heat transfer on solids are presented.

Concerning the 3ω measurement technique, two different approaches are proposed as improved alternatives for extracting thermal conductivity from the raw experimental data of third harmonic of voltage. The experimental results of thermal conductivity extracted with

these assumptions and the well-known slope method, introduced by Cahill, are compared to each other and their accuracy is discussed.

The experimental results of porous Si thermal conductivity in the temperature range 4.2–350K are presented along with a discussion on phonon transport mechanisms which determine this behavior. The experimental data are compared to known analytical models. At very low temperatures these theoretical models were inadequate to explain the observed plateau-like behavior of thermal conductivity. A more detailed analysis for the low temperature regime is made in a following chapter. The reported results in the temperature range 4.2-20K are the first in the literature.

Finally, a comparison is made between the dc and 3ω measurement methods. The obtained results for porous Si are compared to those of bulk c-Si and other known low thermal conductivity materials, such as silicon dioxide and amorphous Si. Porous Si thermal conductivity was found to be four orders of magnitude lower than that of bulk crystalline Si at low temperatures, the corresponding values being comparable to or lower than the thermal conductivity of other thermal insulators in the whole temperature range studied.

3.2 Thermal transport at the nanoscale

Thermal conduction in solids is governed by the Fourier's law (see Equation (1.8)). As it was mentioned earlier, lattice thermal conduction is the dominant thermal conduction mechanism in semiconductors in a large range of temperatures. The phonon properties of semiconductor nanostructures are very different from those of the bulk. In particular, the phonon frequency, group velocity, spectral density, as well as the strength of their interactions, charge carriers etc. are different at length scales below 100nm. This means that the traditional laws of energy transfer may not be readily applicable to nanoscale energy and mass transfer problems.

In bulk materials the dominant scattering mechanisms are the phonon – phonon, and phonon – carrier scattering, as well as the scattering by lattice defects. However, when the engineered characteristic length scale of a material is on the order of the phonon mean free path, additional scattering events occur and dominate, such as phonon scattering with interfaces, inclusions, grain boundaries etc. These scattering effects can dramatically reduce the thermal conductivity of the nanostructured material compared to its bulk counterpart. This will be proved experimentally by porous Si thermal conductivity measurements in this chapter.

3.3 Temperature dependence of thermal conductivity

As it was mentioned in the introduction of this chapter, the temperature dependence of thermal conductivity gives useful information regarding the structure of the material. This is because the phonon properties and scattering mechanisms are greatly varying with temperature. Thus, the thermal conductivity of a material over temperature is a powerful tool which helps to investigate the possible scattering mechanisms, which determine the heat transport in the material. The temperature dependence of thermal conductivity of crystalline materials follows a common trend. That is also the case for amorphous materials and glasses. Both of them are analyzed below and are used later for the interpretation of temperature dependence of thermal conductivity of porous Si investigated in this work.

3.3.1 Crystalline materials

The most common approach concerning the lattice thermal conductivity of lightly doped crystalline solids with low defects is that based on *Debye's equation* for heat transfer in gases [12]:

$$k = \frac{1}{3} C \cdot u \cdot \lambda \quad (3.1)$$

where C is the specific heat capacity ($\text{J} \cdot \text{Kg}^{-1} \cdot \text{K}^{-1}$) due to lattice vibrations, u is the mean phonon group velocity (m/s) and λ is the mean free path of phonons (m).

At quite high temperatures, well above Debye temperature, the thermal resistivity of such crystalline materials is dominated by U_{mklapp} processes, in which momentum is not conserved. At these high temperatures, specific heat and phonon group velocity are constant. Thus, thermal conductivity is defined by the phonon mean free path, which varies inversely proportional with temperature as the vibrations become more and more anharmonic. On the other hand, at low enough temperatures, U_{mklapp} processes become rather improbable. Then, phonon mean free path increases, reaching its limit, which is determined by imperfections or crystal boundaries. Then, thermal conductivity follows the temperature dependence of specific heat capacity which tends to zero as temperature approaches also zero.

3.3.2 Amorphous materials and glasses

Contrary to crystalline solids, amorphous materials and glasses, in general, do not show any maximum of thermal conductivity over temperature. Many glasses have been shown to follow an almost universal temperature dependence of thermal conductivity. Particularly, at very low temperatures thermal conductivity shows a sharp increase with increasing temperature until a constant value is reached between approximately 1-20K. At higher temperatures (above 20K) a positive slope of dk/dT is again observed.

The increase in thermal conductivity with increasing temperature above the plateau was attributed by Kittel [121] to an approximately constant mean free path, considering that its room temperature value is of the order of the disorder in its structure. Thus, thermal conductivity follows specific heat trend. The thermal conductivity of glasses below the plateau has been attributed to phonon scattering from low energy states [12], while the plateau itself has been attributed to different mechanisms [122], such as phonon scattering by enhanced densities of tunnelling systems, elastic scattering by density fluctuations, dimensional crossover of the vibrational density of states, phonon localization and fractons. However, both the plateau [123] and the temperature dependence of thermal conductivity above this constant value [124] are open issues and still under investigation for a common interpretation to be adopted.

3.4 Porous Si layers studied in this thesis

Two different highly porous Si layers with different porosities and morphologies were studied in this thesis. Their thermal conductivity was measured in the temperature range 4.2 - 350 K with dc and 3 ω methods and the corresponding results are compared and discussed. All the steps for the fabrication of the samples are analyzed in the following paragraphs of this section.

3.4.1 Isotropic Porous Si

Porous Silicon samples were fabricated by electrochemical etching of lightly doped p-type bulk c-Si (100) substrate with resistivity in the range of 1-10 $\Omega\cdot\text{cm}$. In order to obtain a uniform porous Si layer, an ohmic contact at the backside of the Si wafers prior to the anodization process was formed by ion implantation and annealing. Before doping, 20nm thick SiO₂ was thermally grown on the wafer to prevent out-diffusion. Then the back side of the wafer was implanted with Boron at a dose of 8 $\cdot 10^{15}$ ions/cm² and energy 60keV. Annealing at 950°C for 30min at nitrogen atmosphere followed and after that the SiO₂ layer was removed by wet etching in BHF solution.

The anodization was made in a Teflon® anodization cell in the dark by applying a constant current density of 80mA $\cdot\text{cm}^{-1}$. The electrolyte used was a mixture of HF: Ethanol with 3:2 volume ratio. The etching rate of the anodization process was measured to be 3.6 $\mu\text{m}/\text{min}$ and thus a total time of 11min & 7sec was used to fabricate porous Si samples with thickness of 40 μm . The resulting porous Si layer is an isotropic and homogeneous layer with sponge like morphology. Its morphology and structure can be better understood from Figure 3.1, which shows cross sectional (a) and top-view (b) SEM images of porous Si layers, which were fabricated under the specific electrochemical conditions.

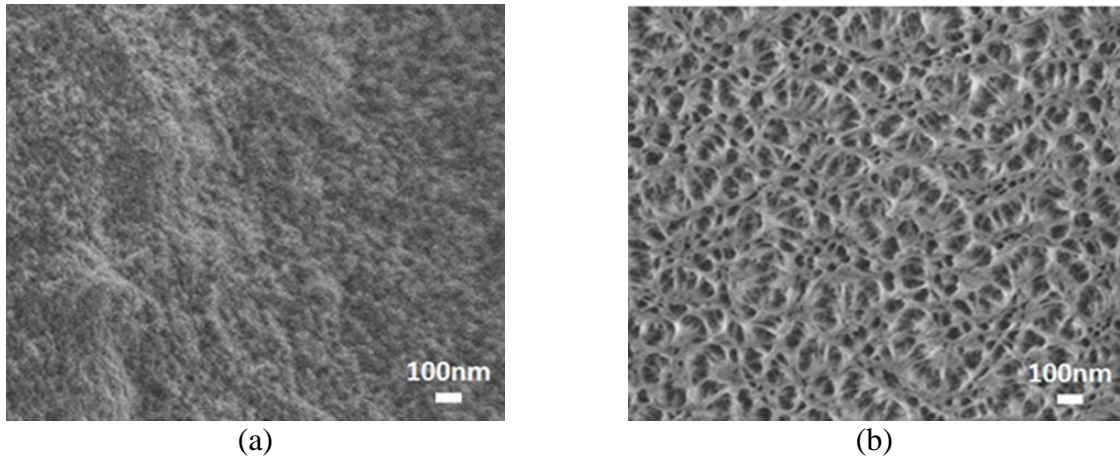


Figure 3.1: SEM images of porous Si layers formed by electrochemical etching of lightly doped p-type c-Si (a) cross sectional (b) top view image after a mild reactive ion etching of the sample with SF_6 for 30sec[15].

It should be mentioned here that the top view image was obtained from a sample subjected to a mild reactive ion etching process with SF_6 for 30sec before imaging. This additional step was necessary so as to clearly reveal the Si skeleton. The particular homogeneous porous Si layer was measured to have a porosity of $63 \pm 3\%$, which was determined using the three-weight measurement technique that was described in Chapter 2.

After porous Si formation, the samples were annealed at 300°C for 2h in O_2 ambient to stabilize their structure and passivate their internal surface area.

3.4.2 Anisotropic Porous Si

The second series of samples examined in this thesis was formed by electrochemical etching of highly doped p-type bulk c-Si substrates (100) with resistivity in the range of $1\text{-}5\text{m}\Omega\cdot\text{cm}$. For this type of wafers uniform layers can be formed without the need of backside implantation. The anodization was made in the dark by applying a constant current density of $20\text{mA}\cdot\text{cm}^{-1}$. The electrolyte used was a mixture of HF: Ethanol with 2:3 volume ratio. The etching rate using these conditions was measured to be $0.75\mu\text{m}/\text{min}$. Samples with two different thicknesses ($40\mu\text{m}$ and $100\mu\text{m}$) were fabricated in this case by adjusting the anodization time. The resulting porous Si layer with porosity $70 \pm 4\%$ is anisotropic with vertical dendritic-like pores, as shown in Figure 3.2 in (a) cross section and (b) top view SEM images respectively. As in the case of isotropic PSi described previously, after PSi formation the samples were similarly annealed at 300°C for 2h in O_2 ambient.

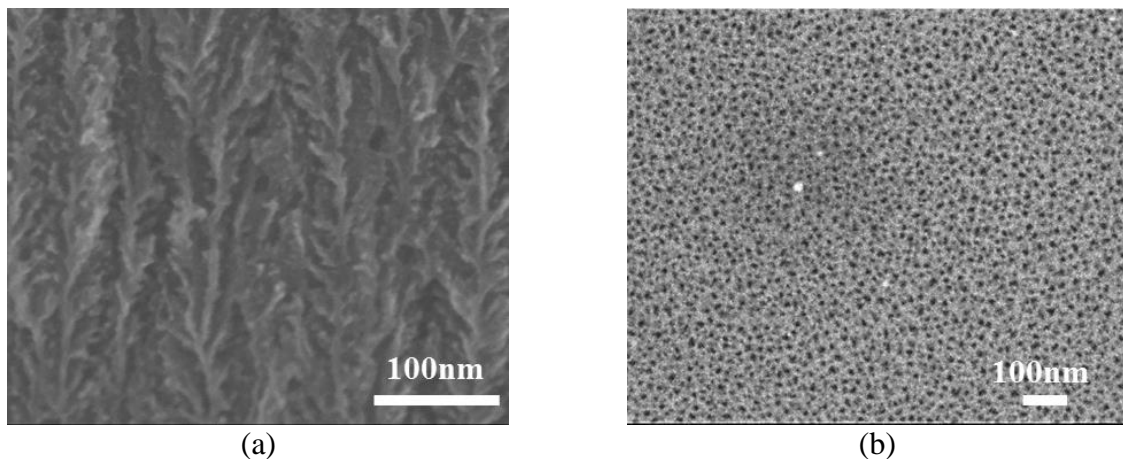


Figure 3.2: SEM images of porous Si layers prepared by electrochemical etching of highly doped p-type c-Si (a) cross sectional [81] and (b) top view

3.4.3 Test structure

In section 1.3.2, the most frequently used thermal conductivity measurement techniques were described. In both dc and 3ω methods a metallic strip is integrated on the sample under test, which acts both as resistor and as thermometer for temperature determination.

In this respect after the porous Si formation, Pt resistors were integrated on the surface of the samples. The Pt films were deposited by sputtering and patterned using optical lithography and lift-off processes. Prior to the deposition of the Pt resistors, 20nm thick TEOS oxide was deposited on the samples for electrical isolation. In order to improve adhesion of the Pt layer, a thin Ti layer was deposited between TEOS and Pt. The thickness of the Pt resistors was 200nm, while its length and width were $640\mu\text{m}$ and $20\mu\text{m}$, respectively in the four-point probe configuration. For the 3ω method the two point probe arrangement was also implemented. In this case the length of the Pt resistor was 3mm. The same steps were also applied to c-Si substrates without the PSi layer and used as reference samples.

Figure 3.3 shows schematically the fabrication process followed for the preparation of the test structures.

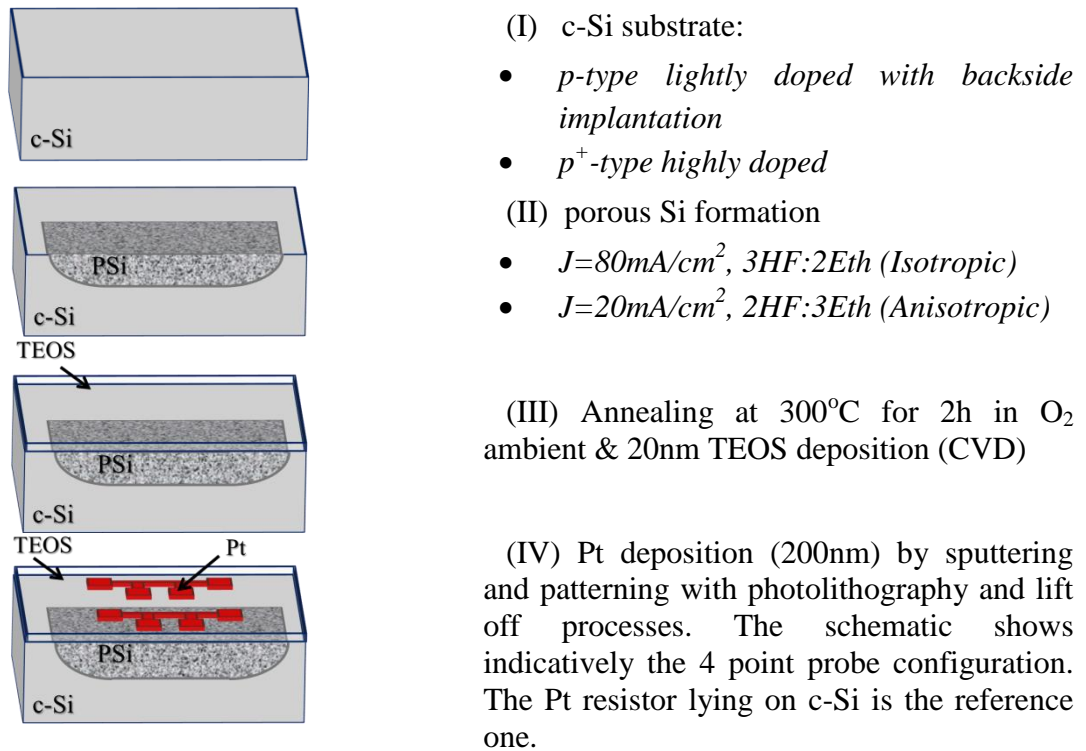


Figure 3.3: Process flow showing all the steps used for test structure fabrication for both dc and 3ω thermal conductivity measurements

3.5 DC method with consequent FEM analysis

As it was mentioned before, the steady-state direct current (dc) method was the first method used for the determination of porous Si thermal conductivity with consequent Finite Element Method (FEM) analysis [13, 14]. This method is based on the measurement of the temperature difference across a Pt resistor lying on the porous Si layer in response to an applied heating power. For the extraction of the porous Si thermal conductivity, a combination of experimental results and FEM analysis is used. In the following chapter the basic considerations on how FEM simulations solve the partial differential equations of heat transport with boundary conditions are presented.

3.5.1 Finite Element Method (FEM) simulations – General considerations

Finite Element Method simulation is a numerical method which finds approximate solutions to partial differential equations with known initial and boundary conditions. FEM has been widely used in simulating many physical problems due to its flexibility to represent complex geometric domains. Since in most cases analytical solutions are difficult to be reached, FEM is used as an alternative to solve and simulate physical phenomena which are described by well-established mathematical equations. FEM is frequently used in thermal, electromagnetic, fluid, chemical and mechanical engineering. What this method practically does, is to divide a problem domain into subdomains, called finite elements and solve the problem by minimizing an associated error function. The finite elements should have a common vertex, common full edge or surface with the neighboring element so that two different elements do not overlap. The vertices formed are called nodes. The solution of a problem is calculated at these nodes. The process of dividing the domain into subdomains is known as meshing and is one of the most important steps in FEM simulations in order to acquire a reliable solution.

In this study, the commercial FEM software COMSOL Multiphysics® was used for heat transfer simulations in order to obtain porous Si thermal conductivity. In the following paragraphs an overview of heat transfer in solids and its display as a boundary value mathematical problem is presented. The heat diffusion equation was finally used and solved to simulate heat transfer in our test structure using FEM.

3.5.1.1 Heat transfer

Heat transfer is energy in transit due to a temperature difference [125]. The fundamental modes of heat transfer are **conduction**, **convection** and **radiation**, all of which are described below.

- **Conduction**

Heat conduction is the energy transport in a medium due to temperature gradients. The physical mechanism of heat conduction is based on random atomic or molecular activity. Practically, on a microscopic scale, conduction refers to the energy transfer from atoms or molecules with higher energy to neighboring particles with lower energy through their interaction. Thus, heat is transferred from more to less energetic particles because of an energetic gradient.

The law of heat conduction is also known as Fourier's law and states that the heat flow rate per unit area perpendicular to the direction of heat flow through a material is proportional to the negative temperature gradient at this direction. For a three-dimensional heat transfer problem shown in Figure 3.4 in an isotropic solid, the total rate of heat flow vector at a point on its surface with $T(x, y, z)$ in Cartesian coordinates is expressed as:

$$\vec{Q} = \dot{Q}_x \vec{i} + \dot{Q}_y \vec{j} + \dot{Q}_z \vec{k} \quad (3.2)$$

$$\vec{Q} = -k(A_x \frac{\partial T}{\partial x} \vec{i} + A_y \frac{\partial T}{\partial y} \vec{j} + A_z \frac{\partial T}{\partial z} \vec{k}) \quad (3.3)$$

where A_x, A_y, A_z denotes the area of the surfaces shown in Figure 3.4 (m^2), k is the thermal conductivity of the material (W/m.K) and $\dot{Q}_x, \dot{Q}_y, \dot{Q}_z$ are the rates of heat flow in the x, y, z directions respectively (W). It should be mentioned at this point that in anisotropic materials the thermal conductivity typically varies with

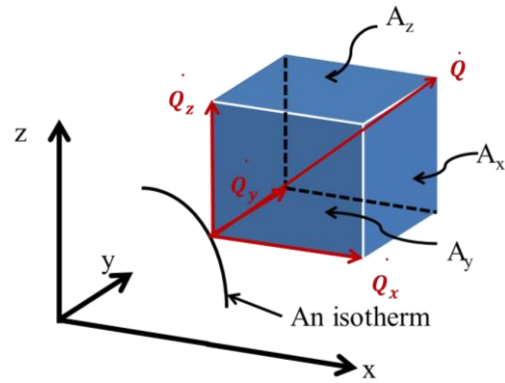


Figure 3.4: Schematic representation showing heat transfer in an isotropic solid through conduction. The vectors of heat flow rate in each direction are indicated along with the perpendicular surfaces that are used in Equation (3.3).

orientation. In this case k is represented by a second-order tensor. For simplicity reasons in the above equation an isotropic and homogeneous medium was assumed and thus k was set to be a constant.

The minus sign in the equation above is indicative of the heat transfer in the direction of decreasing temperature.

For many simple applications, Fourier's law is used in one-dimensional form. For example, for one-dimensional heat flow along the x -axes the Equation (3.3) is simplified to:

$$\dot{Q}_x = -k \cdot A_x \cdot \frac{dT}{dx} \quad (3.4)$$

- *Convection*

The **convective heat transfer**, often mentioned as **convection**, needs some fluid (liquid or gas) in order to occur and involves two mechanisms. In addition to the energy transfer due to the random molecular motion (diffusion), energy is also transferred by a bulk or macroscopic motion of a fluid. Thus, the total heat transfer is the superposition of the two mechanisms.

Two types of convective heat transfer can be distinguished: the **natural** and the **forced** convection. When a fluid is in contact with a hot surface in absence of an external source, density variations of the fluid can be observed due to temperature gradients. Practically, the hotter volume of the fluid transfers heat towards the cooler one. This is a typical example of natural convection heat transfer. On the other hand, when a fluid is forced to flow over a surface using an external source like fans, pumps etc., forced convective heat transfer takes place.

The basic relation describing convective heat transfer is known as **Newton's law of cooling** and states that the heat lost by an object due to convection is proportional to the temperature gradient between the object and its surrounding medium. This relationship is displayed mathematically in the following equation, regardless the particular nature of the convective heat transfer:

$$\dot{Q} = h \cdot A \cdot (T_a - T_f) \quad (3.5)$$

where \dot{Q} is the rate of heat transferred (W), A is the heat transfer surface area (m^2), h is the heat transfer coefficient ($W \cdot K^{-1} \cdot m^{-2}$) and T_a and T_f are the temperatures of the object's surface and fluid respectively (K).

- *Radiation*

Every material in a temperature higher than absolute zero emits **thermal radiation**. Thermal radiation, also called **infrared** radiation, is transported by electromagnetic waves (photons) traveling with the speed of light and does not need any contact between the heat source and the heated object, as in conduction and convection. An ideal surface that emits at any temperature the maximum possible amount of radiation at any given wavelength is called **black-body**. A black-body also absorbs the maximum possible incident radiation at any given wavelength.

The total rate of energy radiated by a grey body (a body which does not absorb all incident radiation like black body) per unit surface area at a temperature T is described by Stefan-Boltzmann equation:

$$j^* = \varepsilon \cdot \sigma \cdot T^4 \quad (3.6)$$

where j^* is called irradiance and has dimensions of energy flux (W/m^2), ε is the emissivity of the grey body (unitless), σ is the Stefan-Boltzmann constant and it has a value of $\sigma = 2.670373 \cdot 10^{-8} W \cdot m^{-2} \cdot K^{-4}$ and T the absolute temperature (K).

- *Heat equation*

Having described all the possible mechanisms of heat transfer in a solid, we proceed to write the basic **heat equation**. The heat equation is a parabolic partial differential equation which describes the distribution of heat in a region over time. It is the relation that was used and solved with FEM using initial and boundary conditions taken from experiments, as it will be described in detail in a following section.

The fundamental law governing all heat transfer mechanisms is the first law of thermodynamics (i.e. conservation of energy). Assuming no mass transfer and no radiation, the heat equation derived from the first law of thermodynamics in Cartesian coordinates is:

$$\frac{\partial}{\partial x} \left(k \frac{\partial T}{\partial x} \right) + \frac{\partial}{\partial y} \left(k \frac{\partial T}{\partial y} \right) + \frac{\partial}{\partial z} \left(k \frac{\partial T}{\partial z} \right) + \dot{Q}_s = \rho \cdot C_p \cdot \frac{\partial T}{\partial t} \quad (3.7)$$

where \dot{Q}_s is the total rate of heat energy per unit volume (W/m^3), ρ is the density of the material (kg/m^3) and C_p is the specific heat capacity of the material ($J \cdot kg^{-1} \cdot K^{-1}$) at constant pressure, which is the amount of energy needed to increase the temperature of one unit mass of the material by one degree.

Considering isotropic material and thus constant thermal conductivity k , the above equation is transformed to the following:

$$\frac{\partial^2 T}{\partial x^2} + \frac{\partial^2 T}{\partial y^2} + \frac{\partial^2 T}{\partial z^2} + \frac{\dot{Q}_s}{k} = \frac{1}{a} \cdot \frac{\partial T}{\partial t} \quad (3.8)$$

where a is the thermal diffusivity of the material (m^2/sec) and measures its ability to conduct thermal energy relative to its ability to store thermal energy.

Assuming a steady-state condition in which there is no change of temperature distribution with time, the heat equation is simplified to the known **Poisson equation**:

$$\frac{\partial^2 T}{\partial x^2} + \frac{\partial^2 T}{\partial y^2} + \frac{\partial^2 T}{\partial z^2} = -\frac{\dot{Q}_s}{k} \quad (3.9)$$

while in the case of zero rate of heat energy, the **Laplace equation** is derived:

$$\frac{\partial^2 T}{\partial x^2} + \frac{\partial^2 T}{\partial y^2} + \frac{\partial^2 T}{\partial z^2} = 0 \quad (3.10)$$

- *Initial and boundary conditions*

The solution of the heat equation depends on the initial and boundary conditions, as well as on whether the heating phenomenon is transient or steady state. The three kinds of most frequently used boundary conditions at a surface $x=0$ for a one-dimensional model are summarized below.

The boundary condition of **first kind** or **Dirichlet** condition is applied when a surface is maintained at a known temperature ($T(0, t) = T_0$). The boundary condition of the **second kind** or **Neumann** condition corresponds to the existence of a known heat flux at the surface ($-k \cdot \frac{\partial T}{\partial x} \Big|_{x=0} = \dot{q}$). A special condition of this kind is the thermal insulation or adiabatic surface with ($-k \cdot \frac{\partial T}{\partial x} \Big|_{x=0} = 0$). Finally, the **third kind** of boundary condition is applied when convective or radiation heat transfer occurs at a surface ($-k \cdot \frac{\partial T}{\partial x} \Big|_{x=0} = h \cdot [T_f - T(0, t)]$). The three kinds of boundary conditions are shown in Figure 3.5 and they are specified at the

surface $x=0$ for a one-dimensional model.

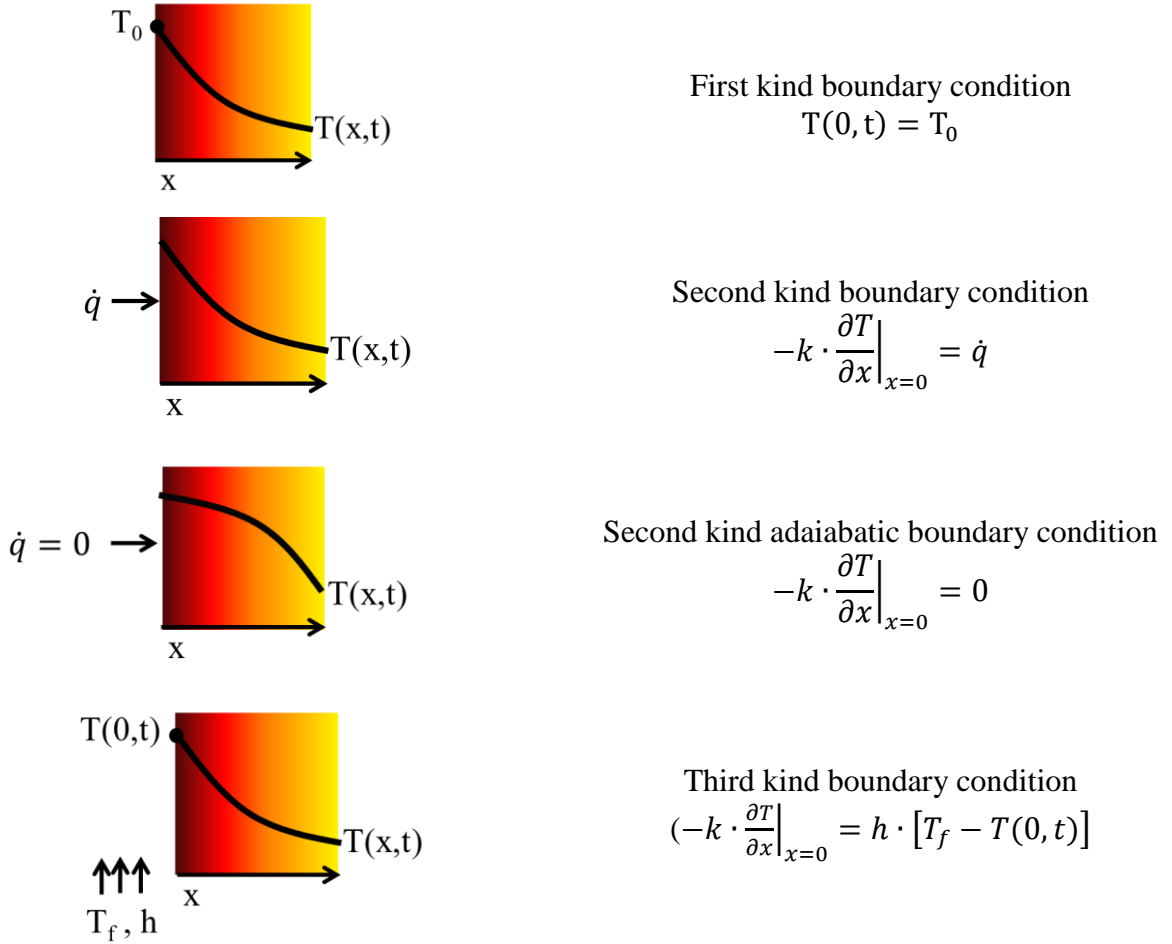


Figure 3.5: Schematic representation of the three kinds of boundary conditions that can be applied at a surface $x=0$ of a one-dimensional heat transfer FEM model.

3.5.2 Implementation of the method

Measurements were obtained using the four-point probe method. Practically, a dc current was applied at the outer pads of the Pt resistors and the voltage was measured at the inner ones (see Figure 3.3 step IV). Keithley 6221 AC and DC current source was used to apply the dc current and the Keithley 2000 multimeter to measure the voltage. Measurements were performed in the whole temperature range 4.2 – 350K using a He cryostat under vacuum. The samples were placed on the chuck of the cryostat using a thermally conductive and electrically isolating paste, specific for these low temperatures. The data were recorded after the steady state condition was reached.

As it has been already mentioned, the Pt resistors acted both as heaters to increase the temperature locally and as thermometers to sense the temperature increment. For temperature determination, the **Temperature Coefficient of Resistance (TCR)** of the integrated Pt strips was first measured. Thus, the resistivity as a function of temperature of the Pt resistors was determined from current–voltage (I-V) measurements, in a low current regime so as to avoid any Joule heating phenomenon. This way, the obtained I-V curves were within the linear regime at each temperature. From these curves, TCR of the Pt resistors was calculated using the following formula:

$$\text{TCR} = \beta_h = \frac{(R_T - R_{\text{ref}})/R_{\text{ref}}}{T - T_{\text{ref}}} \quad (3.11)$$

where R_T is the measured resistance of the Pt heater at temperature T , R_{ref} is the resistance at a reference temperature T_{ref} and TCR is the temperature coefficient of resistance. The measurements to extract TCR were carried out on the reference samples. Figure 3.6 shows the temperature dependence of the Pt resistance in the temperature range measured. A linear behavior was obtained which is described by the following relation:

$$R(T) = 0.0518 \cdot T + 13.8 \quad (3.12)$$

Figure 3.7 depicts an indicative curve of Pt resistance variations as a function of temperature difference for a reference temperature of 305K. From the slope of the curve, a $TCR = 0.0018/K$ was obtained at this temperature. This value is characteristic of the 200nm thick Pt resistor that was used in this study. It is lower than that of bulk Pt ($TCR = 0.0039/K$), in agreement with results in the literature [126]. This difference compared to the bulk value is attributed to the nanometer thickness of the film.

Finally, Figure 3.8 shows the measured values of TCR of Pt films as a function of the reference temperature (circles). In general TCR is different for different reference temperatures, as it is shown below. From the linear trend of the temperature dependence of Pt resistance (see Equation (3.12)), the following relations can be applied:

$$\left. \frac{dR}{dT} \right|_{T=T_{ref}} = 0.0518 \quad (3.13)$$

$$R(T_{ref}) = 0.0518 \cdot T_{ref} + 13.8 \quad (3.14)$$

$$TCR = \frac{1}{R(T_{ref})} \cdot \left. \frac{dR}{dT} \right|_{T=T_{ref}} \Rightarrow TCR = \frac{0.0518}{0.0518 \cdot T_{ref} + 13.8} \quad (3.15)$$

This last equation was used to calculate the TCR at each reference temperature and the calculated values based on this equation are depicted in Figure 3.8 by the red line. As it can be seen, there is very good agreement between the experimental data and the calculated ones using Equation (3.15).

After characterizing the Pt heaters/thermometers in the whole temperature range 4.2-350K, we proceeded to apply higher currents on the heaters, involving Joule heating phenomenon (high current regime) and temperature increase of the Pt resistor. This increment was determined by the intensity of the applied current, and consequently the applied heating power and the thermal properties of the substrate and the environment. Considering that the experiments were carried out in vacuum, the thermal losses to the environment were assumed to be negligible. Therefore, the only factor that defines the induced temperature difference on the surface of the samples is the thermal conductivity of the substrate. The thermal conductivity as a function of temperature was then obtained by comparing the measured and simulated results, as it will be described below.

Before analyzing the method used to extract thermal conductivity from the raw experimental data, we should note the following: in all cases, the reference temperature was measured on the reference samples using as thermometer the Pt resistor lying on bulk crystalline Si, which was identical to the one on porous Si (see Figure 3.3 step IV). Since with

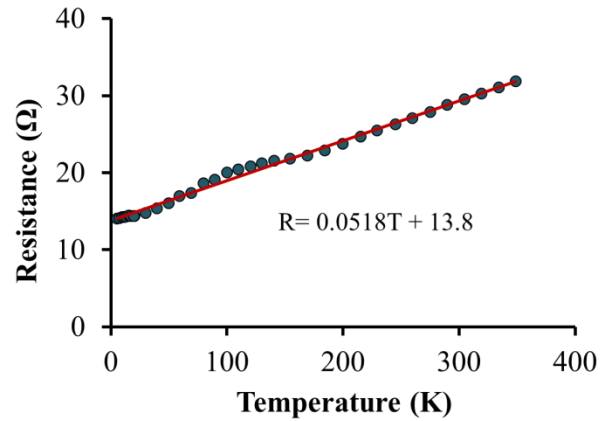
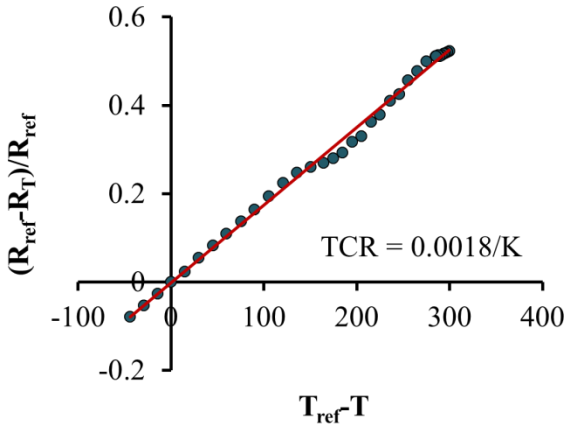


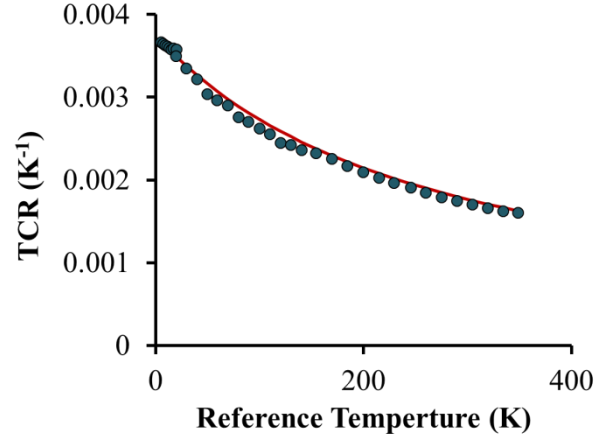
Figure 3.6: Temperature dependence of Pt resistance as a function of temperature

the applied heating power on the Pt resistor the temperature of the porous Si layer was slightly increased, we calculated for each reference temperature the integral of temperature of porous Si on its volume and corrected the measured temperature on bulk Si with the obtained value. However, in all cases this correction did not exceed the 2K.



(a)

Figure 3.7: Normalized resistance variations versus temperature difference for a reference temperature of 305K. From the slope of the curve the TCR is obtained which was calculated at 0.0018/K. The line is the linear fit to the experimental data shown with full circles.



(b)

Figure 3.8: TCR of Pt strips as a function of the reference temperature. The continuous line shows the calculated values using Equation (3.15), while the circles are the experimental data obtained in a similar way as in Figure 3.7 for all the studied temperatures.

The thermal conductivity of PSi was determined, as it was already mentioned, by combining the experimental results with simulations using 3-dimensional (3D) FEM simulations performed with COMSOL Multiphysics® software. The 3D model used for the analysis was designed using the exact dimensions of the fabricated experimental device. Sample architecture was, thus, composed of a 200nm thick Pt resistor on a 380μm thick bulk crystalline Si wafer (reference sample) and 40μm thick porous Si layer on 340 μm bulk c-Si as test sample for porous Si thermal conductivity measurements. The width of the Pt resistor was 20 μm and its length was 640μm in the case of the test PSi sample (four-point probe measurements), and 3mm (two-point probe measurements) in the case of the reference sample. In order to reduce the computational complexity, we used as length of the Pt resistor the length between the inner voltage pads. We tested this approximation by considering few examples with the full 3-D Pt pattern and found that the error stayed always below 0.7%, which is acceptable.

The differential steady state heat conduction equation (see section 3.4.1.1):

$$\nabla T = -\frac{\dot{Q}_s}{k} \quad (3.16)$$

was solved using FEM and boundary conditions determined from the experiment. In all cases the initial condition was the reference temperature and it was applied in all domains. Negligible radiation losses and self-heating phenomena were assumed, and great care was taken in all cases to limit the current to values that do not introduce any self-heating phenomena.

The dissipated power per unit volume (\dot{Q}_s) on the Pt resistor was calculated from the applied current, the measured voltage drop and the dimensions of the Pt resistor. Constant temperature was assumed as boundary condition to the backside of the Si substrate and its value was set to the measured value by the Pt resistors on the reference sample. The continuity boundary condition was used at boundaries in thermal contact: $-n_1 \cdot (-k_1 \cdot \nabla T_1) - n_2 \cdot (-k_2 \cdot \nabla T_2) = 0$, while the adiabatic formula of thermal insulation: $-n \cdot (-k \cdot \nabla T) = 0$

was applied at every other boundary (see Figure 3.9). As it was pointed out before, we assumed no heat transfer between the sample and the environment (thus there was no convective or conductive heat transfer at the external boundaries), as the measurements were performed in vacuum.

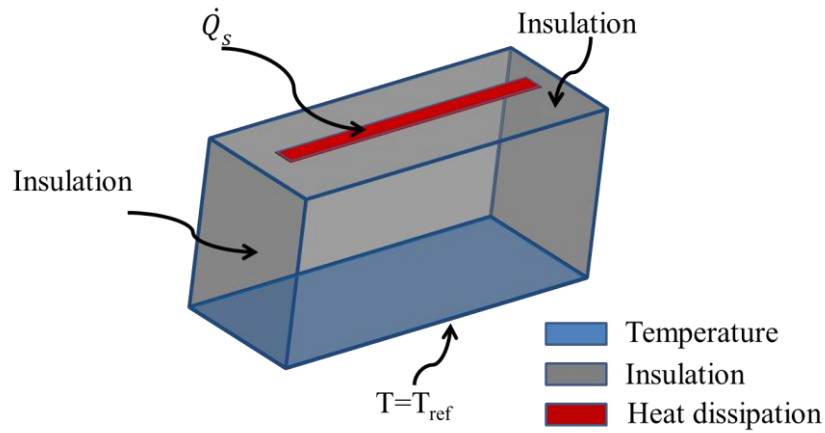


Figure 3.9: 3D Schematic representation of a reference sample showing the boundary conditions used to solve the heat transfer equation with FEM.

The model described above was first applied to bulk c- Si and the results are illustrated in Figure 3.10. In this case, the density and heat capacity of bulk crystalline Si and the density, heat capacity and thermal conductivity of Pt used in the simulation were taken from the literature [16, 127]. Therefore, the thermal conductivity of bulk crystalline Si was the only unknown parameter in the simulation, and it was calculated performing successive iterations until the average temperature over the entire volume of the heater reached the measured temperature of the heater.

The thermal conductivity of p-type bulk crystalline Si was thus obtained in the temperature range 200–290K and compared with experimental and theoretical results from the literature [16, 128]. The results of this work are represented by open triangles in the main Figure 3.10 and in the inset, while experimental results from Glassbrenner & Slack [16] and theoretical results from Rankin [128] are represented by full circles and stars respectively. From Figure 3.10, it is depicted that the results of this work are in good agreement with those of the literature. This way, the validity of our experimental measurement was assessed.

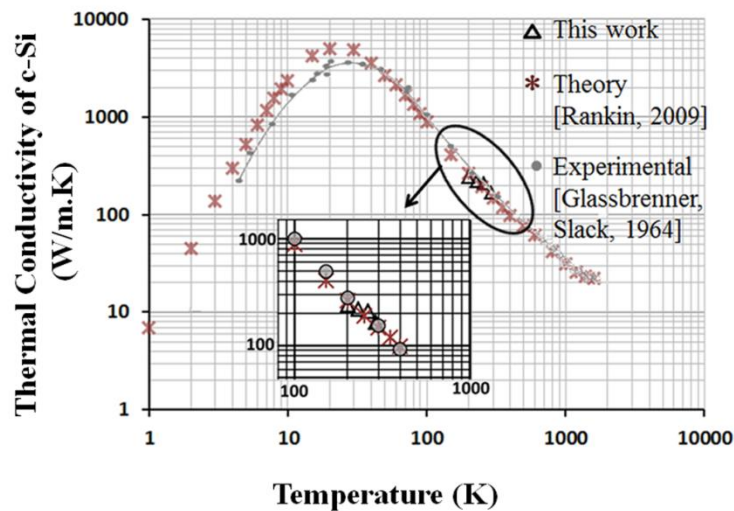


Figure 3.10: Thermal conductivity of bulk crystalline Si as a function of temperature. Results obtained in this work are represented and compared to experimental [16] and theoretical [128] results taken from the literature [15].

The determination of the thermal conductivity of PSi followed that of c-Si. The boundary conditions were also determined experimentally in the same way described previously. The thermal conductivity of bulk c-Si was taken from the literature for the non-measured values. The porous Si density was calculated by taking into account its porosity, while its specific heat capacity was set identical to that of bulk c-Si. This is a common assumption used in the literature due to the lack of experimental measurements in the whole temperature range studied in this work. We also considered porous Si as an isotropic and homogeneous material and thus we set thermal conductivity in heat transfer equation as a constant. This is macroscopically a realistic approximation for the porous Si layer formed on p-type c-Si with sponge-like morphology and homogeneous structure in the micrometer range (Figure 3.3). However, for the anisotropic sample prepared on the p⁺-type Si substrate (Figure 3.4), this assumption is not valid. Thus, by assuming thermal conductivity as a constant, we determine an effective thermal conductivity k_{eff} . Due to the anisotropy of the sample, we expect different in-plane and cross-plane thermal conductivities. This fact will be analyzed in more detail later, in the interpretation of the experimental results acquired for these samples.

3.5.3 Experimental results – Temperature dependence of porous Si Thermal resistance

Thermal resistance is a heat property of materials, which measures its resistance on heat flow. Thermal resistance is the thermal equivalent of electrical resistance and it is obtained as the reciprocal of **thermal conductance**. It can be calculated from the following equation:

$$\Delta T = Q \cdot R_{\text{th}} \quad (3.17)$$

where Q is the heating power (W), ΔT the temperature difference at the ends of the sample (K) and R_{th} is the thermal resistance (K/W).

The thermal resistance of the two porous Si layers studied in this work was also obtained. Using the measured TCR of Pt resistors, the temperature difference on the resistor as a function of the applied electric power was calculated and the corresponding curves $\Delta T = f(Q)$ were plotted. The results obtained for the Pt resistor on PSi for different temperatures are given in Figure 3.11 for the electric power range 0-15mW for both porous Si layers, namely the isotropic (63% porosity) and anisotropic (70% porosity) samples respectively.

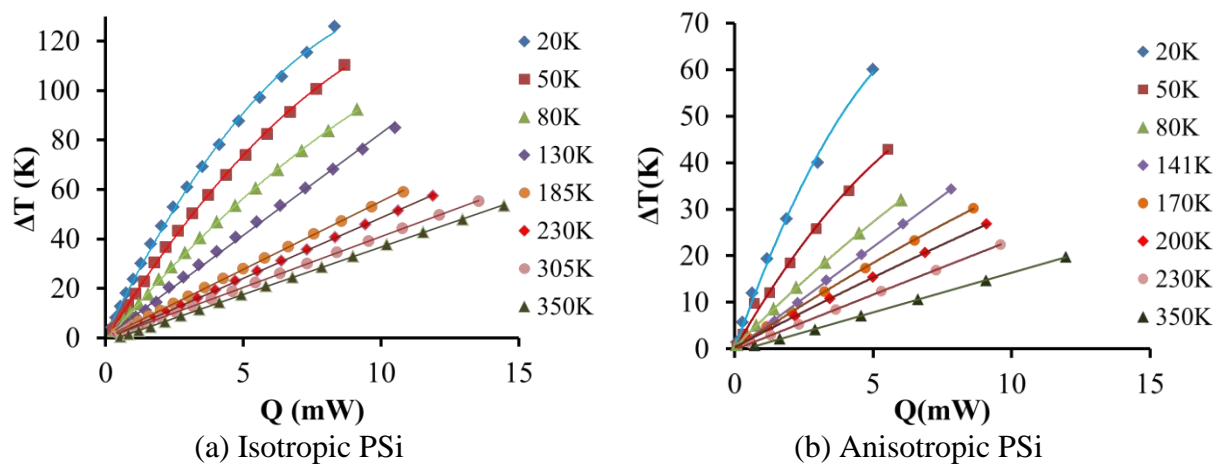


Figure 3.11: Increase of the temperature difference (ΔT) on the Pt resistor as a function of the applied electric power in the range of (0-15mW) for different temperatures for (a) an isotropic porous Si substrate [15] and (b) an anisotropic porous Si substrate

At low Q in both PSi substrates the corresponding curves are linear. The observed curvature at higher Q is a result of the temperature-dependent thermal conductivity of the sample, as it will be indicated in the next chapter. The thermal conductivity increases with increasing

temperature (increasing Q) and therefore the ΔT versus Q slope becomes increasingly shallower at higher temperatures, resulting in the observed negative curvature. This curvature is more prominent in the low temperature curves, as these curves correspond to the temperature region in which the thermal conductivity changes more rapidly with temperature [15]. By comparing the two different substrates, it is observed that for the same heating power the temperature increase that is achieved is higher for the isotropic PSi sample. This is more obvious in Figure 3.12 where the thermal resistance of the porous Si substrate was calculated from the slope of the linear part of the curves. Particularly, for temperatures in the range of 20-80K we limited the applied electric power to values below $\sim 2\text{mW}$, while for temperatures below 20K the applied power was limited below $\sim 1\text{mW}$, so as to ensure that we are in the linear region in both cases.

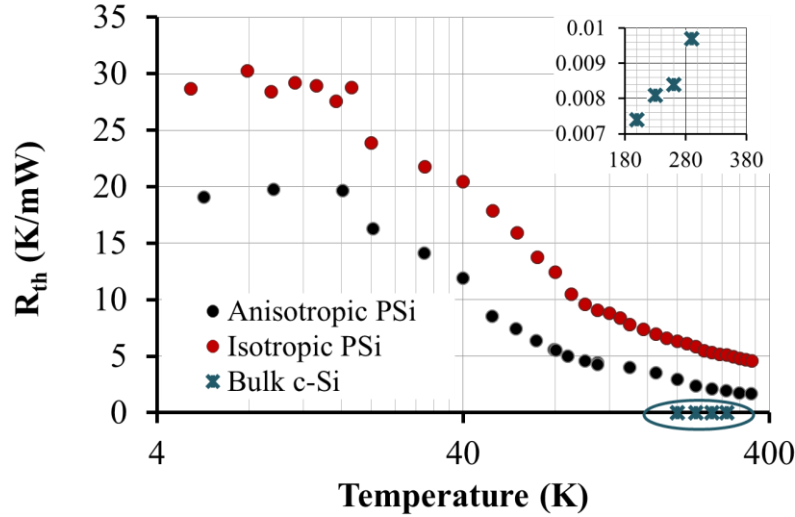


Figure 3.12: Temperature dependence of thermal resistance of isotropic PSi (red circles), anisotropic PSi (black circles) and bulk c-Si (stars). The inset shows a magnification of the absolute values of bulk c-Si.

In fact, by the slope of $\Delta T = f(Q)$ curves, the total thermal resistance of the substrate is calculated, which is composed of the thermal resistance of the PSi layer ($40\mu\text{m}$ thick layer) and the thermal resistance of the c-Si substrate (remaining $340\mu\text{m}$ thick c-Si after the anodization), as the equivalent circuit in Figure 3.13 shows. However, the thermal resistance of bulk Si is much lower than that of PSi and thus the total thermal resistance is dominated by that of PSi. The equivalent thermal circuit is simplified, as in Figure 3.13.

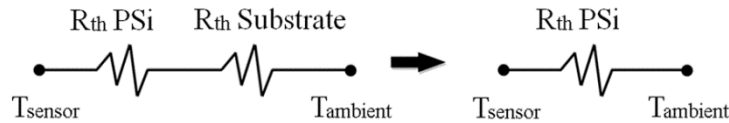


Figure 3.13: Equivalent thermal circuit of the structure under investigation (PSi ($40\mu\text{m}$ thick)/bulk crystalline Si ($340\mu\text{m}$ thick))

In Figure 3.12, a change of the slope of the corresponding characteristic temperature dependence of thermal resistance for both PSi layers is clearly indicated. A much faster increase of R_{th} with decreasing temperature is obtained for temperatures below $\sim 100\text{K}$, while an almost constant value is reached below $\sim 20\text{K}$. The measured thermal resistance of bulk crystalline Si is also illustrated in Figure 3.12 and in the inset. In this case, the measurements were limited to temperatures above $\sim 200\text{K}$, since the electric power needed for lower temperatures was extremely high, because thermal conductivity of c-Si is significantly increased below $\sim 200\text{K}$.

For comparison we also measured all the aforementioned parameters on a thicker anisotropic porous Si layer ($100\mu\text{m}$ thick). Only the porous Si layer formed on p^+ -type Si substrate was tested on thicker layers than $40\mu\text{m}$, because the isotropic one is much more

fragile, so cracks were formed during the drying of the samples. After a series of experiments, the thicker layers achieved were $\sim 50\mu\text{m}$ and thus thicker isotropic samples were not measured.

Figure 3.14a shows the $\Delta T(Q)$ curves at 80K and 230K for both anisotropic porous Si layers of $40\mu\text{m}$ and $100\mu\text{m}$ thicknesses with black and green symbols respectively for comparison, while Figure 3.14b depicts their thermal resistances in the whole temperature range 80-350K.

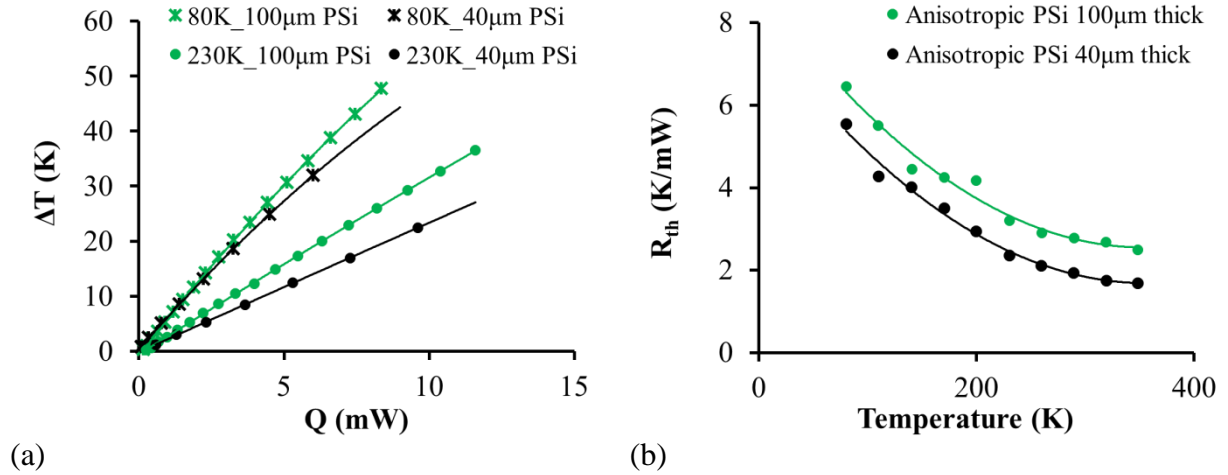


Figure 3.14: (a) Indicative $\Delta T(Q)$ curves at 80K and 230K Pt resistors on anisotropic PSi layers with different thicknesses ($40\mu\text{m}$ and $100\mu\text{m}$). (b) Temperature dependence of thermal resistance of the two identical anisotropic PSi layers with different thicknesses. The experimental data are fitted well with a second order polynomial trend line as it is shown in the graph.

Two basic conclusions derived from the above experimental data, which compare identical porous Si layers of different thicknesses. The thermal resistance of the thinner sample shows the same quadratic trend with temperature with the data of the thicker one ($\sim 1\text{K/mW}$ lower in the R_{th} axes). This is an expected result because the temperature dependence of thermal resistance, and thus thermal conductivity, is determined by the material itself and its intrinsic properties; however, the absolute value of R_{th} depends also on the dimensions of the samples. Thus, for the thicker PSi layer, a higher thermal resistance is obtained for all the measured temperatures with just a constant displacement on higher values compared to the thinner samples.

3.5.4 Experimental results - Temperature dependence of Porous Si thermal conductivity

The experimental results of the temperature dependence of porous Si thermal conductivity measured with the steady state dc method are summarized in Figure 3.15.

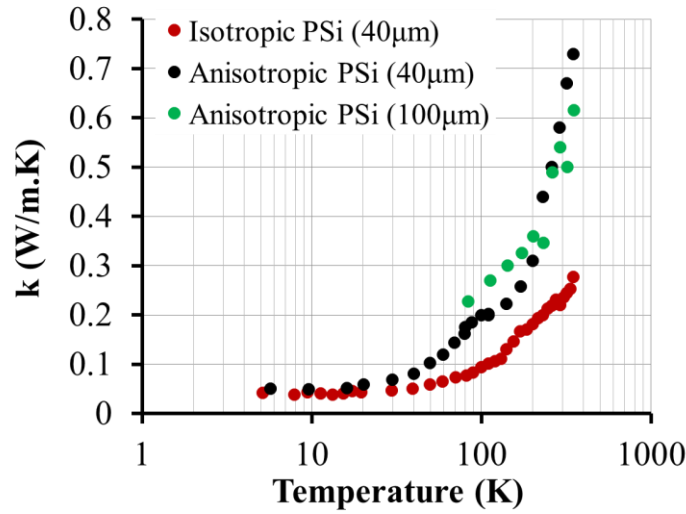


Figure 3.15: Temperature dependence of porous Si thermal conductivity, obtained using FEM and with the experimental results as inputs in the heat conduction equation problem. Both isotropic (63% porosity) and anisotropic porous Si (70% porosity) are depicted, while for the anisotropic one the results from different porous Si thicknesses are presented for comparison.

The thermal conductivity of both the isotropic and anisotropic PSi samples are illustrated in the Figure 3.15. For the anisotropic porous Si layer the values are given for two PSi thicknesses. As it can be seen, the thermal conductivity of both materials shows the same trend with temperature. More specifically, k decreases by decreasing temperature, reaching a plateau at very low temperatures, below $\sim 20\text{K}$. This trend will be analyzed in a following chapter, where a comparison to theory and other crystalline and amorphous materials will be made, giving additional information on the thermal transport mechanisms governing this behavior.

From Figure 3.15, we clearly deduce that the anisotropic PSi layer has higher thermal conductivity values than that of the isotropic one in the whole temperature range measured, even though its porosity is higher. It is generally accepted that the thermal conductivity of PSi decreases significantly with increasing porosity due to the increasing of air/nanostructured Si ratio and phonon confinement in the Si nanostructures. Thus, we would expect the higher porosity sample (the anisotropic one with 70% porosity) to have lower thermal conductivity compared to the lower porosity sample (the isotropic one with 63% porosity). Our measurements reveal that is not the case. This is attributed to the specific structure and morphology of the sample showing strong anisotropy (see Figure 3.16).

In section 3.4.1.1, it was mentioned that thermal conductivity in heat conduction equation should be assumed as a tensor in anisotropic materials. In the implementation of the dc method, we assumed a constant effective value k_{eff} in the simulations. This means that the extracted thermal conductivity shown in Figure 3.15 corresponds also to an effective thermal conductivity. As Figure 3.16b illustrates, the anisotropy in the morphology of the specific PSi layer leads to highly anisotropic heat flow in its volume. The vertically oriented pores form Si nanowires, which act as thermally conductive paths, connecting the surface of the sample to the Si substrate (y direction). On the other hand, the heat flow in the direction perpendicular to the formed nanowires (x direction) is almost completely inhibited by the empty vertical columns. Consequently, it is expected that the in plane thermal conductivity (k_x) in this

material is significantly lower than the cross plane one (k_y). This result has also been proved theoretically by Chung and Kaviani [129], who used Boltzmann transport equation to predict the ratio k_x/k_y in anisotropic PSi layers of different porosity. A ratio of ~ 0.02 was obtained, while more recently Kim and Murphy [130] obtained the same ratio from their experimental results of a $\sim 60\%$ porosity anisotropic PSi layer and found a value of 0.01. Consequently, we expect the corresponding ratio in our higher porosity sample to be more than 0.01. This fact is indicative of the strong anisotropy that this material conducts the heat.

Contrary to the anisotropic PSi sample, the macroscopically isotropic one (Figure 3.16a) shows a homogenous sponge like morphology, which results in a uniform heat flow in both in-plane and cross-plane directions. There are no continuous nanowires formed to connect the surface of the sample with the Si substrate. On the contrary, a complex porous Si network exists with no pronounced thermal paths. Therefore, this sample is more resistant in conducting the heat despite its lower porosity. Phonon scattering is stronger in the complex nanostructured Si skeleton, resulting in lower thermal conductivity. This was proved experimentally from our measurements in the entire temperature range studied.

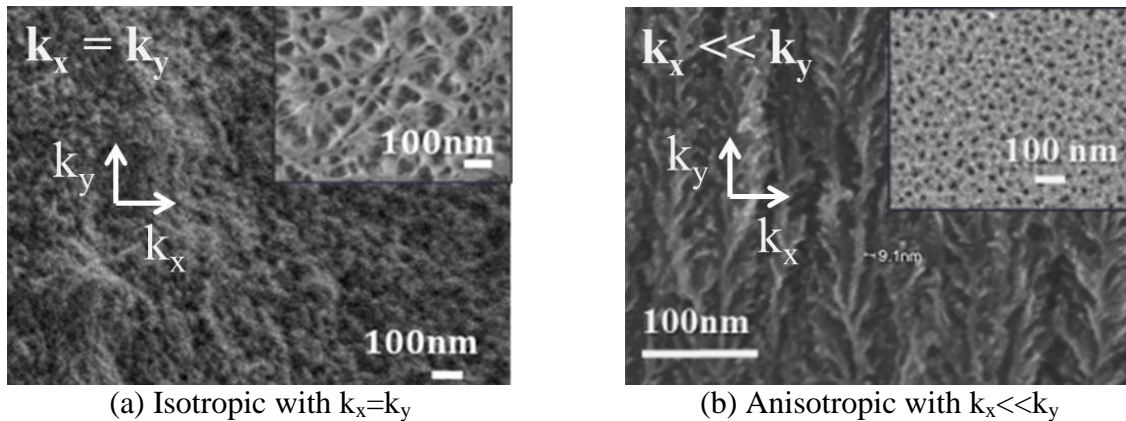


Figure 3.16: SEM cross sectional images with their top views in the insets of (a) isotropic PSi 63% porosity and (b) anisotropic PSi with 70% porosity. In the images the direction of the in plane k_x and cross plane k_y thermal conductivity vectors are drawn.

The results of Figure 3.15 also indicate a sharper increase of thermal conductivity of the anisotropic sample with temperature above $\sim 20\text{K}$ compared to the more smooth increase of the isotropic sample. This is probably due to the larger mean crystallite size of the former sample. Generally, the small size PSi nanostructures of the PSi skeleton limit the phonon mean free path in this material, as it will be shown below using known theoretical models. However, the obtained value is a mean value. Apart from the majority of the phonon modes that their transport is dominated by this value, other phonon modes with different frequencies, velocities and MFPs still exist. Thus, by decreasing the characteristic lengths below the already extreme values, more phonon modes are scattered by the lattice, which reduces the dependence of thermal conductivity on temperature.

From Figure 3.15 it is also deduced that the anisotropic samples with different thicknesses (40 μm and 100 μm) showed almost the same thermal conductivity in the temperature range 80-350K. Small divergences are possibly due to experimental errors. This result was somehow expected because thermal conductivity does not depend on the dimensions of the samples, as is the case of thermal resistance. Thus, considering identical PSi layers, the measured values should coincide, independently of the thickness of the formed layer. However, it is known that porosity slightly increases with etching time and thus with thickness[131]. If this was the case in our samples, the 100 μm thick PSi layer should have higher porosity and thus lower values of thermal conductivity. Nevertheless, this is not observed for all the temperatures shown in the graph. Additionally, during this study we did not observe any change in the morphology or the porosity of our samples at these thicknesses. Thus, we attributed these variations to experimental errors. For this reason and for simplicity, in the following sections when the thermal conductivity of anisotropic PSi is referred to, it

corresponds to the average values for both thicknesses.

3.5.5 Comparison with other materials and theory

A comparison of the obtained thermal conductivity of porous Si with that of bulk crystalline Si, α -Si, a-Si:H and some other C-MOS compatible dielectrics is shown in Figure 3.17. It is clearly seen that the obtained values of thermal conductivity of PSi are much lower than those of bulk crystalline Si. This difference exceeds four orders of magnitude at temperatures below 50K. It is also comparable to/or lower than other materials that are usually used for thermal isolation.

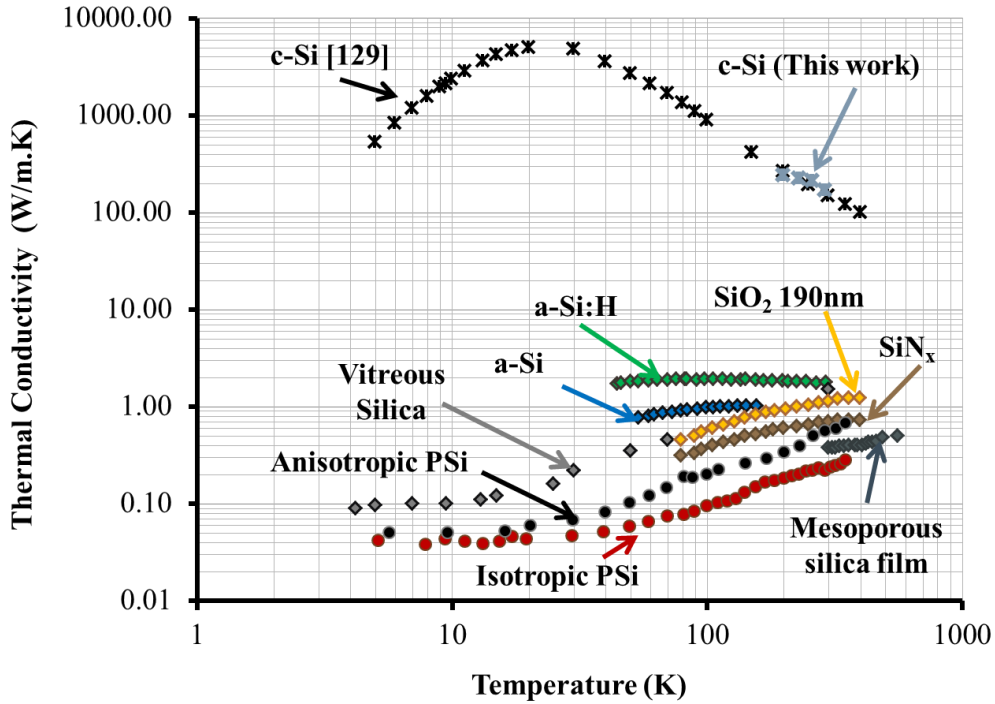


Figure 3.17: Comparison of the thermal conductivity of porous Si (isotropic & anisotropic measured in this thesis) with that of bulk crystalline silicon [128], a-Si [132], a-Si:H [133] and different other CMOS compatible films (mesoporous silica[134], vitreous silica [135] and silicon nitride [136]).

As it was explained in section 3.3.1, there is an almost common trend of the variation of thermal conductivity of crystalline materials with temperature. The temperature dependence of pure bulk crystalline Si follows this trend. It goes through a maximum at a temperature of about ~20K. Below this maximum, the thermal conductivity follows temperature dependence close to that of the specific heat of the lattice ($k = f(T^3)$). Above the maximum, the thermal conductivity decreases with increasing temperature, following the phonon mean free path which is reduced due to increased phonon-phonon scattering (see Figure 3.18).

On the other hand, highly porous Si does not show the same behavior. Due to its structure and morphology, PSi shows much lower thermal conductivity than that of bulk crystalline Si, which, at these high porosities (63 & 70%), is even below the amorphous limit. This is attributed to phonon confinement in the Si nanostructures, phonon scattering at its large internal surface area and the presence of air that forms voids, which separate the nanostructured Si skeleton. Our measurements indicate that, contrary to bulk c-Si, the temperature dependence of thermal conductivity of this type of porous Si layers in the above temperature range is monotonic and does not show any maximum. It is more similar to that of different low thermal conductivity amorphous materials, its value being even lower than that of the most known such materials (amorphous Si, silicon oxide, silicon nitride).

At very low temperatures below ~20K a constant value of thermal conductivity is reached for both PSi structures (on p-type and p⁺-type Si). This plateau-like behavior is common to glasses and disordered materials (i.e. SiO₂, vitreous silica, epoxy resin etc), but unusual in crystalline systems. The plateau-like behavior of porous Si thermal conductivity in the above temperature range will be discussed by considering the fractal nature of the material and the existence of localized vibrational excitations (fractons) that dominate at these temperatures in Chapter 4. Here our analysis focuses on the thermal conductivity behavior above the plateau i.e. T>20K.

It was already mentioned that in porous Si, the thermal conductivity decreases with increasing porosity. There are many different theoretical models that predict this behavior. The most common of them treat the problem using kinetic theory of phonons, molecular dynamic simulations [137] or by using the so-called phonon hydrodynamics model [138], which is a generalization of Fourier's law, incorporating non- local effects and thermal slip along the nanostructure walls.

Based on this last method, an analytical expression of the effective thermal conductivity of porous Si was obtained in reference [138] as a function of porosity (P), characteristic size of the PSi system (a) and phonon bulk mean free path (l_{Si}):

$$k_{eff} = k_{Si} \cdot \frac{1}{\frac{1}{f(P)} + 4.5 \cdot P \cdot \frac{(l_{Si}/a)^2}{1 + A'(l_{Si}/a)} \cdot (1 + \frac{3}{\sqrt{2}} \cdot \sqrt{P})} \quad (3.18)$$

where k_{Si} is bulk c- Si thermal conductivity, $f(P) = (1 - P)^3$ and A' is a numerical function of Knudsen number $K_n \equiv l_{Si}/a$ and varies from 0.7 to 1.164.

We used this analytical expression to calculate the thermal conductivity of our samples as a function of temperature and compare the corresponding theoretical values to our experimental results. The c-Si phonon mean free path was calculated by classical kinetic theory:

$$k_{Si} = \frac{1}{3} \cdot C_{Si} \cdot u_{Si} \cdot l_{Si} \quad (3.19)$$

while A' was calculated by the heuristic form [139] :

$$A' = 0.864 + 0.29 \cdot \exp(-1.25 \cdot \frac{a}{l_{Si}}) \quad (3.20)$$

The parameters used in the calculation for the temperature of 300K are summarized in Table I for the two cases of PSi layers, while Figure 3.18 shows the phonon mean free path (MFP) of c-Si in the whole temperature range 4.2-350K. The green and red lines indicate the characteristic lengths of anisotropic and isotropic PSi layers respectively.

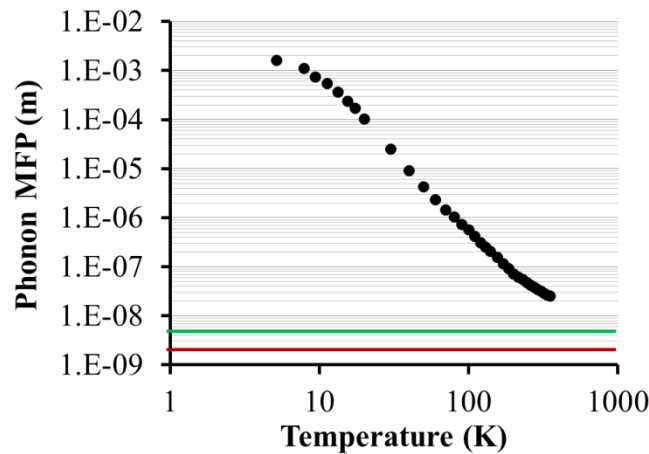


Figure 3.18: Calculated phonon mean free path of bulk c-Si using Equation (3.19) for the temperatures studied in this work. The green and red lines indicate the mean crystallite sizes of anisotropic and isotropic PSi layers that used for thermal conductivity calculations.

Table I: Porosity, characteristic size, bulk c-Si phonon mean free path and A' values used to calculate thermal conductivity of PSi based on the analytical Equation (3.20).

PSi	P (%)	a (nm)	l_{Si} (nm)	A'
Isotropic	63	3	34	1.13
Anisotropic	70	5	34	1.11

It should be mentioned here that, contrary to what we have done in our recent publication [15], the characteristic size of the PSi was not considered as constant, taken from the literature, but was selected so as to provide the best fit to our experimental results. The result for the isotropic sample fitting the experimental results was 3nm, while the value of 5nm was obtained for the anisotropic PSi. This value is consistent with or measurements of the inter-pore distance in such samples using Transmission Electron Microscopy (TEM) images (Figure 3.19).

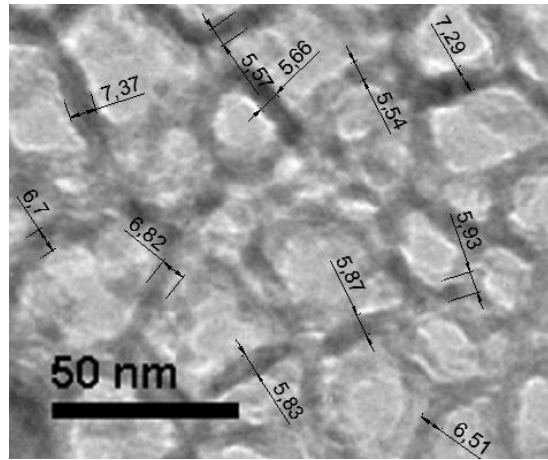


Figure 3.19: TEM image of the anisotropic PSi layer on which measurements of the inter-pore distance are indicated. Their mean value was calculated to be ~5nm.

The obtained theoretical results using the above approach are depicted in Figure 3.20 for the isotropic (a) and for the anisotropic (b) samples respectively. In the same figure, we represent also the results obtained using a simplified model that takes into account only the porosity of the PSi layer and the mean crystallite size of Si (d_k) [119]. More specifically, in this model the mean free path of phonons in PSi is limited by its mean crystallite size because, as the Figure 3.18 clearly shows, it is much smaller than the bulk phonon mean free path in Si in the whole range 4.2-350K.

In this last model the effective thermal conductivity of PSi is given by:

$$k_{eff} = \frac{1}{3} \cdot (1 - P)^3 \cdot \rho_{Si} \cdot C_{Si} \cdot u \cdot d_k \quad (3.21)$$

where $\rho_{Si} = 2329 \text{ kg/m}^3$ the density of Si and $u = 6562 \text{ m/sec}$.

To calculate the thermal conductivity with this model, we assumed that the mean crystallite size of our PSi layer was the same as the corresponding characteristic size used in the phonon hydrodynamics approach (i.e. $d_k=a$). In this way, we were able to compare the two theoretical models. The results are also depicted in Figure 3.20. For comparison, the experimental results obtained in this work are also shown.

From Figure 3.20, it is deduced that the simplified phonon diffusion model is in relatively good agreement with our experimental results, while the phonon hydrodynamic model gives much lower values than the experimental ones at temperatures below ~180K. Both theoretical models predict a sharp decrease with decreasing temperature (at temperatures below 50K for the phonon diffusion model and below ~120K for the phonon hydrodynamic approach). This

is not the case for our experimental results, which show a smooth decrease of k with decreasing temperature. This can be attributed to an inaccuracy of the models at these low temperatures. The plateau like behavior that we obtained experimentally is analyzed comprehensively in a following chapter.

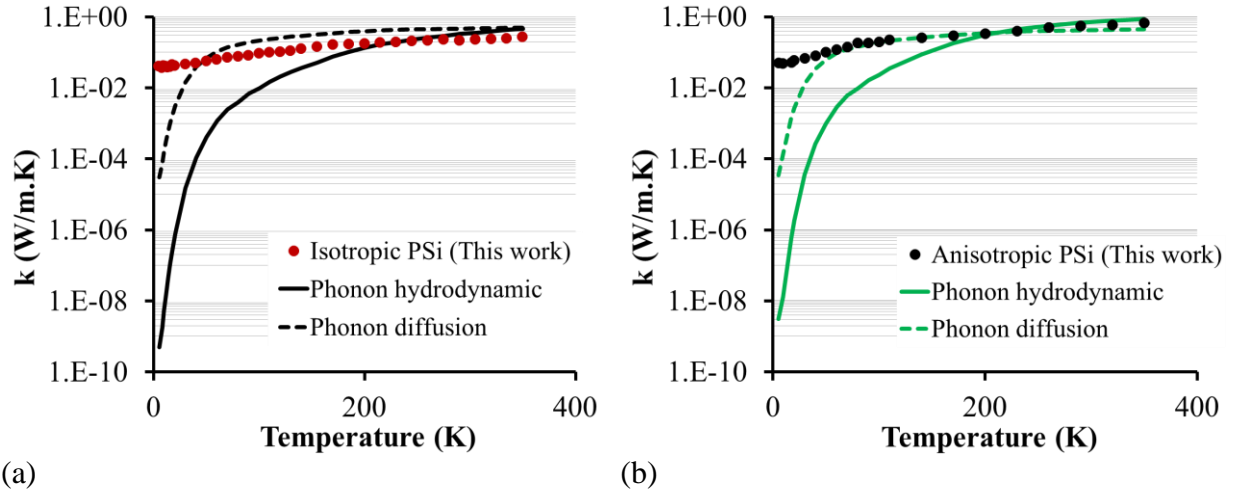


Figure 3.20: Experimental results of PSi thermal conductivity as a function of temperature for the isotropic (a) and anisotropic (b) samples. The dashed lines correspond to the calculated values based on the phonon diffusion model, while the continuous line is obtained using the phonon hydrodynamic approach.

3.6 3ω method

3ω -method is a popular technique for thermal conductivity measurements (see section 1.3.2). In this thesis the 3ω method was also used to measure the temperature dependence of PSi thermal conductivity and the results obtained using this technique were compared to those obtained with the dc method. The 3ω method was implemented with four and two point probe configurations. Alternative approaches to obtain thermal conductivity from the third harmonic of voltage were introduced and compared to the well-known slope method. All these are described in the following paragraphs.

3.6.1 General assumptions and considerations

As it was already mentioned in section 1.3.2., for the implementation of the 3ω measurement technique a thin metal strip is deposited on the sample and acts as heat source and a thermometer. The heater is driven with ac current at frequency ω , which causes heat source to oscillate at frequency 2ω . By monitoring ac voltage as a function of the frequency of the applied ac current, the thermal conductivity can be determined. The measured voltage contains both ω and 3ω components, because the Joule heating of the film causes small perturbation to its resistance with frequency 2ω . This is deduced from the Equation (1.13), which is reproduced below:

$$V_h(t) = I_{ho}R_{ho} \left[(1 + \beta_h \Delta T_{DC}) \cos(\omega t) + \frac{1}{2} \beta_h |\Delta T_{AC}| \cos(\omega t + \varphi) + \frac{1}{2} \beta_h |\Delta T_{AC}| \cos(3\omega t + \varphi) \right] \quad (1.13)$$

From this equation, the amplitude of the third harmonic of voltage is derived as:

$$V_{3\omega} = \frac{1}{2} V_{ho} \beta_h \Delta T_{AC} \quad (3.22)$$

where

$$V_{ho} = I_{ho} \cdot R_{ho} \quad (3.23)$$

$$V_{3\omega} = V_{3\omega,x} + V_{3\omega,y}i \quad (3.24)$$

$$\Delta T_{AC} = \Delta T_{AC,x} + \Delta T_{AC,y}i \quad (3.25)$$

$$\Delta T_{AC,x} = |\Delta T_{AC}| \cdot \cos(\varphi), \text{ in-phase component} \quad (3.26)$$

$$\Delta T_{AC,y} = |\Delta T_{AC}| \cdot \sin(\varphi), \text{ out-of-phase component} \quad (3.27)$$

Cahill has found a solution for the temperature oscillations by considering a radial flow of heat from a line source of heat on the surface of a half volume semi-infinite cylinder [18]. He initiated his work by the use of the heat conduction equation on cylindrical coordinates given by Carslaw and Jaeger [140]. In the following section, the heat transfer equation will be solved to determine the temperature oscillations on the heater, through which the thermal conductivity of the specimen is determined. In order to construct this mathematical model for the determination of the thermal conductivity, the problem will be first solved for simplified geometries and the solution will be then developed in steps, until a geometry closer to the real one is achieved.

Thus, at the beginning, the heat source is considered as a narrow line heater inside an infinite circular cylinder. Then, the infinite cylinder is cut longitudinally from its center to create a heat source at the surface of a semi-infinite solid. The solution is further developed for a heater with finite width.

3.6.1.1 One - dimensional Line heater

Infinite heat source inside an infinite circular cylinder

Starting with Carslaw and Jaeger [140] equation of heat conduction of an infinite heat source inside an infinite circular cylinder and applying a periodic heat flux at the interior boundary, the problem is reduced to a 1D heater encased inside an infinite solid (Figure 3.21).

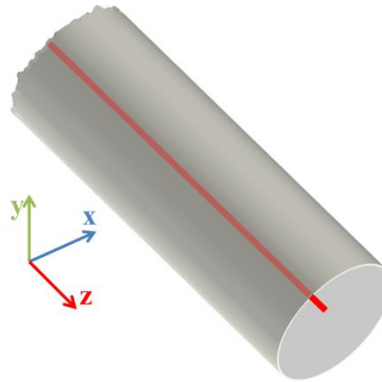


Figure 3.21: Schematic representation of the geometry of 1D heater encased inside an infinite solid used to solve the heat equation

We begin with the equation of conduction expressed in cylindrical coordinates:

$$\frac{1}{r} \frac{\partial}{\partial r} \left(r \frac{\partial T(r, t)}{\partial r} \right) + \frac{1}{r^2} \frac{\partial^2 T(r, t)}{\partial \theta^2} + \frac{\partial^2 T(r, t)}{\partial z^2} = \frac{1}{\alpha} \frac{\partial T(r, t)}{\partial t} \quad (3.28)$$

or

$$\frac{\partial T(r,t)}{\partial t} = \alpha \left(\frac{\partial^2 T(r,t)}{\partial r^2} + \frac{1}{r} \frac{\partial T(r,t)}{\partial r} + \frac{1}{r^2} \frac{\partial^2 T(r,t)}{\partial \theta^2} + \frac{\partial^2 T(r,t)}{\partial z^2} \right) \quad (3.29)$$

where $T(r,t)$ is the instantaneous temperature at a radius r of the cylinder and α is the thermal diffusivity (m^2/sec) defined as:

$$\alpha = \frac{k}{\rho \cdot C_p} \quad (3.30)$$

In the above case, we have a circular cylinder, whose axis coincides with the z axis of the heater, and the initial and boundary conditions are independent of the coordinates θ and z . So, the instantaneous temperature will be a function of r and t only and the Equation (3.29) is reduced to:

$$\frac{\partial T(r,t)}{\partial t} = \alpha \left(\frac{\partial^2 T(r,t)}{\partial r^2} + \frac{1}{r} \frac{\partial T(r,t)}{\partial r} \right) \quad (3.31)$$

In this case, the flow of heat takes place in planes perpendicular to the axis, and the lines of flow are radial.

As it was shown previously for an excitation current with angular frequency ω on a resistor, the applied thermal power ($Q(t) = \frac{1}{2} I_{ho}^2 R_{ho} (1 + \cos(2\omega t))$) has a constant with time dc component ($P_{DC} = \frac{1}{2} I_{ho}^2 R_{ho}$) and an ac one ($P_{AC}(t) = \frac{1}{2} I_{ho}^2 R_{ho} \cos(2\omega t)$). As a result the instantaneous temperature $T(r,t)$ is equal to the ambient temperature T_0 plus the dc temperature rise $\Delta T_{DC}(r)$ and the steady state temperature oscillations $\Delta T_{AC}(r,t)$.

$$\Delta T_{AC}(r,t) = T(r,t) - (T_0 + \Delta T_{DC}(r)) , \text{ with } \Delta T_{DC}(r) = T_{DC}(r) - T_0 \quad (3.32)$$

Substituting in Equation (3.31), we obtain:

$$\frac{\partial \Delta T_{AC}(r,t)}{\partial t} = \alpha \left(\frac{\partial^2 \Delta T_{AC}(r,t)}{\partial r^2} - \frac{\partial^2 \Delta T_{DC}(r)}{\partial r^2} + \frac{1}{r} \frac{\partial \Delta T_{AC}(r,t)}{\partial r} - \frac{1}{r} \frac{\partial \Delta T_{DC}(r)}{\partial r} \right) \quad (3.33)$$

$$\frac{\partial^2 \Delta T_{AC}(r,t)}{\partial r^2} + \frac{1}{r} \cdot \frac{\partial \Delta T_{AC}(r,t)}{\partial r} - \frac{1}{\alpha} \cdot \frac{\partial \Delta T_{AC}(r,t)}{\partial t} = \frac{\partial^2 \Delta T_{DC}(r)}{\partial r^2} + \frac{1}{r} \cdot \frac{\partial \Delta T_{DC}(r)}{\partial r} = 0 \quad (3.34)$$

Equation (3.34) confirms the implicit assumption that dc and ac temperature amplitudes are independent of each other. The dc temperature rise is not taken into account in the solution since the thermal conductivity is extracted from steady state temperature oscillations. We consider only the left hand part of Equation (3.34) and use separation of variables:

$$\Delta T_{AC}(r,t) = \Delta T_{AC}(r) \cdot \Theta(t) \quad (3.35)$$

We know from a previous section that a driven current at frequency ω results in temperature oscillations at 2ω . So,

$$\Theta(t) = \cos(2\omega t) \equiv \Re(e^{i2\omega t}) \quad (3.36)$$

Substituting Equations (3.35) and (3.36) in the left hand of Equation (3.34) we get:

$$\frac{d^2 \Delta T_{AC}(r)}{dr^2} \cdot \cos(2\omega t) + \frac{1}{r} \cdot \frac{d \Delta T_{AC}(r)}{dr} \cdot \cos(2\omega t) - \frac{2\omega i^2}{\alpha} \cdot \sin(2\omega t) \cdot \Delta T_{AC}(r) = 0 \quad (3.37)$$

$$\frac{d^2 \Delta T_{AC}(r)}{dr^2} \cdot \cos(2\omega t) + \frac{1}{r} \cdot \frac{d\Delta T_{AC}(r)}{dr} \cdot \cos(2\omega t) - \frac{2\omega i}{\alpha} (e^{i2\omega t} - \cos(2\omega t)) \cdot \Delta T_{AC}(r) = 0 \quad (3.38)$$

$$\stackrel{q=\sqrt{\frac{2\omega i}{\alpha}}}{\Longleftrightarrow} \Re \left\{ \left(\frac{d^2 \Delta T_{AC}(r)}{dr^2} + \frac{1}{r} \frac{d\Delta T_{AC}(r)}{dr} - q^2 \Delta T_{AC}(r) \right) e^{i2\omega t} \right\} = 0 \quad (3.39)$$

where q : the wavenumber of the thermal wave (rad/m).

Equation (3.39) is simply the real part of the modified Bessel equation $\left(x^2 \cdot \frac{d^2 y}{dx^2} + x \cdot \frac{dy}{dx} - (x^2 + n^2) \cdot y = 0 \right)$, with solution $y = a_1 \cdot I_n(x) + a_2 \cdot K_n(x)$, where $I_n(x)$ is the modified Bessel function of the first kind and $K_n(x)$ is a modified Bessel function of the second kind of order n and argument x . Setting $x=qr$ and $n=0$ we get the zero order modified Bessel function with argument qr . Consequently, the general solution of Equation (3.39) is:

$$\Delta T_{AC}(r, t) = \Re \left((a_1 I_0(qr) + a_2 K_0(qr)) e^{i2\omega t} \right) \quad (3.40)$$

To find the unknown constants a_1 and a_2 , the boundary conditions must be applied.

- $r \rightarrow \infty$

As the distance r from the heater tends to infinity, the steady state temperature oscillations tend to decay. So, $\lim_{r \rightarrow \infty} \Delta T_{AC}(r, t) = 0$

Knowing that $\lim_{r \rightarrow \infty} I_0(qr) = \infty$ and $\lim_{r \rightarrow \infty} K_0(qr) = 0$ and substituting in Equation (3.40), we get $a_1 = 0$.

- $r \rightarrow 0$

The rate of heat conduction in a certain direction is described by the Fourier's law of heat conduction (1D heat conduction) in cylindrical coordinates:

$$\dot{Q} = -k \cdot A \cdot \frac{dT}{dr} \quad (3.41)$$

where \dot{Q} is the rate of heat flow due to the Joule heating in the heater and A is the cross-sectional surface area, which in our case (cylinder) is $A_c = 2\pi r l$ in (m^2).

Thus, we have at the limit of zero radial distance from the center of the cylinder:

$$\dot{Q} = \Re(P_{rms} e^{i2\omega t}) = \lim_{r \rightarrow 0} \left(-k \cdot A_c \cdot \frac{\partial \Delta T_{AC}(r, t)}{\partial r} \right) \quad (3.42)$$

$$\Re(P_{rms} e^{i2\omega t}) = \lim_{r \rightarrow 0} \left(-k \cdot 2\pi r l \cdot \frac{\partial}{\partial r} (\Re(a_2 K_0(qr)) e^{i2\omega t}) \right) \quad (3.43)$$

Knowing that for small values of x , $K_0(x) = -\ln(x)$ [141]:

$$a_2 = \frac{P_{rms}}{2k\pi l} = \frac{p_{rms}}{2k\pi} \quad (3.44)$$

where p_{rms} is the rms power per unit length W/m.

Substituting the known constants a_1 and a_2 in Equation (3.40), we get:

$$\Delta T_{AC}(r, t) = \Re \left(\left(\frac{P_{rms}}{2k\pi} \cdot K_0(qr) \right) \cdot e^{i2\omega t} \right) = |\Delta T_{AC}(r)| \cdot \cos(2\omega t + \varphi) \quad (3.45)$$

where

$$\Delta T_{AC}(r) = \frac{P_{rms}}{2k\pi} \cdot K_0(qr) = \Delta T_{AC,x}(r) + i \cdot \Delta T_{AC,y}(r) \quad (3.46)$$

where

$$\Delta T_{AC,x}(r) = \Re \left(\frac{p_{rms}}{2k\pi} K_0(qr) \right), \text{ in-phase component} \quad (3.47)$$

$$\Delta T_{AC,y}(r) = \Im \left(\frac{p_{rms}}{2k\pi} K_0(qr) \right), \text{ out-of-phase component} \quad (3.48)$$

This last equation shows that the AC temperature oscillations produced in a line heater inside an infinite cylinder have the form of the zero order modified Bessel function of the second kind.

We are not so much interested in determining the temporal evolution of $\Delta T_{AC}(r, t)$, as in determining the spatial evolution of the thermal waves ($\Delta T_{AC,x}(r)$ and $\Delta T_{AC,y}(r)$), with respect to the excitation current as a function of ω . Thus, from now on we will focus on the spatial evolution of the temperature oscillations.

3.6.1.2 Infinite heat source at the surface

Considering that 3ω method is applicable on samples where a heater is deposited on the specimen under study, we have to reconstruct the previous mathematical model of 1D heater inside an infinite solid, to fit to the experimental conditions of 3ω method. A first approach can be obtained, if we simply cut the previous studied infinite cylinder along a plane perpendicular to z axis (see figure 3.22).

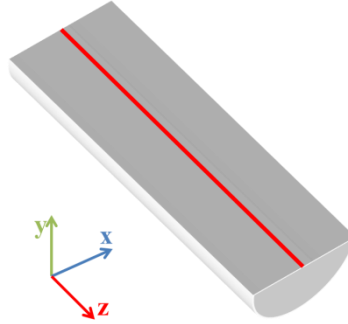


Figure 3.22: Schematic representation of the geometry of 1D heater at a surface of a semi-infinite solid used to solve the heat equation

Cutting the cylinder as it is shown in Figure 3.22, changes the cross-sectional area of the previous study to $A_c = \pi r l$. Following the same steps and using the same boundary conditions, we calculate the constant a_2 :

$$a_2 = \frac{P_{rms}}{k\pi l} \quad (3.49)$$

So, Equation (3.40) is now replaced by:

$$\Delta T_{AC}(r) = \frac{p_{rms}}{k\pi} \cdot K_0(qr) = \Delta T_{AC,x}(r) + i \cdot \Delta T_{AC,y}(r) \quad (3.50)$$

$$\Delta T_{AC,x}(r) = \Re \left(\frac{p_{rms}}{k\pi} K_0(qr) \right), \text{ in-phase component} \quad (3.51)$$

$$\Delta T_{AC,y}(r) = \Im \left(\frac{p_{rms}}{k\pi} K_0(qr) \right), \text{ out-of-phase component} \quad (3.52)$$

It should be mentioned here that we concluded to these equations considering no losses to the environment. Neither conduction/convection nor radiation losses were considered in this study. In practice, as it was pointed out earlier, the samples were placed in a vacuum chamber, to minimize losses to air through conduction and convection. Radiation losses are minimal due to the rapid decay of temperature oscillations. This is a known advantage of the method. Thus, both assumptions used are met with the experimental conditions used.

3.6.1.3 Effect of finite thickness of the substrate

Another divergence of this last model from the reality is that in 3ω measurements the sample is not semi-infinite, but it has finite thickness. So, there is a need to ensure that the thermal penetration depth (λ) of the induced thermal wave does not exceed the thickness of the sample; otherwise we will measure the thermal properties of what there is underneath the sample under test. The thermal penetration depth is given by the following equation:

$$\lambda = \sqrt{\frac{\alpha}{2\omega}} \quad (3.53)$$

Considering that the modified Bessel function of second kind decays rapidly with increasing r (Figure 3.23), and that the temperature oscillations follow this trend, we must ensure that the thermal penetration depth of the induced thermal wave, not only does not exceed the thickness of the sample, but it is much less than this.

It is generally accepted that the specimen thickness must exceed 5 times the λ , in order to be able to apply Equation (3.50) with minimum errors. (i.e. $t > 5\lambda$).

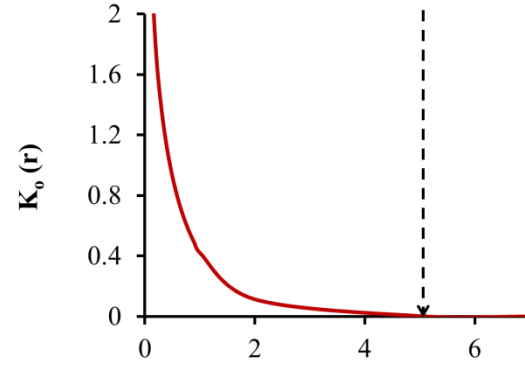


Figure 3.23: Zero order Bessel function of the second kind for a unit length constant ($q=1$). The arrow indicates five length constants.

Considering good thermal contact between the heater and the surface of the sample and small heater thickness, it can be assumed that both the heater and the surface underneath have the same temperature. Thus, in Equation (3.50) by setting $y=0$ and $r=x$, it becomes:

$$\Delta T_{AC}(x) = \frac{p_{rms}}{k\pi} \cdot K_0(qx) \quad (3.54)$$

In Figure 3.24, the temporal evolution of the temperature oscillations of the surface under the heater, based on Equation (3.54), are shown.

$$\Delta T_{AC}(qx, \omega t) = \Re \left(\frac{p_{rms}}{k\pi} \cdot K_0(qx) e^{i2\omega t} \right) \quad (3.55)$$

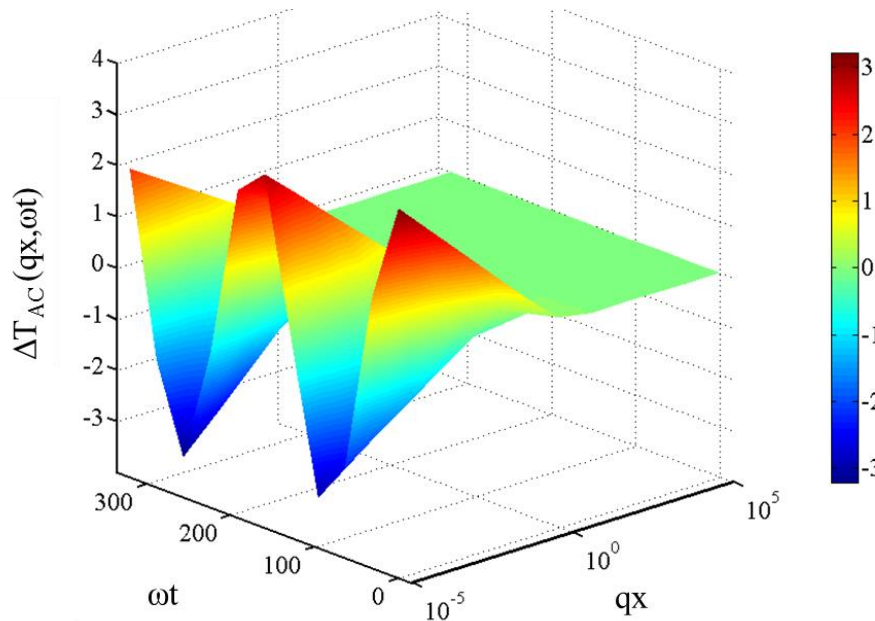


Figure 3.24: 3D scattering plot showing the temporal evolution of temperature oscillations on a PSi surface as a function of the distance away from the heater at room temperature. ($k=0.23\text{W/m.k}$ and $p_{rms}=0.2\text{W/m}$ were assumed).

3.6.1.4 Finite width of the heater

Equation (3.54) was derived for 1D line heater. In order to take into account the finite width of the heater, a superposition of an infinite number of 1D line sources should be assumed [18]. To calculate this convolution integral, it is convenient to use the Fourier (wavenumber) transformation of Equation (3.54) with respect to x coordinate, which gives [142]:

$$\Delta T_{AC}(\eta) = \int_0^{\infty} \Delta T(x) \cdot \cos(\eta x) dx = \frac{p_{rms}}{2k} \left(\frac{1}{\sqrt{\eta^2 + q^2}} \right) \quad (3.56)$$

where η is the wavenumber.

The heat is assumed to enter the sample uniformly across a finite line with width $2b$. This can be expressed as a square wave with values 1 for $x < b$ and 0 elsewhere with the following Fourier transformation in the wavenumber space:

$$\int_0^b \text{rect}(x) \cos(\eta x) dx = \frac{\sin(\eta b)}{\eta b} \quad (3.57)$$

By multiplying Equation (3.56) with Equation (3.57), we get the Fourier transformation of temperature oscillations, including the finite width of the heater:

$$\Delta T_{AC}(\eta) = \frac{p_{rms}}{2k} \cdot \left(\frac{1}{\sqrt{\eta^2 + q^2}} \right) \cdot \frac{\sin(\eta b)}{\eta b} \quad (3.58)$$

Using the inverse Fourier transformation, the following equation is obtained for the temperature oscillations in the real space:

$$\begin{aligned} \Delta T_{AC}(x) &= \frac{2}{\pi} \cdot \int_0^{\infty} \Delta T_{AC}(\eta) \cdot \cos(\eta x) d\eta \\ &= \frac{p_{rms}}{\pi k} \int_0^{\infty} \left(\frac{1}{\sqrt{\eta^2 + q^2}} \right) \cdot \frac{\sin(\eta b)}{\eta b} \cdot \cos(\eta x) d\eta \end{aligned} \quad (3.59)$$

Since the heater measures the average temperature over its width, the magnitude of the temperature oscillations is the average temperature of the heater. Thus:

$$\Delta T_{AC} = \frac{1}{2b} \int_{-b}^b \Delta T_{AC}(x) dx = \frac{p_{rms}}{\pi k} \int_0^{\infty} \left(\frac{1}{\sqrt{\eta^2 + q^2}} \right) \cdot \frac{\sin^2(\eta b)}{(\eta b)^2} d\eta \quad (3.60)$$

Finally the measured temperature oscillation for a finite width heater on a surface is given by:

$$\Delta T_{AC} = \frac{p_{rms}}{\pi k} \int_0^{\infty} \frac{\sin^2(\eta b)}{(\eta b)^2 \sqrt{\eta^2 + q^2(\omega)}} d\eta = \Delta T_{AC,x} + i \cdot \Delta T_{AC,y} \quad (3.61)$$

3.6.1.5 Approximate solution to the exact equation

Equation (3.61) has no close form solution and thus only asymptotic solutions can be obtained with small and large thermal penetration depths assumed. We calculated the integral in this equation using Matlab® and the recursive adaptive Simson quadrature from 10^{-13} to 10^{18} .

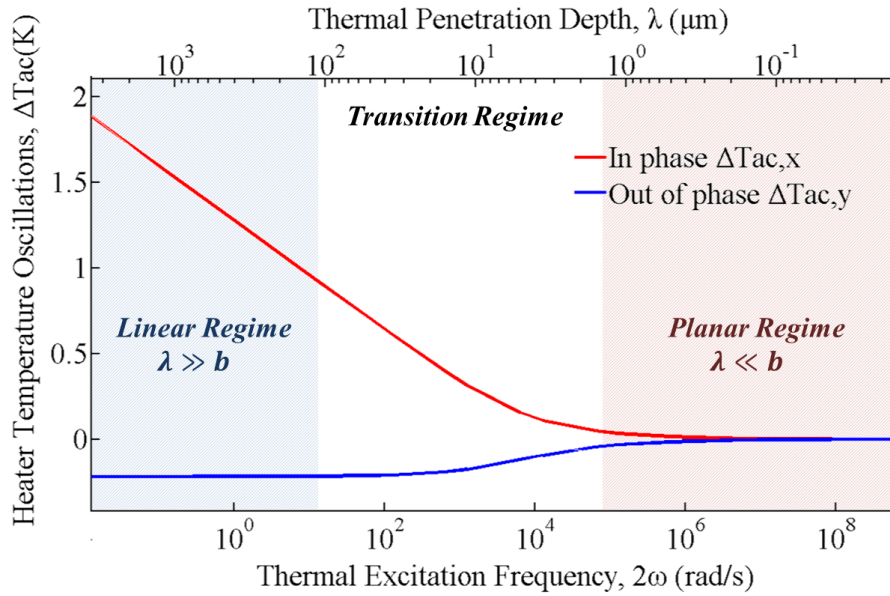


Figure 3.25: Temperature oscillations of a heater lying on an isotropic PSi surface (red line for in-phase component and blue line for the out-of-phase one) as a function of thermal excitation frequency and thermal penetration depth.

Figure 3.25 shows the real (in-phase) and imaginary (out-of-phase) part of the temperature oscillations as a function of thermal penetration depth (λ) and thermal excitation frequency (2ω). The graph was obtained using the thermal parameters of isotropic PSi, as they were measured with the dc method at room temperature, and the half width of the Pt heater used in the experiments (i.e. $k=0.23\text{W/m.K}$, $p_{\text{rms}}=0.2\text{W/m}$, $\alpha=0.16\text{mm}^2/\text{s}$ and $b=10\mu\text{m}$).

There are three discrete regions in this graph. For $\lambda \gg b$ (blue shaded), there is a linear decay of the in phase temperature with $\log(2\omega)$, called “**Linear Regime**”, where the out-of-phase component of temperature oscillations has a negative constant. For $\lambda \ll b$ (red shaded), the in-phase and out-of-phase temperature magnitudes are equal, but with opposite signs. This region is called “**Planar regime**”. And finally, between these regions there is a “**Transition Regime**” (un-shaded area).

By taking the limits of each regime, closed form solutions can be obtained. So, for the **Linear Regime**, where the thermal penetration depth is much larger than the heater half width, by taking $\lambda \gg b$ we have from Equation (3.61):

$$\lim_{b \rightarrow 0} \left(\frac{\sin(\eta b)}{(\eta b)} \right) = 1 \quad (3.62)$$

Since large wavenumber oscillations have almost negligible amplitude and decay quickly, the integral in Equation (3.61) is dominated by values of η such that $(1/\lambda < \eta < 1/b)$. Substituting Equation (3.62) to (3.61) and the upper limit of the integral to $1/b$, the following equation is obtained:

$$\Delta T_{\text{AC}} = \frac{p_{\text{rms}}}{\pi k} \int_0^{1/b} \frac{1}{\sqrt{\eta^2 + q^2}} d\eta \approx -\frac{p_{\text{rms}}}{\pi k} (\ln(qb) - \xi) \quad (3.63)$$

where ξ is a fitting constant with reported values 0.923 and 1.05 [136]. Rewriting Equation (3.63) in terms of ω we get:

$$\xrightarrow{q=\sqrt{\frac{2\omega i}{\alpha}}} \Delta T_{AC}(2\omega) = -\frac{p_{rms}}{\pi k} \left(\ln \left(\sqrt{\frac{2\omega i}{\alpha}} b \right) - \xi \right) \quad (3.64)$$

$$\Delta T_{AC}(2\omega) = -\frac{p_{rms}}{2\pi k} \left(\ln(2\omega) + \ln \left(\frac{b^2}{\alpha} \right) - 2\xi + \frac{i\pi}{2} \right) \quad (3.65)$$

From Equation (3.65) and in consistency with Figure 3.25, it is deduced that the in-phase component of temperature oscillations has a linear dependence on $\ln(2\omega)$, while the out-of-phase one is constant in the linear regime.

On the other hand, for the **Planar Regime**, where $b \gg \lambda$, one can use the mathematical identity of the Dirac delta function [143]:

$$\lim_{b \rightarrow \infty} \frac{1}{\pi b} \left(\frac{\sin(\eta b)}{\eta} \right)^2 = \delta(\eta) \quad (3.66)$$

to obtain from Equation (3.61):

$$\begin{aligned} \Delta T_{AC} &= \frac{p_{rms}}{bk} \int_0^\infty \left(\frac{1}{\sqrt{\eta^2 + q^2}} \right) \cdot \frac{\sin^2(\eta) \delta(\eta)}{\eta^2} d\eta \approx \frac{p_{rms}}{2bkq} \xrightarrow{q=\sqrt{\frac{2\omega i}{\alpha}}} \Delta T_{AC}(2\omega) \\ &= \frac{p_{rms}}{2bk\sqrt{\frac{2\omega}{\alpha}}} e^{-i\frac{\pi}{4}} \end{aligned} \quad (3.67)$$

From this last equation, it is deduced that at the planar regime the in-phase and out-of-phase temperature oscillations have the same magnitude and opposite signs, as it was also noticed in the Figure 3.25.

The limits of each regime are somehow arbitrary and practically they depend on the acceptable error in the results. It is generally accepted that the boundary of the linear regime is set such that $\lambda > 5b$, which results in a maximum rms error of 0.25%. Similarly, the limit for the planar regime is set to $\lambda > b/5$ for an error of 0.15%. Given that the samples to be measured have finite thickness t (with the limitation of $t > 5\lambda$, as it was assumed before) the boundaries in the linear regime finally become:

$$\frac{t}{5} > \lambda > 5b \Rightarrow t > 25b \quad (3.68)$$

3.6.2 Experimental setup

In this study, both four and two point probe 3ω measurements were used. In the latter case a Wheatstone bridge was used to cancel the first harmonic of the voltage and thus do not affect the small 3ω signals. The obtained 3ω voltage signals, measured using the bridge, were proved to be more stable with time. A schematic representation of the measurement setup for 3ω measurements is shown in Figure 3.26, while the test structures were the same used in the dc method (Figure 3.3).

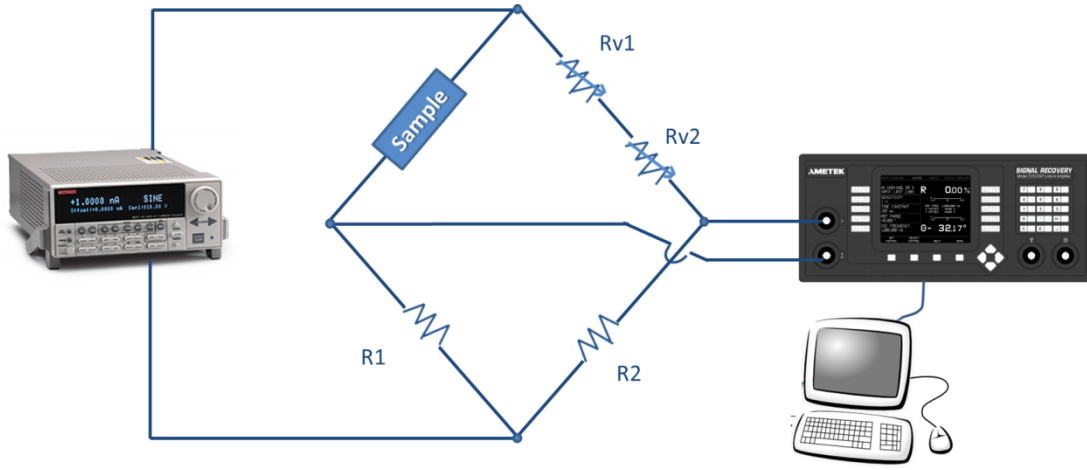


Figure 3.26: Setup that was used for two point-probe 3ω measurements showing the Wheatstone bridge for 1ω voltage cancellation.

By selecting the resistance of R_1 to be 100 times smaller than R_2 , it is possible to direct 99% of the current through the arm of the bridge, which contains the sample. This helps to get a relatively high 3ω voltage measurement with simultaneously minimizing any spurious third harmonic voltage from the variable resistors.

The ac current was applied with Keithley 6221 AC – DC current source, the 1ω voltage was measured using a Keithley 2000 multimeter, while the 3ω in-phase and out-of-phase voltage components were measured with a Signal Recovery 7270 DSP lock-in amplifier. For the placement of the samples and the TCR measurements of the Pt heaters/thermometers see section 3.5.2.

3.6.3 Data analysis

Having analyzed the basic principles of the 3ω method and the mathematical models which incorporate its implementation, possible ways to extract thermal conductivity of the samples under test from the raw experimental data are discussed in the following paragraphs. At first, the Cahill's slope method is presented, and then two different approaches are proposed.

3.6.3.1 The slope method

Cahill used the Equation (3.22), which is reproduced here:

$$V_{3\omega} = \frac{1}{2} V_{ho} \beta_h \Delta T_{AC} \quad (3.22)$$

It should be mentioned here, that when a Wheatstone bridge is used, as shown in Figure 3.26, the measured voltage $V_{w,3\omega}$ is related to the $V_{h,3\omega}$ through the following relation:

$$V_{w,3\omega} = \frac{R_1}{R_{ho} + R_1} \cdot V_{3\omega} \quad (3.69)$$

The temperature oscillations on the heater can be calculated using the measured 3ω voltage and plot the in-phase and out-of-phase components of ΔT_{AC} as a function of the logarithm of 2ω . From the slope of the curve (c) obtained in the linear region of in-phase component and the Equation (3.65):

$$\Delta T_{AC}(2\omega) = -\frac{p_{rms}}{2\pi k} (\ln(2\omega) + \ln\left(\frac{b^2}{\alpha}\right) - 2\xi + \frac{i\pi}{2}) \quad (3.65)$$

the thermal conductivity of the sample is calculated as follows:

$$k = -\frac{V_{ho}^3 \beta_h}{4\pi l R_{ho}} \cdot \frac{1}{c} \quad (3.70)$$

In the same way, thermal conductivity can also be calculated from the constant value of the out-of-phase component, however Cahill proved experimentally that the slope of the in-phase 3ω voltage is more accurate [18].

The simplified analytical models that are used to determine thermal conductivity with this method, known as *slope method*, are subjected to a variety of constraints that may not be always possible to be satisfied. For this reason, many authors the last years re-examined theoretically and extended 3ω method in an effort to eliminate errors that are introduced from these approximations [144–146], while Borca-Tasciuc et al. [147] and Ding et al. [148] compared their theoretical studies to experimental data.

In this thesis, a systematic investigation of porous Si thermal conductivity as a function of temperature, in the temperature range 77-300K was made. We introduced an improved way to extract thermal conductivity, using both the in-phase and out-of-phase temperature oscillation components and the solution of Cahill's integral form. This approach of extracting thermal conductivity is proposed to be a useful tool in measuring thermal conductivity of samples with unknown properties in a broader frequency range. Using this assumption, the very low frequency regime, which has deviation from Cahill's formula when a thicker resistor is used [145] or when the layer studied is not sufficiently thick, can be neglected, without narrowing the frequency range of the measurements. This can be achieved by incorporating data which are not necessarily in the linear or constant regime of in-phase and out-of-phase temperature oscillations, respectively.

The results are also compared to values of thermal conductivity that were extracted using FEM simulations and discussed. This last method to extract thermal conductivity is proved to be more accurate, however it is time consuming and it is not preferred when a lot of measurements are needed. The details of the proposed approaches are found below, while the experimental results follow.

3.6.3.2 Extracting thermal conductivity using Cahill's integral form – Approach 1

In order to include more frequency data in the determination of thermal conductivity and be confident that we do not overcome the limitation of the linear region of the function $\Delta T_{AC}(\ln\omega)$, as well as to consider both the in-phase and out-of-phase components of temperature oscillations simultaneously, we also used a different approximation to extract thermal conductivity. We found thermal conductivity by best fitting the nonlinear function $\Delta T_{AC}(\omega)$ to the measured values ΔT_{AC} at different frequencies in the least-squares sense using Matlab®. Practically, thermal conductivity was the only adjustable parameter that should be found to best fit the asymptotic solutions of Equation (3.61) to the experimental data of in-phase and out-of-phase temperature oscillations on the heater.

3.6.3.3 3ω method with consequent FEM analysis – Approach 2

In the second approach, we made FEM simulations to calculate thermal conductivity using the experimental parameters, as in the case of the dc method described previously. The only difference here is that the transient 3D heat conduction equation was solved, while the dissipation power in the heater was calculated at each temperature from the equation: $\dot{Q}(t) = \frac{1}{2} I_{ho}^2 R_{ho} (1 + \cos(2\omega t))$. The thermal conductivity was calculated through iteration until the amplitude of simulated temperature oscillations of the heater met the measured values. The simulations were run for two frequencies (70 and 225Hz) at each temperature and the results that are presented in this work are their average value. More specifically, the simulated 3D structure was exactly the same as the experimental test structure, as in the dc method (see in Figure 3.27 a meshed example in a 2-point probe configuration and thus 3mm length of the heater, 100 μ m PSi layer and 280 μ m c-Si).

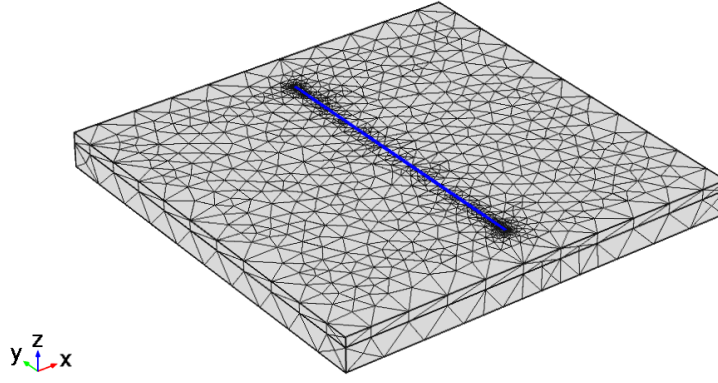


Figure 3.27: 3D meshed model used to calculate the temperature distribution in the structure using the 3ω method.

From the experimentally applied ac current on the heater, the induced thermal power $Q(t)$ was calculated (see an example in Figure 3.28) and set as a boundary condition on the Pt heater (boundary condition of the second kind, see section 3.5.1.1).

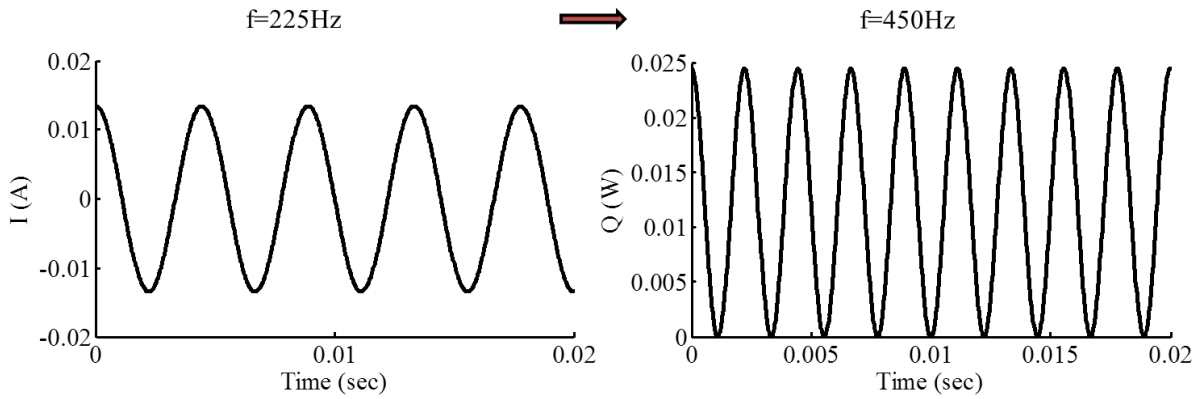


Figure 3.28: Example of an applied ac current on the Pt heater ($R_{ho}=135.6 \Omega$) with $I_{rms}=9.5mA$ and $f=225Hz$ and the induced heating power $Q(t)$ as a function of time. $Q(t)$ was set as boundary condition in the FEM 3D transient heat conduction problem, which was solved using Comsol Multiphysics® at a reference temperature of 273K.

Constant temperature was set at the bottom of the c-Si substrate and insulation/symmetry in every other boundary. The 3D transient heat conduction problem was solved and the data of temperature oscillations with time were extracted. In practice, the temperature oscillations were calculated by taking the average value of temperature of the Pt heater in its volume in each time step. An example of $T_{ac}(t)$ curve obtained by this way is shown in Figure 3.29.

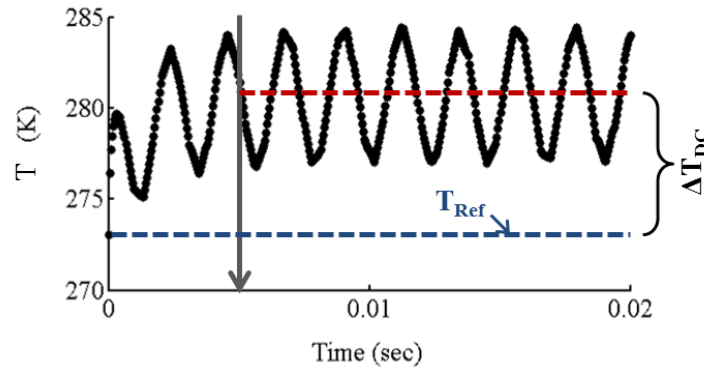


Figure 3.29: Average temperature on Pt heater as a function of time as it was calculated with FEM simulations. The arrow indicates the time after which a permanent condition is reached.

As it has already been referred to and it is also shown in Figure 3.29, the total temperature increment on the heater due to the applied ac current is composed of two parts, such that:

$$\Delta T(t) = \Delta T_{DC} + |\Delta T_{AC}| \cos(2\omega t + \varphi) \quad (3.71)$$

To determine the amplitude and phase of the ac component of temperature we fitted the extracted data of the simulations for the permanent region shown in Figure 3.29 to the equation below in the least square sense using Matlab®:

$$T(t) = T_{ref} + \Delta T_{DC} + A_1 \cos(2\omega t + A_2) \quad (3.72)$$

Figure 3.30 shows the data and the fitted curve for the values of figure 3.29 ($A_1=3.5$ and $A_2=-0.4$ were found to best fit the data).

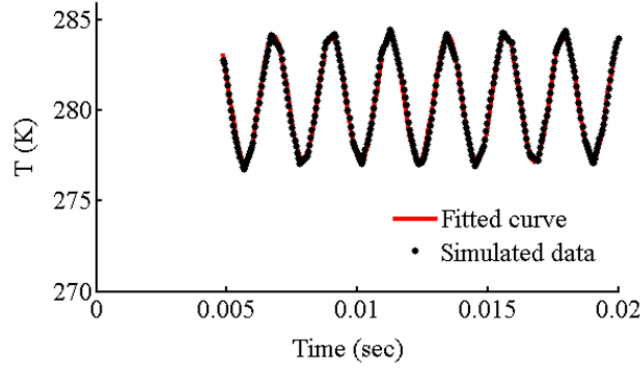


Figure 3.30: Simulated temperature data as a function of time with the corresponding curve that best fits the data according to Equation (3.72).

As in the case of the dc method, data from the literature were used for Pt and c-Si, while the only unknown was the thermal conductivity of the porous Si substrate, which was finally calculated performing successive iterations until the amplitude of temperature oscillations (A_1 in Equation (3.72)) reached the measured such value of the Pt heater.

3.6.4 Experimental results

3.6.4.1 Bulk c-Si covered with a thin TEOS oxide

The 3ω slope method was first applied to the bulk c-Si sample (reference sample) in order to validate the technique. In this case, a thin TEOS oxide layer was deposited on Si prior to Pt deposition, as described in section 3.4.3. Due to the small thickness of the TEOS dielectric film, the through-thickness heat transport in this layer simply adds a frequency independent ΔT_f to the thermal response of the Si substrate ΔT_{Si} . Thus, the slope ΔT_{AC} or equivalent $V_{3\omega}$ versus $\ln(2\omega)$ yields the thermal conductivity of the Si substrate [136]. Using this assumption, we measured the thermal conductivity of bulk c-Si ($\rho=1.5\text{m}\Omega\cdot\text{cm}$) at 135K, 180K and 300K in a two point probe configuration with Wheatstone bridge (see Figure 3.26). Figure 3.31 shows examples of third harmonic of voltage as a function of excitation frequency for such samples at temperatures 135K and 180K, respectively.

As it can be seen in Figure 3.31, a linear behavior is obtained for a limited range of frequencies. This is due to the finite thickness of the substrate that leads the data to bend upward at low frequencies. Practically, at these low frequencies the thermal penetration depth λ exceeds the thickness of the substrate. The limit frequency from which the λ “sees” what is underneath the sample depends on its thickness, as well as on its thermal properties. Based on such measurements, and using the analytical models described previously, the thermal conductivity of c-Si was measured and the results are shown in Figure 3.32, in comparison to results from the literature. The results obtained with the dc method are also depicted.

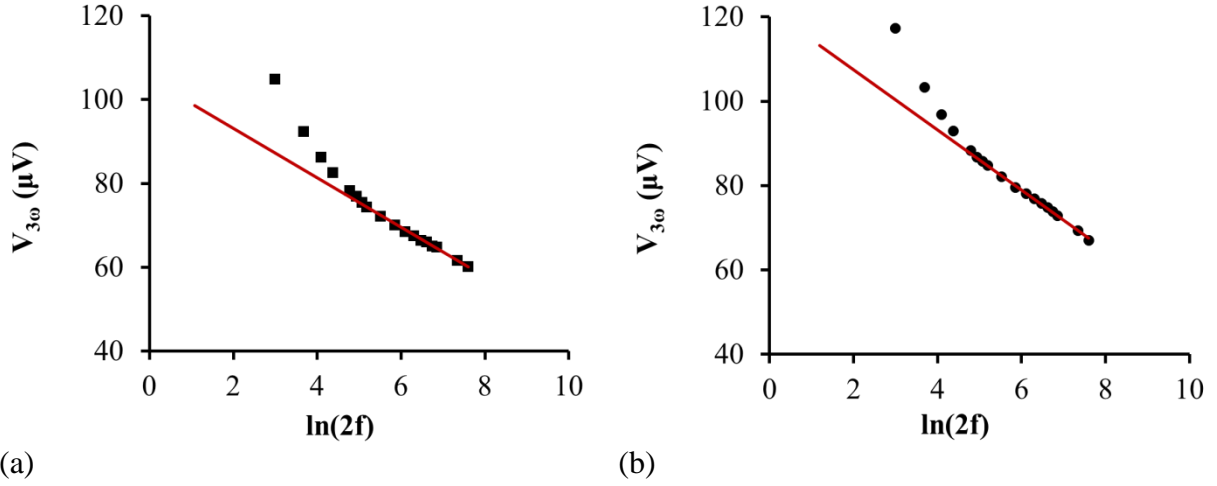


Figure 3.31: Amplitude of third harmonic of voltage as a function of excitation frequency on a heater of the reference sample at temperatures of 135K (a) and 180K (b). Due to the finite thickness of the Si substrate, the data bend upward at low frequencies [136], thus the data used to calculate the slope of the curve were limited to higher frequencies.

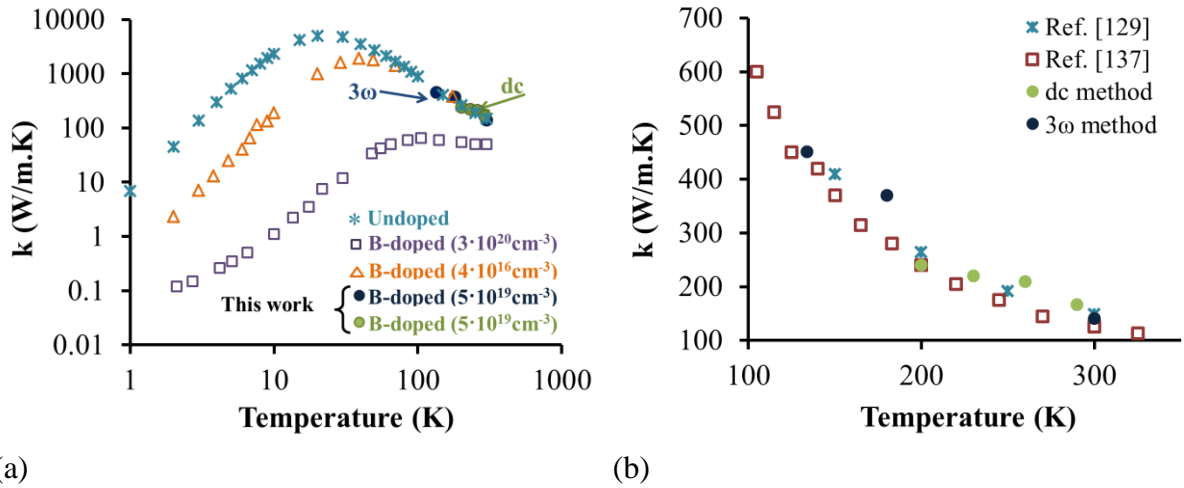


Figure 3.32: Thermal conductivity of bulk c-Si as a function of temperature for the temperature range 1-1000K (a) and the temperature range 100-320K (b). With full circles the data obtained with the 3 ω method (blue) and dc method (green) in this work are depicted, while results taken from the literature are depicted with stars for undoped c-Si [128], with open triangles for boron doped c-Si with doping concentration $3 \cdot 10^{20}$ atoms/cm³ [149] and with open rectangles for boron doped c-Si with doping concentration $4 \cdot 10^{16}$ atoms/cm³ [150]. In (b) data from ref. [136] were also added corresponding to boron doped Si with doping concentration $4 \cdot 10^{14}$ atoms/cm³ and depicted with open red rectangles.

From Figure 3.32 it is deduced that our measurements are in a quite good agreement with those found in the literature. As it can be seen in Figure 3.32(a), below ~ 100 K the doping of the c-Si affects significantly the thermal conductivity. Particularly, the electrically active impurity atoms strongly reduce thermal conductivity at low temperatures due to phonon – free carrier scattering [151], while at higher temperatures impurities do not play such a critical role due to the increased phonon-phonon scattering. We restricted our measurements to relatively high temperatures, because our scope was at this point only to assess the validity of our measurements.

In this respect, we also extracted thermal conductivity of TEOS silicon oxide, which was used as an insulating layer between the heater and the c-Si substrate. It was pointed out previously that this thin dielectric film adds a frequency independent ΔT_f to the thermal response of the Si substrate ΔT_{Si} . Thus, having measured the thermal conductivity of the c-Si

substrate, combined with specific heat values taken from the literature and the width of the Pt heater 2b, the expected thermal response ΔT_{Si} can be calculated using Equation (3.22). Then, ΔT_f is simply given by $\Delta T_f = \Delta T - \Delta T_{Si}$. Figure 3.33 shows an example of calculated ΔT_{Si} ($\ln 2\omega$) curve with the corresponding measurements at 135K. In the graph the temperature drop due to TEOS oxide layer ΔT_f is indicated.

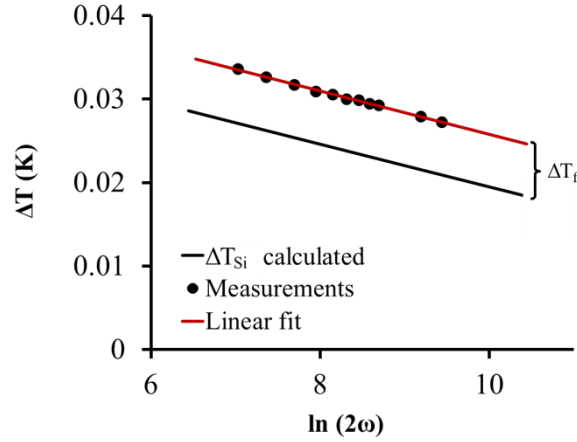


Figure 3.33: Example of calculated ΔT_{Si} and measured amplitude of the temperature oscillations ΔT as a function of the logarithm of frequency at 135K. The indicated ΔT_f is the temperature drop through the thickness of the TEOS layer.

Since the thickness of the TEOS layer was far smaller than the width of the heater, heat flow in its volume can be assumed as one-dimensional and the apparent thermal conductivity of the layer can be calculated from the following equation:

$$k_f = \frac{P_{rms} \cdot t}{\Delta T_f \cdot 2b} \quad (3.73)$$

Using Equation (3.73), we obtained values of 1.1W/m.K and 1.8W/m.K at temperatures 135K and 180K respectively. The obtained values are in quite good agreement with others given in the literature for silicon dioxide at these temperatures; however a direct comparison was not possible, since we did not find data for Si oxide fabricated with the same method.

3.6.4.2 Anisotropic porous Si - 70% porosity

Having assessed the validity of the 3ω method on c-Si and TEOS oxide, we proceeded to measurements of thermal conductivity of anisotropic porous Si with this method. In this section, the results of improved approaches to extract thermal conductivity will be presented and compared to both the 3ω slope method and the dc method analyzed in section 3.5.4. In general, in order for the 3ω slope method to be applicable to a sufficient range of frequencies, the thickness of the film must be at least 5 times the width of the metal strip to avoid reflections [18, 152]. For this reason, anisotropic porous Si samples measured with the 3ω method had a thickness of 100 μ m (considering that the width of the heater was 20 μ m).

In order for the 3ω method to be applicable, the observed 3ω voltage must be proportional to I^3 [153]. Figure 3.34(a) shows an example of measured 1ω and 3ω voltage as a function of the applied amplitude of current for the case of a p^+ -type anisotropic porous Si layer, while 3.34(b) depicts the linear dependence of $V_{3\omega}$ as a function of I^3 . It should be mentioned, however, that the lower possible currents were used, so as to achieve a measurable stable $V_{3\omega}$ signal and avoid increasing temperature in other electronic components of the circuit that could insert parasitic phenomena in the measurement.

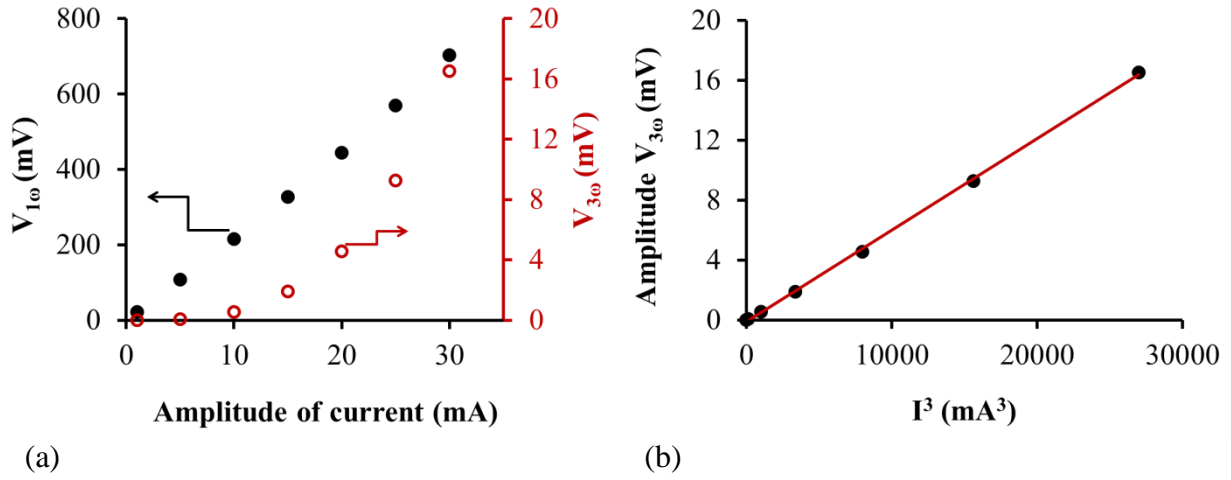


Figure 3.34: Example of $V_{1\omega}$ and corresponding $V_{3\omega}$ measurements as a function of the amplitude of the applied current on the heater for the anisotropic porous Si layer (a) and example of $V_{3\omega}$ dependence on the cube of the amplitude of the applied current, showing a linear dependence (b). The results concern measurements at room temperature.

As it was mentioned before, in porous Si layers both 4-point and 2-point probe arrangements were tested. Figure 3.35 shows the experimental results of the 3ω slope method, compared to those obtained previously with the dc method. Thus, the thermal conductivity in the graph was extracted from the slope of the in-phase temperature oscillations of the heater versus the logarithm of frequency.

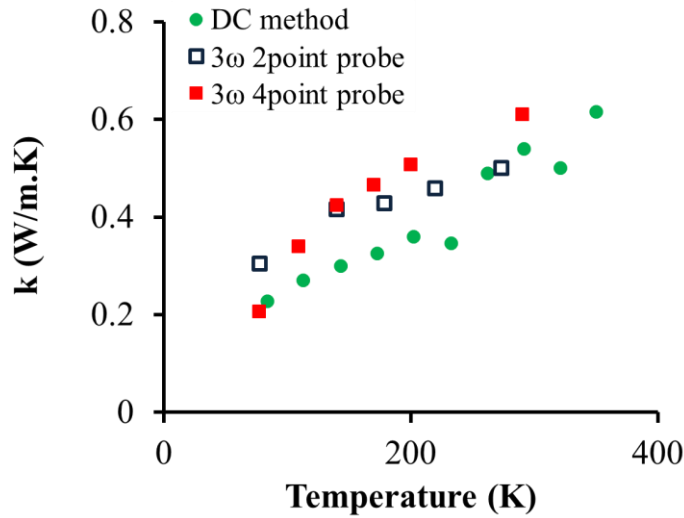


Figure 3.35: Comparison of experimental results of anisotropic porous Si thermal conductivity in the temperature range 77-300K, measured with the 3ω slope method with both two and four point probe configurations, compared to the dc method. In the two point probe measurement a Wheatstone bridge was used as a cancellation technique.

From Figure 3.35 it is deduced that there is a quite good agreement between the two measurement techniques and between the two configurations of the 3ω method. It can be noted that the two point probe configuration gives slightly lower values of thermal conductivity compared to the 4 point probe in the majority of the measurements presented. A possible reason is the contact resistance which is added in the total measured resistance of the heater in the 2 point probe case, while with the 4 point probe measurement this resistance is eliminated. As the heater is also a thermometer, the additional contact resistances lead to a larger total resistance and thus to a higher amplitude of temperature oscillations on the surface of the sample, which is finally interpreted as a lower value of thermal conductivity. Another reason is the thermal conduction, which takes place from the sample to the metallic probes. This effect is doubled in the 4 point probe measurement and results in measuring lower

temperature on the heater, and thus higher thermal conductivity. On the other hand, in the 2-point probe configuration, a Wheatstone bridge was used to cancel the large 1ω voltage. In this case, the 3ω voltages measured were more stable and accurate. Thus, it is difficult to reach a safe conclusion on which of the two configurations gives the results with the minimum measurement error.

From Figure 3.35 it is deduced that a systematic overestimation of thermal conductivity measured with the 3ω method is observed, compared to that measured using the dc method. This will be explained later, after the presentation of the other two proposed approaches.

An example of measured data and fitting curves obtained using approach 1 at temperature 77K is shown in Figure 3.36. It should be pointed out here that the Matlab® program used to fit the data was set to calculate the thermal penetration depth λ for each obtained value of k and check if it remained below the thickness of porous Si (i.e. $100\mu\text{m}$). If by the fitting the obtained k value exceeded the thickness of the layer, the program was run again excluding the frequency data that reached or overcome the porous Si thickness. For example, in Figure 3.36(b) the first measurement was not taken into account in the fitting procedure, however, all the measured points in such graphs are depicted.

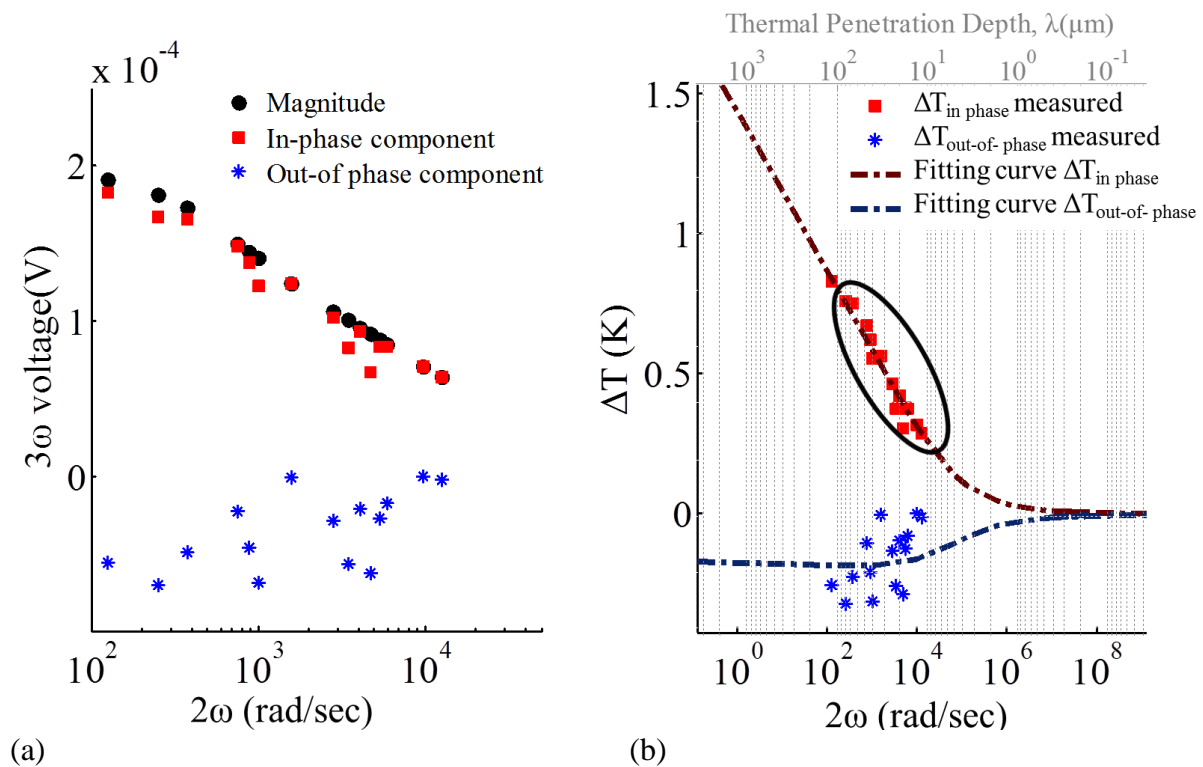


Figure 3.36: a) Magnitude, in-phase and out-of-phase components of 3ω voltage measured on the Pt heater lying on porous Si at 77K when an ac current with rms value of 3mA was applied b) in phase and out-of-phase temperature oscillations with the corresponding curves of the best fit, resulting in a value of thermal conductivity of 0.33W/m.K . Only the data in the circle were used in the fitting. The first point was excluded because it corresponded to thermal penetration depth larger than the thickness of the porous Si layer.

As it can be seen, the out-of-phase component is noisier than the in-phase one, as Cahill firstly noticed. However, with this approach, we used both components in our calculations to extract thermal conductivity of porous Si. A comparison between the thermal conductivity values extracted with this approach and the values obtained from the slope method is depicted in Figure 3.37.

It is clear from the graph that there is a good agreement between the two methods used to calculate the thermal conductivity from the experimental data of third harmonic voltage. However, by calculating k from fitting to both temperature components, the values are higher than by using the slope in the linear region. A possible reason for this is the fact that the limits

of the linear region are not strictly defined. Particularly, the out-of-phase component that we incorporated in the thermal conductivity calculations was not in all cases constant in the whole frequency range for which the in-phase component seemed to be in the linear region. The limits of the linear region of the in-phase component of temperature oscillation with frequency change depending on the thickness and width of the heater, the thickness of the studied film, the thermal contact resistance between the heater and the film under study, its thermal conductivity and specific heat capacity [148] and are not well defined, a fact that may introduce errors in the measurement. Although the values extracted using approach 1 are somehow higher, their trend as a function of temperature is smoother, following exactly the same behavior with the values acquired with the dc method.

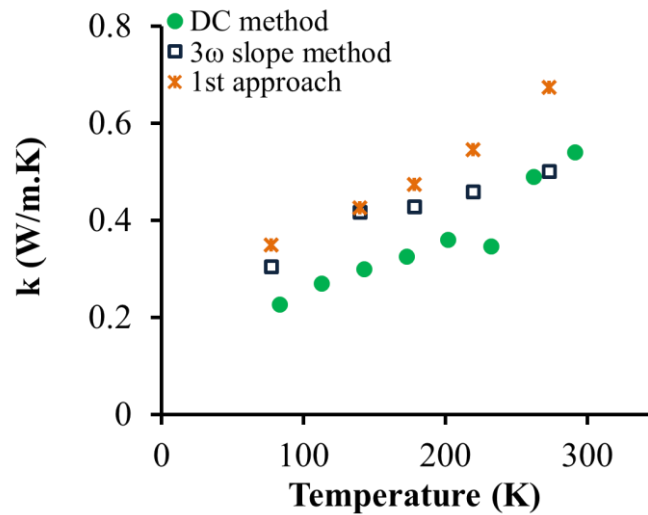


Figure 3.37: Comparison of thermal conductivity values extracted from the slope of in-phase temperature oscillations as a function of $\ln(2\omega)$ (blue squares) and the values calculated from fitting the experimental data of both the in-phase and the out-of-phase temperature oscillations to Cahill's integral form (stars). The results acquired by the dc method are also depicted for comparison.

Figure 3.38 depicts a comparison of thermal conductivity values obtained with both 3ω approaches and with the dc method. It clearly shows that the results obtained by fitting the data to the exact solution and the values extracted using FEM analysis have the same trend with temperature. However, in the first case (stars), the values again are higher than in the latter one (triangles).

Our experimental results can be explained by the theoretical study of Ding et al. [148], who introduced a new quadrupole model to find the limitations of Cahill's and Duquesne's formula [154]. In their study, they showed that their model is in an excellent agreement with results of FEM analysis, while at frequencies above 10Hz, they are in good agreement with results obtained with Duquesne's formula. This is an analytical expression based on the integral form of Cahill's formula (Equation (3.61)). However, Ding et al. showed that Duquesne's formula underestimates the real part of temperature oscillations and thus this is interpreted as an overestimation of thermal conductivity. This is exactly what we observe in our results. Thermal conductivity values obtained using FEM simulations are lower than those extracted using Cahill's integral formula, while the trend with temperature is the same and only a shift in values is observed. This fact indicates that the extraction of thermal conductivity using FEM simulation is the most accurate method of all studied in this work. However, it needs long computational times and it is not convenient when a lot of measurements must be taken.

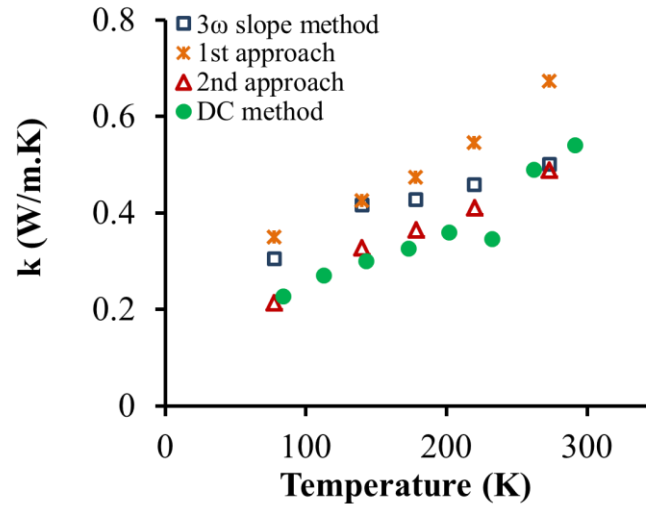


Figure 3.38: Comparison of thermal conductivity values extracted using fitting of the data to the Cahill's integral formula - approach 1 (stars) and extracting using the experimental data and consequent 3D heat conduction model with FEM analysis- approach 2 (triangles), slope 3ω method (rectangles) and results from dc method (circles).

In Figure 3.38 there is also a comparison with the measured values of thermal conductivity with the dc method. As it can be seen there is a very good agreement between the dc and 3ω method with consequent FEM analysis in both cases, while there is a larger deviation compared to values calculated by fitting data to the Cahill's integral formula. This is a verification of the better accuracy of approach 2 in calculating thermal conductivity.

To summarize, the experimental results of the third harmonic voltage at each temperature with modulated frequency were used to extract thermal conductivity with 3 different ways: using the linear fit of in-phase temperature oscillations with frequency (3ω slope method), by fitting the data to the Cahill's integral formula (approach 1) and solving transient heat conduction problem with FEM simulations using COMSOL Multiphysics® software (approach 2). The latter method was proved to be more accurate and in a very good agreement with the dc method discussed in section 3.5.4. On the other hand, Cahill's equations, both the analytical approximate one and the integral one, proved to overestimate the thermal conductivity of porous Si. However, the values obtained by fitting the experimental data to the Cahill's integral form have the same trend with temperature as the temperature dependence calculated using FEM analysis, which is a time consuming method.

3.6.4.3 Isotropic porous Si - 63% porosity

In this section, the same methodology as above was applied for measurements on the isotropic porous Si layer with 63% porosity. Unfortunately, as it was mentioned earlier, we were unable to fabricate very thick such layers, thus the measurements were made on $40\mu\text{m}$ porous Si layers, recognizing the fact that additional errors may be introduced in the 3ω slope method.

Figure 3.39 depicts an indicative example of measured data and fitting curves obtained using approach 1 at a temperature of 138K. Again, only the data that correspond to penetration depths smaller than the thickness of the porous Si layer were considered in the fitting.

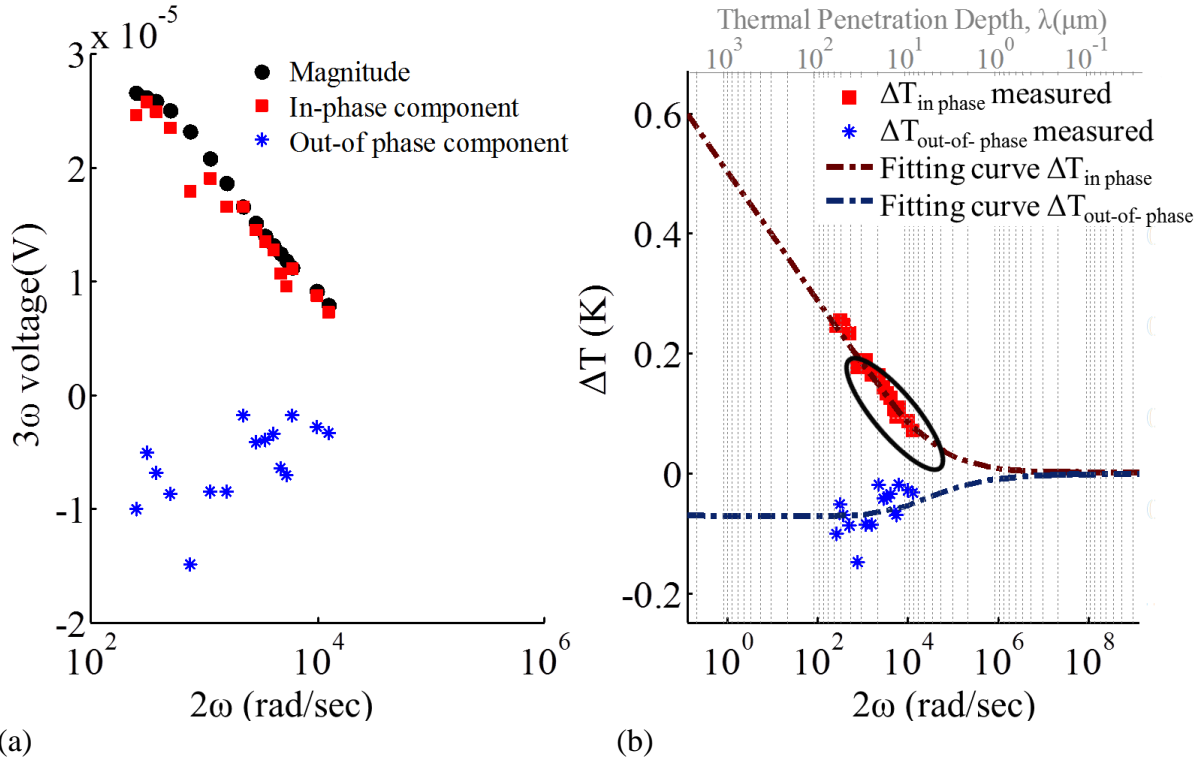


Figure 3.39: a) Magnitude, in-phase and out-of-phase components of 3ω voltage measured on the Pt heater lying on isotropic porous Si sample at 138K when an ac current with rms value of 1.5mA was applied b) in phase and out-of-phase temperature oscillations with the corresponding curves of the best fit, giving a value of thermal conductivity of 0.28W/m.K. Only the data in the circle were used in the fitting because the other data correspond to thermal penetration depths larger than the thickness of the porous Si layer (40μm).

As it can be seen from the graph, data out of the frequency limits which correspond to the linear regime are suppressed. This is a characteristic example where approach 1 should be considered so as data in the transition regime could also be included in the thermal conductivity calculation.

Figure 3.40 summarizes the results of thermal conductivity of isotropic PSi sample with all the 3ω approaches considered in this thesis and the results obtained using the dc method. From Figure 3.40, the same conclusions as for the anisotropic PSi layer can be deduced.

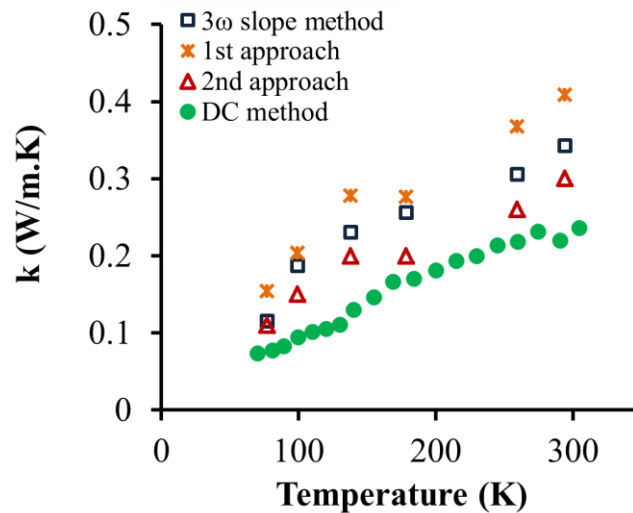


Figure 3.40: Comparison of thermal conductivity values extracted using fitting of data to the Cahill's integral formula - approach 1 (stars); extracted using experimental data and consequent 3D heat conduction model with FEM analysis- approach 2 (triangles), slope 3ω method (rectangles) and results from dc method (circles).

3.7 Conclusions

In this chapter, the role of nanoscale dimensions in thermal transport was introduced. The fabrication process of the porous Si layers studied in this thesis was presented along with their structural characterization using SEM and TEM measurements.

Thermal conductivity of both isotropic and anisotropic layers was measured. Two measurement methods were used in this respect: the dc method with consequent FEM analysis and the 3ω method. The basic assumptions and considerations regarding each method were presented in detail with their mathematical representations. The validity of the measurement techniques was assessed by measuring thermal conductivity of bulk c-Si substrate which, in a specific range of temperatures, can be assumed to be independent of the doping level. A good agreement was obtained between the two techniques. A comprehensive review of all the steps followed for the implementation of each method was reported, including the experimental setup and the data analysis.

Concerning the 3ω technique, two improved approaches were proposed for extracting thermal conductivity from the raw 3ω voltage measurements as a function of frequency: fitting experimental data to the Cahill's integral formula taking into account both in-phase and out-of-phase components of temperature oscillations and analyzing the data by solving the time-dependent heat transfer equation using the FEM method. The values obtained with the two approaches were compared to each other and to the well-known slope method and discussed. The 3ω method with consequent FEM analysis was proved to be more accurate than the others and in a good agreement with the dc method. On the other hand, Cahill's equations, both the analytical approximate one and the integral one, proved to overestimate the thermal conductivity of porous Si, in consistency with reported studies in this field.

The thermal conductivity of isotropic and anisotropic PSi shows the same variation trend with temperature. Particularly, k decreases monotonically by decreasing temperature, reaching a plateau at very low temperatures, below $\sim 20\text{K}$. The obtained values at high temperatures were explained by considering known analytical models, however these models failed to interpret the results at lower temperatures. For this reason, an analytical discussion based on the fractal nature of PSi will be presented in a following chapter.

The anisotropic PSi layer showed higher thermal conductivity at all temperatures compared to the isotropic one. This was attributed to differences in structure and morphology of the samples and particularly to the strong anisotropy of the porous Si layer prepared on p^+ c-Si wafer.

A comparison of the obtained thermal conductivity of porous Si with that of bulk crystalline Si, α -Si, a-Si:H and some other C-MOS compatible dielectrics demonstrated the effectiveness of porous Si as thermal isolation platform since its thermal conductivity has been measured to be much lower than that of bulk crystalline Si and comparable to/or lower than that of other materials usually used for thermal isolation. Its effectiveness for thermal isolation on the Si wafer will be demonstrated in the following chapter, based on experimental results and FEM simulations.

Chapter 4

Thermal conductivity of PSi in the temperature range 4.2-20K – Interpretation of the plateau

Everyone is familiar with fractal objects. Perhaps we noticed that entire cities (especially the metro of Paris) have tenuous structures that look similar at different size scales. Perhaps, we saw that snow crystals, all have the same pattern, each part of a branch being similar to itself. In fact, to “see” something at all – fractal or non-fractal – requires that the nerve cells in the eye’s retina send a signal, and these retinal nerve cells are themselves fractal objects.

Bunde A, Havlin S (1996) Fractals and Disordered Systems. doi: 10.1007/978-3-642-84868-1

4.1 Introduction

Thermal conductivity of nanoscale systems are often comparable to thermal conductivity of bulk amorphous materials and the characteristic length scales are often compared to the dominant values of the phonon mean free path and the phonon wavelength [155]. As it has already been mentioned, porous Si is one such system. Due to its structure and morphology, it shows much lower thermal conductivity than that of bulk crystalline Si, which is even below the amorphous limit, at porosities exceeding 60%.

Although, there are few studies concerning the temperature dependence of porous Si thermal conductivity [15, 119, 120], until our recent paper [156], no data for temperatures below 20K have been reported. Thus, in this thesis, we extended these measurements down to liquid helium temperature (4.2K) for both isotropic and anisotropic PSi. It was found that at these low temperatures (4.2 – 20K) porous Si thermal conductivity is almost stable with T, showing a plateau-like behavior (see section 3.5.4). This trend is common in glasses and disordered materials (i.e. SiO₂, vitreous silica, epoxy resin etc), but unusual in crystalline systems. Due to the lack of data in this temperature range, we focused on explaining the observed constant value of thermal conductivity for the two types of porous Si layers studied in this thesis.

In the present chapter, the plateau-like behavior of porous Si thermal conductivity in the above temperature range will be discussed by considering the fractal nature of the material and the existence of localized vibrational excitations (fractons) that dominate heat transport at these temperatures. In this respect, a brief introduction in fractal objects and their physical properties will be presented. Then, porous Si will be characterized as a fractal material by calculating its Hausdorff dimension using SEM image analysis with box-counting algorithm. Finally, a detailed discussion about the additional evidences that led us to adopt the “fracton” interpretation of our experimental results will be presented.

4.2 Fractals and their physical properties

Fractal systems, in general, show new physical properties and anomalous behavior. This is particularly interesting in the field of transport processes (e.g. thermal transport). Thus, fractals have been used extensively in modeling of disordered and random media, as well as in determining characteristics from the trails made by diffusing particles. In this chapter, we will introduce the basics of fractals, focusing mainly on the aspects related to the understanding of thermal transport mechanisms in such materials. More details on this subject can be found in books and comprehensive reviews [157–159].

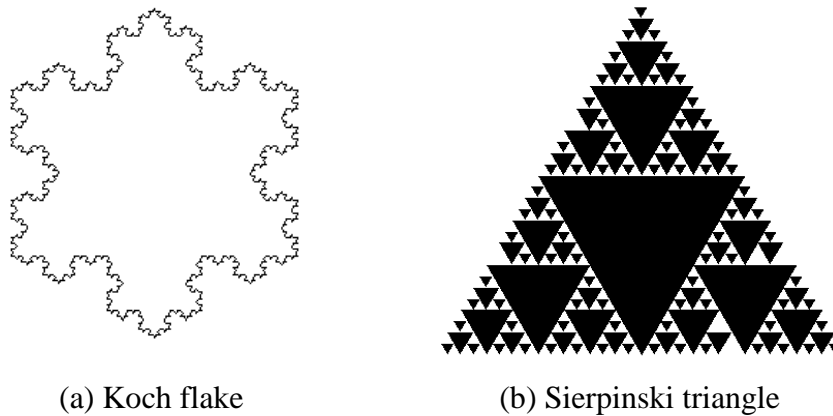
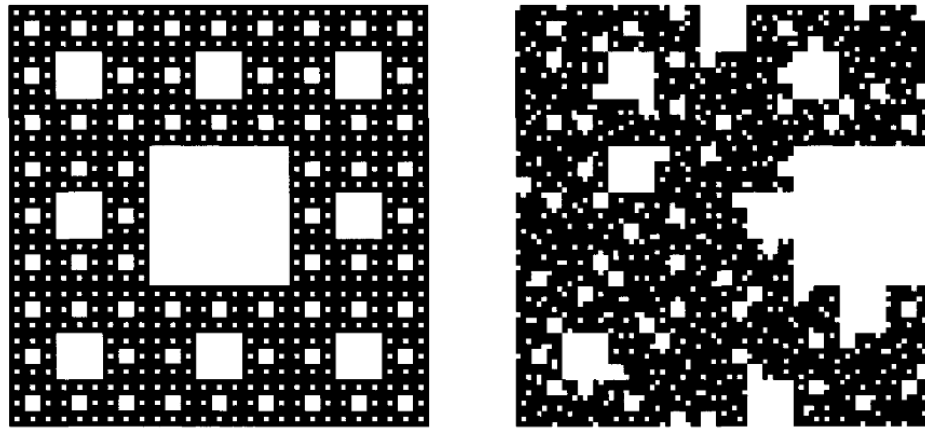


Figure 4.1: Examples of deterministic fractals after 4 iterations

Fractals are commonly divided into two categories: the *deterministic* and the *non-deterministic* ones. *Deterministic fractals* are idealized geometrical structures with the property that parts of them are similar to the whole and they are created by repeated self-

projection of some simple mathematical function on defined subspace. This “self-similarity” is a general property of fractals. Some well-known deterministic fractals, which were produced using the open access image analysis software FracLac [160] after 4 iterations, are shown in Figure 5.1.

The other category of the so called *non-deterministic or random fractals* is a group of objects that are usually ruled by laws too complex to be defined in exact mathematical terms, but they show fractal properties of self-similarity. The most common examples of non-deterministic fractals in every day environment are coast lines, trees, snowflakes etc. Thus, random fractals are useful as models for natural phenomena. Indeed, the fractal shown in Figure 5.2(b) is more like a real sponge than the deterministic Sierpinski carpet drawn in Figure 5.2(a).



(a) Deterministic Sierpinski carpet

(b) Random Sierpinski carpet

Figure 4.2: Comparison of deterministic (a) and random (b) fractal geometries

The fractal geometry of a material has a significant effect on its physical properties. The randomness of self-similarity, the specific morphology and the connectivity of the existing networks in its volume can affect carrier and phonon transport by multiple ways. Particularly, the randomness has been proved to introduce strong scattering in all the transport properties, while in some cases it is responsible for localization [157]. Thus, the specific fractal nature of a material can considerably affect all its physical properties (mechanical, thermal, electrical etc), while it can even be the dominant factor that would determine their behavior, which is expected to follow scaling and power laws. The determination of these scaling relations based on experimental data could be a powerful tool in modeling and predicting the physical properties of materials with similar structure and morphology. In the following, we will examine the effect of fractal nature of porous Si on its thermal properties based on our measurements of thermal conductivity at cryogenic temperatures.

4.2.1 Fractal dimension

The most important property of fractals is their self-similarity, which is described by the *fractal dimension or Hausdorff dimensionality* (D_f). This dimension is often not an integer and describes the character of the fractal. The fractal dimension of a bounded set A in Euclidean n-space is defined as [161]:

$$D_f = \lim_{r \rightarrow 0} \frac{\log(N_r)}{\log(1/r)} \quad (4.1)$$

where N_r is the least number of distinct copies of A in the scale r. The union of N_r distinct copies must cover completely the set A.

Both deterministic and random fractals are characterized by their fractal dimension. Even though a random fractal is not exactly self-similar (see Figure 4.2(b)), it can be considered as self-similar in a statistical sense by taking into account that the distribution of holes looks

similar at all length scales [158]. Additionally, the black areas in the Figure 4.2(b) increase by a factor of 8 when space is expanded by a factor of 3. Thus, both deterministic and random Sierpinski carpets shown in Figure 4.2 have the same fractal dimension $D_f = \ln 8 / \ln 3 = 1.88$.

It should be mentioned at this point, that there is a critical length scale, namely the **correlation length** ξ , up to which a cluster is self-similar and can be regarded as a fractal. For length scales larger than ξ , the cluster is not self-similar any longer and it can be treated as homogenous. The crossover from the fractal behavior at length scales below ξ to a homogeneous behavior at length scales above ξ is best illustrated in Figure 4.3. The Figure shows a lattice composed of Sierpinski gasket unit cells of size ξ [157].

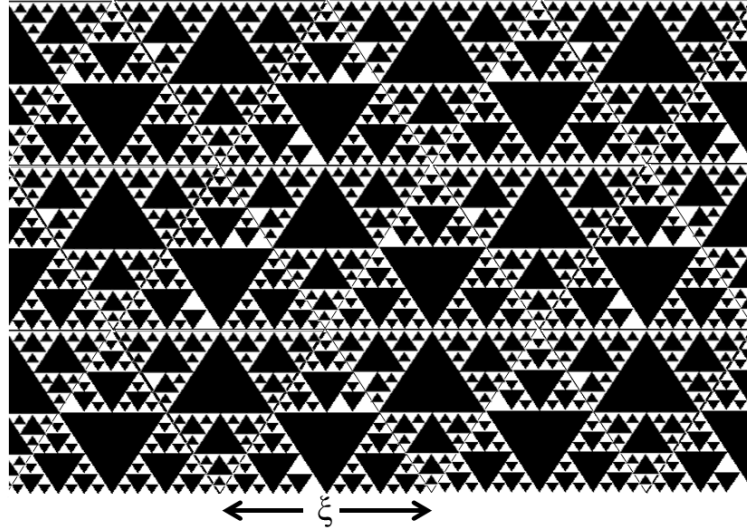


Figure 4.3: Lattice composed of Sierpinski gasket cells of size ξ

Of course, the fractal dimension itself is not sufficient to fully characterize a fractal object. There are also other characteristic dimensions concerning its ramification, translation-invariance, shortest length path connecting two points etc. However, in this study we focused on the Hausdorff dimensionality to characterize our porous Si samples, because this is the most important one. Moreover, as it will be shown below, the absolute value of porous Si fractal dimension strengthens our assumption of fracton interpretation of the observed plateau in thermal conductivity of porous Si between 4.2 - 20K.

4.2.2 Methods of measuring fractal dimension

Hausdorff dimensionality of a material with fractal structure (e.g. glasses, polymers, gels compressed powders, porous media etc) can be measured numerically by their SEM or TEM image analysis or using scattering experiments [157]. In the following, we will focus on the first method, which is the one used in this thesis.

4.2.2.1 Scattering experiment

Coherent scattering from fractal objects can be used to extract structural parameters of a material. In this case, the sample under test is illuminated with a monochromatic beam and the scattered radiation is measured. Then, the scattering intensity is simply proportional to a structural factor, which is the Fourier transformation of the density-density correlation function. More details concerning this experimental technique can be found elsewhere [157, 158].

4.2.2.2 Image analysis

Microscope images can be used for fractal dimension calculations because they depict the exact fractal structure of a material. Among the numerical methods used for this calculation, the **box-counting algorithm** has the advantages of simplicity and automatic computability.

Thus, it is the most frequently used technique and it is briefly discussed in this chapter.

4.2.2.2.1 Box counting algorithm

Box counting is a method of gathering data for analyzing complex patterns by breaking a dataset, object, image, etc. into smaller and smaller pieces, typically “box-shaped” and analyzing the pieces at each smaller scale. The investigation is practically made by changing the size of the element used to inspect the pattern. The technique derived from fractal analysis and is used in this and other related fields, such as lacunarity and multifractal analysis.

In the case of a digitalized image, the box counting method is implemented by dividing the analyzed area into boxes, creating a grid over the image data. For an image with black drawings of some shape on white background, the box counting dimension D_B is simply given by:

$$N_B = s_B^{-D_B} \quad (4.2)$$

where N_B is the number of boxes of a linear size s_B necessary to cover the whole object.

By measuring the distribution of N_B for different box sizes, the D_B can be then obtained by a power law fit of the obtained distribution, using the negative limit of the ratio of the log of the number of boxes at a certain scale over the log of that scale. Thus:

$$D_B = - \lim_{s_B \rightarrow 0} \left(\log N_B / \log s_B \right) \quad (4.3)$$

4.3 Fractons

The vibrational excitations in fractals are called **fractons** [162] or otherwise, a fracton is a collective quantized vibration on a substrate with a fractal structure [163]. Fractons are assumed to be the fractal analog of phonons. In fact, there is critical frequency ω_ξ of the lattice vibrations, below which the vibrational density of states $z(\omega)$ shows normal phonon behavior, while above this value, it shows anomalous fracton behavior. The frequency regime $\omega < \omega_\xi$ corresponds to large time and length scales while the fracton regime $\omega > \omega_\xi$ corresponds to small time and length scales. Thus, in the phonon regime, large regions of the lattice are vibrating and phonons are assumed to represent extended vibration modes. On the other hand, in the fracton regime only local vibrations exist and consequently fractons are considered to represent localized vibrational modes [157]. Because fractons are spatially localized, they cannot contribute to the heat current; only phonons can carry heat. However, the introduction of anharmonicity in the vibrational modes of a lattice allows phonon-fracton interaction through phonon-induced fracton hopping mechanism, which can contribute to heat current [164]. Particularly, the vibrational anharmonicity results in two important phonon-fracton anharmonic interaction processes, which are illustrated in Figure 4.4. The first one is important for the behavior of thermal conductivity of fractal materials at and above the plateau temperature regime while the second one for the fracton-“hopping” contribution to the thermal conductivity.

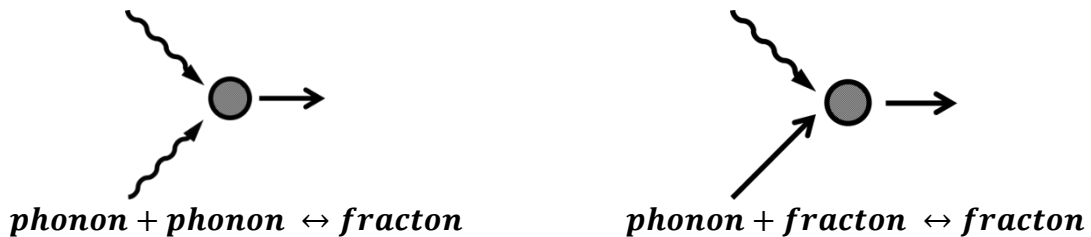


Figure 4.4: Possible anharmonic phonon-fracton interaction processes. The wavy lines denote phonons, while the straight ones fractons.

4.4 Fractal nature of porous Si

In general, fractal geometry is observed in porous materials. Several works were devoted to the investigation of the fractal geometry of porous Si [165, 166] and the use of the fractal nature of this material in order to explain its different physical properties, as for example its ac electrical conductivity [165].

Porous Si constitutes an interesting system for the study of fundamental properties of disordered nanostructures. There are no grain boundaries as in crystalline solids and no sizable bond angle distortions, as these found in disordered non-crystalline systems, e.g. in amorphous materials. Porous silicon is thus considered as a simple mathematical "percolation" model system, which is created by randomly removing material from a homogeneous structure, but still maintaining a network between the remaining atoms. Percolation theory has been recently used in the literature to describe thermal conduction in porous silicon nanostructures [167], amorphous and crystalline Si nanoclusters [168], nanotube composites [169] and other materials.

Based on the fractal nature of porous Si, in the following section its Hausdorff dimensionality is calculated using the box-counting algorithm described before.

4.4.1 Porous Si fractal dimension

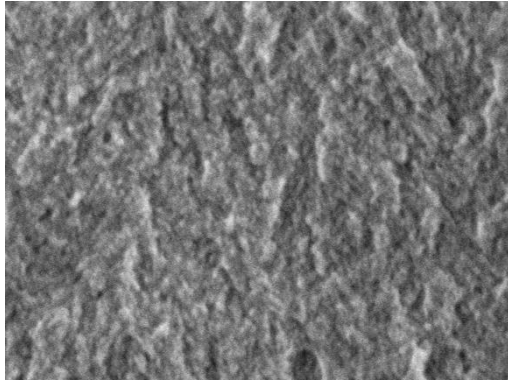
Both isotropic and anisotropic porous Si were investigated as fractal objects. Their Hausdorff dimension was derived using scanning electron microscopy (SEM) images and the box counting algorithm [170]. This method has extensively been used for the determination of the Hausdorff dimensionality of many fractal materials. Yusuke Ono et al. [170] used this method to calculate fractal dimensionality of porous-silica samples, Smyntyna et al. [171] made a fractal analysis to images of nanostructured silicon surfaces while more recently Agboola et al. [172] used the same method and made porous and fractal analysis on the permeability of nanofiltration membranes.

The SEM images, as explained before, reflect the fractal microstructure of the material. We used the maximum possible different grid positions for analyzing each image in order to ensure the accuracy of the calculations, while we calculated the box counting dimension for both cross-sectional and top view SEM images of different magnifications. We also used SEM images from different samples that were prepared with the same electrochemical conditions.

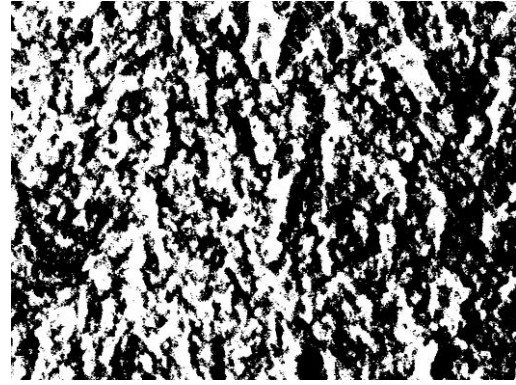
The open access software "Image J" [173] was used for the SEM image processing, while the open access software "FracLac" [160] was used to calculate the Hausdorff dimension of our SEM images using the standard non-overlapping box counting method.

4.4.1.1 Isotropic Porous Si

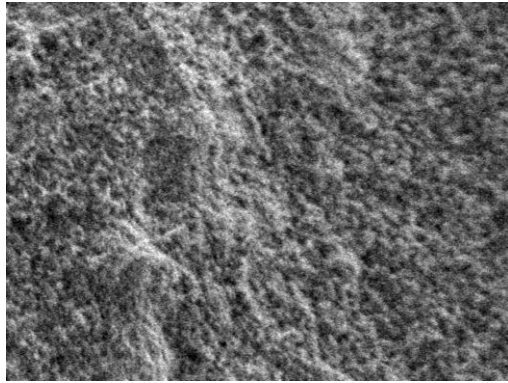
Some examples of the images used and their corresponding binary ones are shown in Figure 4.5 (cross sectional images) and 4.6 (top view images). Under each image the corresponding magnification is indicated.



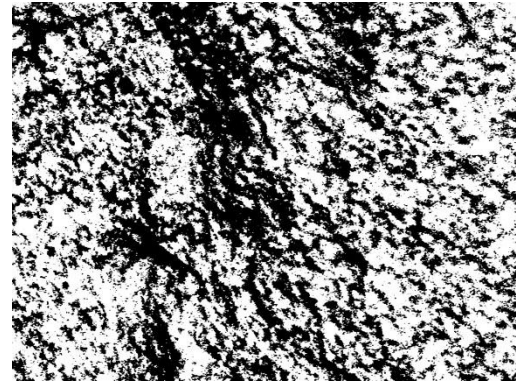
SEM cross sectional image (x140.000) [156]



Corresponding binary image
 $D_f=1.8225\pm0.0899$ [156]

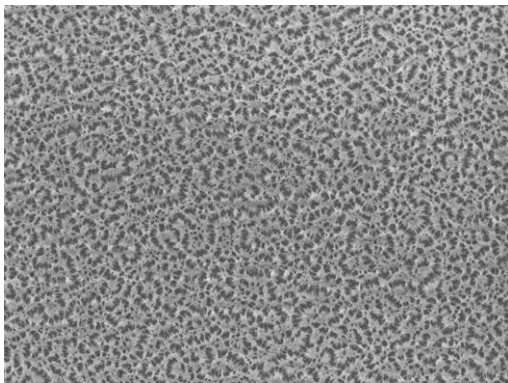


SEM cross sectional image (x55.000)

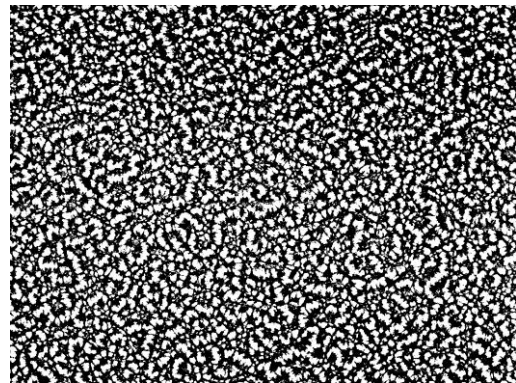


Corresponding binary image
 $D_f=1.823\pm0.0888$

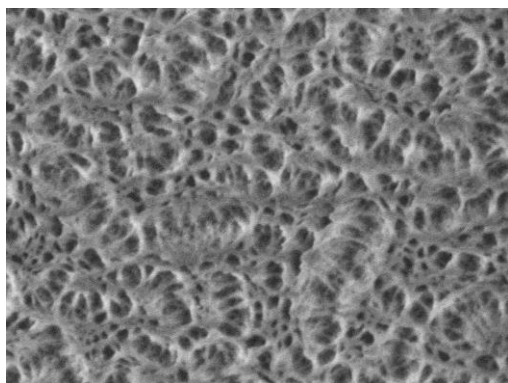
Figure 4.5: SEM cross sectional images and their corresponding binary ones from which the Hausdorff dimensionality of isotropic porous Si was extracted



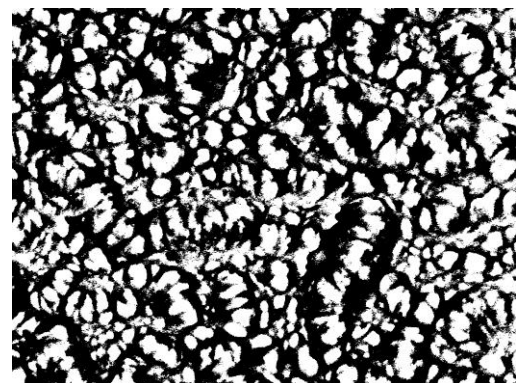
Top view SEM image after mild plasma processing (x20.000)



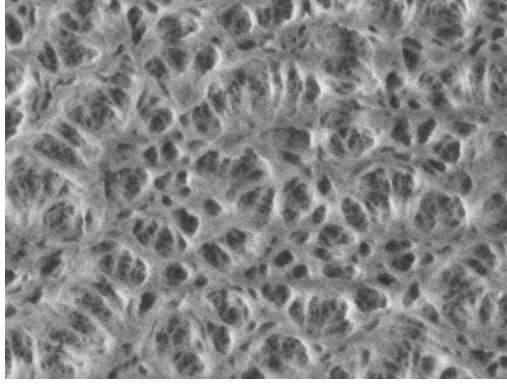
Corresponding binary image
 $D_f=1.8307\pm0.0913$



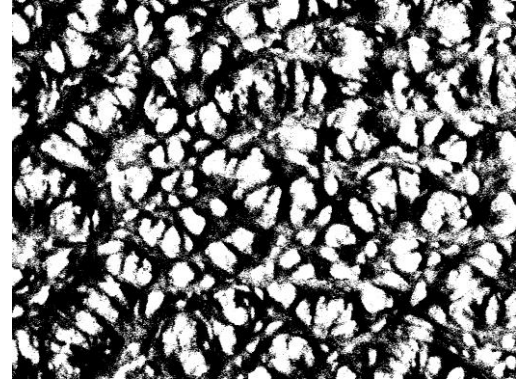
Top view SEM image after mild plasma processing (x70.000)



Corresponding binary image
 $D_f=1.8074\pm0.0897$



Top view SEM image after mild plasma processing (x100.000) [156]



Corresponding binary image
 $D_f = 1.8178 \pm 0.0881$ [156]

Figure 4.6: SEM top view images and their corresponding binary ones from which the Hausdorff dimensionality of isotropic porous Si was extracted.

As it can be seen, in all cases the calculated Hausdorff dimension was found to be less than two including the standard error, with an average value of approximately 1.822 ± 0.084 .

Figure 4.7 depicts an example of a log-log plot of the number of boxes N_B that have foreground pixels in them as a function of size s_B of the boxes, from the slope of which the fractal dimension was obtained.

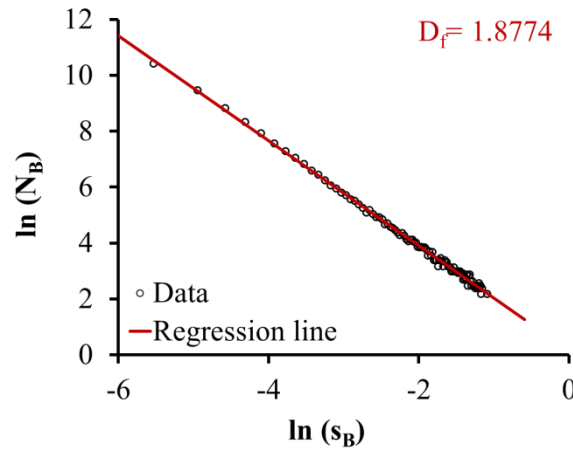
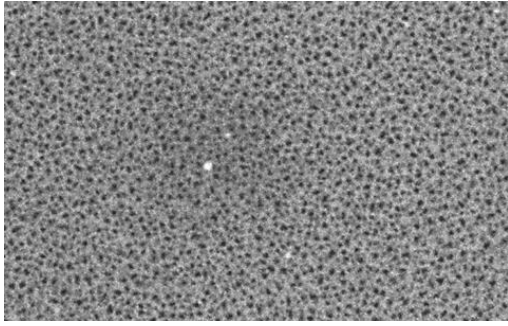


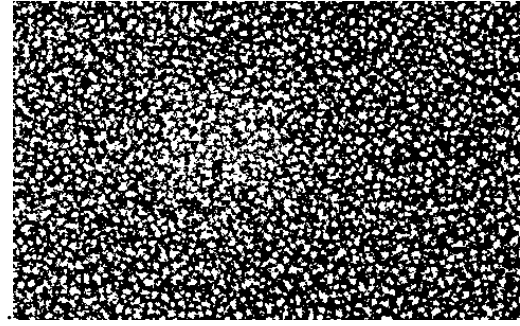
Figure 4.7: Example of the data obtained using box-counting algorithm for the SEM image of isotropic porous Si (x 20.000). From the slope of such curves corresponding to different grid positions, a mean Hausdorff dimension was calculated.

4.4.1.2 Anisotropic porous Si

Examples of used SEM images of the anisotropic porous Si layer are presented in Figure 4.8 (top view) and 5.9 (cross sectional). Again, in all cases the calculated Hausdorff dimension was found to be less than two including the standard error, while the average value was calculated to be approximately 1.8888 ± 0.05238 .



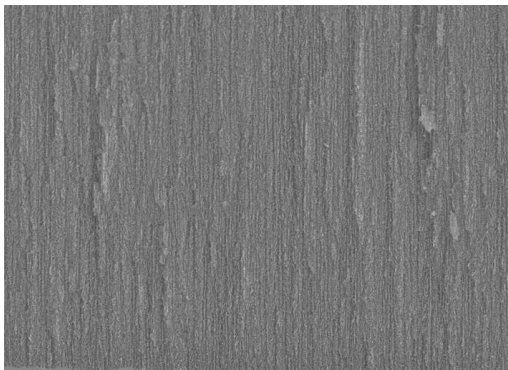
SEM image top view (x 50.000)



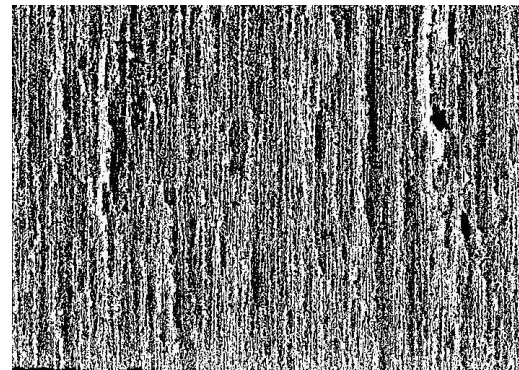
Corresponding binary image

$$D_f = 1.9047 \pm 0.0624$$

Figure 4.8: SEM top view image and its corresponding binary one, from which the Hausdorff dimensionality of anisotropic porous Si was extracted.

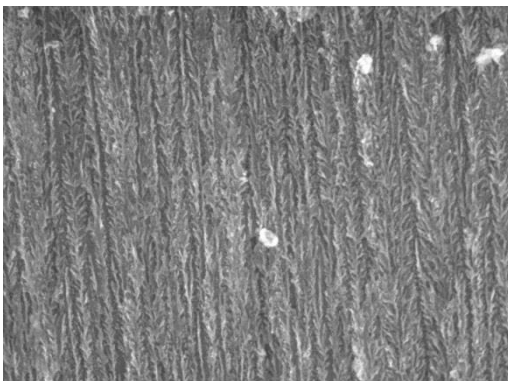


SEM cross sectional image (x20.000)

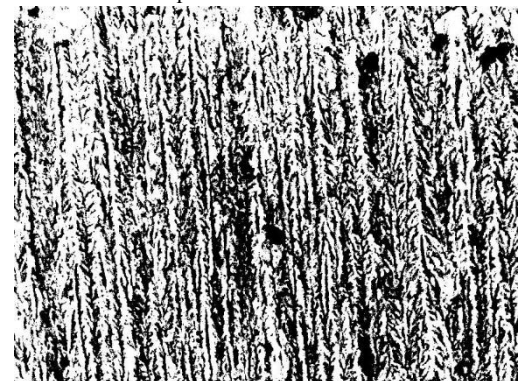


Corresponding binary image

$$D_f = 1.9087 \pm 0.067$$

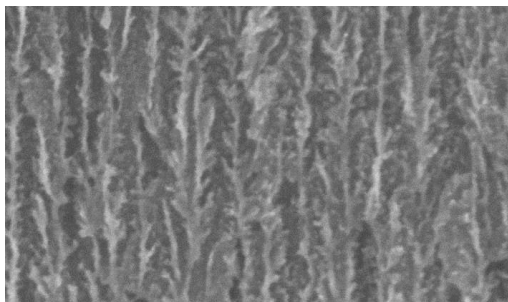


SEM cross sectional image (x75.000)

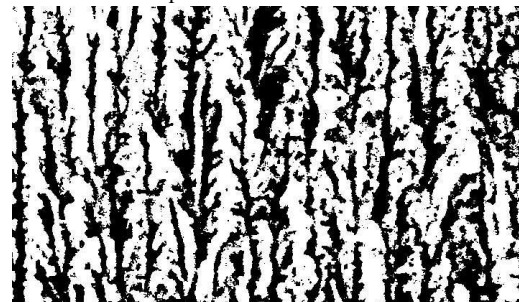


Corresponding binary image

$$D_f = 1.9009 \pm 0.0502$$

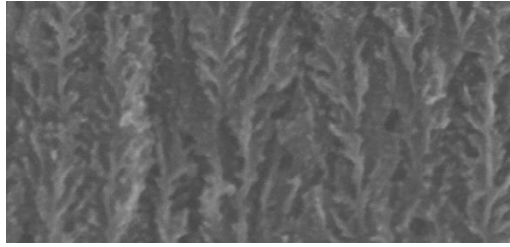


SEM cross sectional image (x220.000)

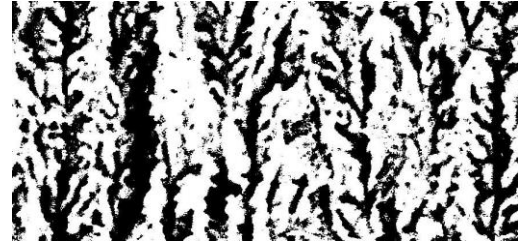


Corresponding binary image

$$D_f = 1.8761 \pm 0.0443$$



SEM cross sectional image (x270.000)



Corresponding binary image

$$D_f = 1.8515 \pm 0.0361$$

Figure 4.9: Cross sectional SEM images and their corresponding binary ones, from which the Hausdorff dimensionality of anisotropic porous Si was extracted

Figure 4.10 shows an indicative example of data calculated with the box-counting algorithm by analyzing a cross sectional SEM image of the anisotropic porous Si sample.

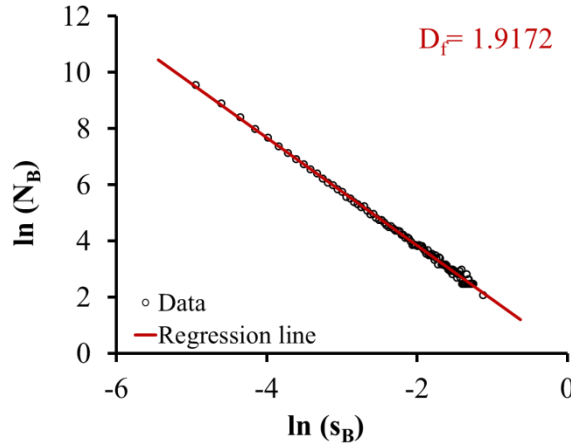


Figure 4.10: Example of the data obtained using box-counting algorithm for the SEM image of anisotropic porous Si (x 20.000). From the slope of such curves corresponding to different grid positions, a mean Hausdorff dimension was calculated.

From the above analysis, it is deduced that the anisotropic porous Si sample (porosity 70%) has slightly higher fractal dimension compared to the isotropic one (porosity 63%). This is in consistency with Tang et al. [174], who showed that the fractal dimension of porous metal materials increases gradually by increasing porosity.

4.5 Plateau-like behavior of porous Si thermal conductivity at cryogenic temperatures – Interpretation based on its fractal geometry

In Chapter 3, we discussed the plateau-like behavior of the temperature dependence of thermal conductivity at low temperatures, which is common trend observed in glasses and disordered materials. Different explanations for this behavior have been proposed in the literature [122], based on phonon scattering by enhanced densities of tunneling systems, elastic scattering by density fluctuations, dimensional crossover of the vibrational density of states, phonon localization and fractons. However, there is still no consensus about its origin.

In section 3.5, the results of temperature dependence of porous Si thermal conductivity were presented down to 4.2K and the plateau like behavior between 4.2-20K was pointed out for both porous Si layers examined [156]. Based on this outcome and the fractal nature of porous Si, as it was investigated in the previous chapter, we will discuss the obtained results using basic principles of the scaling theory of localization proposed by Rammal & Toulouse [175].

Particularly, in references [175] and [162] the authors considered the dynamics of a percolating network and developed a fundamental model for describing geometrical features of random systems. By taking a self-similar fractal structure, they evaluated the density of

states for vibrations of a percolation network with the introduction of the *fracton dimension* \tilde{d} :

$$\tilde{d} = \frac{2 \cdot D_f}{(2 + \theta)} \quad (4.4)$$

where θ is a positive exponent giving the dependence of the diffusion constant on the distance. Fracton dimension is a key dimension for describing the dynamical properties of fractal networks, in addition to the fractal dimension. The fracton dimension practically characterizes an anomalous diffusion in a fractal system. A direct way to measure fracton dimension \tilde{d} is to measure the density of states (DOS). Incoherent inelastic neutron-scattering experiments, for example, measure the amplitude weighted DOS and can be used for the direct determination of fracton dimension. More details about the problem of fracton excitations in fractal structures and generally the dynamical properties of fractal networks are found in reference [176].

Based on their models, Rammal & Toulouse [175] showed that fractons are spatially localized vibrational excitations of a fractal lattice and are met in materials with fracton dimension $\tilde{d} < 2$.

Considering that in ideal fractal systems the density vanishes for large samples, a fracton contribution in highly porous Si is possible because of its very small density. One more reason is the observed fractal structure of porous Si, which was investigated previously. In section 5.4, the fractal dimension D_f of porous Si was calculated using SEM images and the box-counting algorithm. It was shown that for both layers the Hausdorff dimension is lower than two. Thus, it is evident from Equation (4.4) that the fracton dimension \tilde{d} of porous Si is also lower than two, since θ is a positive quantity. The condition for the existence of fractons in porous Si systems is thus fulfilled.

From the above analysis, it is deduced that the observed plateau-like behavior of porous Si thermal conductivity at temperatures in the range 4.2-20K can be attributed to the existence of fractons, as in the case of other disordered materials [163, 177]. Apart from that, there are some more evidences that strengthen our assumption and are discussed below.

The fracton formalism is also supported by the existence of the so-called “Boson peak” in the Raman spectra and by the Brillouin spectra of porous Si, observed by different groups in the literature. The Boson peak is considered as a signature of the existence of localized vibrational modes in amorphous materials. Shintani et al. [178] correlated the Boson peak for glasses with the Ioffe-Regel frequency, which is the frequency reached when the mean free path for phonons approaches their wavelength and it is a limit above which transverse phonon modes no longer propagate [179]. Foret et al.[180] investigated acoustic localization in fused silica and claimed that the states near the Boson peak are localized and satisfy the Ioffe-Regel criterion.

If at this point one considers that in a fractal geometry, the non-propagating phonon modes are called fractons [162], we can claim that in a fractal geometry there is a link between the appearance of a Boson peak in the Raman spectra and the existence of fractons [156]. Thus, in the following we will review the literature results concerning the observation of a Boson peak in porous Si and porous Si – like materials that were found in the literature.

Low frequency Raman modes of nanometric Si crystallites were first observed in porous Si [181, 182]. Gregora et al. [181] observed a well-defined peak at 37cm^{-1} in the low frequency spectra of nanostructured porous silicon with 70% porosity. Confined acoustic phonons were also observed in Si nanocrystals of diameter 3.1nm dispersed in SiO_2 [183] and a broad peak between $20\text{-}40\text{cm}^{-1}$ was observed both in polarized and depolarized spectra. This peak could be attributed to a Boson peak, even though the authors did not explicitly name it as such. In addition, the Raman spectrum of porous silicon studied in reference [184] revealed a Boson peak at 150cm^{-1} . In a recent work, Claudio et al. [185] observed a Raman peak at 6meV

($\sim 50\text{cm}^{-1}$) in doped polysilicon nanoparticles exposed to air and sintered to form nanocrystalline silicon, a material with similar structure to that of our studied porous Si layer. They attributed this peak to a Boson peak.

On the other hand, Brillouin spectroscopy is also a method to study the different phonon modes of a material. By applying it to porous Si with 80% porosity, Lockwood et al.[186] identified two acoustic phonon peaks exhibiting large peak widths. They attributed these peaks to the existence of fractons. However, in a more recent work by the same authors [187], the peak at 8 GHz was absent from their Brillouin spectra. The peak at 14GHz was again observed, but in that case it was attributed by the authors to the bulk transverse Rayleigh mode. In a recent paper by Polomska-Harlick et al.[188], the Brillouin spectrum of porous Si with 59% porosity was obtained and a peak at $\sim 8\text{GHz}$, as previously observed by Lockwood et al.[186], was again identified. Even though the authors characterized this peak as “unknown”, we think that it could be attributed to the existence of the phonon-to-fracton crossover suggested by Lockwood for porous Si and also observed in other disordered materials [177]. Its intensity increased with $\sin\theta$ and saturated at $\sin\theta \sim 0.9 \Rightarrow \theta \sim 65^\circ$. Based on the above two references, if we consider the Brillouin peak frequency at $\sim 8\text{GHz}$ as the crossover frequency f_{co} , a crossover temperature $T_{co} \sim 0.4\text{K}$ is calculated [156]. However it should be pointed out here that the crossover temperature does depend on the density of the material as Posselt et al. [189] showed experimentally for the case of silica aerogel. Thus, we expect this value to be different for the isotropic and anisotropic porous Si layer due to their different porosity.

In amorphous materials, the high temperature limit of the plateau is at around 20K. Above the plateau, a linear increase of the thermal conductivity with increasing temperature is observed. Alexander et al.[164] introduced the anharmonic interaction between fractons and phonons in order to explain this linear increase. While fractons do not carry heat, and as a result their existence leads to a constant value of thermal conductivity with temperature, through the fracton-phonon interaction phonon-induced fracton hopping can contribute to the heat current, generating a thermal conductivity which increases linearly with increasing temperature.

Consequently, the phonon-fracton model predicts the following form for thermal conductivity [176]:

$$k_{\text{total}} = k_{\text{ph}} + k_{\text{hop}} \xrightarrow{T > T_{co}} k_{\text{total}} = A + B \cdot T \quad (4.5)$$

where k_{ph} is phonon thermal conductivity, k_{hop} is the fracton hopping contribution to the total thermal conductivity, which depends linearly on temperature, and A, B are constants.

Alexander et al. [164], based on their theoretical model, suggested that one should observe an additional contribution to k from the fracton hopping, which simply “adds on” to the plateau value of k , if the phonon mean free path does not change. Given this condition, the following expression can be written as:

$$k = k_{\text{plateau}} + B \cdot T, \quad T > T_{\text{plateau}} \quad (4.6)$$

where k_{plateau} , T_{plateau} are the thermal conductivity and temperature where the plateau occurs.

Having this theoretical background, we can now move on to the thermal conductivity measurements of porous Si presented in this work. Our porous Si thermal conductivity results show a plateau in the temperature range 4.2-20K for the isotropic sample and 5.7-16K for the anisotropic one, with a constant value of $\sim 0.04\text{W/m.K}$ and $\sim 0.05\text{W/m.K}$, respectively. Above these temperatures a monotonic increase of the thermal conductivity with temperature was measured.

Particularly, as the Figure 4.11(a) shows for the anisotropic PSi sample, linear temperature dependence is observed up to 232K after a transition region between 16-50K. By fitting the

data in this region to a first order polynomial function, the following equation is obtained:

$$k_{\text{anis}}(T) = 0.0015T + 0.0521 \quad (4.7)$$

By extrapolating the thermal conductivity to $T=0\text{K}$ as shown in Figure 4.11(a), the value of $k_{\text{plateau}} = \sim 0.05\text{W/m.K}$ is obtained in agreement with Equation (4.6). It is thus deduced that in the linear region 50-232K the fracton hopping mechanism is responsible for the linear trend of the curve, while the phonon mean free path did not change with increasing temperature. Additionally, the transition regime between 16-50K is again in agreement with Alexander et al. [164] for measurements on epoxy resin samples and it is attributed to the smooth crossover of the vibrational modes from phonon to fracton regime. Above 232K the same anharmonic interactions described previously quench the fracton-hopping rate due to the lifetime broadening of the fracton states with increasing temperature [190]. This fact leads to deviations from the previous linear dependence.

In agreement with Posselt et al. [189] results for silica aerogels, and to the phonon diffusion model by Gesele et al. [119], presented in section 3.5.5, at these high temperatures thermal conductivity is proportional to specific heat capacity, considering the temperature-independent phonon mean free path, which is limited by the crystallite size of porous Si. A comparison of our experimental results with the phonon diffusion [119] and phonon hydrodynamic [138] models was made in section 3.5.5 and quite good agreement with both models was obtained.

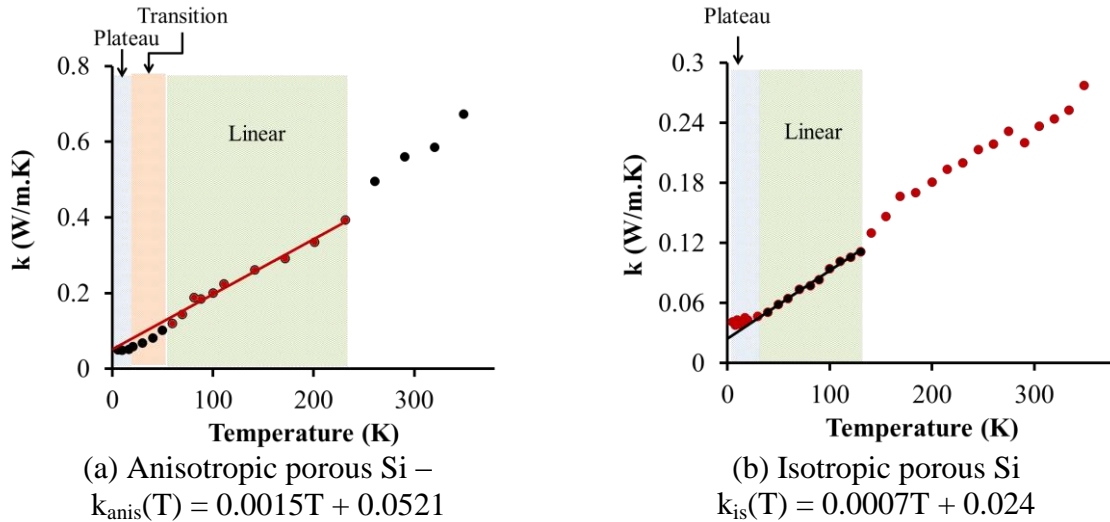


Figure 4.11: Temperature dependence of (a) anisotropic and (b) isotropic porous Si thermal conductivity, respectively. The circles represent the experimental data, while the solid lines indicate the linear dependence on temperature at temperatures above the plateau, which is in agreement with Equation (4.5). In each case, the linear $k(T)$ function is indicated.

Similar conclusions can be deduced for the isotropic porous Si sample (see Figure 4.11(b)). In this case the plateau is observed between 4.2-20K. A linear dependence, which is described by the following linear function, is obtained in the temperature range 20-130K:

$$k_{\text{is}}(T) = 0.0007T + 0.024 \quad (4.8)$$

Contrary to the anisotropic sample, the extrapolation of $k_{\text{is}}(T)$ to $T=0$ gives a value of 0.024W/m.K , which is slightly lower than the value of the plateau $\sim 0.04\text{W/m.K}$. This is attributed to a decrease in the low-frequency phonon mean free path [164]. Another interesting note is that the constant B for isotropic sample is almost half of that calculated for the anisotropic sample. This difference is caused by its specific morphology, indicating that both phonon and phonon-fracton interactions contribute much less in the total heat flow in the material. Finally, above 130K the same trend with the anisotropic porous Si layers is observed and it was discussed in Chapter 3.

It is worth to note here that discrepancies between the experimental results and the different

theoretical models in the whole temperature range studied in this thesis are mainly due to the very complicated structure of porous Si. Nanostructured porous Si is composed of interconnected Si nanowires and nanocrystals, covered by a native oxide shell and separated by voids. The ratio of the native oxide compared to the Si core plays a critical role in the determination of the mechanism of thermal conduction in the different temperature ranges, especially at cryogenic temperatures [191]. This is attributed to the different temperature dependence of vibrational modes in the two systems (the Si backbone and the shell oxide) and different dominant scattering mechanisms in each case.

4.6 Conclusions

To summarize, in this chapter an interpretation of the plateau-like behavior of porous Si thermal conductivity at cryogenic temperatures, as well as the linear trend that follows, was given, based on the fractal nature of the material. After a brief introduction to fractals and their basic properties, the fractal dimension of anisotropic and isotropic porous Si layers was calculated using SEM image analysis and the box-counting algorithm. The anisotropic sample was found to have slightly higher fractal dimension, consistent with its higher porosity, while both layers were found to have a fractal dimension lower than two, a necessary condition of the fracton formalism to be adopted. The obtained linear dependence of thermal conductivity on temperature above the plateau was also characterized by the fracton model. Particularly, it was shown that the phonon-induced fracton-hopping mechanism fits our experimental results pretty well. Above the linear region, thermal conductivity is proportional to specific heat capacity, as it was indicated in a previous chapter by comparing the experimental results to other analytical models based in this assumption.

Literature results concerning micro-Raman and Brillouin spectra in porous Si were reviewed as further evidence to support the fracton formalism. The existence of the so-called “Boson peak” in the micro-Raman spectra of porous Si with a similar porosity than that of the porous Si layer was observed by many authors. The existence of this peak in a material is in general considered as a signature of the presence of localized vibrational modes (“fractons” in a fractal lattice). In addition, literature results of Brillouin spectra of porous Si also showed localized vibrational modes that support fracton interpretation.

Chapter 5

Effectiveness of porous Si as a thermal insulating platform on the Si wafer

The history of thermal insulation materials is not as long as that of other materials, but the necessity of insulation is as old as building activity. Prehistoric people built shelters to protect themselves from the elements, originally using organic materials and later more durable substitutes. Processing organic materials produced the first insulated panels in the 19th century: meanwhile an increasing range of artificial materials were developed. The overall growth of these products has been substantial due to a wide range of reasons...

Bozsaky, D (2010) The historical development of thermal insulation materials. Period. Polytech. Archit. 41:49. doi: 10.3311/pp.ar.2010-2.02

5.1 Introduction

One of the most important building blocks of any thermal device is the incorporated thermally insulating material. Such a material should:

- *have sufficiently low thermal conductivity so as to minimize thermal losses by heat conduction*
- *be stable and robust*
- *be fabricated by an easy and low cost process*
- *be compatible to CMOS processing for integration on the Si wafer*

The advantages of being able to integrate different types of devices, including thermal and thermoelectric ones, on the Si wafer are tremendous, as it was also mentioned in chapter 1. Microelectronics and microsystems play a vital and increasingly important role in current and future human life and society. The future will bring a plethora of new products and processes based on new concepts with limited past experience to build upon. In this respect, much of the research of microstructures involves thermal management in one way or another. It is thus very important to find ways to integrate miniaturized thermal devices on the Si wafer because: (a) Si technology is a batch technology that allows cost reduction, (b) the integration of sensors with Si electronics opens important new possibilities for the realization of smart devices and (c) the size of the sensor and the corresponding system, including its encapsulation housing, can be significantly reduced [192]. The low thermal conductivity membranes used as a substrate for the integration of thermal devices are usually called “micro-hotplates”.

Bulk crystalline Si wafers are inappropriate to act as “micro-hotplate” devices due to their high thermal conductivity ($\sim 145 \text{ W/m.K}$ at room temperature, while it can reach values as high as $\sim 4500 \text{ W/m.K}$ at $\sim 20 \text{ K}$). What is usually used instead is thin Si or Silicon Nitride free standing membranes or cantilever beams with high thermal resistance, which can be realized by micromachining of bulk c-Si. However, these solutions are fragile and show poor mechanical stability [193]. A flexible solution towards the on-chip integration of miniaturized thermal devices is the fabrication of a local substrate on the Si wafer [194], on which the sensor parts can be integrated. Such a material is porous Si. As the temperature dependent thermal conductivity measurements demonstrated, porous Si at high porosities has very low thermal conductivity in a wide range of temperatures. It, thus, constitutes an excellent local platform on the Si wafer for the integration on it of different thermal and thermoelectric devices [192].

The main advantages of using porous Si as “micro-hotplate” are as follows: a) very thick porous Si layers can be fabricated locally on the Si wafer by a simple and low-cost procedure (see Chapter 2) b) depending on its porosity and structure, these layers are robust and mechanically stable c) porous Si formation is compatible with standard Si processing and d) porous Si technology offers the advantage of having planar topography with the Si wafer.

In this respect, in the present chapter the effectiveness of porous Si as a thermal insulating platform will be demonstrated, based on thermal conductivity measurements presented in Chapter 3. Using FEM simulations, the temperature distribution in the volume of a “micro-hotplate” device will be depicted, while the effect of porous Si thickness on the output of such device will be assessed. The simulated results will be compared to corresponding structures on c-Si.

5.2 Temperature distribution in a test device incorporating a thermal insulating porous Si layer

Using the measured values of thermal conductivity obtained and showed in Chapter 3, the temperature distribution within a device incorporating Si, porous Si and a Pt resistor (like the test structure used in the measurements) is presented.

Figure 5.1(a) illustrates a 3D temperature distribution within 40 μ m isotropic P*Si* layer by applying a heat power of 3mW on the Pt heater at a reference temperature of 290.5K, while in (b) a 1D representation of the temperature distribution on the P*Si* surface on the left and right side of the Pt resistor for the above applied heat power is depicted. A cross sectional view of the temperature distribution in porous Si under the above conditions is given in Figure 5.1(c), while in 5.1(d) the one-dimensional (1-D) representation of the temperature variation as a function of depth, with the zero taken at the Pt/P*Si* interface, is shown. It is depicted that for the given reference temperature (290.5K), the achieved temperature on the heater is \sim 304K for an applied heat power of only 3 mW, while the temperature on the P*Si* surface at \sim 100 μ m from the heater is equal to the reference temperature. The high temperature difference around the heater on P*Si* is due to the effective thermal isolation from the Si substrate by the thick P*Si* layer [15].

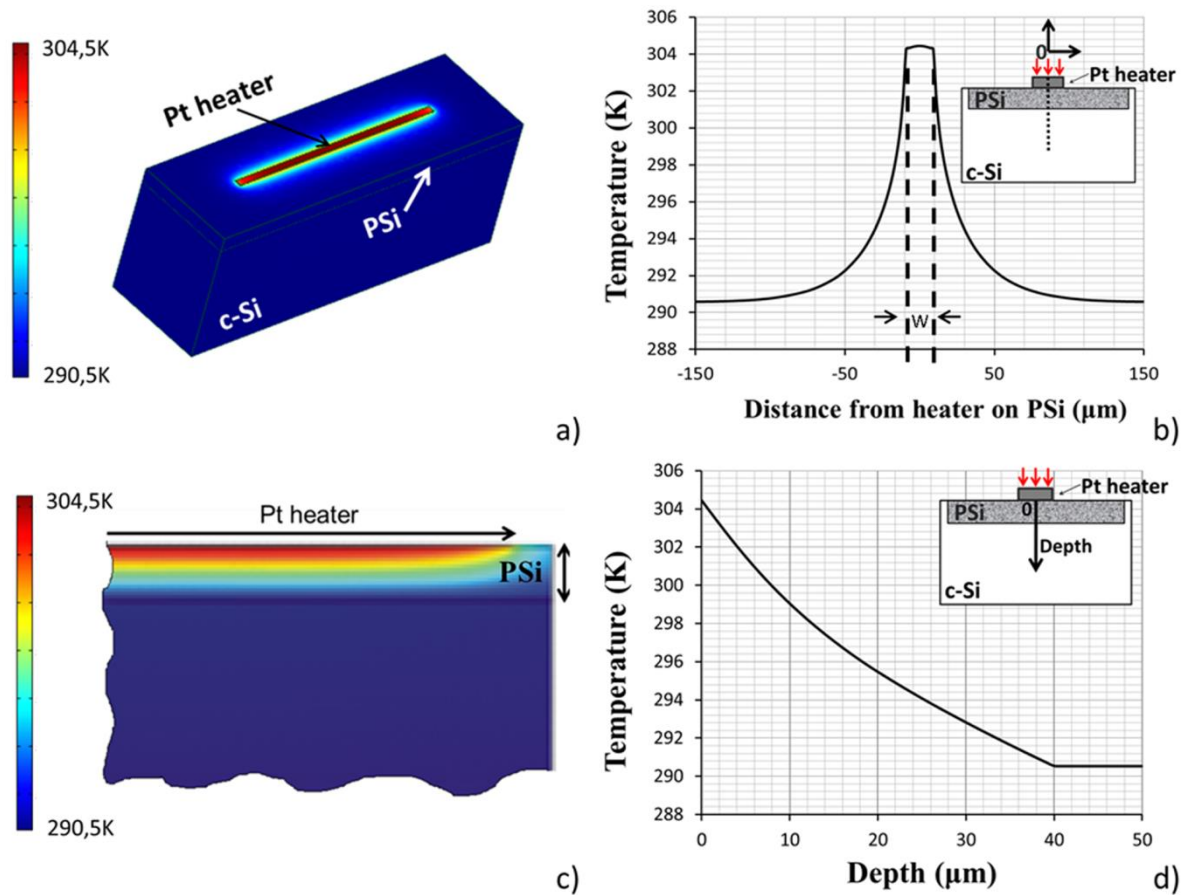


Figure 5.1: 3D schematic representation of temperature distribution on the Si surface around the heater (a), and in a cross sectional view of the structure underneath the heater (c) for an applied heat power of 3 mW. The graphs in (b) and (d) show the temperature distribution as a function of the distance from the heater (b) and as a function of depth from the metal/P*Si* interface (d) for the given heat power on the heater [15].

Due to the much lower thermal conductivity of porous Si at low temperatures, the above temperature difference on the P*Si* surface under an applied heating power on the heater is much higher at lower temperatures.

5.3 Effect of applied power

We used simulations to obtain the temperature distribution around the surface of the PSi layer for two reference temperatures, 20K and 290K and for different values of the heating power. The results for the isotropic porous Si layer are given in Figure 5.2.

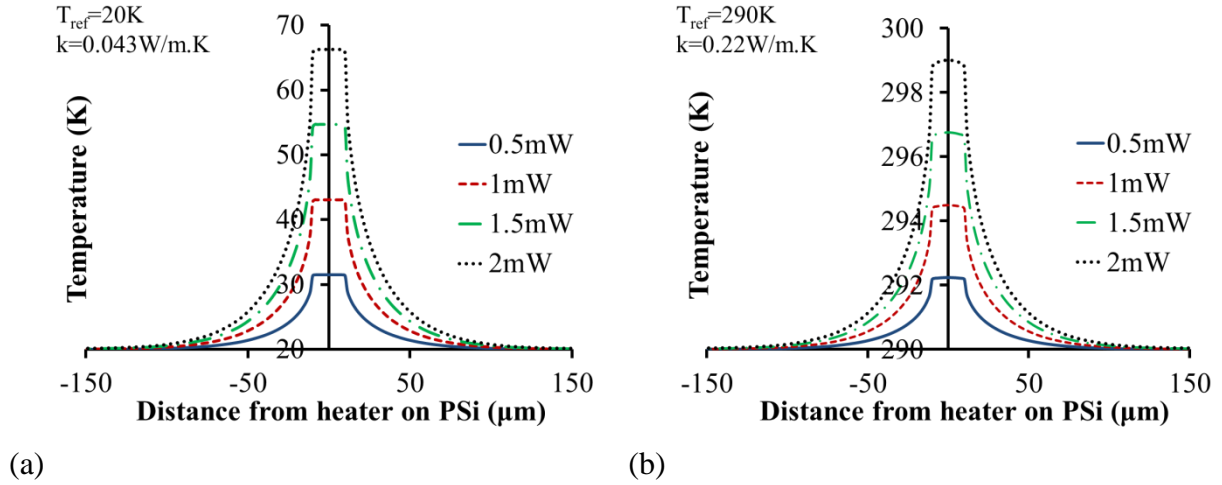


Figure 5.2: Temperature distribution on the PSi surface around the heater for different values of the applied heat power for two different reference temperatures, namely 20K and 290K. The Pt heater is lying on a 40μm isotropic PSi layer [15].

For a heat power of 2mW, the temperature difference on the heater is ~9K at a reference temperature of 290K, while it is more than 45K at a reference temperature of 20K for the isotropic porous Si sample. This huge difference is achieved due to its lower thermal conductivity at this temperature, which is about one order of magnitude lower compared to the k value at 290K.

The corresponding graphs for the anisotropic sample with the same thickness (i.e. 40μm) are represented in Figure 5.3.

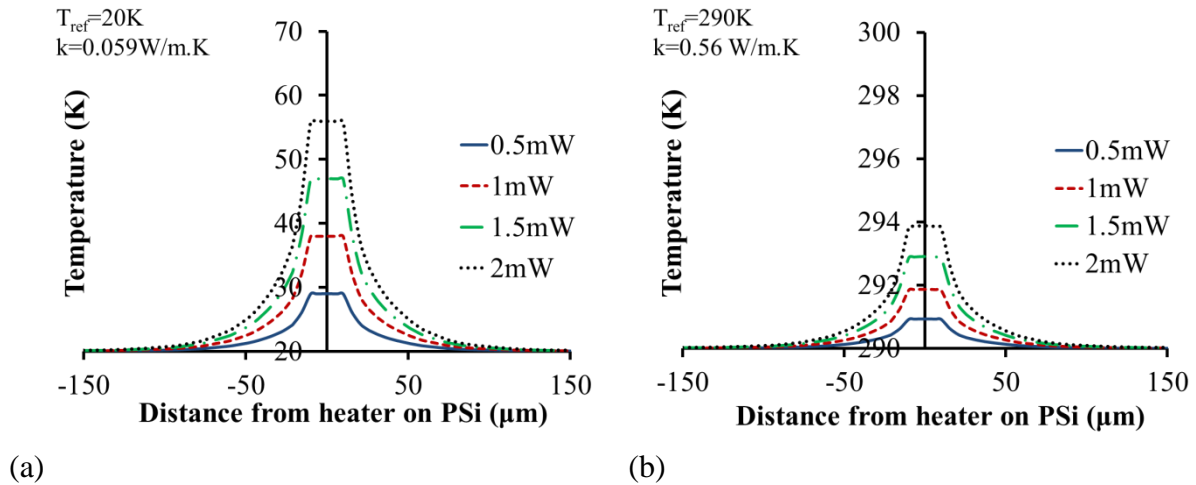


Figure 5.3: Temperature distribution on the PSi surface around the heater for different values of the applied heat power for two different reference temperatures, namely 20K and 290K. The Pt heater is lying on 40μm anisotropic PSi layer.

In this case, for a heat power of 2mW, the temperature increase on the heater is less than 4K at a reference temperature of 290K, while it is approximately 35K at a reference temperature of 20K for the anisotropic porous Si sample. Similar to the previous porous Si layer presented in Figure 5.2, this large difference is achieved by its lower thermal conductivity at this temperature, which is again about one order of magnitude lower compared to the k value at 290K. However, the maximum increment on the PSi surface in this case is significantly lower than the corresponding temperature increase that was achieved with the

isotropic PSi. This was an expected result if one considers the differences in their thermal conductivity. In fact, the percentage of reduction in thermal conductivity is directly interpreted as the same percentage increase in the maximum temperature that can be achieved on the PSi layer by applying the same amount of heating power on the heater. This is clearly indicated in the table below.

Table II: Thermal conductivity values of isotropic and anisotropic PSi layers and the maximum temperature difference observed at their surface by applying a heating power of 2mW on the heater. The percent difference in their thermal conductivity results in approximately the same percent difference of the maximum temperature induced on the heater.

	Isotropic PSi	Anisotropic PSi	Difference (%)
k at 20K (W/m.K)	0.043	0.059	27% increase in k
ΔT_{\max} at 20K (K)	45.9	35.9	21.7% decrease in ΔT_{\max}
k at 290K (W/m.K)	0.22	0.56	60.7% increase in k
ΔT_{\max} at 290K (K)	9.5	3.9	58.9% decrease in ΔT_{\max}

5.4 Effect of porous Si layer thickness

The effect of PSi layer thickness on the temperature distribution in such test structure was also investigated. In this respect, the temperature as a function of depth from the PSi surface for an applied heating power of 3mW at 290K is presented in Figure 5.4(a) for the isotropic PSi sample. The average temperature increase on the heater as a function of PSi layer thickness for the same heating power and for two reference temperatures, 290K and 20K, are illustrated in Figure 5.4(b) for isotropic and anisotropic porous Si layers. PSi layer thickness was taken between 1 and 100 μm .

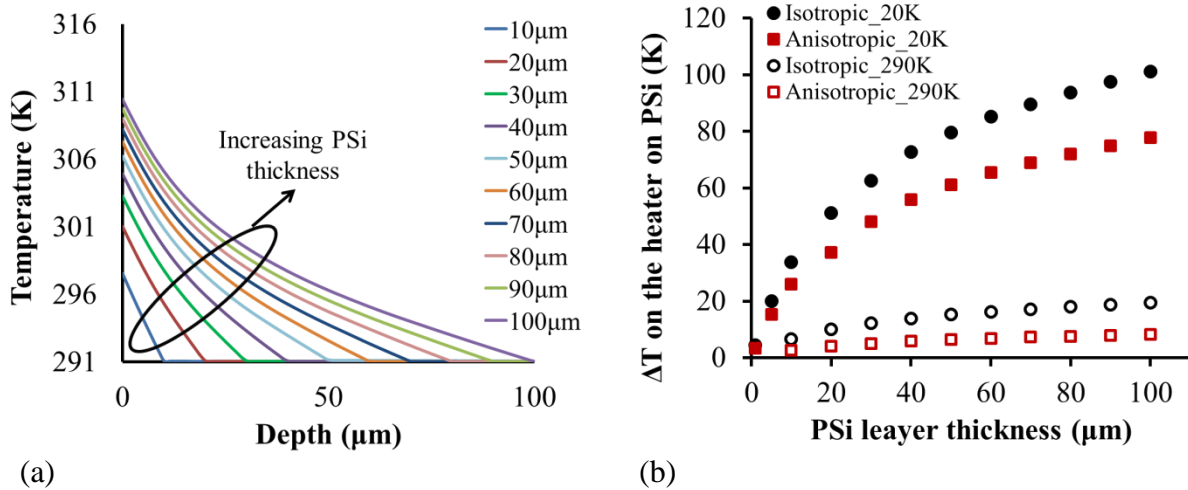


Figure 5.4: (a) Simulation results of the temperature distribution as a function of depth for different values of isotropic PSi layer thickness [15] and (b) the temperature difference on the heater for an applied heat power of 3 mW for two different values of the reference temperature (20 and 290K) for both isotropic and anisotropic PSi layers. At 20K the obtained temperature difference in both porous Si layers studied, is much higher than that at 290K, due to the much lower thermal conductivity of PSi.

The obtained average temperature difference on the heater, under an applied heating power, increases significantly with increasing PSi layer thickness for thicknesses below $\sim 40\mu\text{m}$, while it tends to saturate for higher thicknesses at room temperature. For lower temperatures (see points corresponding to 20K), for porous Si layer thickness above $40\mu\text{m}$ the temperature

difference on the heater with increasing thickness is almost saturated. This is why we have chosen this thickness in our experiments, since it is sufficient to provide almost maximum thermal isolation from the Si substrate, while it is small enough to guarantee a mechanically stable PSi layer in the case of the isotropic sample.

From the results above, it is clear that thick porous Si layer technology provides an efficient local thermal isolation technology on the Si wafer that is much more efficient at cryogenic temperatures. This makes the above technology very promising for application as a local substrate on the Si wafer for the integration of high performance cooling devices, as for example low temperature Si bolometers.

5.5 Comparison to bulk c-Si and other CMOS compatible thermal insulators

A three-dimensional (3D) representation of the temperature distribution around the Pt heater for a temperature of 17.3K was obtained using FEM simulations for the case of the isotropic sample [195]. The result is depicted in Figure 5.5b, in which an example of a 3D scattering plot of the temperature distribution around the heater on porous Si is depicted, compared to that on bulk crystalline Si (Figure 5.5(a)) for an applied heating power of $\sim 0.59\text{mW}$ and a temperature of 17.3K.

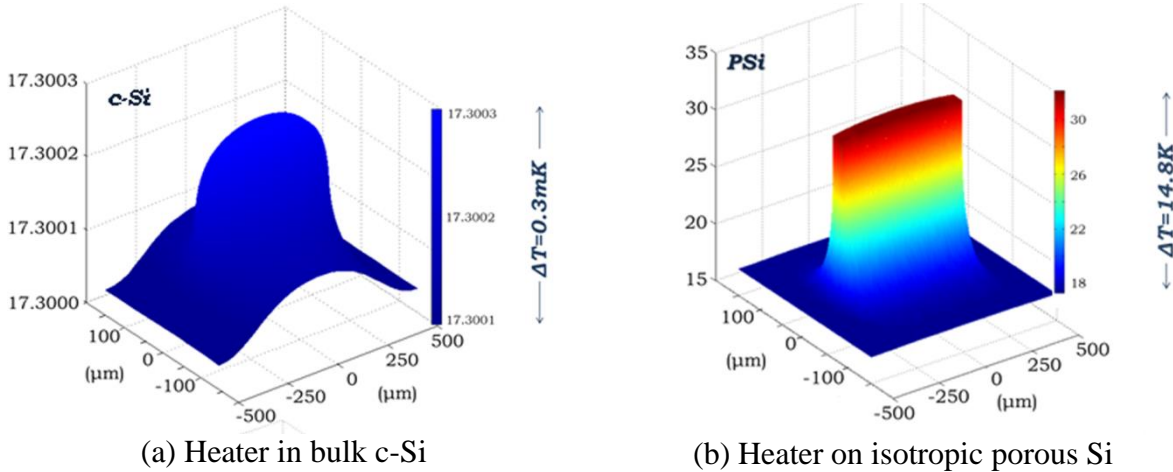


Figure 5.5: 3D scattering plots of the temperature distribution profile around the Pt heater on bulk c-Si (a) and on PSi (b) for an applied heating power of $\sim 0.59\text{mW}$ at a reference temperature of 17.3K [195].

It is clearly shown that with the same applied power, a temperature increase of 14.8K can be achieved on PSi, while there is almost no increase of the temperature of the same heater lying on bulk crystalline silicon. This is due to the very high difference between the thermal conductivity of porous Si ($\sim 0.04\text{ W/m}\cdot\text{K}$ at 17.3K) and that of bulk c-Si ($\sim 4.600\text{ W/m}\cdot\text{K}$ at this temperature). This is more pronounced in the following simulated device (Figure 5.6) where three identical resistors were integrated on its surface; two of them on the bulk c-Si surface and the last one on a predefined isotropic PSi layer, $40\mu\text{m}$ thick. The ambient temperature was set at 20K and the same heating power of $\sim 0.7\text{mW}$ was applied to each of the three resistors. The simulation output is illustrated in Figure 5.6. The presented device can be used as an efficient low temperature micro-hotplate for achieving a temperature increase of more than 15K on predefined areas on the Si wafer by applying a power less than 1mW without affecting the temperature of the Si wafer outside the porous Si area, where other devices can be integrated and continue to operate at ambient temperature.

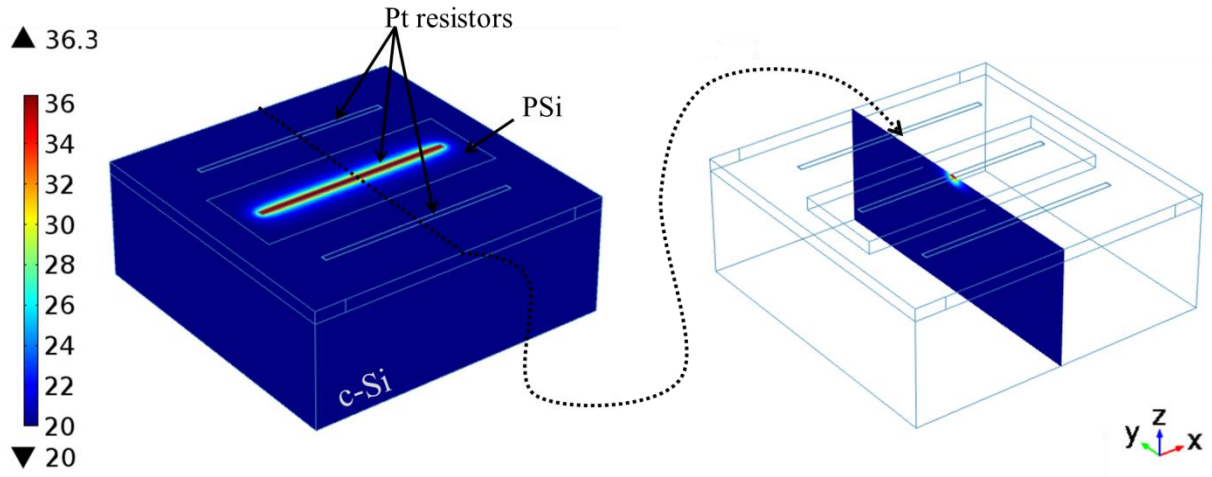


Figure 5.6: Simulated device which demonstrates the effectiveness of PSi as a micro-hotplate for low temperature operation (20K). Although the same amount of heating power is applied on the three Pt resistors shown in the Figure, only the one lying on PSi results in a temperature increment more than 15K on the surface of the device with only ~0.7mW of heating power.

5.6 Conclusions

In this chapter, the effectiveness of porous Si as a thermal insulator locally grown on the Si wafer was demonstrated using the measured values of thermal conductivity presented in Chapter 3 and FEM simulations. Particularly, the effect of the applied heating power on a heater lying on isotropic porous Si layer has been compared to the anisotropic one. As expected, higher temperature differences were obtained in the former case at all the temperatures. This is because of the lower thermal conductivity of the isotropic porous Si compared to the anisotropic one.

The effect of the porous Si layer thickness was also examined using same test structures. The results of the simulations showed that above 40 μ m the temperature increment that can be achieved on a heater for a specific value of applied power saturates at room temperature. On the other hand, at low temperatures the rate of temperature increase with increasing thickness almost saturates for a thickness above 40 μ m.

Finally, heaters were also integrated on bulk crystalline Si and the temperature increase on this substrate was compared to that on porous Si. Especially at low temperatures it was demonstrated that a power lower than 1mW is sufficient to locally increase the temperature by more than 15K on the PSi layer, while the rest c-Si around the predefined porous Si areas remain at ambient temperature. This is a characteristic example of an effective micro-hotplate. Thus, porous Si is highlighted as an excellent platform on which local temperature increase can be achieved with minimum applied power.

Chapter 6

Seebeck coefficient of porous Si as a function of porosity

Tomas Johann Seebeck received a medical degree in 1802 but preferred to study physics. In 1808, he was the first to produce and describe the amalgam of potassium while in 1810 he observed the magnetic properties of nickel and cobalt. In 1818 Seebeck discovered the optical activity of the solutions of sugar. In 1821 Seebeck found that a circuit made from two dissimilar metals with junctions at different temperatures would deflect a compass magnet. Seebeck initially believed this was due to magnetism induced by the temperature difference. However, it was quickly realized that it was an electric current that is induced, which by Ampere's law deflects the magnet. Today, this effect is known as the Peltier–Seebeck effect.

https://en.wikipedia.org/wiki/Thomas_Johann_Seebeck

6.1 Introduction

In Chapter 1, the motivation of studying thermoelectrics was introduced while the need of developing efficient Si-based thermoelectric materials was pointed out based on sustainability and feasibility issues. Considering that Silicon is an abundant and cheap material with well-known properties and processes for its engineering, the scientific community is “desperately seeking silicon” as a thermoelectric material [40]. In this respect, a number of works have been recently published on Si-based thermoelectrics [196], (see also section 1.5).

Nanostructural engineering has been proved to enhance material's zT [26, 29, 197, 198]. Concerning Si, researchers showed that by nanostructuration, the Seebeck coefficient is enhanced and the thermal conductivity is reduced, thus the figure of merit zT is increased. Instead of studying nanoengineered Si fabricated using complicated patterning techniques (nanowires, nanomeshes etc), a more massive and low cost technique is electrochemistry. Porous silicon is a known, CMOS compatible, cheap and easily fabricated example of nanostructured Si with very different properties than bulk c-Si. Its exceptional low thermal conductivity (see Chapter 3) makes it a promising material for thermoelectric applications both as a substrate for thermal isolation (see Chapter 5) and as a thermoelectric element [199, 200].

The enhancement of Seebeck coefficient (S) by creating pores in different Si-based thermoelectric materials has been proved theoretically [42, 200–202], while less experimental work has been devoted to it [45, 203, 204]. In the above papers, high porosity samples were used (porosity above 50%), which is not the best choice. Indeed, by increasing the porosity the thermal conductivity is considerably decreased [15, 156, 193], however the electrical conductivity is also decreased. The study of lower porosities seems to be a better strategy.

Thus, in this chapter, measurements of room temperature Seebeck coefficient of porous Si with porosities ranging from 40% to 85% are presented. Free standing porous Si membranes were used, while a home-built setup was fabricated and used for the measurements. Its design, contact geometry, data acquisition and analysis are presented and the validity of measurements is assessed. Based on the experimental results, the possible mechanisms involved are discussed, supported by structural characterization and photoluminescence measurements. The decrease in nanostructure size and increase in carrier depletion with increasing porosity, together with the complex structure and morphology of porous Si, are at the origin of complex energy filtering and phonon drag effects. All the above contribute to an anomalous behavior of thermopower as a function of porosity and will be discussed.

The objective is to continue with systematic characterization of the thermal and electrical conductivity of the specific samples in order to determine their overall figure of merit as thermoelectric materials. Samples with even lower porosities should be fabricated, which are more promising as thermoelectric devices.

6.2 Study of porous Si free standing membranes

Porous Si free standing membranes were fabricated at room temperature by electrochemical etching of highly doped p-type c-Si ($1-5\text{m}\Omega\cdot\text{cm}$) in a single-tank Teflon cell, in the dark. A two-step electrochemical process was used (see section 2.2.4). The PSi layer was initially formed by anodization on predefined areas of the Si wafer through a masking layer [98]. The fabrication process step-by-step and the characterization of the resulting porous Si layers are analyzed in the following paragraphs.

6.2.1 Fabrication process

A masking layer for anodization was used, which was a bilayer of polycrystalline/ SiO_2 . It was first formed on the c-Si wafer. After a cleaning process, oxidation was performed so as to form a 100nm thick SiO_2 layer on the Si wafer. A 300nm polycrystalline Si layer was then deposited on the samples using Low Pressure Chemical Vapor Deposition (LPCVD). Both layers were removed from the backside of the wafers with plasma etching. Photolithography and plasma etching were used to open windows on predefined areas of the front side of the samples.

A two-step electrochemical process was used for porous Si membrane formation and detachment from the substrate. In the first step, current densities below the critical value J_{ps} , for electropolishing were applied (see Figure 2.4). More specifically, current densities between $2-100\text{mA}/\text{cm}^2$ were used, resulting in porous Si layers with different porosities. In a second step, the current density was increased above J_{ps} ($\sim 500\text{mA}/\text{cm}^2$) in order to detach the membranes from the Si substrate (see section 2.2.4 for more details). In both steps the electrolyte used was a mixture of Hydrofluoric Acid (HF) and Ethanol in two different volume concentrations, namely 7HF:3Ethanol or 4HF:6Ethanol. The HF concentration of the electrolyte was changed in order to be able to fabricate samples with high porosities, because, as it can be seen in Figure 6.1, the porosity as a function of current density for the electrolyte with 70% HF tends to saturate for current densities above $\sim 50\text{mA}/\text{cm}^2$. Figure 6.1(a), (b) shows respectively the etch rate and porosity as a function of the current density used for the two different electrolytes, while table III summarizes all the electrochemical conditions used for PSi membrane formation.

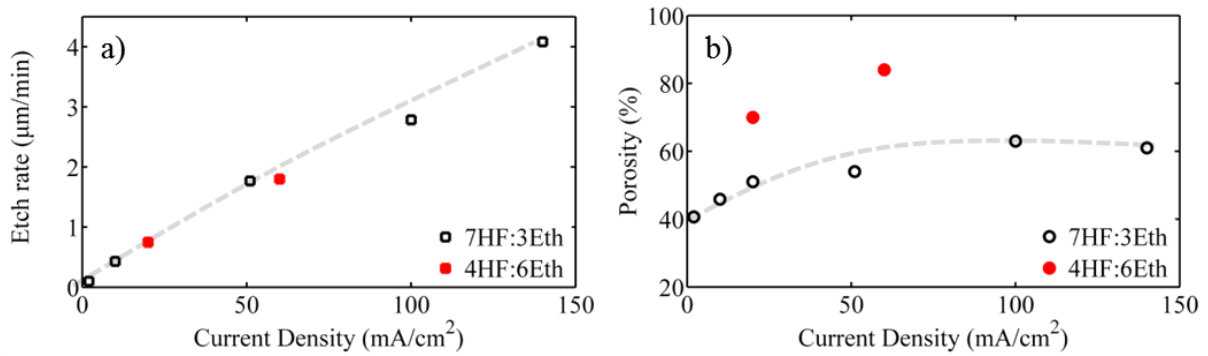


Figure 6.1: Etch rate (a) and porosity (b) versus the anodization current density for two different electrolytes. Dashed lines are guides to the eye.

Using these electrochemical conditions, we fabricated free standing PSi membranes with porosities between 40% - 84%. For the porosity determination, the three weight measurement method was used (see section 2.4).

Table III: Electrochemical conditions used for PSi membrane formation

PSi	Electrolyte	Current density (mA/cm ²)	Thickness (μm)	Anodization time (min)	Porosity (%)
1	3Eth:7HF	2	64	495	41
2	3Eth:7HF	10	120	240	46
3	3Eth:7HF	20	100	128	51
4	3Eth:7HF	51	100	52	54
5	3Eth:7HF	100	100	36	63
6	6Eth:4HF	20	100	133	70
7	6Eth:4HF	60	100	55	84

6.2.2 SEM and TEM characterization

Figure 6.2 shows representative SEM images of porous Si layers with increasing porosity. The samples with 46, 70 and 84% porosity are depicted. As it is clearly shown, with increasing porosity the pores widen, while they become smoother losing their branching.

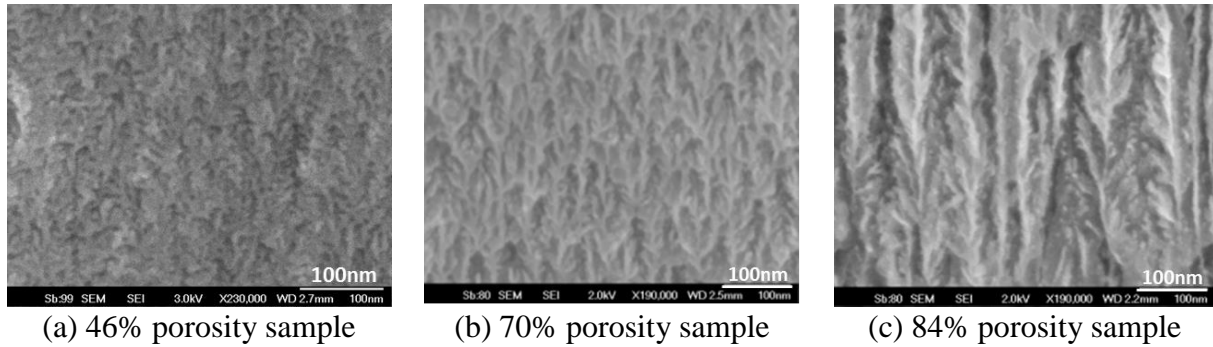


Figure 6.2: Cross sectional SEM images of PSi membranes with three different porosities, namely 46% (a), 70% (b) and 84% (c) are depicted.

Figure 6.3 shows representative Transmission Electron Microscopy (TEM) images of the 70% porosity sample shown in Figure 6.2(b). From such images the average pore wall was calculated to be ~6nm.

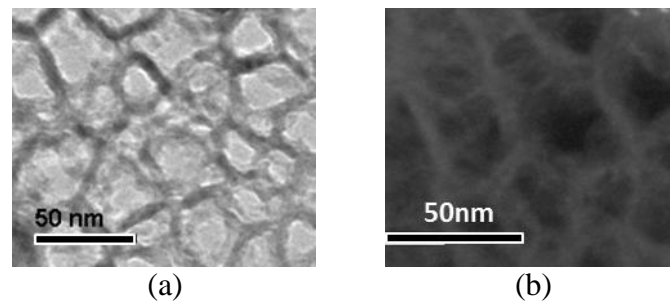


Figure 6.3: Bright-field (a) and dark-field (b) TEM images of the 70% porosity sample shown in Figure 6.2b.

6.2.3 PL measurements

When the mean crystallite size of a Si skeleton approaches the dimension of free exciton (~4.9nm) of bulk Si, photoluminescence (PL) starts to appear. For PL measurements, the Ar laser line at $\lambda=457.8\text{nm}$ (2.7eV) was used and Figure 6.4 depicts the obtained PL spectra of three PSi membranes with different porosity, namely 55%, 63% and 70%.

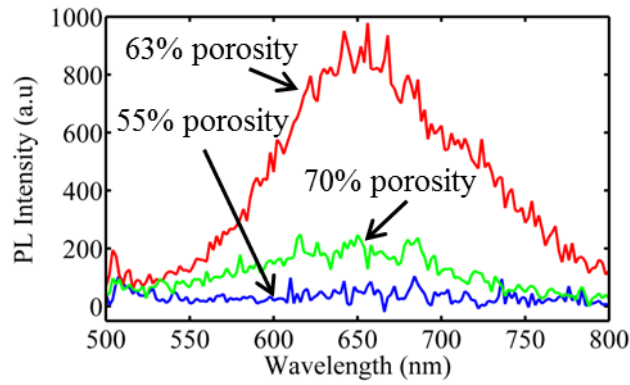


Figure 6.4: a) PL spectra of porous Si membranes with different porosities. The sample with the highest porosity (green line) was fabricated using different electrolyte composition than the others (see experimental conditions in table III)[205]

It is obvious from the figure above that membranes with 55% porosity do not emit any light. On the contrary, the 63 and 70% porosity membranes emit red light, with the 63% porosity sample being more efficient than the 70% porosity sample. Samples with even higher porosities show PL signals with increased intensity. The above results, combined with the SEM and TEM images shown before, give useful information concerning the structure and morphology of the porous Si layers.

More specifically, the 55% porosity sample and all the membranes with lower porosity do not show any photoluminescence, because, as deduced from the SEM image of Figure 6.2(a), the nanostructure size of the porous Si skeleton is quite large. The remaining Si wall is ~20nm wide, a value much higher than ~4.9nm. By increasing porosity, room temperature PL starts to appear. A strong peak at 650nm is observed for the 63% porosity sample, suggesting the existence of nanocrystals with sizes below ~5nm within the Si skeleton. Strong quantum confinement starts to occur, leading to the appearance of photoluminescence.

On the other hand, in the 70% porosity sample the mean size of nanostructures therein is higher, as it was confirmed both from the colour of that sample (blackish) and its TEM image depicted in Figure 6.3. From this image, we deduce that the mean distance of the Si walls of the PSi structure is ~6nm, which explains the almost absence of PL from this sample. This is also in agreement with the value of 5nm, which was calculated to best fit the temperature dependence of thermal conductivity data to the phonon hydrodynamic model for this specific sample (see section 3.5.5). The weak PL peak observed is thus attributed to the fact that the percentage of tiny nanocrystals with size below ~5nm is smaller than in the case of the 63% porosity sample, which shows much more intense red PL (peak at 650nm (1.9eV))[205]. This result is attributed to the different morphology and structure of PSi due to the difference in the electrolyte used during porous Si formation [206].

It is worth to note that in porous Si samples with Si nanocrystals of ~5nm, large differences in PL were observed (see Figure 6.4) by changing the average crystallite size by 1 to 2nm. However, this is not the case for the Seebeck coefficient dependence on porosity, as it will be proved later in this chapter.

6.3 Seebeck coefficient measurements

A home-built setup was used for differential quasi-steady-state two probe Seebeck Coefficient measurements [207]. The general considerations concerning this method were given in Chapter 1. In the present section, a description of how we implement this method in a home-built setup, as well as all the diagnostic tests used to assess the validity of the measurements, will be presented. Generally, in Seebeck coefficient metrology, the diversity in apparatus designs, data acquisition and contact geometry has resulted in conflicting materials' data [7]. Thus, a comprehensive study for our measurement setup and consequent data

analysis is presented in order to assure the accuracy and validity of our experimental results.

6.3.1 Home-built setup description

A plexiglas platform is used, on which two thick Cu blocks are fixed. The distance between them is 2mm. One of these blocks serves as a “hot” contact and the other as a “cold” one. The free standing PSi membranes are fixed as a bridge between the two blocks using silver paint to ensure good electrical contacts. A power resistor is placed on the Cu block and is used as a heater. The experimental setup used for Seebeck coefficient measurements is shown in Figure 6.5 in a 3D schematic representation[205]

A temperature difference (ΔT) is created between the two ends of the membrane by applying a dc current pulse of one minute duration on the heater situated at the “hot” contact. By modulating the amplitude of the current pulse applied on the power resistor, different heating rates can be achieved. The temperature is monitored for a total time of 30min. Pt1000 Resistance Temperature Detectors (RTDs) of class A are used for sensing the temperature on the two copper plates. RTDs in general tend to be more accurate, precise and stable than thermocouples [208], which are frequently used for sensing temperature in Seebeck coefficient measurement setups. The two RTDs are fixed on each copper plate with a double sided polyimide tape, which is thermally conductive and electrically insulating.

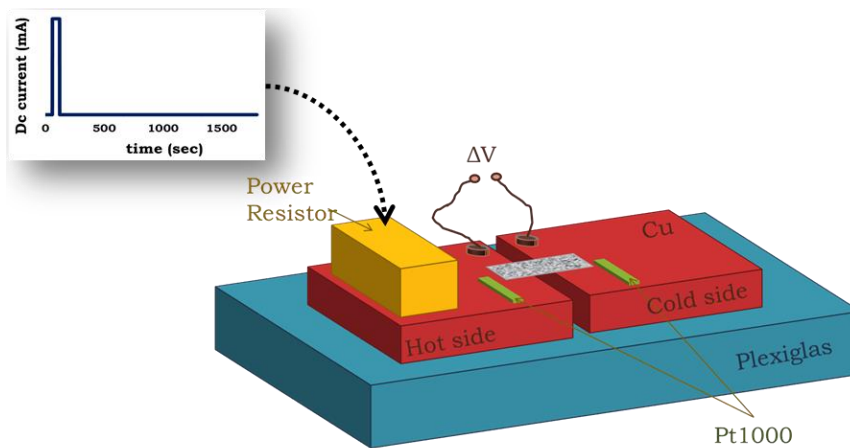


Figure 6.5: 3D schematic representation of the home-built setup used for Seebeck Coefficient measurements. The free standing PSi membrane is fixed as a bridge between two thick copper blocks which serve as “hot” and “cold” contacts and are used to create a temperature difference at the ends of the sample under test.

Two Keithley 2400 source meters are used to measure the resistances of the two RTDs and a Keithley 2000 digital multimeter is used to measure the resulting thermovoltage.

6.3.2 Data analysis

All the instruments are connected to a PC using General Purpose Interface Board (GPIB) bus trigger. The measurement data acquisition is accomplished programmatically using Labview® by recording the data in sequence. Three experimental parameters are recorded, namely the resistance of each RTD at the cold and hot sides of the setup and the corresponding thermovoltage.

The total time that is needed for recording all three experimental parameters (resistance of RTD at the hot side, resistance of the RTD at the cold side and thermovoltage) is 145.3msec. Although the total time of each complete set of measurements (T_{hot} , T_{cold} and ΔV) is sufficient short, in order to eliminate any distortion error that can be introduced to the measurement due to the different time during which each value is recorded, we used

interpolated data in order to have the best accuracy [11]. Thus, the instantaneous ΔT is recorded with the resulting thermovoltage (ΔV). In order to eliminate the effect of voltage offsets, the S values are extracted from the slope of the ΔV versus ΔT curves for temperature differences below 2K. The S values are extracted for data acquired when no current is passing through the power resistor, so as to avoid any spurious electrical signal that could affect the measurement [11, 207].

6.3.3 Validity of the measurements

Because the setup used for Seebeck coefficient measurements was a home-built one, the validity and accuracy of the measurements had to be ensured. Thus, a number of tests and validation techniques were implemented and are explained below.

6.3.3.1 Seebeck coefficient of highly doped p-type Si

In order to assess the accuracy of our measurements, we first measured the room temperature Seebeck coefficient of p-type silicon with resistivity 1-5m Ω .cm, (carrier concentration $\sim 5 \cdot 10^{19}$ atoms/cm³), from which the porous Si membranes were fabricated. A value of 299.3 μ V/K was found, which is in agreement with values in the literature. Table IV shows a comparison of the obtained value of S for bulk c-Si with values found in the literature for c-Si samples with similar doping concentrations.

Table IV: Seebeck coefficient of bulk c-Si – Comparison between the experimental results of this study with values found in the literature for similar doping concentrations

Type	Carrier Concentration (cm ⁻³)	Seebeck coefficient (μ V/K)	Reference
p-type	$5 \cdot 10^{19}$	299	This work
p-type	$1.2 \cdot 10^{19}$	300	[204]
p-type	$1.5 \cdot 10^{19}$	480	[209]
p-type	$5.1 \cdot 10^{18}$	404	[210]
p-type	$5 \cdot 10^{19}$	415	[211]
n-type	$1.7 \cdot 10^{19}$	420	[6]
n-type	$2.7 \cdot 10^{19}$	300	[209]

From the above table it is deduced that there is a relatively large dispersion in the measured values. The differences in the carrier concentrations, the type of the dopants and the errors induced from the measurement itself result in these variations between the measured values. However, our measurement results are in the range of values reported in the literature, namely 300-480 μ V/K.

As it was pointed out in Chapter 1 (section 1.4), in general, the Seebeck coefficient increases as the carrier concentration decreases (Figure 1.14). It was also mentioned in the same chapter that Seebeck coefficient is composed of two parts: the diffusion and phonon drag parts. In bulk semiconductors at room temperature the phonon drag effect is in general considered to be important in the case of the undoped or lightly doped material and smaller in the heavily doped material. Figure 6.6 shows some representative data from the literature [6, 212] relating S , S_d and S_{ph} of bulk c-Si with doping concentration. A large dependence of S on doping is observed, a fact that will be proved useful in the explanation of porosity dependence of S of porous Si membranes.

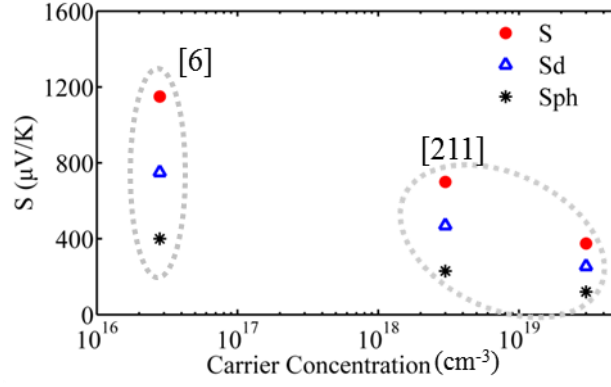


Figure 6.6: Total Seebeck coefficient and contributions of S_d and S_{ph} in bulk c -Si at different carrier concentrations [205]. S , S_d and S_{ph} were deduced from two different references in the literature [6, 212].

6.3.3.2 Diagnostic test measurements for hysteretic behavior

After assessing the validity of our measurements on standard materials, we proceeded to measurements on the porous Si free standing membranes. The linearity and absence of hysteresis effect in the ΔV versus ΔT measurements was tested. In this respect, two different heating rates were used, namely 20mK/sec and 0.8mK/sec. Indicative results on the 40% porosity sample, are depicted in Figure 6.7, both by increasing and decreasing ΔT . From Figure 6.7 it is deduced that the two curves nicely coincide and there is no hysteresis effect between measurements obtained by increasing or decreasing ΔT . By using a linear fit to the two different sets of measurements, the S values of 804.7 μ V/K for the 20mK/sec heating rate and 791.2 μ V/K for the 0.8mK/sec heating rate, were obtained. The dispersion between the two values is only $\sim 1.7\%$. This is an indication that measurements with our system are accurate and do not exhibit any thermal or electrical contact problems.

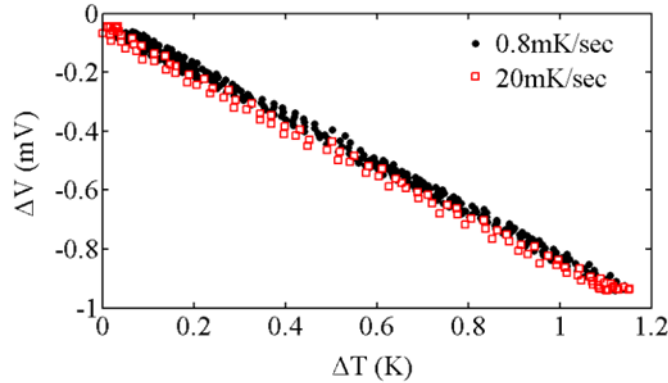


Figure 6.7: Testing for possible hysteretic behavior showing thermovoltage versus temperature difference for two heating rates, namely 20mK/sec (red open squares) and 0.8mK/sec (black dots). The two curves coincide, which is an indicator of good thermal contacts and absence of hysteresis effect.

An example of ΔV and ΔT versus time data, obtained with a 46% porosity sample, is given in Figure 6.8(a). In Figure 6.8(b) the ΔV versus ΔT curve is plotted, from which S is extracted using a linear fit to the data (see Figure 6.8(b)) (red line). A perfect linear fit is obtained, giving the value of $S=916.9\mu$ V/K.

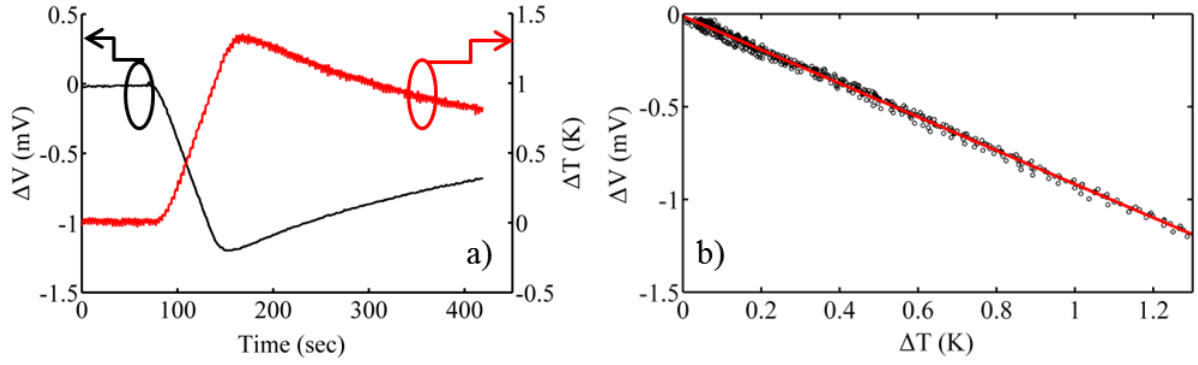


Figure 6.8: Example of experimental data for the 46% porosity sample depicting the thermovoltage and the temperature difference versus time (a) and ΔV versus ΔT curve (b), from which S is determined by a linear fit to the data. A perfect linear fit is achieved.

6.3.3.3 Comparison with simulations

The most critical parameters concerning the accuracy of the Seebeck coefficient metrology are the temperature and thermovoltage measurements to be taken at the same points of the thermoelectric material. In order to validate our measurements, we used transient thermal transport simulation using Comsol Multiphysics®, with experimental conditions used as input parameters. Convective heat flux was also considered, since the experiments were performed in the air. An example of simulation results of temporal dependence on temperature of the “cold” and “hot” sides compared to measured values is depicted in Figure 6.9(a), while the temperature distribution in the setup by applying $\sim 0.58\text{W}$ on the power resistor after 500sec is shown in Figure 6.9(b). For the simulations, we use the measured room temperature thermal conductivity of a 70% porosity porous Si membrane with dimensions $4.8 \times 2.8\text{mm}^2$ and thickness $140\mu\text{m}$. The thermal properties of all other materials of the simulated structure (plexiglas, copper, aluminum, plastic, air) were taken from the literature.

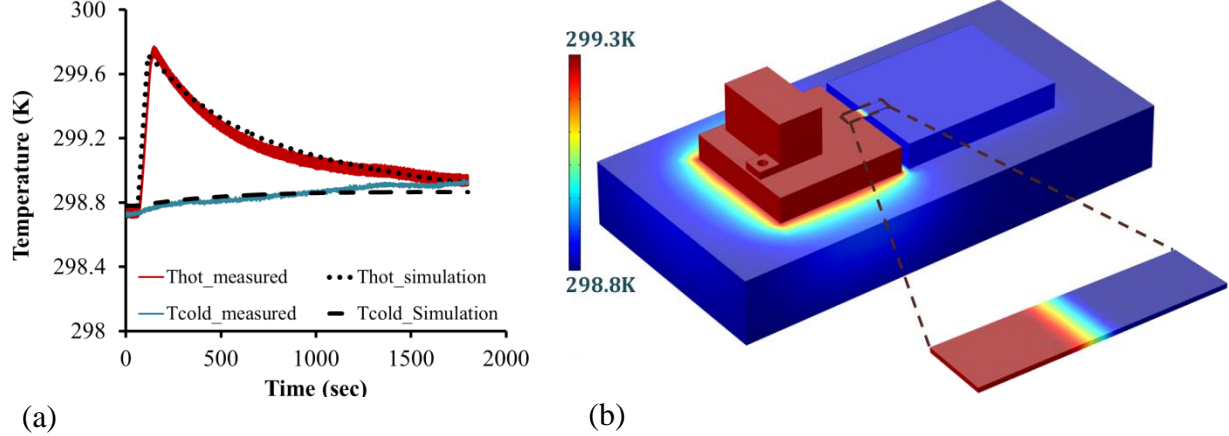


Figure 6.9: Simulation results of the time dependence of temperature on the “hot” and “cold” side of the sample compared to experimental values (a) and temperature distribution on the setup at $t=500\text{sec}$ (b).

As it can be seen, there is very good agreement between the measured temperature and the values obtained from simulations. This was the last validation test. Thus, in the following section the experimental results of porosity dependence of S for porous Si membranes is presented and discussed.

6.4 Experimental results – Porosity dependence of porous Si Seebeck coefficient

Table V summarizes the S values obtained for seven different porosity samples.

Table V: Porosity dependence of PSi Seebeck coefficient

Porosity (%)	40	46	51	55	63	70	84
S ($\mu\text{V/K}$)	781	917	1014	903	636	584	662

The measured S values of all PSi samples are positive, suggesting that electrical transport in the material is governed by hole transport. This is expected, if we consider that the starting Si wafer was p-type. Holes are due to boron impurities in the “mother” Si wafer. This result is controversial to that reported by Mathur et al. [203], who reported negative values of S for porous Si layers, formed also by anodization of p-type Si. However, our results agree in this respect with those reported by Yamamoto et al. [204] for porous Si layers formed on p-type c-Si wafer with resistivity $5\text{m}\Omega\cdot\text{cm}$.

The Seebeck coefficient as a function of porosity for all samples measured is plotted in Figure 6.10. The measured S value of crystalline Si (zero porosity) is also plotted for comparison. As stated above, unfortunately we were obliged to change the HF:ethanol ratio of the electrolyte for the higher porosity samples. The exact conditions of current density, electrolyte composition, anodization time and membrane thickness for all samples used in this work are summarized in Table III.

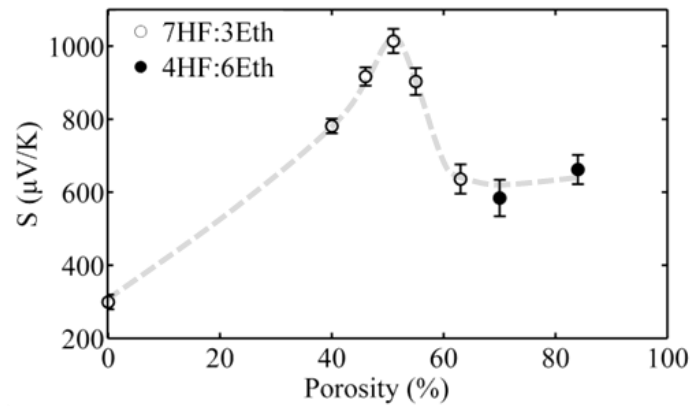


Figure 6.10: Seebeck Coefficient versus porosity of PSi membranes. The open circles correspond to the electrolyte with 70% HF concentration and the full ones with 40% HF concentration [205]. The dashed line is a guide to the eye.

From Figure 6.10, it is deduced that by increasing porosity, S increases up to a certain porosity value ($\sim 50\%$ porosity), and then decreases for higher porosities, and stabilizes at around $\sim 600\mu\text{V/K}$. The Seebeck coefficient of porous Si is in all cases is much higher than that of the corresponding bulk crystalline Si, used as starting material. A similar trend of the Seebeck coefficient versus porosity was reported by Yamamoto et al. [204] using also porous Si formed on highly doped p-type crystalline Si, but formed with an electrochemical solution slightly different than ours (composition 1HF:1Ethanol for all measurements). They also showed an increase in S with porosity up to a certain value and then a sharp decrease, however, the observed maximum was at a different porosity compared to our results. In addition, the decrease in S with porosity was more monotonous than in our case, where we see that S stabilizes at $\sim 600\mu\text{V/K}$ for all porosities above $\sim 60\%$ (see Figure 6.10). In order to explain our results, we have to consider the structure and morphology of the porous Si

samples as a function of porosity.

Porous Si has a very complex material structure and morphology. It is composed of interconnected Si nanowires and nanocrystals surrounded by a shell native oxide and separated by voids (pores). By increasing porosity, the complexity of the material increases. The ratio between nanowires, nanocrystals and pores composing the material changes with porosity. This ratio does not depend only on porosity, but also on the electrolyte used and the type and resistivity of the starting Si wafer. Multiple distinct phenomena are responsible for the porosity dependence of S . Apart from the increase of electrical resistivity with porosity due to carrier depletion, the interplay between energy filtering effect, phonon drag and boundary scattering determines the S dependence on porosity.

The difference in structure and morphology of our different porosity samples is at the origin of the observed complicated S variation with porosity. In general, the Seebeck effect arises from the diffusion of charge carriers along a temperature gradient and it is enhanced by the drag imposed to carriers from the accompanying diffusion of phonons. The thermoelectric power S is thus expressed as the sum of a diffusion part S_d and a phonon drag part S_{ph} (see Chapter 1). The diffusion part results from the spatial variation of the occupation probability of the carriers, caused by the temperature gradient along the sample, while the phonon drag part is due to momentum transfer from the phonon system to the electron one by electron-phonon scattering. In low dimensional semiconductors and porous media, different effects affect the above two factors. The low dimensionality of a porous material introduces quantum confinement and strong scattering effects, affecting carrier and phonon transport. Most authors in the literature attribute the large S in porous materials to the strong scattering in material boundaries, which is accompanied by energy filtering effects [201, 204, 213], resulting in S_d enhancement. Energy filtering results from the more efficient scattering of low energy carriers compared to high energy carriers. Consequently, the Seebeck coefficient, which measures an average energy of electrons contributing to electrical conductivity, is enhanced. The coupling between electrons and phonons, resulting in phonon drag, has to be also considered. There are limited data in the literature concerning phonon drag in low-dimensional systems.

In the case of our porous Si samples the low dimensionality of the material should be taken into account. Porous Si is a complex system, composed of a skeleton of interconnected nanowires and nanocrystals, separated by voids. These nanostructures are depleted from carriers, with carrier concentration decreasing with increasing porosity. At the lower porosities (below ~60%) the nanostructure size involved is relatively large (no confinement) and the material can be considered as bulk-like, so as $S = S_d + S_{ph}$. Both S_d and S_{ph} increase with decreasing doping concentration in the material. The observed S increase with porosity for porosities up to 60% can thus be attributed to the decrease in dopant concentration and the increasing internal surface area, which increases carrier scattering. For porosities above 60% the mechanisms involved are more complicated. Si nanowires and nanocrystals become very small and exhibit confinement effects. Their size and percentage in the material change non-monotonically with changing porosity. It is thus very difficult to separate the contribution of the different effects involved. The internal surface area is very large, contributing to very strong boundary scattering. There are interesting results in the literature concerning the Seebeck coefficient of Si nanowires and nanocrystals. Boukai et al. [41] studied highly doped individual Si nanowires of diameter 10 and 20 nm and reported an anomalous phonon drag enhancement at room temperature. A recent study on an array of Si nanowires with diameter ~ 100nm and doping concentration ~ 10^{19}cm^{-3} (surface roughness 0.4 nm) [212] contradicts the above and concludes that at 300K, boundary scattering of phonons in the specific highly doped Si nanowires completely quenches drag and reduces S . If we now consider Si nanocrystals, recent studies [214] demonstrated that in quite small nanocrystals, of diameter 2.4 nm, the thermopower was by one order of magnitude lower than in nanocrystals with sizes of 5.6 and 8.3 nm. It was also found that the 2.4 nm nanocrystals exhibited a three-fold

stronger coupling of carriers with LO and acoustic phonons, they were thus expected to show higher Seebeck coefficient, which was not the case. This discrepancy was attributed by the authors to strong scattering of phonons and likely reduction of phonon lifetime with decreasing nanocrystal size, resulting in much shorter carrier diffusion and reduced phonon drag, with corresponding reduction in thermopower.

Based on the above discussion, we conclude that the results presented in Figure 6.10 can be explained as follows: at low porosities, the increase in S with increasing porosity is due to the decreasing carrier concentration, resulting in both an increasing S_d due to energy filtering effects and an increasing S_{ph} . At higher porosities, the very strong increase in boundary scattering due to the decrease in nanowire and nanocrystal size, together with the confinement effects involved, result in reduced carrier diffusion and a quenching of phonon drag, with consequent reduction in the total S [205].

6.5 Conclusions

In conclusion, in this chapter we systematically measured the in-plane Seebeck coefficient of free-standing porous Si membranes with porosities 40-84% and anisotropic structure, comprising vertical pores and vertical Si nanowires, decorated with nanocrystals.

After describing the home-built setup used and assessing measurement validity and accuracy using different validation techniques, the experimental results on porosity dependence of porous Si Seebeck coefficient were presented. An increase in S with increasing porosity was observed, reaching a maximum value of $\sim 1\text{mV/K}$ at 51% porosity. Further increase of the porosity, lead to a sharp decrease in Seebeck coefficient, which stabilizes at a value of $\sim 600\mu\text{V/K}$. The initial increase in S with porosity is mainly attributed to energy filtering and phonon drag effects. At very high porosities, the material structure is more complicated. Scattering effects become very strong, but also carrier confinement is important, resulting in phonon drag quenching.

Considering that the final objective is to increase the zT of the porous Si membranes, our scope is to continue with the thermal and electrical conductivity measurements. However, due to carrier depletion, we expect the material to show low electrical conductivity and thus less competitive zT value. In this respect, the next step is to try to enhance this property by, for example, introducing metal nanoparticles in the porous Si network. A study on filling the pores with Nickel nanoparticles and nanowires has been already completed [215] and we are planning zT measurements to characterize such composite structures as thermoelectric materials.

Chapter 7

Thermoelectric performance of LPCVD polycrystalline Si thin films

In 1808, Humphry Davy proposed the name “silicium” for silicon because he believed it was a metal. Silicon was given its present name in 1817 by Thomas Thomson because he believed that it was a nonmetal similar to boron and carbon. In 1823, Berzelius prepared amorphous silicon and he is usually given credits for the element’s discovery. Si in its more common crystalline form was not prepared until 31 years later, by Deville. Nowadays, Si has a large impact on the modern world economy. Because Si is the most important element in high-technology devices, many places in the world bear its name. Silicon Valley in California, Silicon Fen in England, Silicon Glen in Scotland and Silicon Saxony in Germany are some of such examples.

<https://en.wikipedia.org/wiki/Silicon>

7.1 Introduction

In the frame of studying Si-based thermoelectrics, nanograined bulk-materials are attractive candidates [50], because it is a great challenge to incorporate high zT Si nanostructures, like Si nanowires and nanomeshes, in the mainstream planar CMOS configuration. Thus, nanocrystalline silicon is a promising alternative. A lot of research, both experimental [43, 64, 216] and theoretical [48, 217, 218], has been devoted to this subject the last years, while on-chip applications have already been published [53, 64].

The room temperature zT of thick doped polycrystalline silicon layers has been measured by many authors to be ~ 0.01 [219–221] while no significant enhancement was observed by Xie et al. by changing the doping concentration [222].

The low thermoelectric efficiency of polycrystalline Si is mainly attributed to its relatively high thermal conductivity. One way to decrease this parameter and enhance the overall thermoelectric performance of a thermoelectric material is to increase scattering sites within the material with the aim to inhibit thermal transport in its volume [223–225]. By reducing the grain size down to the nanometer scale in a polycrystalline material, grain boundary surface area increases significantly and consequently phonon-boundary scattering becomes important. The most easy, cheap and CMOS compatible way to reduce the grain size of polycrystalline Si is to decrease the thickness of the layer.

Therefore, in this chapter, a study on thickness dependence of zT of polycrystalline Si, deposited by LPCVD, is presented. After a brief introduction on polycrystalline Si and description of its fabrication using LPCVD, the polysilicon thin films fabricated in this thesis are presented and characterized using TEM imaging. Particularly, polycrystalline Si layers with thicknesses between 100–500nm are examined. The thickness dependence of each parameter influencing zT , namely electrical and thermal conductivity and Seebeck coefficient, is studied and compared to recent theoretical models found in the literature. In this respect, the test structures and methods used for each measurement are described.

By decreasing thickness down to 100 nm, an enhancement of the thermoelectric figure of merit is achieved, reaching a value as high as 0.033, which is three times higher than in the 500nm thick film. To our knowledge, there is very little work in the literature [64] on the thickness dependence of the thermoelectric properties and figure of merit of polycrystalline silicon thin films. This study strengthens the validity of recently reported theoretical models, while the enhancement of the zT with easy and fully compatible CMOS processes expands the potential of using polysilicon in effective, low cost, Si-based thermoelectrics.

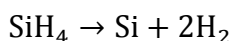
7.2 Polycrystalline Silicon

A polycrystalline material is composed of small crystallites of different crystallographic orientation, joined together by grain boundaries. The structure at the interior of each crystallite is close to that of bulk crystalline material; however, the grain boundaries show a complex structure. *Polycrystalline Si (polysilicon)* is composed of crystalline Si grains which are surrounded by grain boundaries. Polysilicon can be fabricated by different methods, the most commonly used being Low Pressure Chemical Vapor Deposition (LPCVD), which is the one used in this thesis and will be described in the following section.

7.2.1 Low Pressure Chemical Vapor Deposition (LPCVD)

Chemical Vapour Deposition (CVD) is a chemical process used to produce high quality, and high-performance solid thin films. The process is often used in semiconductor industry to produce thin films like polysilicon, silicon nitride and silicon dioxide. During this process, the substrate is placed in a deposition chamber, and the constituents of the film are delivered through the gas phase to its surface, where the film is formed. Frequently, volatile by-products are also produced, which are removed by gas flow through the reaction chamber. CVD has historically been used in integrated circuit technology, mainly for silicon and dielectric deposition. CVD is generally preferred because it forms good quality films with very good step coverage [226].

Silane is most often used for polysilicon deposition following the decomposition reaction:



The deposition temperature is relatively low (575-650°C) and the pressure between 0.2-1 torr. The use of low pressure improves uniformity and results in less gas usage. On the other hand, the reason for using low temperatures during the process is to minimize thermal budget of the substrate, reduce dopant diffusion and material degradation, create smoother and better adhering films and produce a material with relatively small grains [226].

All the thermoelectric parameters of polysilicon depend strongly on its micro-structure i.e. grain morphology and size, and dopant distribution. Thus, more details concerning grain growth, resulting grain sizes and the effect of doping are given below.

7.2.2 Microstructure of undoped polysilicon films deposited by LPCVD

The temperature, at which the deposition of silicon film takes place, is the dominant factor that determines the structure of the as-grown film. Below a certain temperature (~600°C), the grown silicon layer is amorphous, whereas above this temperature, it is polycrystalline. Usually the grains of the deposited film are columnar and in some cases grains are quite tall (depending on the thickness) and narrow. The average diameter at the top of the grains is often a little larger than at their bottom tips. Polysilicon films can show preferential crystallographic orientation, meaning that the majority of the grains are oriented or closely oriented to a specific orientation. For example, <110> is the most commonly observed grain orientation of textured polysilicon films prepared using typical polysilicon deposition conditions [226].

Silane pressure can also affect the microstructure of as-grown polysilicon films. Particularly, it has been shown that by reducing the pressure to a few mbar, the <110> texture with conical or columnar grains changes into a <100> oriented texture with larger grains. Thus, it is possible to obtain the same polysilicon film by adjusting temperature and pressure accordingly. For example, compensating the effect of a decreased pressure by lowering the deposition temperature, results in an unchanged microstructure of the deposited polysilicon film [227].

Table VI summarizes literature results on the average grain size of as-grown polysilicon films (500nm thick) deposited at different temperatures. In all cases referred in the table the average grain sizes were calculated using TEM images of the corresponding samples.

Table VI: Average grain size of as-grown polysilicon films of 500nm thickness deposited by LPCVD at different deposition temperatures by different groups.

Deposition temperature (°C)	Average grain size (nm)	Reference
560	5	[228]
570	9.5	[228]
580	14	[228]
600	23	[228]
600	53	[229]
620	31	[228]
625	87	[229]
640	40	[230]
650	72	[229]
675	74	[229]
700	73	[229]
725	86	[229]

From the table it is deduced that there is a discrepancy between grain sizes obtained by different groups, even at the same deposition temperature. The silane pressure, the used substrate on which the films are grown and the uncertainty introduced from the image processing of the TEM images are the basic parameters that could affect the observed microstructure of the films.

7.2.3 Microstructure of doped polysilicon films deposited by LPCVD

Polysilicon can be n-type or p-type-doped, either during the deposition process (in-situ) or ex-situ by implantation or diffusion. It is generally accepted that doping conditions significantly affect grain growth in both cases of doping. Doping by ion implantation followed by annealing though, gives more reproducible results [227] and thus it is preferred in integrated circuit technology.

High doping with phosphorus or arsenic significantly increases the grain size of as-deposited films. Any subsequent annealing also slightly increases the average grain size [226]. Generally, there is a significant increase in the grain growth rates for n-type dopants and quite moderate enhancement for the p-type dopants [230].

It should be mentioned, however, that the final size of the grains depends on all the aforementioned parameters and thus each formed polysilicon film should be investigated specifically, taking into account deposition and anneal temperatures, anneal time, dopants, impurities and film thickness.

7.2.4 Polysilicon grain growth

Grain growth is a process with driving force the minimization of “surface” energy. In the case of polysilicon, “surface” is either the surface of a grain or a grain boundary. Since the grain boundaries have higher energies compared to the intragrain region, the total energy of the system is reduced by increasing grain size, which results in reduced relative amount of grain boundary areas [226].

Generally, grain growth is distinguished in two mechanisms, namely *normal (primary)* grain growth and *abnormal (secondary)* grain growth. In the first case, the grain size distribution remains unimodal while in the latter case a bimodal distribution occurs during the process [231]. In the case of normal grain growth the transition of the grains is continuous, which means that the grains are growing from a large amount of tiny grains to a small amount of large grains. Figure 7.1 shows schematically the two grain growth mechanisms and the corresponding distribution of grain sizes, as they are observed in thin films.

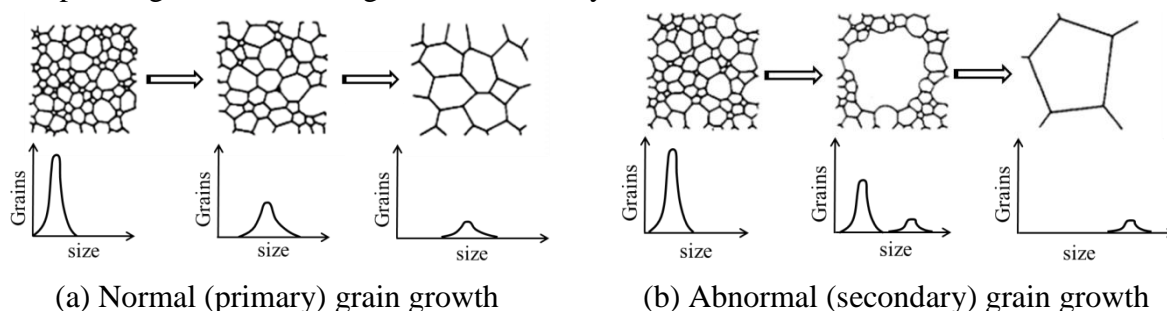


Figure 7.1: Schematic representation of a) normal and b) secondary grain growth and the corresponding grain size distribution in a thin film [232].

Polysilicon, however, is primarily growing via secondary grain growth. In this case, small grains continue to grow, but larger grains grow at much higher rates by consuming their neighboring grains. Practically, during the growth process larger grains coalesce with adjacent smaller grains to form secondary grains. This grain growth continues until the secondary grains consume all normal grains [230, 231].

7.3 Polycrystalline Si thin films studied in this thesis

After introducing the basics of the fabrication and morphology of LPCVD polysilicon films, we move to the description of the polysilicon films fabricated and studied in this thesis. Two different series of samples have been fabricated and all the thermoelectric parameters of the polysilicon thin films were measured. For the Seebeck coefficient and electrical resistivity measurements, polysilicon thin films were deposited on a quartz substrate, while for thermal conductivity measurements silicon substrate was used. In the following section there is a description of sample fabrication and the methods used to measure all the thermoelectric parameters needed to extract the zT of polysilicon thin films.

LPCVD polysilicon thin films with thicknesses between 100-500nm were deposited on both substrates at 610°C. Boron implantation followed, at a dose of 10^{16} and energy 60keV. The samples were annealed in nitrogen atmosphere at 1050°C for 30min in order to electrically activate dopants, obtain uniform doping profile and remove the implantation damage in the crystalline structure.

7.3.1 Structural characterization

As it was described previously, a number of parameters affect and determine the average grain size and the grain size distribution in polysilicon thin films. The structure of the samples was characterized using TEM cross sectional and plane view images. From the cross sectional view images we were able to understand the structure and specific morphology, as well as the shape of the grains in the film, while from the plane view images the average grain size was calculated, as well as the grain size distribution.

Figure 7.2 shows representative cross sectional images of the polysilicon samples studied in this work.

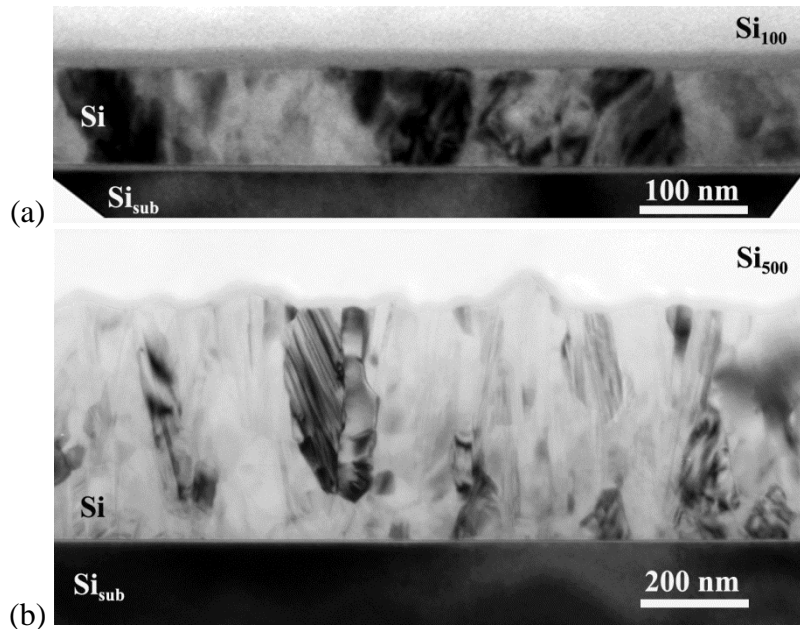


Figure 7.2: TEM cross sectional images of polysilicon thin films 100nm (a) and 500 nm (b) thick.

As it is expected, in both films grain size in z-axis is the same as the film thickness, namely 100 and 500nm respectively. The 500nm thick film is composed of conical grains, which are narrower at the bottom and widen as they grow up until they exceed the thickness of the film. On the other hand, the 100nm thick has more spherical grains, some of them being larger in the x plane compared to the thickness of the film, indicative of the secondary growth mechanism.

Figure 7.3 shows the corresponding top view bright and dark field TEM images of the polysilicon films shown in Figure 7.2.

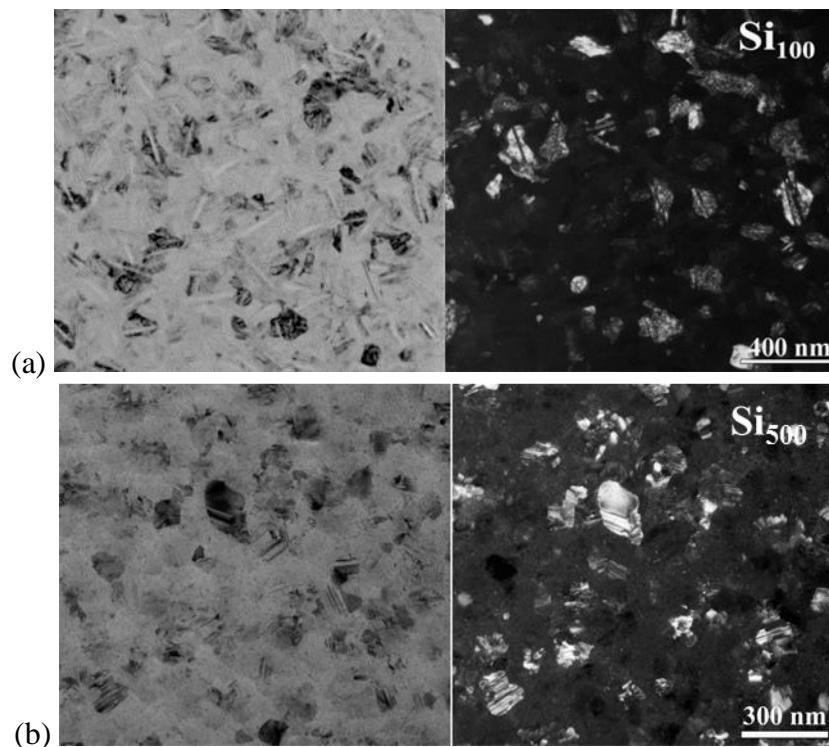


Figure 7.3: Plane view TEM images of the polysilicon films of thickness 100nm (a) and 500nm (b).

From such images the average grain size of each film, as well as the grain size distribution, were measured. More specifically, the mean grain size of the 100nm thick film was measured to be 70nm, while that of the 500nm thick film 112nm. As expected, the mean grain size

decreases with decreasing film thickness. The normalized grain size distribution obtained from plane view TEM images is shown in Figure 7.4.

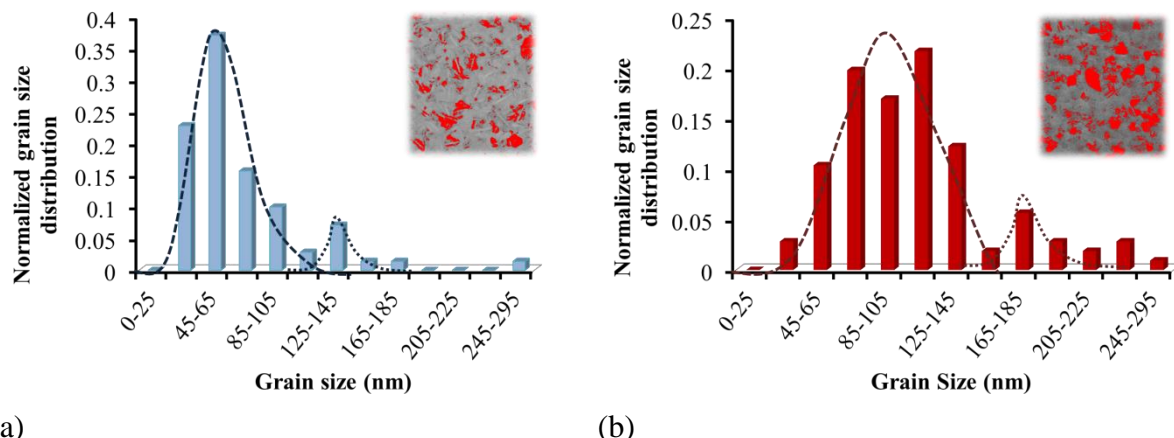


Figure 7.4: Normalized grain size distribution for 100nm (a) and 500nm (b) thick polysilicon layers, measured from plane view TEM images similar to those shown in Figure 7.2.

As it is deduced from Figure 7.4, while the mean value of grain size of the 100nm thick sample is 70nm, the majority of the grains have sizes between 25-65nm. This result is very useful for the interpretation of the measured thermoelectric properties of such film and particularly its thermal conductivity. Considering that the thermal transport of the material depends mainly on the dominant grain size, we used the experimental value of 50nm for the 100nm thick film in all the calculations in the experimental part of this chapter. This corresponds to the peak of the distribution shown on Figure 7.4a.

On the other hand, for the 500nm thick sample the average value of grain size was measured to be 112nm. This value coincides with the peak of the distribution shown in Figure 7.4b. In this film small grains still persist, but their number is limited, while grains with sizes as high as ~300nm co-exist with the smaller ones. It is also interesting to note that the distribution of grain sizes is narrower for the 100nm thick sample, while it is much wider in the case of the thickest film. Particularly, the 75% of the grains have sizes between 25-85nm in the thinner polysilicon film, while approximately the same percentage is extended between 45-145nm in the thicker one. Similarly, the corresponding grain sizes for the 200nm and 300nm thick films were obtained and summarized in table VII.

Table VII: Film thickness and corresponding average grain size of the polysilicon films studied

Film Thickness (nm)	Average grain size (nm)
100	50
200	90
300	100
500	112

The bimodal grain size distribution is obvious in both cases of the 100nm and 500nm films and it is indicative of the secondary grain growth mechanism, which results in the larger secondary grains observed in both cases. Similar results have been reported in the literature for phosphorus doped polysilicon films after annealing [231].

7.4 Electrical resistivity and TCR

7.4.1 Test structure

Quartz substrate was used for electrical resistivity measurements. The polysilicon films were grown on its surface under the conditions described in section 7.3. Then, Aluminum was deposited on the top and patterned with optical photolithography and wet chemical etching to form pads for the measurements. The samples were then annealed at 420°C for 30min. The aim was to form good Ohmic contacts in order to assure the accuracy of the measurements. Figure 7.5 shows a 3D schematic representation of the test structure used in this case.

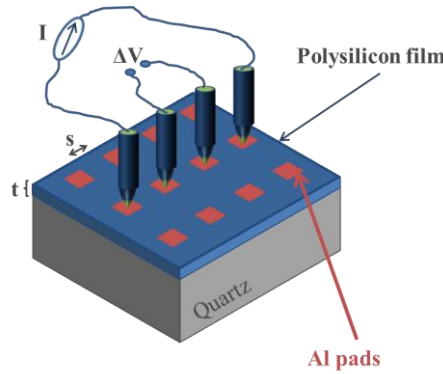


Figure 7.5: Test structure used for the electrical resistivity and TCR measurements.

7.4.2 Measurement method

Four point probe dc method was used for electrical resistivity and TCR measurements. As it is shown in Figure 7.5, a dc current is applied at the outer pads and the electrical potential is measured at the inner ones. For a thin semiconducting layer deposited on an insulating substrate and for equal probe spacing with $t < s/2$, where t : the thickness of the film and s : the distance between the pads, the resistivity of the layer is given by $\rho = 4.532t \frac{V}{I}$, where I is the applied current and V is the measured voltage [22]. More details for this method can be found in Chapter 1.

For the temperature measurements, the samples were placed in a He cryostat under vacuum in the whole temperature range 180 – 350K. The samples were placed on the chuck of the cryostat using thermally conductive and electrically insulating paste, durable at all studied temperatures.

7.4.3 Experimental results

7.4.3.1 Electrical resistivity

Figure 7.6(a) shows the experimental results of electrical resistivity of doped polysilicon thin films as a function of their thickness. The electrical resistivity of the films increases with decreasing their thickness. This is more pronounced below the thickness of 200nm. In general, the observed increase is mainly attributed to the additional scattering due to the smaller thickness of the layers, which also results in smaller grain size. This behavior is known for both boron [233] and phosphorus [234] LPCVD doped polysilicon layers and is mainly attributed to the decrease in the grain size of the samples. This fact is also observed in our samples and it can be seen in Figure 7.6(b), where the sheet resistance and grain size of the polysilicon films is depicted as a function of film thickness.

This is in consistency with the results reported by Lu [233], who showed quantitatively that the carrier trapping effect due to grain-size variation at different film thicknesses is the

dominant factor determining this behavior for their boron doped samples. However, this is inconsistent with Zhou et al. [64] who recently reported an almost constant value of electrical resistivity of all their studied samples with film thicknesses between 50-300nm. However, those authors mentioned neither the fabrication process of the polycrystalline thin films nor doping method used. No description of the morphology and grain size of their samples was mentioned. It is thus difficult to compare their results with ours. A direct comparison with those results is not applicable.

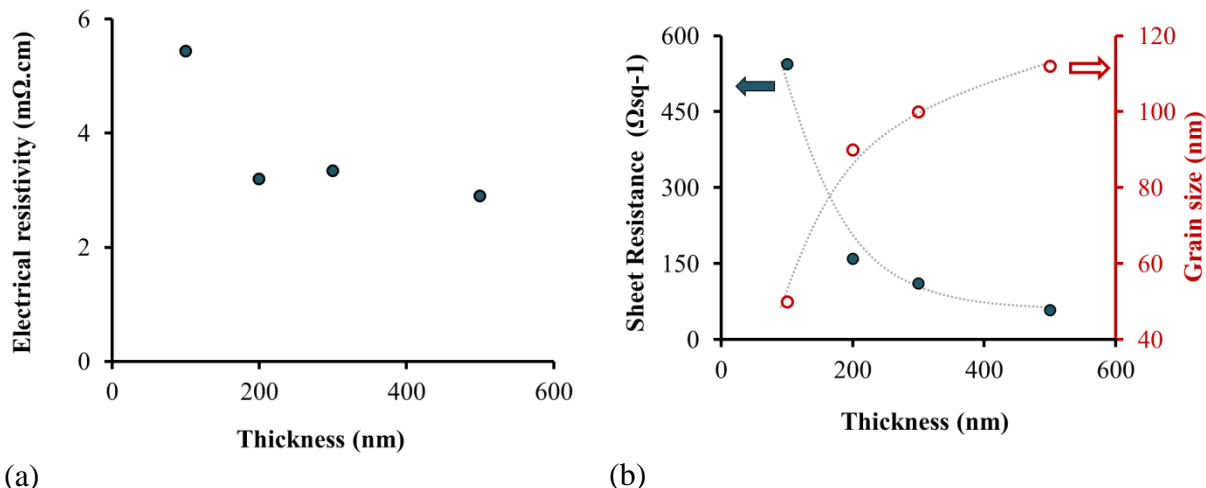


Figure 7.6 a) Experimental results of electrical resistivity of polysilicon thin films as a function of their thickness. The electrical resistivity of the samples increases with decreasing film thickness, following power law. **b)** Experimental results of sheet resistance and grain size as a function of film thickness.

7.4.3.2 TCR

We measured the temperature dependence of the 500nm thick polysilicon layer in the temperature range 180-340K [235]. Figure 7.7(a) shows normalized resistivity of the sample as a function of temperature. Taking values between 300-350K the Temperature Coefficient of Resistance (TCR) was obtained, from the slope of the curve depicted in Figure 7.7(b). The value is positive and is calculated to be $7 \cdot 10^{-4}/^{\circ}\text{K}$. The positive value of TCR indicates that TCR of 500nm thick polysilicon is determined by the TCR of the grain and not that of the grain boundary [236].

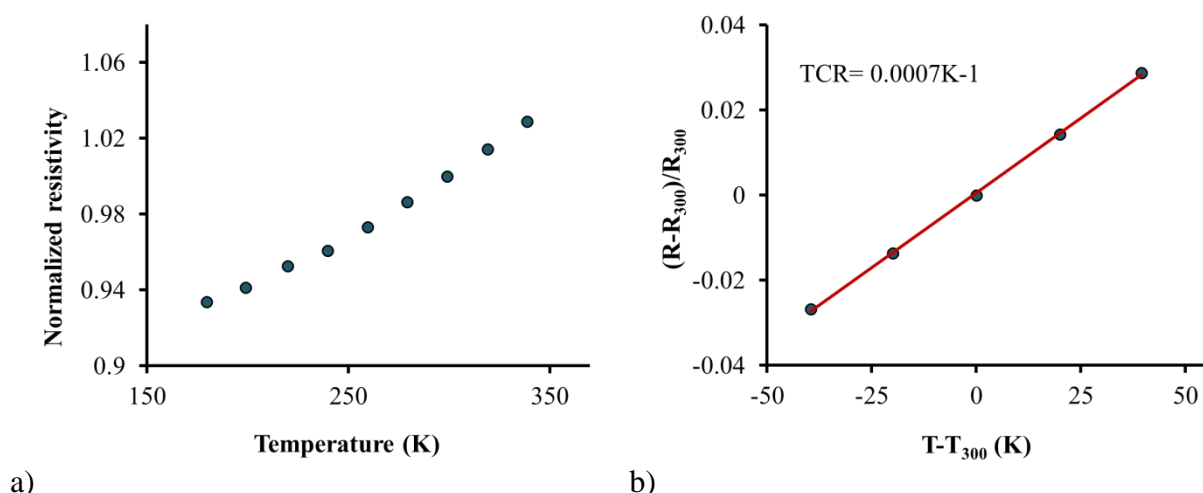


Figure 7.7: a) Normalized resistivity as a function of temperature for the 500nm thick polysilicon layer and **b)** resistance variation as a function of temperature difference for the same sample. From the slope of the curve, the TCR of 500nm thick polysilicon layer is extracted.

7.4.3.3 Comparison with theory

We used the physics-based compact model proposed by Spessot et al. [237] in order to fit the experimental data shown in Figure 7.7(a) in a least-squares sense and the results are depicted in Figure 7.8 [235].

Particularly, Spessot et al. considered the total polysilicon resistance as a series of intragrain (g) and Grain – Boundary (GB) resistances and proposed the following equation for the resistivity:

$$\rho_{TOT}(T) = \rho_g(T) + \rho_{GB}(T) = A \cdot T^{0.57} + B \cdot e^{(E_{eff}/kT)} \quad (7.1)$$

where ρ_{TOT} is the total resistivity, and A and B are fitting parameters, T is the temperature, E_{eff} is an effective energy barrier describing thermally activated hopping mechanism and k is the Boltzmann constant. We also let E_{eff} as an adjustable parameter, which was found to be $E_{eff} = 5meV$ to best fit the experimental results. The value obtained for the fitting is in agreement with the calculated values by Seto et al. [238] for this doping concentration ($\sim 3.9e^{19}cm^{-3}$). We have to mention here that Spessot et al. used the simplified expression of $\mu \propto T^{-0.57}$ for the hole mobility dependence on temperature in Equation (7.1), a relation which will be used again in the interpretation of the thickness dependence of Seebeck coefficient of polysilicon samples in our case.

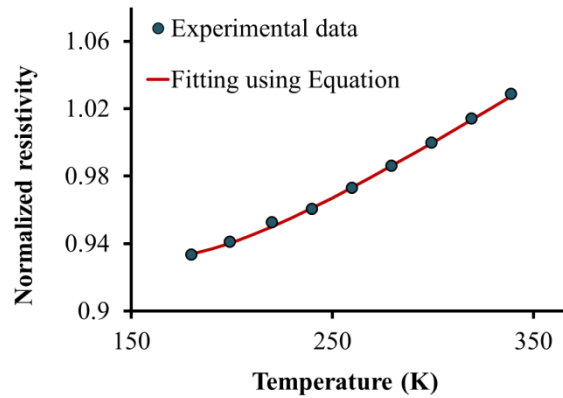


Figure 7.8: The full dots represent the experimental data shown in Figure 7.7(a), which were obtained using four point probe measurements for the 500nm thick polysilicon film. The line corresponds to the theoretical curve that best fits the measurements using least-square fitting and Equation (7.1).

It can be seen that there is a very good agreement between the experimental results and the temperature trend described by Equation (7.1). The thermally activated hopping mechanism taking into account the intragrain conductivity, can accurately describe the electrical properties of the material. Particularly, the fitting parameters were calculated to be $A=0.02$ and $B=0.4$, indicating that the dominant mechanism determining the electrical transport is the thermally activated hopping, while the intragrain resistance contributes much less.

7.5 Seebeck coefficient

7.5.1 Test structure

A quartz substrate of specific predefined dimensions was used for S measurements. The whole process was the same as the one described for the electrical resistivity measurements. Aluminum pads were also formed on the top of polysilicon films, but a two point configuration was used in this case. The test structure for S measurements is depicted in Figure 7.9. Each sample was placed on the home-built platform, which was described in detail

in section 6.3.1, so that Al pads were in contact with the copper plates. Silver paint was used to attach the samples on the platform and assure good electrical contacts.

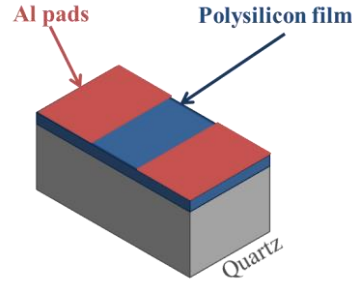


Figure 7.9: Schematic representation of the test structure fabricated for Seebeck coefficient measurements.

7.5.2 Measurement method

The differential quasi-steady-state two probe method was used for Seebeck Coefficient measurements [207] (see section 1.31 for the description of the method). In general, a plexiglas platform was used on which two thick Cu blocks were fixed. One of those blocks served as a “hot” contact and the other as a “cold” one. The sample under test was placed between the two copper blocks as a bridge. A temperature difference (ΔT) was created between the two ends of the sample and the resulting thermovoltage (ΔV) was measured. The Seebeck coefficient was then extracted from the slope of the ΔV versus ΔT curves for temperature differences below 1.5K. More details about the whole setup and the data analysis were given in chapter 6.3. All the validation techniques described there, were again tested before each measurement.

All the measurements were taken at room temperatures ($\sim 21^\circ\text{C} = 294\text{K}$). In order to extract the temperature of the sensors, the prototype DIN IEC 751 between 0-850 $^\circ\text{C}$ was used together with the equation $R_T = R_0(1 + A \cdot T + B \cdot T^2)$, where $A = 3.9083 \cdot 10^{-3} \text{ }^\circ\text{C}^{-1}$ and $B = -5.775 \cdot 10^{-7} \text{ }^\circ\text{C}^{-1}$.

7.5.3 Experimental results

Figure 7.10 shows the experimental results of room temperature Seebeck coefficient of the polysilicon thin films as a function of their thickness. In consistency with the electrical resistivity measurements, it is observed that Seebeck coefficient increases as the film thickness decreases [235].

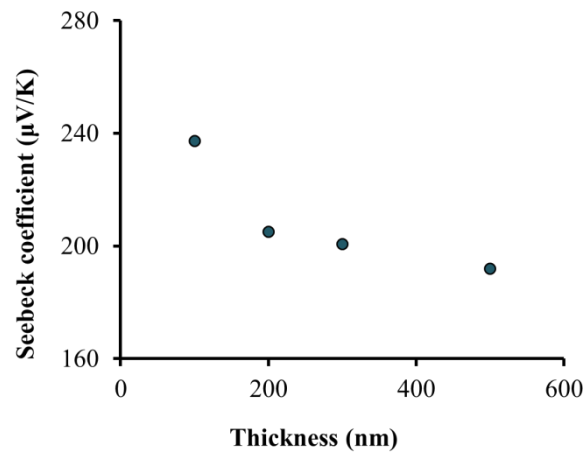


Figure 7.10: Experimental results of Seebeck coefficient of the polysilicon thin films as a function of their thickness. The Seebeck coefficient of the samples increases with decreasing film thickness.

7.5.3.1 Comparison with theory

It is a general rule that, in doped semiconductors and metals, the higher the carrier concentration, the lower the thermopower (see also section 1.4). This relation is attributed to Pisarenko in the book “Physics of Semiconductors” by A.F. Ioffe [239].

Ioffe considered separately the phenomena taking place in the bulk of a semiconductor and at its boundaries to calculate the total thermopower induced at the ends of a rod, where a temperature gradient exists. He concluded that the potential difference produced by gradients in concentration in the bulk is balanced by the difference of the contact potential at its boundaries. Thus, the experimentally observed thermal electromotive force is not related to the temperature dependence of the concentration of the free carriers. Contrary, only their absolute concentration in the material appears in the equation, which describes the total observed thermopower [239].

Particularly, Ioffe calculated the thermal electromotive force for non-degenerated semiconductors and derived the so-called Pisarenko formula for a semiconductor with current carriers of only one type [239]:

$$S = \frac{k_B}{e} \left[A + \ln \left(\frac{2(2\pi m^* k_B T)^{\frac{3}{2}} e \mu}{h^3} \right) - \ln(\sigma) \right] \quad (7.2)$$

where k_B is the Boltzmann constant, e the electronic charge, $A = r + 2$ with r being the scattering parameter, m^* is the DOS effective mass of carriers, T the absolute temperature, μ the mobility of carriers, h the Planck's constant and σ the electrical conductivity.

We used the above expression to fit our experimental results of S as a function of electrical conductivity. A was extracted from the temperature dependence of the effective mobility mentioned before [237, 239] and was set to be 1.93. For the DOS hole effective mass, the value $m^* = 1.15m_0$ was used (where m_0 is the free electron mass) [240], while μ was set as fitting parameter to our experimental results and a value of $92 \text{ cm}^2 \text{ V}^{-1} \text{ s}^{-1}$ was obtained. Figure 7.11 shows the experimental results and the curve corresponding to best fit of the results. As it can be seen, our experimental results are nicely described by the Pisarenko plot.

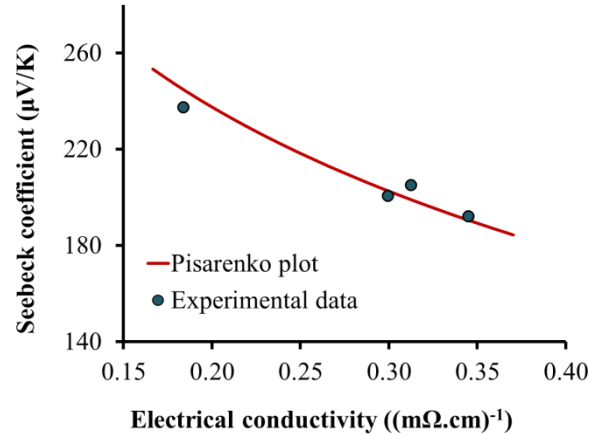


Figure 7.11: Experimental results of Seebeck Coefficient of polysilicon thin films as a function of their electrical conductivity. The experimental data follow the so called Pisarenko formula.

For the calculation using Equation (7.2), we assumed that the mobility is not appreciably affected at these doping concentrations [235]. This is a good approximation, as it has been proved theoretically [218] and experimentally [241] for the range of grain sizes studied in this work. Particularly, the obtained value for the effective mobility is slightly higher than that of the doped bulk c-Si [242] but in agreement with recently reported experimental values of 200nm thick LPCVD polysilicon films [216]. We should note, however, that carrier concentration determined by considering the doping concentration in bulk Si is not the same

as in polysilicon, due to carrier depletion caused by the built-in potential at grain boundaries. The effective doping concentration to be considered is thus different. In addition, in large grain polysilicon, as is the case of our 500nm sample, the free carrier concentration in the depletion layer, caused by the built-in potential at grain boundaries, can be appreciable. Using the depletion approximation leads to inaccurate values of the barrier heights. The mobility is exponentially dependent on barrier height, so as any inaccuracy in the calculated potential barrier height strongly affects the calculated mobility values.

7.6 Thermal conductivity

7.6.1 Test structure

A second series of samples was fabricated for thermal conductivity measurements. A lightly doped p-type silicon substrate with resistivity 5-6 Ω .cm was used in this respect. A 5nm thick SiO₂ layer was thermally grown at 900°C before polysilicon thin film deposition. Boron implantation and annealing of the samples was followed using the same conditions as those described in section 7.3, for both processes. A second SiO₂ layer, 10nm thick, was thermally grown on the polysilicon thin films and then platinum was deposited on top and patterned using optical photolithography and lift off process. A similar sample without the polysilicon layer was prepared and used as a reference. Figure 7.12 shows a schematic representation of this series of samples.

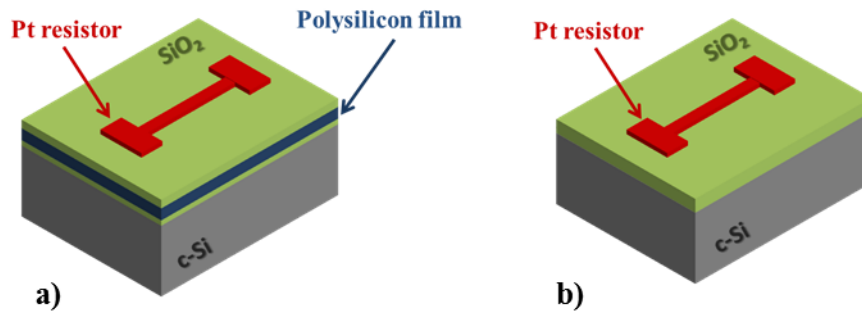


Figure 7.12: 3D schematic representation of the test structures used for thermal conductivity measurements. In a) the sample which incorporates the polysilicon thin film to be characterized is depicted, while in b) the reference sample is shown

7.6.2 Measurement method

The differential 3ω two point probe method with Wheatstone bridge as a cancellation technique was used for thermal conductivity measurements. At this point we summarize briefly that for the implementation of this method an alternative current (ac) at frequency ω is applied on the Pt resistor and the resulting small voltage oscillations at the third harmonic, 3ω , are measured using a lock-in amplifier. The temperature coefficient of resistance (TCR) of the platinum film at room temperature (section 3.5.2) was then used to calculate the temperature oscillations on the heater. The temperature drop, ΔT_f , through the thickness of the polysilicon film was determined by comparing the polysilicon sample (Figure 7.12a) with the reference one (Figure 7.12(b)). The condition “film thicknesses ($t=100\text{-}500\text{nm}$) far smaller than the width of the heater ($w=20\mu\text{m}$)” was fulfilled for all film thicknesses and thus Equation (3.73) could be used, which is written again here for simplicity:

$$k_f = \frac{p_{rms} \cdot t}{\Delta T_f \cdot 2b} \quad (3.73)$$

More details concerning this method and its implementation for thin film thermal conductivity measurements can be found in section 3.6.4.

7.6.3 Experimental results

Before obtaining the results of thermal conductivity, the method's validity was again tested, as in section 3.6.4. Figure 7.13(a) shows an example of measured $V_{3\omega}$ as a function of I^3 for the 500nm thick sample, while 7.14(b) shows an example of measurements on the reference sample from the slope of which the thermal conductivity of Si was obtained. A value of 146.4W/m.K was measured, which is in an excellent agreement with the value that can be found in the literature for bulk c-Si at room temperature. The linear dependence shown in Figure 7.13(a) and the measured k value of Si demonstrate the validity of the measurement technique.

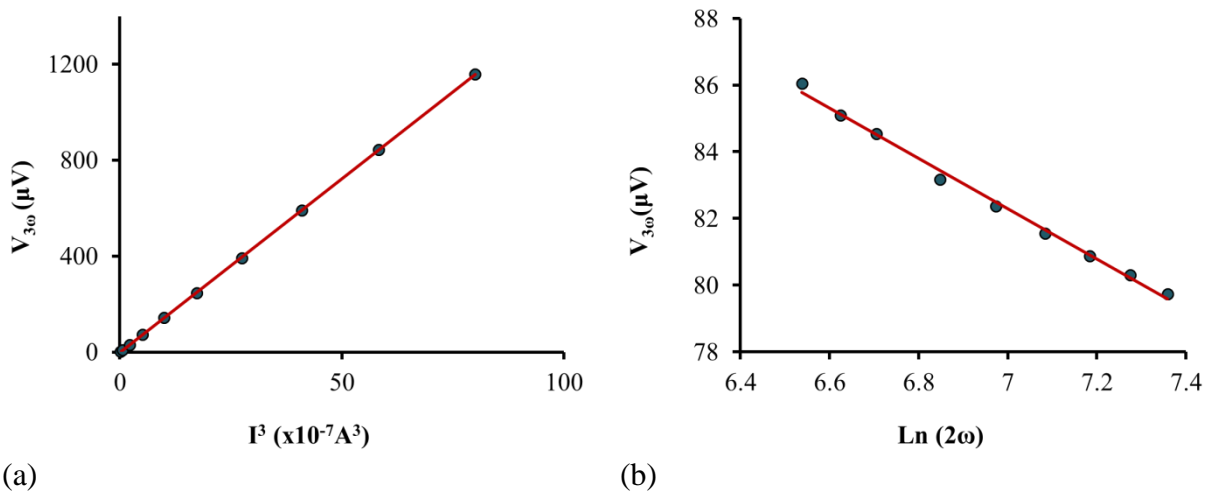


Figure 7.13: a) Third harmonic of voltage as a function of the cubic amplitude of the applied current and b) third harmonic of voltage as a function of frequency from the slope of which the thermal conductivity of bulk c-Si was extracted. The graph corresponds to an applied power of 10mW on the Pt heater of the reference sample.

Figure 7.14 shows the experimental results of thermal conductivity of polysilicon thin films as a function of their thickness.

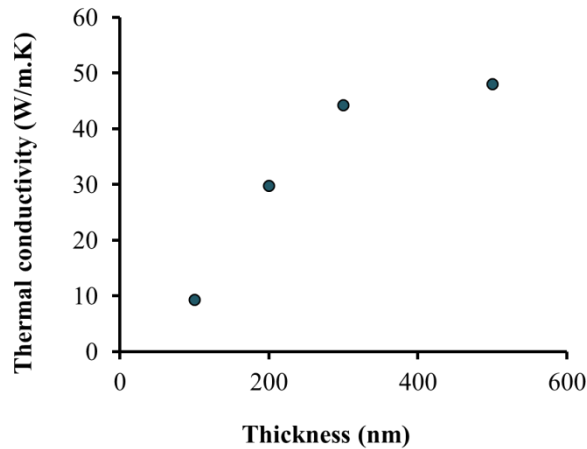


Figure 7.14: Experimental results of thermal conductivity of polysilicon thin films as a function of their thickness, measured using the 3ω differential method. The experimental data show a sharp reduction in the thermal conductivity with decreasing film thickness below 300nm

As it was experimentally shown and explained using existing theoretical models, both

electrical conductivity and Seebeck coefficient dependence on polysilicon film thickness is determined by the morphology of the films and particularly by the grain size and the intragrain region. This is exactly what is determining the thermal conductivity of the films, as our experimental results indicate. As it is shown in Figure 7.14, all the values are measured to be much lower than that of single crystal Si ($k_0 = 146 \text{ W/m.K}$), as it was expected, with the 100nm thick sample showing more than an order of magnitude reduction. Our 500nm thick polysilicon film has a thermal conductivity of 48 W/m.K , in agreement with McConnell et al. [243] and the 300nm thick layer shows a value of 44.3 W/m.K consistently with M. von Arx et al. [244]. However, thermal conductivity is strongly dependent on the fabrication process, film thickness, doping type and concentration, grain sizes and their distribution and thus there is a variation of thermal conductivity measurements in the literature.

7.6.4 Comparison with theory

At present, it is quite generally accepted that the thermal conductivity of polycrystalline materials decreases with decreasing grain size [245]. Phonon-phonon scattering and scattering at surfaces, grain boundaries, impurity atoms, free carriers, point defects and imperfections in the crystal are supposed to be at the origin of this reduction. Particularly, in our case the model recently proposed by Dong et al. [224], incorporating both the thermal resistance from grain boundaries (Kapitza resistance R_k/d) and size effects (intragranular thermal resistance R_{intra}) to obtain total lattice thermal conductivity of nanocrystalline materials, is proved accurate to describe the measurements. Dong et al. conclude in the following analytical expression, calculating thermal conductivity as a function of grain size of nanocrystalline materials:

$$k = \frac{k_0/(1 + l_0/d^a)}{1 + [R_k(k_0/(1 + l_0/d^a))]/d} \quad (7.3)$$

where, k thermal conductivity of a nanocrystalline material (W/m.K), k_0 single crystal thermal conductivity (W/m.K), l_0 single crystal phonon mean free path (PMFP) (nm), d grain size (nm), a an affirmatory exponent ranging between $1/2$ and $3/4$ and R_k the Kapitza resistance ($\text{m}^2\text{K/W}$).

Although the electronic part of thermal conductivity in such doping levels is small enough, we calculated it, using Wiedemann-Franz law [243] (Equation 1.21) and the electrical resistivity measurements, and we thus extracted the lattice thermal conductivity of the samples. Then, we used Equation (7.3) with a and R_k as adjustable parameters to fit our experimental results of lattice thermal conductivity versus grain size of the polysilicon films. For the corresponding single crystal values, we used $k_0 = 146 \text{ W/m.K}$, which was obtained using the 3ω method and $l_0 = 300 \text{ nm}$, taken from the literature [246]. Figure 7.15(a) shows the experimental results and the fitting curve using the above equation, while experimental results of polycrystalline silicon from the literature are also presented for comparison.

Values of $a = 0.75$ and $R_k = 1.95e^{-9} \text{ m}^2\text{K/W}$ were obtained for the fitting of Equation (7.3) to our experimental results. The value of a was found to be 0.75, while the Kapitza resistance value is in a very good agreement to calculated values of Moldovan [223] for these grain sizes. Although the fitting was made using our experimental results, as it can be seen in the Figure 7.15 the fitting curve agrees well also with the experimental values obtained by Wang et al.[217] and McConnell et al.[243]. As it was mentioned before, this theoretical model assumes that the total thermal resistance of the polysilicon layer R_t is the sum of intergrain and intragrain thermal resistances, thus $R_t = R_k/d + R_{intra}$. In order to get an idea about the relative contribution of each component to the total lattice thermal conductivity of the samples, their ratio to R_t , was calculated and presented in Figure 7.15(b). The shadowed part of the graph corresponds to the studied grain sizes of our polysilicon thin films. As it can be seen, the contribution of intragrain resistance increases from 0.15 to 0.28 as the grain size

increases from 50 to 112nm. Consequently, we observe that the intragrain thermal resistance increases with increasing the mean grain size, as it was also shown in the case of the electrical resistance of the films. Although grain boundary scattering is still the dominant scattering parameter, the intragrain resistance plays an important role in the reduced values of lattice thermal conductivity compared to single crystalline Si [235].

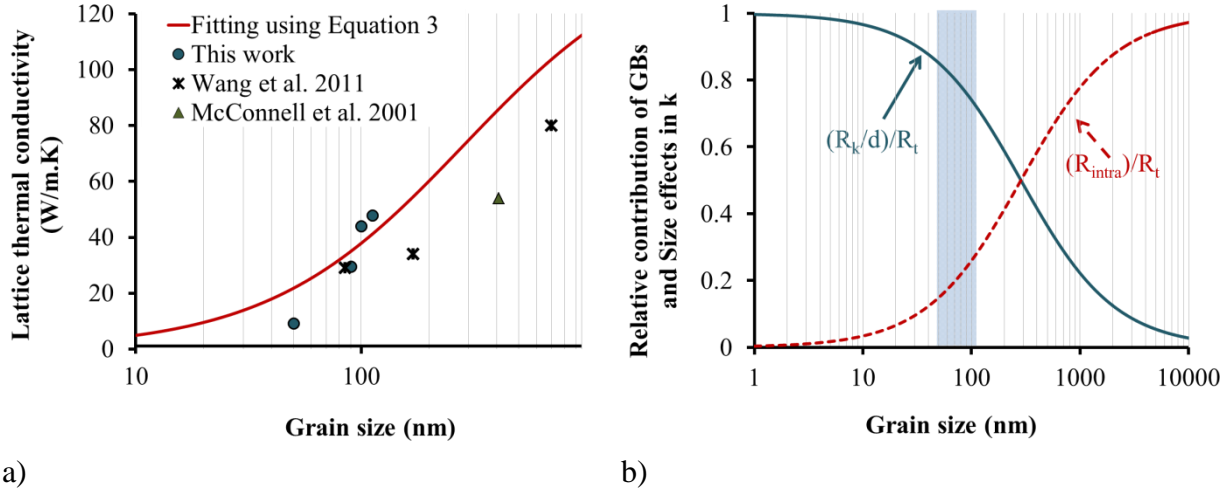


Figure 7.15: a) Experimental results of thermal conductivity of polysilicon thin films as a function of their mean grain size compared to values found in the literature b) Relative contribution of each of the inter and intragrain thermal resistances to the total thermal resistance as a function of the mean grain size. The experimental data are in very good agreement with the theoretical model proposed by Dong et al.[224]

7.7 Power factor & Figure of merit

Having measured and discussed all the thermoelectric parameters of the thin polysilicon layers, the power factor and the thermoelectric figure of merit zT of the polysilicon thin films were obtained and are summarized in Figure 7.16(a) and (b) respectively [235].

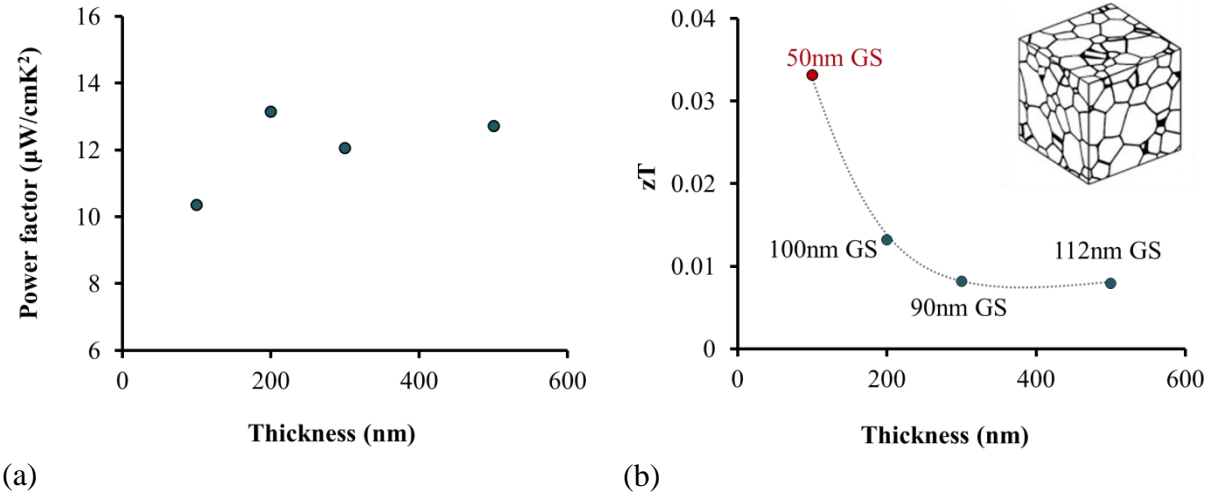


Figure 7.16: a) Power factor and b) zT of polysilicon thin films as a function of their thickness. In b) the corresponding grain sizes (GS) are also indicated.

Two basic remarks must be made at this point: 1) the power factor of the samples does not follow the zT trend as a function of film thickness and 2) a threefold increase was obtained for the room temperature zT of the films by just reducing the film thickness down to 100nm.

Regarding the first point, it is very important to comment that by considering only the power factor, which is commonly used by many authors to characterize thermoelectric materials, may lead to erroneous interpretation of the overall thermoelectric performance of the material. Thermal conductivity is a key parameter, which can potentially change the

thermoelectric profile of the material, as our measurements indicate. Particularly, the 100nm thick polysilicon film shows the lower power factor, while its zT is measured to be more than three times higher than that of the 500nm thick layer. While S and ρ did not show any significant change with the reduction of the film thickness (thus the power factor is almost constant), thermal conductivity decreased sharply, leading to this high zT value of 0.033.

Figure 7.16(b) shows that zT increases logarithmically by decreasing film thickness and practically by decreasing the grain size of the samples. Above 300nm, zT seems to reach a plateau at ~ 0.01 , while below 200nm there is a sharp increase in the zT of the samples. The high zT of the thinnest layer is comparable to p-doped polysilicon thin films with phononic crystal nanopatterning that have recently been reported [247]. However, the process that Nomura et al. followed for the fabrication of the samples is much more expensive. We achieved this result by just reducing the thickness of the film, without using expensive equipment and processes or rare and exotic materials. A fully compatible CMOS process was followed. Thin doped nanocrystalline silicon films were demonstrated as an attractive candidate for the fabrication of integrated thermoelectric devices on the Si wafer [235].

7.8 Comparison with other works on polysilicon films found in the literature

The zT of the polysilicon films studied in this chapter was also compared to that of other boron doped LPCVD polysilicon layers that can be found in the literature. The results are summarized in Figure 7.17.

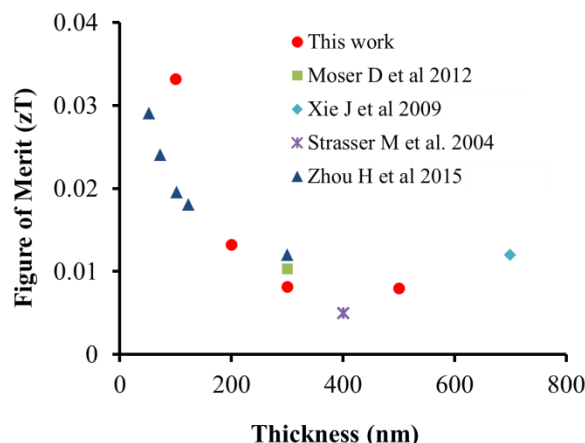


Figure 7.17: Thermoelectric figure of merit of p-type polysilicon thin films of this work in comparison with other values found in the literature. (circles (this work), rectangles (Moser et al. [221]), rhombus (Xie et al. [248]), stars (Strasser et al. [219]) and triangles (Zhou et al.[64]).

As it is deduced from the Figure above 7.17, the obtained zT values in this work are in a good agreement with all the reported values found in the literature, while our 100nm thick sample shows slightly higher value than any other p-type polysilicon film reported so far. Another interesting point is that most authors study only thick layers and until very recently there was no other systematic study of thickness dependence of zT of polysilicon films. In fact, only Zhou et al. [64] made a similar study very recently, but as it was mentioned earlier, the fabrication process of their polysilicon samples was not specified. In any case, the measured zT value of 0.033 of our 100nm thick boron doped LPCVD polysilicon film is a competitive result in the area of room temperature Si-based thermoelectrics.

7.9 Conclusions

In conclusion, in this chapter the basics of LPCVD polysilicon thin film fabrication were introduced, while an accurate and systematical study of all thermoelectric properties of boron-doped LPCVD polycrystalline silicon thin films as a function of their thickness was presented. It was shown that for thicknesses below 200nm, there is a sharp increase in zT due to the decrease of the mean grain size down to 50nm and thus the strong reduction of thermal conductivity. A threefold increase of zT was obtained for this sample. It was proved experimentally and using known theoretical models that all the thermoelectric parameters (S , ρ , k) are strongly dependent on the grain size and the intragrain region of the films. It was shown that, although the intragrain region contributes less to both the electrical and the thermal properties of the films, it affects significant the electrical and thermal transport in the film. Our study strengthens the validity of recently reported theoretical models, while the enhancement of the zT with easy and fully compatible CMOS processes expands the potential of using polysilicon in Si-based, low cost thermoelectrics.

Conclusions

The basic conclusions of this thesis are briefly summarized in the following points:

- ✓ A literature review on Si-based thermoelectrics and thermal devices was performed, which revealed the interest of the field in applications.
- ✓ Thermal conductivity of porous Si layers (porosity 63% and 70% respectively), with both isotropic & anisotropic structure, was measured in the temperature range 4.2-350K. A plateau-like dependence with temperature was obtained, which is followed by a monotonic increase of thermal conductivity with temperature. This behavior is commonly observed in glasses and disordered materials and it is attributed to the specific structure and morphology of PSi. By characterizing its fractal nature and determining the fractal dimension of both PSi layers studied to be lower than 2, the fracton model was adopted for the interpretation of the $k(T)$ temperature dependence at cryogenic temperatures, while for temperatures above ~200K the simplified phonon diffusion model was proved to be adequate to explain the experimental results. These results show similar temperature dependence to that of the specific heat capacity.
- ✓ The 3ω and DC methods were used to measure the thermal conductivity of PSi and the corresponding results were compared and discussed. The 3ω method was proved to overestimate the values of thermal conductivity. Two improved approaches were proposed for the extraction of thermal conductivity by the frequency dependence of the small third harmonic voltage signals, which are compared to each other and to the well-known slope method, first introduced by Cahill.
- ✓ Porous Si thermal conductivity was measured to be much lower than that of bulk c-Si, while it was also lower than or comparable to that of other known CMOS compatible low thermal conductivity materials, like silicon dioxide and silicon nitride. Phonon-phonon scattering, phonon-boundary scattering at the large internal surface area of PSi and the existence of air (voids) within the material are supposed to be at the origin of this strong reduction of its thermal conductivity compared to that of bulk crystalline Si.
- ✓ The PSi sample with anisotropic structure was measured to have slightly higher thermal conductivity compared to that of the film with the isotropic structure. This indicates that the morphology and structure of porous Si, and not only its porosity, determine its thermal behavior in response to a thermal stimulus.
- ✓ Based on the measured low k values and FEM simulations, PSi layers were demonstrated to constitute an excellent platform for local thermal isolation on the Si wafer. Its effectiveness for local thermal isolation was assessed, based mainly on the results taken at low temperatures. It was shown that on PSi locally formed on the Si wafer, it is possible to achieve a significant temperature increase with the application of very low electric power. This temperature increase is locally limited, while on bulk Si the temperature is kept at room temperature. This result is very important towards the on-chip integration of efficient thermoelectric and thermal devices.
- ✓ Room temperature Seebeck coefficient of porous Si was also studied as a function of porosity. Free standing PSi membranes with porosities between 40-84% were systematically measured using the fabricated home-built setup. Values as high as 1mV/K were obtained for intermediate porosities, while a further increase of porosity leads to a sharp S reduction due to strong boundary scattering. This phenomenon suppresses phonon drag effect, which, at lower porosities, is supposed to contribute significantly, together with energy filtering, to the measured high S values of PSi. The interpretation of these results is also supported by photoluminescence measurements

and SEM and TEM characterization.

- ✓ All thermoelectric properties of boron doped polycrystalline Si thin films of different thickness, down to 100nm, were fully and accurately measured and the effect of decreasing layer thickness down to 100 nm on the thermoelectric properties was assessed. A significant increase of zT by decreasing layer thickness below ~200 nm was observed (threefold increase), the obtained value being equal to 0.033 for the zT of the 100nm thick polysilicon layer, which is the highest reported in the literature so far for boron doped LPCVD polysilicon at room temperature. This increase in zT is attributed to the reduction in grain size of the material with decreasing thickness, which leads to a decrease of thermal conductivity due to an increase in phonon - grain boundary scattering and other size effects. All the thermoelectric parameters of polysilicon films and their dependence on grain size and thickness were fitted using recently reported theoretical models and a good agreement was found. Our measurements strengthen the validity of these models and contribute to the understanding of the electrical and thermal transport mechanisms in nano-grained materials.
- ✓ The power factor of polysilicon thin films does not follow the same dependence on film thickness as the zT . This means that by measuring only the power factor of a thermoelectric material, without exactly determining the thermal conductivity of the same material, as many authors do, an erroneous result concerning its overall thermoelectric performance could be obtained. Thermal conductivity is demonstrated to be a key parameter in the thermoelectric characterization of a material.

Perspectives

The outcome of this research opens important new possibilities in the field of Si-based thermoelectrics. More specifically:

- The 100nm thick polysilicon film can be used as thermoelectric material in a improved performance thermal or thermoelectric devices
- Additional nanostructuration of the developed polysilicon thin films can be used for further reducing thermal conductivity and increasing zT
- Porous Si has been proved to constitute an excellent platform for local thermal isolation on a Si wafer. A large number of applications using this property can be developed, including thermal sensors and thermoelectrics
- The low thermal conductivity of porous Si is an interesting property. If its electrical conductivity is improved, one should envisage developing porous Si also as a thermoelectric material. One idea that we propose is the incorporation of metal nanoparticles into the pores, in order to improve its electrical conductivity. Care should be taken to keep thermal conductivity as low as possible.

Résumé Long

Introduction

Le domaine de la thermoélectricité est un domaine de recherche qui évolue rapidement ces dernières années à cause de la nécessité urgente de trouver des sources d'énergie alternatives et résoudre les problèmes énergétiques actuels. La production d'énergie en utilisant les différences de température existantes stimule la communauté de recherche pour trouver des dispositifs thermoélectriques qui peuvent transformer de façon efficace cette différence en énergie électrique. Malgré le fait que les dispositifs existants ont un faible rendement, l'objectif d'utiliser l'énergie thermique globale pour produire de l'énergie utilisable, continue de constituer un objectif important et constitue l'objet principal de cette thèse.

Dans la recherche de dispositifs utilisant des matériaux disponibles et durables, les nanostructures de Si constituent un choix préférentiel. Mis à part le principal avantage qui est leur abondance, l'autre avantage évident est leur intégrabilité avec des dispositifs et circuits intégrés microélectroniques, qui constituent la base des systèmes d'information à semi-conducteurs.

Cette thèse a été consacrée à l'étude de deux systèmes utilisant des nanostructures à base de Si, qui sont intéressants pour la fabrication de générateurs thermoélectriques : le Si poreux et le Si nanocristallin en forme de film mince.

Le Si poreux est un matériau nanostructuré qui peut se former par dissolution électrochimique de Si, cette technique étant massive, à faible coût et compatible avec les technologies CMOS de fabrication de circuits intégrés à base de silicium. Ces propriétés sont ajustables par les conditions électrochimiques de fabrication utilisées. Le Si poreux, matériau à faible conductivité thermique, a été étudié et utilisé comme substrat local sur plaquette de Si pour l'intégration de capteurs thermiques et de générateurs thermoélectriques.

Le group Nano4NPS de NCSR Demokritos (<http://nano4nps.imel.demokritos.gr/>), a une longue expérience et expertise sur des dispositifs thermiques et thermoélectriques utilisant le Si poreux. Cette connaissance de base a été utilisée et développée davantage dans cette thèse dans l'objectif d'améliorer la performance de dispositifs existant et de comprendre en profondeur les propriétés des matériaux utilisés. Le group Nano4NPS avait développé des capteurs thermiques [73, 74, 249] et des générateurs thermoélectriques [53] sur Si pour différentes applications. Le principe de fonctionnement de ces capteurs thermiques est basé sur l'isolation thermique par rapport au substrat Si en utilisant localement un film épais de Si poreux sur Si. Sur cette surface mixte Si poreux/Si, une différence de température peut se créer entre la surface du Si poreux et celle du Si massif. Des thermocouples composés de Si polycristallin/Al en contact, sont intégrés sur la surface mixte, ayant le contact chaud sur le Si poreux et le contact froid sur Si monocristallin. La différence de température induit une différence de potentiel entre les deux extrémités des thermocouples, due à l'effet Seebeck. Le signal correspondant est calibré en fonction du flux de liquide au-dessus des thermocouples. De l'autre côté, en exploitant la différence de température entre la surface de Si poreux et celle de Si et en utilisant la même configuration que celle des thermocouples, il est possible de créer un générateur thermoélectrique.

Il y a deux paramètres critiques qui définissent la sensibilité et l'efficacité des dispositifs thermoélectriques : 1) l'efficacité d'isolation thermique du substrat local qui assure un maximum de différence de température et 2) l'efficacité thermoélectrique des matériaux utilisés. Dans le cadre de cette thèse, nous avons étudié ces deux paramètres séparément, en étudiant le Si poreux comme matériau d'isolation thermique et le Si nanocristallin comme matériau thermoélectrique pour la fabrication des thermocouples. Pour le Si poreux, nous avons étudié sa conductivité thermique dans la gamme de températures 4.2K-350K en fonction de la structure et de la morphologie du matériau et pour des porosités différentes. Nous avons également étudié le coefficient Seebeck du Si poreux pour différentes porosités. Pour le Si polycristallin, nous avons étudié ses propriétés thermoélectriques en fonction de l'épaisseur des films (et par conséquent en fonction de la taille des grains). En combinant les

deux matériaux étudiés, le Si poreux comme matériau substrat à faible conductivité thermique et le Si polycristallin comme matériau thermoélectrique, des dispositifs performants à base de Si peuvent être fabriqués.

Cette thèse a été divisée en 7 chapitres comme suit :

Dans le chapitre 1, les notions fondamentales concernant les matériaux et dispositifs thermoélectriques ont été introduites. Les trois paramètres utilisés pour caractériser un matériau thermoélectrique, ainsi que les méthodes utilisées pour le déterminer, sont présentés. Les matériaux existants dans la littérature et présentant les performances maximales ont été cités.

Dans le chapitre 2, la technologie du Si poreux a été introduite, et plus spécialement le processus de fabrication, sa morphologie et sa structure en fonction des paramètres électrochimiques utilisés.

Le chapitre 3 a été consacré à la conductivité thermique (k) du Si poreux, étudiée en fonction de la température dans la gamme 4,2-350K. Deux méthodes ont été utilisées pour cette étude : la méthode DC et la méthode 3ω . Des structures "test" utilisées, ainsi que la façon d'implémenter chaque méthode, sont présentées. La validité des méthodes a été évaluée. Les résultats expérimentaux obtenus sont comparés entre eux, mais aussi avec ceux du Si monocristallin et avec ceux d'autres matériaux compatibles-Si bien connus. La dépendance de la conductivité thermique du Si poreux avec la température a été interprétée en se basant sur des modèles théoriques existants, qui se sont avérés pourtant insuffisant pour expliquer la dépendance de k avec la température dans la gamme de températures cryogéniques. Ceci a fait l'objet de chapitre 4, le chapitre 5 étant consacré à l'évaluation de l'efficacité du Si poreux comme matériau d'isolation thermique, basé sur des résultats expérimentaux et des simulations FEM.

La conductivité thermique du Si poreux a été interprétée en tenant compte de la nature "fractal" du Si poreux. Pour cela, une introduction a été faite sur la théorie des "fractals" et leurs propriétés physiques, et un modèle de "fractons" a été présenté et analysé. Le Si poreux a été ensuite caractérisé comme un objet "fractal" en déterminant sa dimension "fractal" par des images de microscopie électronique et l'algorithme "box counting". Le modèle des fractons s'est avéré suffisant pour l'interprétation de nos résultats.

Dans le chapitre 6, nous avons premièrement présenté le dispositif expérimental, qui a été fabriqué, calibré, testé et utilisé dans le cadre de cette thèse. Nous avons ensuite étudié la dépendance expérimentale du coefficient Seebeck du Si poreux avec la porosité, ainsi que les mécanismes mis en jeu, qui ont été analysés en tenant compte des mesures de photoluminescence et microscopiques (obtenues par microscopie SEM et TEM), qui renseignent sur la structure et la morphologie des échantillons étudiés.

Finalement, dans le chapitre 7, nous avons étudié des films minces de Si polycristallin, utilisés comme matériaux thermoélectriques et qui sont compatibles avec la technologie Si. Une étude systématique du rendement thermoélectrique (zT) des films minces de Si polycristallin dopés bore et fabriqués par la technique LPCVD, a été menée. Il a été démontré que zT augmente en diminuant l'épaisseur des films, résultant de la diminution de la taille des grains, et par conséquent de la conductivité thermique. Une augmentation par un facteur 3 du rendement thermoélectrique des films de Si polycristallin a été obtenue en diminuant l'épaisseur du film de 500nm à 100nm, une valeur de 0.033 étant obtenue pour zT .

Dans la suite nous allons décrire plus en détail le contenu de chaque chapitre de cette thèse.

Matériaux et dispositifs thermoélectriques (Chapitre 1)

Ce chapitre est consacré à l'introduction des matériaux et dispositifs thermoélectriques. En général, la performance thermoélectrique d'un matériau dépend des paramètres suivants : le coefficient Seebeck (S), la conductivité électrique (σ) et la conductivité thermique (k). Ces paramètres ne sont pas indépendants l'une de l'autre. Il a été démontré, aussi bien expérimentalement que théoriquement, que par "nanostructuration", le rendement thermoélectrique d'un matériau s'améliore.

Une étude bibliographique des matériaux thermoélectriques les plus prometteurs étudiés actuellement a donné les résultats présentés sur la Figure 1. En général, le rendement maximum est obtenu par des matériaux exotiques, la plupart d'entre eux étant aussi toxiques. De l'autre côté, les matériaux basés sur le Si ne sont ni toxiques, ni exotiques, mais sont abondants dans la nature et à faible coût. D'autre part le Si est le matériau de base des circuits intégrés microélectroniques et par conséquent des infrastructures importantes et une connaissance accumulée existent pour la technologie correspondante, ce qui rend tout dispositif intégré sur la même plate-forme avec du Si, technologiquement très important.

Une revue des dispositifs thermoélectriques basés sur le Si est faite dans ce chapitre et présentée sur la Figure 1b. Figure 1a présente de façon plus générale les matériaux thermoélectriques existants les plus efficaces.

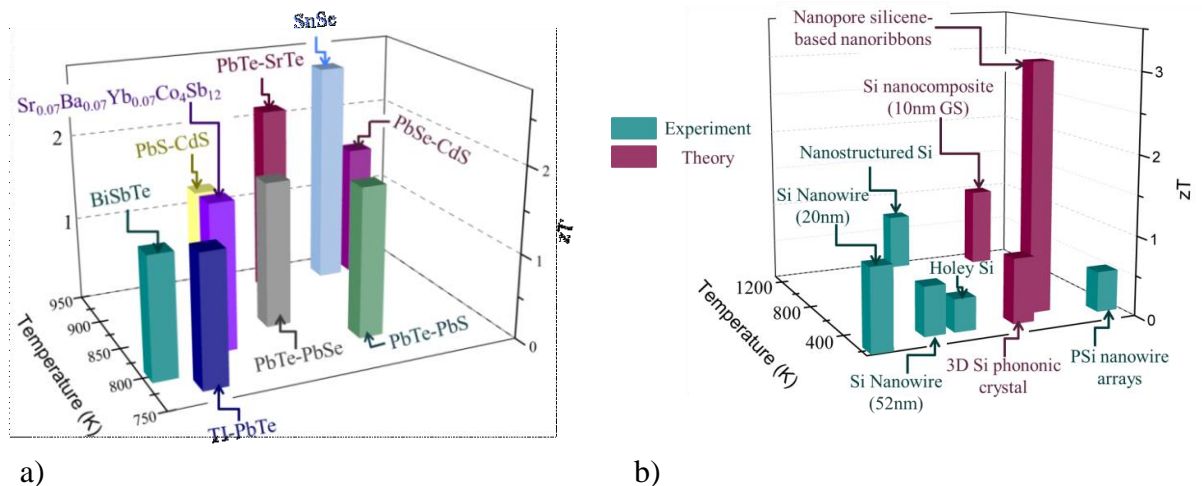


Figure 18: a) Etat de l'art de matériaux thermoélectriques de type p - b) matériaux compatible-Si de la littérature.

Les références correspondantes sont : BiSbTe [30], $Sr_{0.07}Ba_{0.07}Yb_{0.07}Co_4Sb_{12}$ [31], TI-PbTe [32], PbTe-PbS [33], PbTe-PbSe [34], PbTe-SrTe [35], PbS-CdS [36], PbSe-CdS [37] et SnSe [38], nanofils de Si de taille de 20nm [41], Si nanostructuré massif [43], nanofils de Si de dimension 52nm [44], holey Si [45], nanofils poreux de Si [46], cristaux photoniques de Si [47], matériaux composites Si avec taille de grains de 10nm [48], nanorubans à base de "silicène" avec nanopores [42].

Le Si poreux est un matériau intéressant à utiliser en thermoélectricité de deux façons différentes :

- Comme substrat à faible conductivité thermique pour l'intégration de générateurs thermoélectriques.
- Comme matériau thermoélectrique (quand il a une faible porosité).

Par la suite, nous allons décrire les différentes propriétés du Si poreux que nous avons étudiées et qui incluent la conductivité thermique et le coefficient Seebeck.

Formation et propriétés du Si poreux (Chapitre 2)

Ce chapitre est consacré au Silicium poreux qui est un matériau très important pour différentes applications. Une introduction est faite sur les méthodes de fabrication et sur sa structure et sa morphologie, qui sont à l'origine des propriétés spécifiques qui intéressent les dispositifs thermoélectriques, ainsi que la méthode de fabrication locale sur plaquette de Si.

Le Si poreux est un matériau complexe qui est formé par voie électrochimique dans une solution chimique contenant de l'HF. Il est composé de nanostructures de Si (nanofils, nanocristaux) interconnectées et séparées par du vide. Cette structure, ainsi que la morphologie correspondante, dépendent des conditions électrochimiques utilisées, mais aussi du type et résistivité du substrat Si utilisé. Le Si poreux a des propriétés très différentes de celle du Si massif, qui sont ajustables en changeant les conditions de formation. Selon l'application, nous sommes intéressés par des propriétés différentes. Pour l'application aux dispositifs thermiques et thermoélectriques, les propriétés qui nous intéressent sont la conductivité électrique et thermique, ainsi que le coefficient Seebeck. En plus, nous sommes intéressés par la porosité du matériau, la taille des nanostructures qui le composent, l'épaisseur des films de Si poreux et les méthodes de fabrication sur des régions localisées d'une plaquette de Si.

Conductivité thermique du Si poreux dans la gamme de température 4.2-350K (Chapitre 3)

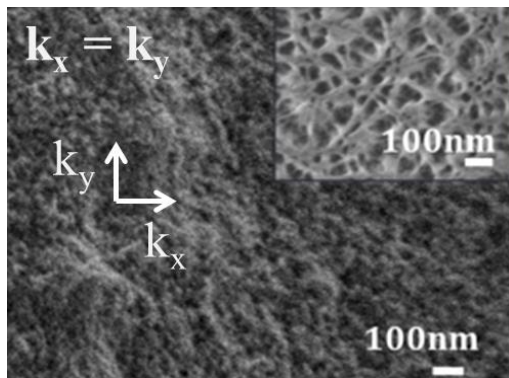
Différentes méthodes sont utilisées pour mesurer la conductivité thermique du Si poreux, comme par exemple la méthode Raman, la méthode 3ω , la méthode photo acoustique, la méthode d'état stabilisé (steady state) en combinaison avec une analyse à éléments finis (FEM) etc. La conductivité thermique du Si poreux dépend fortement de sa structure et de sa porosité, ce qui fait que les différentes équipes qui travaillent sur ce matériau, étudient souvent des matériaux différents, et ceci explique la divergence des valeurs rapportées dans la littérature. La conductivité thermique du Si poreux à température ambiante a été étudiée par différents groupes, par contre moins de recherches ont été faites pour sa variation avec la température [15, 119, 120, 156], ce qui a fait le sujet de cette thèse. Nous avons étudié de façon systématique la variation de k avec la température dans la gamme de 4,2-350K. Les mesures effectuées à des températures de 4.2K à 20K sont les premières reportées dans la littérature [156].

La mesure de la conductivité thermique du Si poreux a été effectuée en utilisant deux méthodes différentes, la méthode 3ω et la méthode de courant DC en état d'équilibre, en combinaison avec une analyse utilisant des éléments finis. Afin d'évaluer la validité des techniques utilisées, nous avons examiné des échantillons de conductivité thermique connue, comme le Si massif.

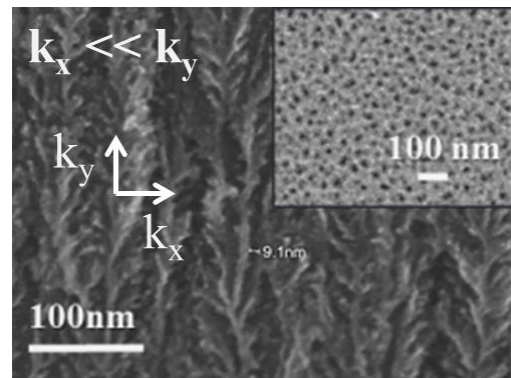
Les mesures de la conductivité thermique du Si poreux ont été effectuées sur deux échantillons différents, le premier étant formé sur Si de type p (résistivité de 1-10 Ω .cm) et le second sur Si de type p⁺ (résistivité 1-5m Ω .cm). Les conditions de fabrication de chaque échantillon, ainsi que la porosité résultante, sont données dans le tableau I. La Figure 2 montre des images de microscopie électronique à balayage de ceux deux échantillons.

Table: Conditions électrochimiques et porosité des échantillons de Si poreux étudiés

	Résistivité de la plaquette de Si ($\Omega.cm$)	Electrolyte utilisé	Densité de courant d'anodisation (mA/cm^2)	Taux de gravure ($\mu m/min$)	Porosité (%)
PSi isotrope (Figure 2a)	1-10	3HF:2Eth	80	3.6	63±3
PSi anisotrope (Figure 2b)	0.001-0.005	2HF:3Eth	20	0.75	70±4



(a) PSi isotrope dont la morphologie est de type spongieuse



(b) PSi anisotrope présentant des pores verticaux dendritiques

Figure 2: Images SEM, vue en coupe (image principale) et vue de dessus (image insérée) d'échantillons de Si poreux ayant des porosités de a) 63% et b) 70%. k_x et k_y sont les composantes du vecteur de conductivité thermique.

Le dispositif de mesure (un film de Si épais, formé localement sur du Si, d'épaisseur de $40\mu m$, ainsi que la structure de la résistance de Pt utilisée pour faire les mesures), est présenté schématiquement sur la figure 3. Un film de SiO_2 , d'épaisseur 20nm, a été déposé par LPCVD (oxyde TEOS) sur la surface du Si poreux pour réaliser une isolation électrique, mais aussi comme matériau d'adhérence du Pt sur du Si poreux. La structure en Pt est utilisée aussi bien comme résistance de chauffage que comme capteur de température. La même structure est déposée sur du Si pour mesurer la température correspondante.

Les résultats expérimentaux de conductivité thermique des deux échantillons poreux en fonction de la température sont présentés sur la Figure 4, par comparaison avec celle du Si massif et d'autres matériaux à faible conductivité thermique à base de Si (SiO_2 , a-Si, vitreous silica, SiN_x etc).

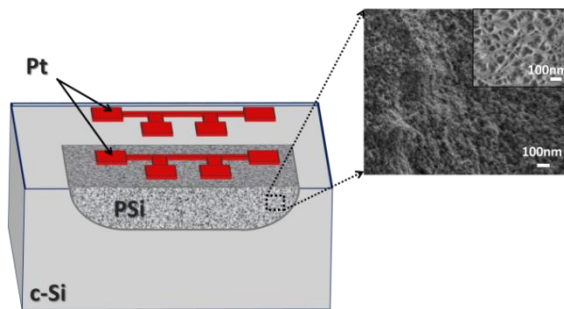


Figure 3: Représentation schématique des structures de test utilisées pour la mesure de conductivité thermique (méthode de 4-points)

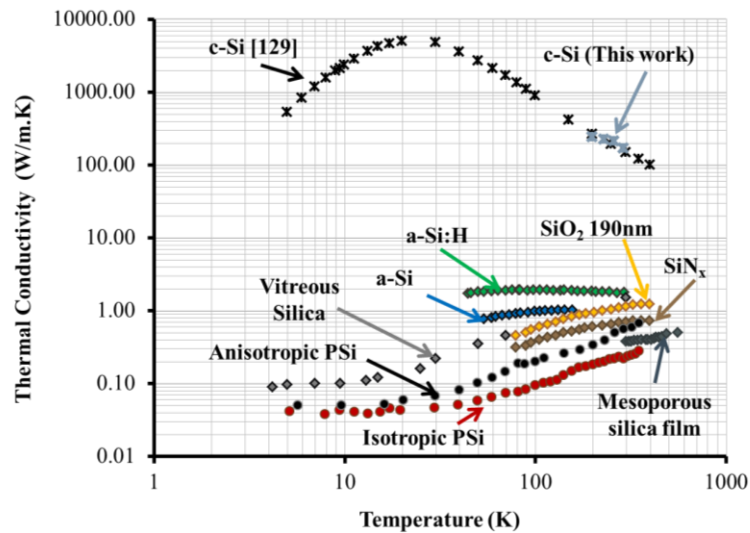


Figure 4: Conductivité thermique des deux échantillons de Si poreux étudiés dans cette thèse (échantillon à structure isotrope et échantillon à structure anisotrope) par comparaison avec celle du Si massif [128] et d'autres matériaux à base de Si : a-Si [132], a-Si:H [133], mesoporeux SiO₂[134], vitreous silica [135] et nitrure de Si [136]).

Les valeurs de conductivité thermique, obtenues pour les échantillons étudiés (porosité 63% et 70%) sont bien inférieures à celles du Si cristallin. A des températures inférieures à 50K cette différence est de plus de quatre ordres de grandeur et les valeurs correspondantes sont comparables ou inférieures à celles des meilleurs matériaux utilisés pour réaliser l'isolation thermique. Les faibles valeurs de conductivité thermique du Si poreux sont attribuées au confinement de phonons dans les nanostructures, ainsi qu'aux collisions des phonons sur la grande surface interne de Si poreux et à la présence de l'air dans le volume poreux.

Il a été démontré que le Si poreux ayant une structure anisotrope a une conductivité thermique supérieure à celle du matériau à structure isotrope des pores. Cette différence est attribuée à la structure et à la morphologie différentes des deux matériaux (Figure 2). Par ailleurs, la variation de k avec la température est la même dans les deux cas. Nous observons une variation monotone de k avec la diminution de la température, et une saturation à des températures inférieures à 20K. Les valeurs obtenues à hautes températures s'expliquent en considérant des modèles analytiques et plus spécialement le modèle hydrodynamique des phonons et le modèle classique de diffusion des phonons. Cependant, ces modèles ne permettent pas d'expliquer les résultats obtenus pour des températures inférieures à ~200K. Pour cette raison, une discussion détaillée est présentée pour cette gamme de températures dans le chapitre suivant.

Dans le présent chapitre, nous avons également élaboré deux approches différentes pour extraire les valeurs de la conductivité thermique par des mesures obtenues par la technique 3ω . La première considère l'accord des valeurs expérimentales avec la solution asymptotique de la formule intégrale de Cahill, en tenant compte des deux composantes des oscillations de température, celle qui est en phase et celle qui est déphasée. La seconde permet de faire une analyse des données en considérant la solution dépendant du temps de l'équation de transport de la chaleur, en utilisant la méthode des éléments finis (FEM). Sur la Figure 5, nous comparons les résultats expérimentaux obtenus avec la méthode décrite auparavant avec ceux obtenus par la méthode de pente, introduite par Cahill, ainsi que la méthode du courant continu (DC). La seconde approche, introduite auparavant, s'est avérée plus juste et en accord avec la méthode DC. D'un autre côté, les équations de Cahill, aussi bien l'analytique que l'intégrale, surestiment les valeurs de k du Si poreux. Une discussion détaillée concernant les résultats expérimentaux et leur analyse, est présentée en détail dans cette thèse.

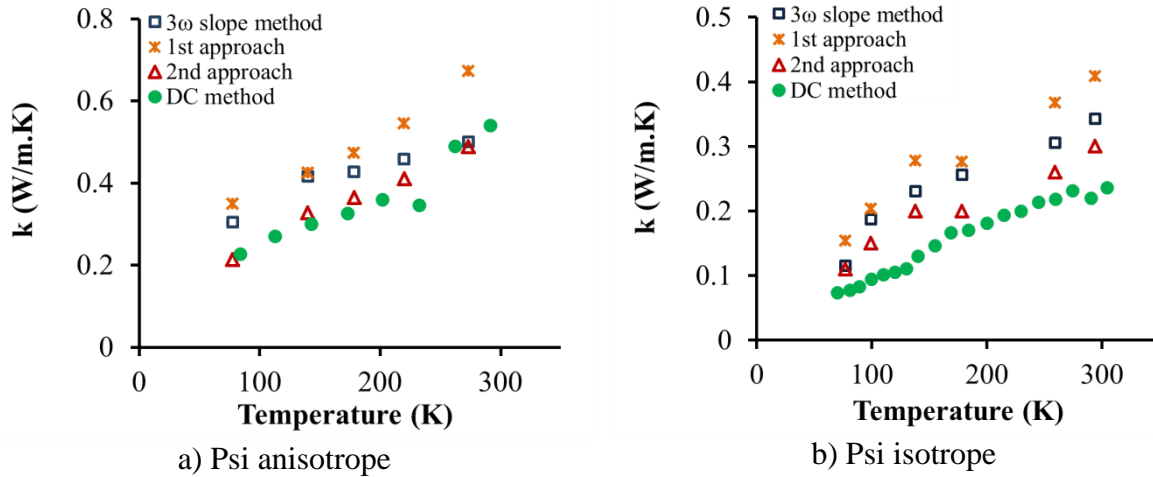


Figure 5: Comparaison des valeurs de conductivité thermique des deux échantillons étudiés (isotrope et anisotrope), obtenues en utilisant différentes approches : Etoiles : “fitting” de nos résultats expérimentaux avec la formule intégrale de Cahill ; triangles : valeurs obtenues en considérant les résultats expérimentaux, combinés avec l’analyse à éléments finis, basée sur le modèle 3D de conduction thermique ; cercles : résultats de la méthode DC.

Conductivité thermique du Si poreux dans la gamme de températures 4.2-20K - Interprétation du plateau (Chapitre 4)

Le manque de données concernant la conductivité thermique du Si poreux dans la gamme de température 4.2-20K nous a incité à effectuer des mesures et à interpréter les résultats obtenus en tenant compte de la nature “fractale” du Si poreux. Une interprétation de la saturation de k à des températures inférieures à 20K et de la partie linéaire de la courbe pour des températures supérieures à 20K, a été proposée en tenant compte du formalisme des fractons.

Les excitations vibrationnelles dans un matériau “fractal” sont appelées fractons [162]. Après une brève introduction concernant les “fractals” et de leurs principales propriétés, la dimension “fractale” des échantillons de Si poreux isotrope et anisotrope a été calculée à partir d’une analyse d’images microscopiques SEM et de l’algorithme “box-counting”. L’échantillon anisotrope présente une dimension “fractale” légèrement supérieure à celle de l’échantillon isotrope, cela étant en accord avec sa plus grande porosité. Dans les deux cas d’échantillons utilisés, la dimension fractale était inférieure à 2. Cela constitue la condition nécessaire pour appliquer le formalisme des fractons [175] pour l’interprétation des résultats. Le formalisme des “fractons” explique aussi bien la saturation de k à des températures en dessous de 20K, que la variation linéaire à des températures supérieures à 20K. Plus particulièrement, il a été démontré que le mécanisme de “phonon induced fracton hopping” permet d’expliquer les résultats à des températures au-dessus de 20K. Par contre, au-dessus de la partie linéaire, la conductivité thermique suit l’évolution de la capacité de chaleur spécifique.

Le mécanisme des fractons proposé pour le Si poreux à basses températures a été supporté par des mesures de la littérature en utilisant les techniques de spectroscopie Micro-Raman et des spectres Brillouin. Plus particulièrement, l’existence du pic “Boson” dans le spectre Micro-Raman et des modes de vibration localisés dans les spectres Brillouin du Si poreux, aident pour l’interprétation des fractons, comme nous l’avons démontré par l’analyse effectuée.

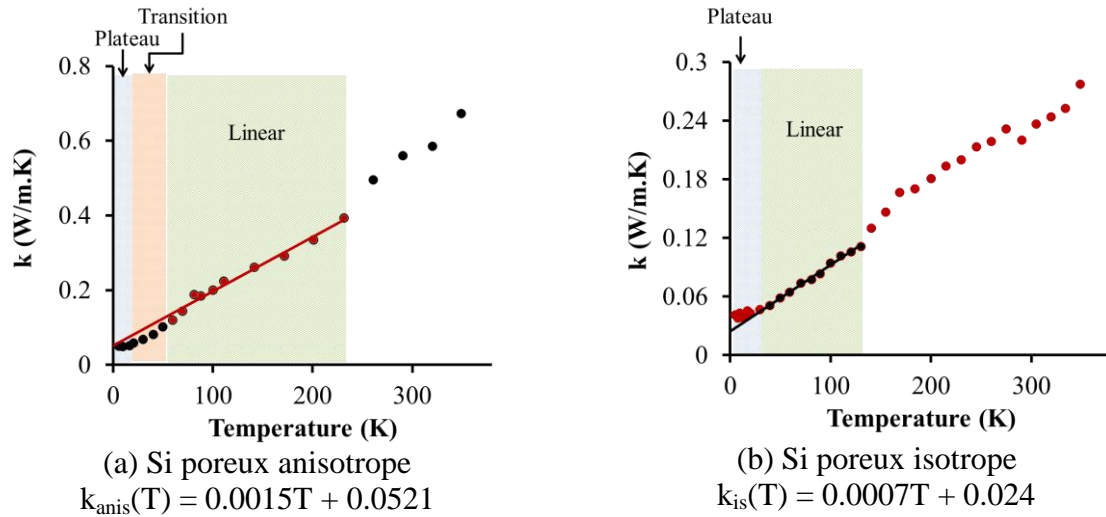


Figure 6: Dépendance à la température de la conductivité thermique du Si poreux a) anisotrope et b) isotrope. Les cercles noirs représentent les données expérimentales. Par contre, les lignes continues donnent la partie linéaire de la dépendance à la température de k .

Efficacité du Si poreux utilisé comme plateforme d'isolation thermique du Si (Chapitre 5)

Dans ce chapitre, nous avons évalué l'efficacité du Si poreux comme substrat local d'isolation thermique sur une plaquette de Si. Pour cela, nous avons utilisé les valeurs mesurées de k en combinées avec des valeurs simulées par FEM. Plus particulièrement, on compare l'effet d'application d'une impulsion de puissance thermique à une résistance de chauffage située soit sur du Si poreux isotrope, soit sur du Si poreux anisotrope. Comme prévu, la différence de température créée est plus importante dans le premier cas dans toute la gamme de températures étudiées, cela est dû à la plus faible conductivité thermique du film de Si poreux isotrope. En plus, à faibles températures, le taux d'augmentation de la température avec l'augmentation de l'épaisseur est presque à son maximum si l'épaisseur du film poreux est supérieure à $40\mu\text{m}$.

En utilisant des simulations, combinées avec des résultats expérimentaux, il a été démontré qu'une puissance électrique inférieure à 1mW sur la résistance chauffante est suffisante pour créer une augmentation de température de 15K sur Si poreux, alors que la température sur du Si cristallin restant constante.

Ce résultat est caractéristique d'un dispositif de micro-plaque chauffante. Il a été, donc démontré que le Si poreux constitue une plaque chauffante très efficace, formée très localement sur une plaquette Si.

Coefficient Seebeck du Si poreux en fonction de la porosité (Chapitre 6)

Dans ce chapitre, nous avons systématiquement mesuré le coefficient Seebeck des membranes librement supportées (free standing) de Si poreux avec porosité entre 40 et 84% ayant une structure anisotrope, résultante de l'anodisation du Si de type p^+ . Les mesures ont été effectuées dans le plan de propagation de la chaleur.

En général, le coefficient Seebeck (S) augmente en introduisant des pores dans des matériaux thermoélectriques. Ceci a été démontré aussi bien théoriquement [42, 200–202],

qu'expérimentalement en considérant des matériaux avec des pores introduits par gravure [45, 203, 204]. Dans ces études expérimentales nous avons utilisé des échantillons dont la porosité est assez élevée, ce qui n'est pas le meilleur choix pour obtenir un matériau thermoélectrique performant. En effet, en augmentant la porosité, le coefficient Seebeck augmente et la conductivité électrique diminue, ce qui n'est pas le résultat recherché. Dans cette étude, en commençant par des valeurs de porosité élevées, nous avons essayé de fabriquer aussi des échantillons à plus faible porosité afin d'examiner leur coefficient Seebeck. Néanmoins, il s'est avéré assez difficile d'obtenir des échantillons de grande épaisseur avec une porosité inférieure à 40%, car ceci conduit à une augmentation excessive du temps d'anodisation. On est donc limité à des porosités de 40%. Pour les mesures, nous avons utilisé une plate forme fabriquée spécialement pour ces mesures, qui a été testée préalablement pour assurer l'exactitude des mesures.

La variation du coefficient Seebeck (S) avec la porosité obtenue expérimentalement, est donnée sur la Figure 7. S augmente avec la porosité jusqu'à une certaine valeur, de l'ordre de 1mV/K pour le film dont la porosité est de 51% et ensuite diminue et se stabilise à une valeur autour de $600\mu\text{V/K}$. L'augmentation initiale de S avec la porosité est attribuée à des effets de filtrage d'énergie et du "phonon drag". Pour des porosités très élevées, la structure du matériau est très complexe, ce qui est à l'origine de la variation complexe de S . Des phénomènes de collisions sur les pores et de confinement des porteurs dans les nanostructures sont dominants et conduisent à une diminution de la diffusion des porteurs et à une suppression du "phonon drag" ce qui conduit à une diminution de S . Pourtant, malgré la valeur très élevée de S obtenue et la très faible valeur de conductivité thermique du Si poreux, ce matériau conserve une faible performance thermoélectrique. Afin de le rendre plus efficace et plus compétitif, il faut trouver des solutions pour augmenter sa résistivité électrique. Cela pourra être l'objet de la suite de cette thèse.

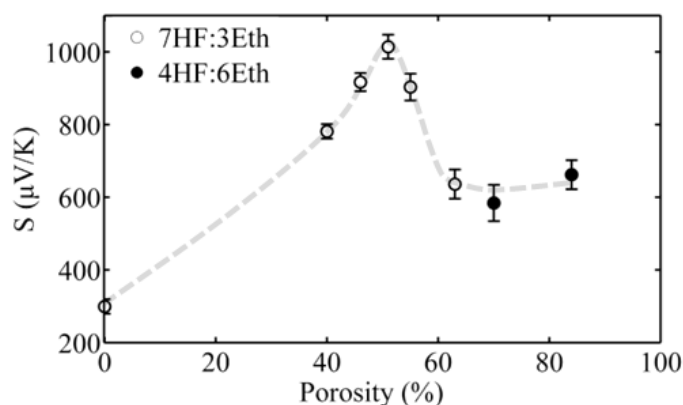


Figure 7: Coefficient Seebeck en fonction de la porosité pour les différents échantillons mesurés. Les cercles vides représentent des échantillons fabriqués avec un électrolyte à concentration HF de 70% et les cercles pleins avec concentration HF de 40% [205].

La performance thermoélectrique des films minces de Si nanocristallin (Chapitre 7)

Le Si nanocristallin est un matériau prometteur dans le domaine des dispositifs thermoélectriques à base de Si, car il est déjà utilisé en microélectronique Si et il est complètement compatible avec les procédés de fabrication des circuits intégrés. Des films épais dopés de Si polycristallin sont déjà utilisés dans des dispositifs thermoélectriques [53]. Leur rendement thermoélectrique zT a été mesuré par plusieurs groupes à température ambiante [219–221] et la valeur trouvée est ~ 0.01 . Une façon d'augmenter cette valeur est d'introduire dans le matériau des sites supplémentaires de collisions, qui diminuent le

transport thermique sans affecter de façon significative le transport électrique et le “facteur de puissance”. Cela peut se réaliser en diminuant la taille des grains du matériau polycristallin, cela pouvant s’effectuer simplement en diminuant l’épaisseur des films correspondants.

Dans ce chapitre, une étude systématique de la dépendance du facteur zT du Si polycristallin en fonction de l’épaisseur des films a été effectuée. Les films ont été préparés par la technique LPCVD. Nous présentons d’abord la fabrication des films et la caractérisation de leur structure par microscopie électronique à transmission (TEM) pour des films d’épaisseur 100-500nm et nous déterminons ensuite chaque paramètre qui influence le facteur zT , c’est à dire les conductivités thermique et électrique, et le coefficient Seebeck. Nos résultats expérimentaux ont été comparés avec des valeurs théoriques en utilisant des modèles présentés récemment dans la littérature. Les échantillons de test qui sont utilisés, ainsi que les méthodes de mesure, sont décrit en détail.

Nous avons trouvé qu’en diminuant l’épaisseur des films de 500nm à 100nm, le facteur zT augmente de 0.01 à 0.033, c’est à dire d’un facteur 3. Cette augmentation est principalement attribuée à la diminution de la taille des grains dans les films minces.

La diminution de la taille des grains induit une augmentation de la résistivité électrique des films et une diminution de la conductivité électrique d’un facteur 2, néanmoins le coefficient Seebeck est augmenté de 30% et la conductivité thermique est diminuée d’un facteur 8. Cette dernière diminution est principalement à l’origine de l’augmentation du rendement thermoélectrique des films de 100nm. Nos résultats expérimentaux sont présentés sur la Figure 8.

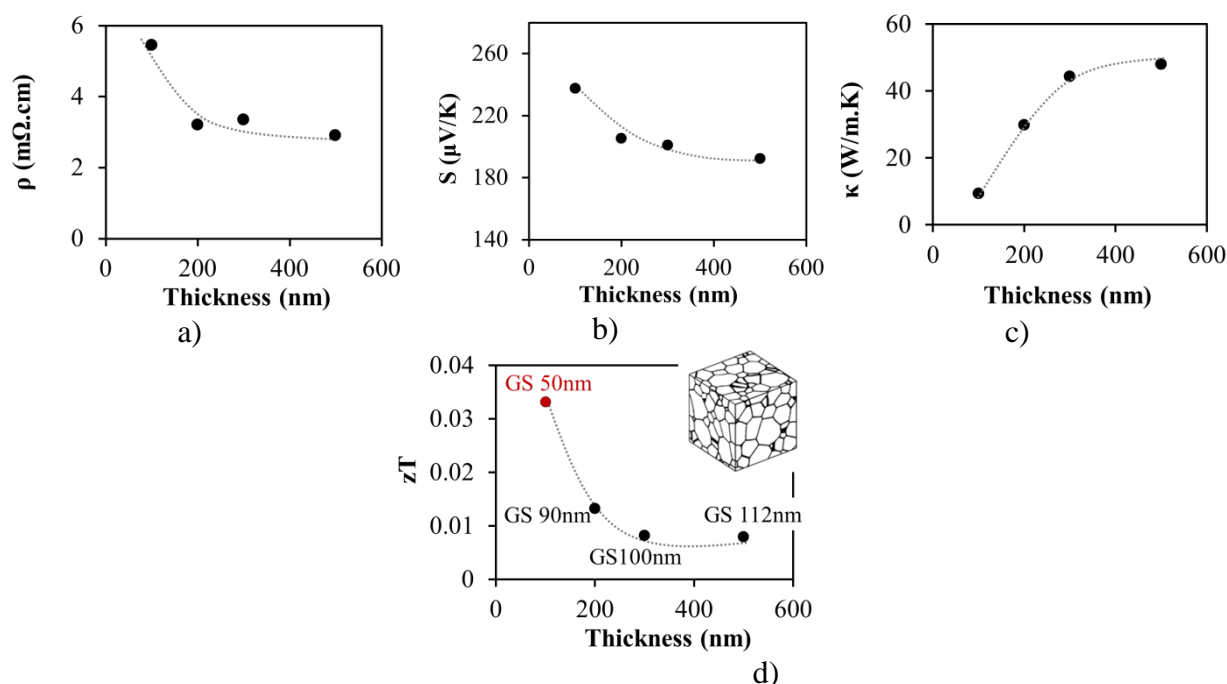


Figure 8: Résultats expérimentaux de a) la résistivité électrique b) le coefficient Seebeck c) la conductivité thermique et d) le rendement thermoélectrique zT des films polycristallins de différentes épaisseurs (GS : taille des grains) [235].

Une analyse des mécanismes mis en jeu est aussi présentée en détail dans ce chapitre. Notre étude vient de conforter les modèles théoriques concernant le facteur zT du Si nanocristallin. Elle montre aussi que le Si nanocristallin est un matériau prometteur pour des dispositifs thermoélectriques efficaces à base de Si.

Conclusions

Les points et conclusions principaux de cette thèse sont les suivants :

- ✓ Une étude bibliographique a été faite concernant les dispositifs thermoélectriques et thermiques à base de Si, qui a permis de montrer l'intérêt de ces matériaux pour ces applications.
- ✓ La conductivité thermique de membranes de Si poreux à structure soit isotrope, soit anisotrope a été mesurée dans la gamme de température 4,2-350K. A des températures de 4,2-20K, la valeur de conductivité thermique suit un plateau, par contre elle augmente de façon monotone pour des températures supérieures. Ce comportement est commun aux verres et matériaux désordonnés et il est dû à la structure et à la morphologie du Si poreux. En caractérisant la nature fractale et en déterminant la dimension fractale des deux types d'échantillons étudiés, qui s'est trouvé être inférieure à 2, le modèle de fractons a été adopté pour l'interprétation de la dépendance de k avec la température à des températures cryogéniques. Par contre, pour des températures supérieures à $\sim 200K$, le modèle simple de diffusion de phonons permet d'expliquer de façon satisfaisante nos résultats. La dépendance avec la température dans ce cas suit celle de la capacité de chaleur spécifique.
- ✓ Les méthodes DC et 3ω ont été utilisées pour mesurer la conductivité thermique du Si poreux et les résultats correspondants ont été analysés et comparés. Il a été trouvé que la méthode 3ω donne des valeurs légèrement surestimées. Pour améliorer cela, nous avons proposé deux approches différentes, qui permettent d'extraire la valeur de k en fonction de la fréquence du 3^{ème} harmonique de la tension. Ces approches ont été comparées entre elles, ainsi qu'à la méthode de pente, introduire par Cahill.
- ✓ La conductivité thermique du Si poreux mesurée est bien inférieure à celle de Si massif, mais aussi à celle d'autres matériaux à faible conductivité thermique à base de Si et compatibles avec des procédés CMOS, comme par exemple l'oxyde de Si et le nitrure de Si. Les collisions phonon-phonon et phonon-surface sur la large surface interne du Si poreux, aussi bien que l'existence de l'air dans le volume du matériau, sont à l'origine de cette diminution très significative de la conductivité thermique du Si poreux, comparée à celle de Si massif.
- ✓ L'échantillon de Si poreux à structure anisotrope présente une conductivité thermique légèrement supérieure à celle du matériau isotrope. Ceci montre qu'aussi bien la structure et la morphologie, que la porosité, conditionnent la valeur de k .
- ✓ A partir de très faibles valeurs de k mesurées, en combinaison avec des simulations FEM, nous sommes arrivés à la conclusion que le Si poreux constitue une excellente plate forme locale pour réaliser une isolation thermique sur une plaquette de Si. Nous avons évalué l'efficacité d'isolation à température ambiante, mais aussi à basses températures. Sur un film épais de Si poreux sur Si massif, nous pouvons augmenter très localement et de façon significative, la température sur une résistance thermique, en appliquant une très faible puissance thermique, ce qui n'est pas possible sur du Si massif. Ce résultat est très important pour la réalisation de dispositifs thermiques et thermoélectriques sur Si.
- ✓ Le coefficient Seebeck (S) de Si poreux à température ambiante a été étudié en fonction de la porosité. Des membranes auto-supportées, avec porosité dans la gamme 40-84%, ont été utilisées. Pour nos mesures, nous avons fabriqué une plateforme spécifique. Nous avons trouvé qu'à faible porosité le coefficient S augmente de façon monotone jusqu'à une valeur maximale de l'ordre de 1mV/K. Après le maximum, S diminue et se stabilise à une valeur inférieure. La variation de S à faible porosité est attribuée à des effets de filtrage d'énergie et à l'effet de phonon drag. La diminution après le maximum est attribuée à des effets importants de collisions, mais aussi à des

effets importants de confinement quantique.

- ✓ Les paramètres thermoélectriques des films minces polycristallins de Si d'épaisseur comprise entre 100 et 500nm, ont été étudiés en détail à température ambiante. Ces films sont intéressants à combiner avec le substrat de Si poreux, car ils sont tout à fait compatibles avec la technologie Si. Nous avons trouvé qu'en diminuant l'épaisseur des films de 500nm à 100nm, le rendement thermoélectrique zT augmente d'un facteur 3, arrivant à la valeur de 0,033, qui est la valeur la plus grande de la littérature pour des films polycristallins de Si dopés avec du B. Cette augmentation est attribuée à la réduction de la taille des grains obtenue en diminuant l'épaisseur des films, ce qui conduit à une diminution de la conductivité thermique à cause de l'augmentation des collisions phonon-joints de grains, mais aussi à cause d'autres phénomènes de dimension. Tous les paramètres thermoélectriques et leur dépendance à la taille des grains et à l'épaisseur des films ont été ajustés et comparés à des modèles théoriques de la littérature et ont été trouvés en bon accord avec ces modèles. Nos mesures confirment la validité de ces modèles et contribuent à mieux comprendre les mécanismes de transport électronique et thermique des matériaux à nano-grains.
- ✓ Nous avons trouvé que le facteur de puissance thermoélectrique de films minces polycristallins ne suit pas la même tendance en fonction de l'épaisseur que zT . Cela veut dire la mesure unique du facteur de puissance d'un matériau thermoélectrique, comme beaucoup d'autres groupes le font, n'est pas suffisante pour estimer le zT du matériau. La conductivité thermique est un paramètre important, qui doit être également considéré.

Perspectives

Cette thèse a démontré que le Si poreux constitue une solution compétitive pour l'intégration des dispositifs thermiques et thermoélectriques sur une plaquette de Si, avec des C.I. La conductivité thermique du matériau a été évaluée dans une large gamme de températures, mettant en évidence l'importance du Si poreux utilisé comme substrat local sur du Si. L'étude des mécanismes de transport thermique dans ce matériau a permis de poser les bases de la compréhension des effets mis en jeu, afin de pouvoir concevoir des dispositifs efficaces correspondants aux besoins.

La caractérisation des films minces de Si polycristallin dopé B, complètement compatibles avec aussi bien les procédés de fabrication du Si que ceux du Si poreux, ouvre des perspectives importantes dans le domaine des dispositifs thermoélectriques intégrés sur Si. La diminution de la taille des grains s'est avérée une stratégie importante pour augmenter le rendement thermoélectrique que de ces films. Les matériaux étudiés peuvent ensuite être intégrés dans des dispositifs thermiques et thermoélectriques, afin d'améliorer leurs performances.

References

1. Lawrence Livermore National Laboratory and the Department of Energy, Data is based on DOE/IEA-0035(2013-05), May, 2013, Rearranged by NETL.
2. Hicks LD, Dresselhaus MS: **Effect of quantum-well structures on the thermomagnetic figure of merit.** *Phys. Rev. B* 1993, **47**:727–731.
3. Heremans JP, Dresselhaus MS, Bell LE, Morelli DT: **When thermoelectrics reached the nanoscale.** *Nat. Nanotechnol.* 2013, **8**:471–3.
4. Rowe DM: *Thermoelectrics handbook: macro to nano.* Boca Raton: CRC/Taylor & Francis,; 2006.
5. Rowe DM: *CRC Handbook of Thermoelectrics.* Boca Raton: CRC Press LLC; 1995.
6. Weber L, Gmelin E: **Transport properties of silicon.** *Appl. Phys. A Solids Surfaces* 1991, **53**:136–140.
7. Martin J: **Protocols for the high temperature measurement of the Seebeck coefficient in thermoelectric materials.** *Meas. Sci. Technol.* 2013, **24**:085601.
8. Lowhorn ND, Wong-Ng W, Lu ZQ, Thomas E, Otani M, Green M, Dilley N, Sharp J, Tran TN: **Development of a Seebeck coefficient Standard Reference Material.** *Appl. Phys. A* 2009, **96**:511–514.
9. Martin J, Tritt T, Uher C: **High temperature Seebeck coefficient metrology.** *J. Appl. Phys.* 2010, **108**:1–12.
10. Borup K A, de Boor J, Wang H, Drymiotis F, Gascoin F, Shi X, Chen L, Fedorov MI, Müller E, Iversen BB, Snyder GJ: **Measuring thermoelectric transport properties of materials.** *Energy Environ. Sci.* 2015, **8**:423–435.
11. de Boor J, Müller E: **Data analysis for Seebeck coefficient measurements.** *Rev. Sci. Instrum.* 2013, **84**:065102.
12. Tritt TM: *Thermal Conductivity: Theory, Properties, and Applications.* Springer US; 2004.
13. Stojanovic N, Yun J, Washington EBK, Berg JM, Member S, Holtz MW, Temkin H: **Thin-Film Thermal Conductivity Measurement Using Microelectrothermal Test Structures and Finite-Element-Model-Based Data Analysis.** *J. Electromechanical Syst.* 2007, **16**:1269–1275.
14. Siegert L, Capelle M, Roqueta F, Lysenko V, Gautier G: **Evaluation of mesoporous silicon thermal conductivity by electrothermal finite element simulation.** *Nanoscale Res. Lett.* 2012, **7**:427.
15. Valalaki K, Nassiopoulou AG: **Low thermal conductivity porous Si at cryogenic temperatures for cooling applications.** *J. Phys. D. Appl. Phys.* 2013, **46**:295101.
16. Glassbrenner C, Slack G: **Thermal Conductivity of Silicon and Germanium from 3°K to the Melting Point.** *Phys. Rev.* 1964, **134**:A1058–A1069.
17. Maldonado O: **Pulse method for simultaneous measurement of electric thermopower and heat conductivity at low temperatures.** *Cryogenics (Guildf).* 1992, **32**:908–912.
18. Cahill D: **Thermal conductivity measurement from 30 to 750 K: the 3 ω method.** *Rev. Sci. Instrum.* 1990, **2501**:802–808.
19. Capinski W, Maris H, Ruf T, Cardona M, Ploog K, Katzer D: **Thermal-conductivity measurements of GaAs/AlAs superlattices using a picosecond optical pump-and-probe technique.** *Phys. Rev. B* 1999, **59**:8105–8113.

20. Srinivasan R, Jayachandran M, Ramachandran K: **Photoacoustic studies on optical and thermal properties of p-type and n-type nanostructured porous silicon for (100) and (111) orientations.** *Cryst. Res. Technol.* 2007, **42**:266–274.
21. Kraftmakher YA: **Advances in modulation calorimetry and related techniques.** *High Temp. - High Press.* 1992, **24**:145–154.
22. Deen M, Pascal F: **Electrical Characterization of Semiconductor Materials and Devices.** In *Springer Handb. Electron. Photonic Mater.* edited by Kasap S, Capper P Boston, MA: Springer US; 2006:409–438.
23. van der Pauw LJ: **A method of measuring specific resistivity and Hall effect of discs of arbitrary shape.** *Philips Res. Reports* 1958, **13**:1–11.
24. Dughaish ZH: **Lead telluride as a thermoelectric material for thermoelectric power generation.** *Phys. B Condens. Matter* 2002, **322**:205–223.
25. Jones W, March NH: *Theoretical Solid State Physics: Perfect lattices in equilibrium.* Courier Corporation; 1973.
26. Snyder GJ, Toberer ES: **Complex thermoelectric materials.** *Nat. Mater.* 2008, **7**:105–114.
27. Enrique Maciá-Barber: *Thermoelectric Materials: Advances and Applications.* Pan Stanford; 2015.
28. Dresselhaus MS, Chen G, Tang MY, Yang R, Lee H, Wang D, Ren Z, Fleurial JP, Gogna P: **New directions for low-dimensional thermoelectric materials.** *Adv. Mater.* 2007, **19**:1043–1053.
29. Zhao L-D, Dravid VP, Kanatzidis MG: **The panoscopic approach to high performance thermoelectrics.** *Energy Environ. Sci.* 2014, **7**:251.
30. Poudel B, Hao Q, Ma Y, Lan Y, Minnich A, Yu B, Yan X, Wang D, Muto A, Vashaee D, Chen X, Liu J, Dresselhaus MS, Chen G, Ren Z: **High-Thermoelectric Performance of Nanostructured Bismuth Antimony Telluride Bulk Alloys.** *Science (80-.).* 2008, **320**:634–638.
31. Rogl G, Setman D, Schafler E, Horky J, Kerber M, Zehetbauer M, Falmbigl M, Rogl P, Royanian E, Bauer E: **High-pressure torsion, a new processing route for thermoelectrics of high ZTs by means of severe plastic deformation.** *Acta Mater.* 2012, **60**:2146–2157.
32. Heremans JP, Jovovic V, Toberer ES, Saramat A, Kurosaki K, Charoenphakdee A, Yamanaka S, Snyder GJ: **Enhancement of Thermoelectric Efficiency in PbTe by Distortion of the Electronic Density of States.** *Science (80-.).* 2008, **321**:554–557.
33. Girard SN, He J, Zhou X, Shoemaker D, Jaworski CM, Uher C, Dravid VP, Heremans JP, Kanatzidis MG: **High performance Na-doped PbTe-PbS thermoelectric materials: Electronic density of states modification and shape-controlled nanostructures.** *J. Am. Chem. Soc.* 2011, **133**:16588–16597.
34. Pei Y, Shi X, LaLonde A, Wang H, Chen L, Snyder GJ: **Convergence of electronic bands for high performance bulk thermoelectrics.** *Nature* 2011, **473**:66–69.
35. Biswas K, He J, Blum ID, Wu C-I, Hogan TP, Seidman DN, Dravid VP, Kanatzidis MG: **High-performance bulk thermoelectrics with all-scale hierarchical architectures.** *Nature* 2012, **489**:414–418.
36. Zhao L, He J, Hao S, Wu C, Hogan TP, Wolverton C, Dravid VP, Kanatzidis MG: **Raising the thermoelectric performance of p-type PbS with endotaxial nanostructuring and valence-band offset engineering using CdS and ZnS.** *J. Am. Chem. Soc.* 2012, **134**:16327–36.
37. Zhao L, Hao S, Lo S, Wu C, Zhou X, Lee Y, Li H, Kanatzidis MG: **High Thermoelectric Performance via Hierarchical Compositionally Alloyed Nanostructures.** 2013.

38. Zhao L-D, Lo S-H, Zhang Y, Sun H, Tan G, Uher C, Wolverton C, Dravid VP, Kanatzidis MG: **Ultralow thermal conductivity and high thermoelectric figure of merit in SnSe crystals.** *Nature* 2014, **508**:373–7.
39. Yadav GG, Susoreny JA, Zhang G, Yang H, Wu Y: **Nanostructure-based thermoelectric conversion: an insight into the feasibility and sustainability for large-scale deployment.** *Nanoscale* 2011, **3**:3555–3562.
40. Vining CB: **Materials science. Desperately seeking silicon.** *Nature* 2008, **451**:132–3.
41. Boukai AI, Bunimovich Y, Tahir-Kheli J, Yu J-K, Goddard W a, Heath JR: **Silicon nanowires as efficient thermoelectric materials.** *Nature* 2008, **451**:168–171.
42. Sadeghi H, Sangtarash S, Lambert CJ: **Enhanced thermoelectric efficiency of porous silicene nanoribbons.** *Sci. Rep.* 2015, **5**:9514.
43. Bux SK, Blair RG, Gogna PK, Lee H, Chen G, Dresselhaus MS, Kaner RB, Fleurial J-P: **Nanostructured Bulk Silicon as an Effective Thermoelectric Material.** *Adv. Funct. Mater.* 2009, **19**:2445–2452.
44. Hochbaum AI, Chen R, Delgado RD, Liang W, Garnett EC, Najarian M, Majumdar A, Yang P: **Enhanced thermoelectric performance of rough silicon nanowires.** *Nature* 2008, **451**:163–7.
45. Tang J, Wang H-T, Lee DH, Fardy M, Huo Z, Russell TP, Yang P: **Holey silicon as an efficient thermoelectric material.** *Nano Lett.* 2010, **10**:4279–83.
46. Zhang T, Wu S, Xu J, Zheng R, Cheng G: **High thermoelectric figure-of-merits from large-area porous silicon nanowire arrays.** *Nano Energy* 2015, **13**:433–441.
47. Yang L, Yang N, Li B: **Thermoelectric Properties of Nanoscale three dimensional Si Phononic Crystal.** *ArXiv* 2014:16.
48. Hao Q, Zhu G, Joshi G, Wang X, Minnich A, Ren Z, Chen G: **Theoretical studies on the thermoelectric figure of merit of nanograined bulk silicon.** *Appl. Phys. Lett.* 2010, **97**:063109.
49. Fu G, Zuo L, Longtin JP: **Review of Waste Energy Resource in Vehicle Engine Exhaust.** In *Vol. 1 Heat Transf. Energy Syst. Theory Fundam. Res. Aerosp. Heat Transf. Gas Turbine Heat Transf. Transp. Phenom. Mater. Process. Manuf. Heat.* ASME; 2012:381–387.
50. Nielsch K, Bachmann J, Kimling J, Böttner H: **Thermoelectric Nanostructures: From Physical Model Systems towards Nanograined Composites.** *Adv. Energy Mater.* 2011, **1**:713–731.
51. LeBlanc S: **Thermoelectric generators: Linking material properties and systems engineering for waste heat recovery applications.** *Sustain. Mater. Technol.* 2014, **1-2**:26–35.
52. Zebarjadi M, Esfarjani K, Dresselhaus MS, Ren ZF, Chen G: **Perspectives on thermoelectrics: from fundamentals to device applications.** *Energy Environ. Sci.* 2012, **5**:5147.
53. Hourdakis E, Nassiopoulou AG: **A thermoelectric generator using porous Si thermal isolation.** *Sensors (Basel).* 2013, **13**:13596–608.
54. Huesgen T, Woias P, Kockmann N: **Design and fabrication of MEMS thermoelectric generators with high temperature efficiency.** *Sensors Actuators A Phys.* 2008, **145-146**:423–429.
55. Kao P-H, Shih P-J, Dai C-L, Liu M-C: **Fabrication and characterization of CMOS-MEMS thermoelectric micro generators.** *Sensors (Basel).* 2010, **10**:1315–25.
56. Bar-Cohen A, Wang P: **On-chip Hot Spot Remediation with Miniaturized Thermoelectric Coolers.** *Microgravity Sci. Technol.* 2009, **21**:351–359.
57. Chowdhury I, Prasher R, Lofgreen K, Chrysler G, Narasimhan S, Mahajan R, Koester D,

- Alley R, Venkatasubramanian R: **On-chip cooling by superlattice-based thin-film thermoelectrics.** *Nat. Nanotechnol.* 2009, **4**:235–238.
58. Hourdakis E, Sarafis P, Nassiopoulou AG: **Novel air flow meter for an automobile engine using a Si sensor with porous Si thermal isolation.** *Sensors (Basel).* 2012, **12**:14838–50.
59. Kaltsas G, Nassiopoulou AG: **Gas flow meter for application in medical equipment for respiratory control: study of the housing.** *Sensors Actuators A Phys.* 2004, **110**:413–422.
60. Pagonis DN, Petropoulos A, Kaltsas G, Nassiopoulou AG, Tserepi A: **Novel microfluidic flow sensor based on a microchannel capped by porous silicon.** *Phys. status solidi* 2007, **204**:1474–1479.
61. Goustouridis D, Kaltsas G, Nassiopoulou AG: **A Silicon Thermal Accelerometer Without Solid Proof Mass Using Porous Silicon Thermal Isolation.** *IEEE Sens. J.* 2007, **7**:983–989.
62. Wang DB, Liao XP, Liu T: **A thermoelectric power sensor and its package based on MEMS technology.** *J. Microelectromechanical Syst.* 2012, **21**:121–131.
63. Modarres-zadeh MJ, Abdolvand R: **High-responsivity thermoelectric infrared detectors with stand-alone sub-micrometer polysilicon wires.** *J. Micromechanics Microengineering* 2014, **125013**:125013.
64. Zhou H, Kropelnicki P, Lee C: **Characterization of nanometer-thick polycrystalline silicon with phonon-boundary scattering enhanced thermoelectric properties and its application in infrared sensors.** *Nanoscale* 2015, **7**:532–541.
65. Uhler A: **Electrolytic Shaping of Germanium and Silicon.pdf.** *Bell Syst. Tech. J.* 1956, **35**:333–347.
66. Imai K: **A new dielectric isolation method using porous silicon.** *Solid. State. Electron.* 1981, **24**:159–164.
67. Y. Watanabe, Y. Arita TY and YI: **Formation and Properties of Porous Silicon and Its Application.** *J. Electrochem. Soc.* 1975, **122**:1351.
68. Canham LT: **Silicon quantum wire array fabrication by electrochemical and chemical dissolution of wafers.** *Appl. Phys. Lett.* 1990, **57**:1046 – 1048.
69. Fauchet PM, Tsybeskov L, Peng C, Duttagupta SP, von Behren J, Kostoulas Y, Vandyshev JMV, Hirschman KD: **Light-emitting porous silicon: materials science, properties, and device applications.** *IEEE J. Sel. Top. Quantum Electron.* 1995, **1**:1126–1139.
70. Collins RT, Fauchet PM, Tischler MA: **Porous Silicon: From Luminescence to LEDs.** *Phys. Today* 1997, **50**:24.
71. Torres-Costa V, Martín-Palma RJ: **Application of nanostructured porous silicon in the field of optics. A review.** *J. Mater. Sci.* 2010, **45**:2823–2838.
72. Levitsky I: **Porous Silicon Structures as Optical Gas Sensors.** *Sensors* 2015, **15**:19968–19991.
73. Pagonis DN, Kaltsas G, Nassiopoulou AG: **Fabrication and testing of an integrated thermal flow sensor employing thermal isolation by a porous silicon membrane over an air cavity.** *J. Micromechanics Microengineering* 2004, **14**:793–797.
74. Kaltsas G, Nassiopoulos AA, Nassiopoulou AG: **Characterization of a silicon thermal gas-flow sensor with porous silicon thermal isolation.** *IEEE Sens. J.* 2002, **2**:463–475.
75. Harraz FA: **Porous silicon chemical sensors and biosensors: A review.** *Sensors Actuators B Chem.* 2014, **202**:897–912.
76. Kaltsas G, Nassiopoulou AG, Siakavellas M, Anastassakis E: **Stress effect on suspended**

- polycrystalline silicon membranes fabricated by micromachining of porous silicon.** *Sensors Actuators A Phys.* 1998, **68**:429–434.
77. Lang W, Steiner P, Richter A, Maruszczyk K, Weimann G, Sandmaier H: **Application of porous silicon as a sacrificial layer.** *Sensors Actuators A Phys.* 1994, **43**:239–242.
 78. RoyChaudhuri C: **A review on porous silicon based electrochemical biosensors: Beyond surface area enhancement factor.** *Sensors Actuators B Chem.* 2015, **210**:310–323.
 79. Santos HA, Mäkilä E, Airaksinen AJ, Bimbo LM, Hirvonen J: **Porous silicon nanoparticles for nanomedicine: preparation and biomedical applications.** *Nanomedicine (Lond).* 2014, **9**:535–54.
 80. Sarafis P, Hourdakakis E, Nassiopoulou AG, Roda Neve C, Ben Ali K, Raskin J-P: **Advanced Si-based substrates for RF passive integration: Comparison between local porous Si layer technology and trap-rich high resistivity Si.** *Solid. State. Electron.* 2013, **87**:27–33.
 81. Sarafis P, Nassiopoulou AG: **Dielectric properties of porous silicon for use as a substrate for the on-chip integration of millimeter-wave devices in the frequency range 140 to 210 GHz.** *Nanoscale Res. Lett.* 2014, **9**:418.
 82. Gautier G, Leduc P: **Porous silicon for electrical isolation in radio frequency devices: A review.** *Appl. Phys. Rev.* 2014, **1**:011101.
 83. Kaltsas G, Pagonis DN, Nassiopoulou GG: **Planar cmos compatible process for the fabrication of buried microchannels in silicon, using porous-silicon technology.** *J. Microelectromechanical Syst.* 2003, **12**:863–872.
 84. Canham LT: “*Properties of porous silicon*” *Emis Datareviews. Ser. No18, IEE, an INSPEC Publ.UK, edited by L.T.Canham.* INSPEC; 1997.
 85. Canham L: *Handbook of porous Silicon.* Springer International Publishing; 2015.
 86. Sailor MJ: *Porous Silicon in Practice.* Weinheim, Germany: Wiley-VCH Verlag GmbH & Co. KGaA; 2011.
 87. X.G. Zhang: *Electrochemistry of Silicon and its Oxide.* Kluwer Academics/Plenum Publishers; 2003.
 88. Halimaoui A: **Porous Silicon Formation by Anodisation.** In *Prop. Porous Silicon.* edited by Leigh Canham DERA, Malvern, UK: INSPEC; 1997.
 89. Archer RJ: **Stain films on silicon.** *J. Phys. Chem. Solids* 1960, **14**:104–110.
 90. Lehmann V, Gösele U: **Porous silicon formation: A quantum wire effect.** *Appl. Phys. Lett.* 1991, **58**:856–858.
 91. Zhang GX: **Porous Silicon: Morphology and Formation Mechanisms.** In *Mod. Asp. Electrochem.* 39. edited by Vayenas CG, White RE, Gamboa-Adelco ME Boston, MA: Springer US; 2006, **39**.
 92. Lehmann V: **Minority Carrier Diffusion Length Mapping in Silicon Wafers Using a Si-Electrolyte-Contact.** *J. Electrochem. Soc.* 1988, **135**:2831.
 93. Shih S, Jung KH, Hsieh TY, Sarathy J, Campbell JC, Kwong DL: **Photoluminescence and formation mechanism of chemically etched silicon.** *Appl. Phys. Lett.* 1992, **60**:1863.
 94. Splinter A, Stürmann J, Benecke W: **Novel porous silicon formation technology using internal current generation.** *Mater. Sci. Eng. C* 2001, **15**:109–112.
 95. Li X, Bohn PW: **Metal-assisted chemical etching in HF/H₂O₂ produces porous silicon.** *Appl. Phys. Lett.* 2000, **77**:2572.
 96. Scheeler SP, Ullrich S, Kudera S, Pacholski C: **Fabrication of porous silicon by metal-assisted etching using highly ordered gold nanoparticle arrays.** *Nanoscale Res. Lett.* 2012, **7**:450.

97. Nassiopoulou AG: **Local formation and patterning of porous silicon.** In “*Properties porous Si*”, *emis data Rev. Ser. No 18, IEEE, an INSPEC Publ. UK.* edited by Canham L1997.
98. Kaltsas G, Nassiopoulou AG: **Frontside bulk silicon micromachining using porous-silicon technology.** *Sensors Actuators A Phys.* 1998, **65**:175–179.
99. Meade SO, Chen MY, Sailor MJ, Miskelly GM: **Multiplexed DNA detection using spectrally encoded porous SiO₂ photonic crystal particles.** *Anal. Chem.* 2009, **81**:2618–2625.
100. Meade SO, Sailor MJ: **Microfabrication of freestanding porous silicon particles containing spectral barcodes.** *Phys. Status Solidi - Rapid Res. Lett.* 2007, **1**:71–73.
101. Starkov V V, Gavrilin EY, Konle J, Presting H, Vyatkin AF, König U: **SU8 photoresist as an etch mask for local deep anodic etching of silicon.** *Phys. Status Solidi Appl. Res.* 2003, **157**:150–157.
102. Hourdakis E, Nassiopoulou AG: **Single photoresist masking for local porous Si formation.** *J. Micromechanics Microengineering* 2014, **24**:117002.
103. Wang H, Welker B, Gao Y, Federici JF, Levy RA: **Photolithographic patterning of porous silicon using silicon nitride and silicon carbide masks.** *Mater. Lett.* 1995, **23**:209–214.
104. Shor JS, Kurtz AD: **Photoelectrochemical Etching of 6 H-SiC.** *J. Electrochem. Soc.* 1994, **141**:778–781.
105. Defforge T, Capelle M, Tran-Van F, Gautier G: **Plasma-deposited fluoropolymer film mask for local porous silicon formation.** *Nanoscale Res. Lett.* 2012, **7**:344.
106. Bao X-M, Yang H-Q: **Control of porous silicon luminescent pattern formation by ion implantation.** *Appl. Phys. Lett.* 1993, **63**:2246.
107. Duttagupta SP: **Enhancement and suppression of the formation of porous silicon.** *J. Vac. Sci. Technol. B Microelectron. Nanom. Struct.* 1995, **13**:1230.
108. Pagonis DN, Nassiopoulou a. G, Kaltsas G: **Porous Silicon Membranes over Cavity for Efficient Local Thermal Isolation in Si Thermal Sensors.** *J. Electrochem. Soc.* 2004, **151**:H174.
109. Canham L: **Porous Si membranes.** In *Hanb. Porous Silicon.* edited by Canham L Springer International Publishing; 2015.
110. Sing KSW: **Reporting physisorption data for gas/solid systems with special reference to the determination of surface area and porosity (Recommendations 1984).** *Pure Appl. Chem.* 1985, **57**:603–619.
111. Brumhead D, Canham LT, Seekings DM, Tufton PJ: **Gravimetric analysis of pore nucleation and propagation in anodised silicon.** *Electrochim. Acta* 1993, **38**:191–197.
112. Halimaoui A: **Determination of the specific surface area of porous silicon from its etch rate in HF solutions.** *Surf. Sci.* 1994, **306**:L550–L554.
113. Bell TE, Gennissen PTJ, DeMunter D, Kuhl M: **Porous silicon as a sacrificial material.** *J. Micromechanics Microengineering* 1999, **6**:361–369.
114. Hull R: *Properties of Crystalline Silicon.* London: INSPEC; 1999.
115. Lettieri S, Bernini U, Massera E, Maddalena P: **Optical investigations on thermal conductivity in n- and p-type porous silicon.** *Phys. status solidi* 2005, **2**:3414–3418.
116. Benedetto G, Boarino L, Spagnolo R: **Evaluation of thermal conductivity of porous silicon layers by a photoacoustic method.** *Appl. Phys. A Mater. Sci. Process.* 1997, **64**:155–159.
117. Périchon S, Lysenko V, Roussel P, Remaki B, Champagnon B, Barbier D, Pinard P: **Technology and micro-Raman characterization of thick meso-porous silicon layers for**

thermal effect microsystems. *Sensors Actuators A Phys.* 2000, **85**:335–339.

118. Lysenko V, Perichon S, Remaki B, Barbier D, Champagnon B: **Thermal conductivity of thick meso-porous silicon layers by micro-Raman scattering.** *J. Appl. Phys.* 1999, **86**:6841.

119. Gesele G, Linsmeier J, Drach V, Fricke J, Arens-Fischer R: **Temperature-dependent thermal conductivity of porous silicon.** *J. Phys. D. Appl. Phys.* 1997, **30**:2911–2916.

120. de Boor J, Kim DS, Ao X, Hagen D, Cojocar u., Föll H, Schmidt V: **Temperature and structure size dependence of the thermal conductivity of porous silicon.** *EPL (Europhysics Lett.)* 2011, **96**:16001.

121. Kittel C: **Interpretation of the Thermal Conductivity of Glasses.** *Phys. Rev.* 1949, **75**:972–974.

122. *Phonon Scattering in Condensed Matter V.* Berlin, Heidelberg: Springer Berlin Heidelberg; 1986, **68**.

123. D'Angelo G, Crupi C, Tripodo G, Salvato G: **Relation between low-temperature thermal conductivity and the specific heat of cesium borate glasses.** *J. Phys. Chem. B* 2010, **114**:2467–75.

124. Salamatov EI, Taranov A V., Khazanov EN: **Peculiarities in the transport characteristics of phonons in glasses and glass-like crystals at helium temperatures.** *J. Exp. Theor. Phys.* 2015, **121**:267–273.

125. Incropera FP, DeWitt DP: *Fundamentals of Heat and Mass Transfer.* 4th edition. New York: Wiley; 1996.

126. Puente D, Arana S, Gracia J, Ayerdi I: **Thermal behavior of freestanding microstructures fabricated by silicon frontside processing using porous silicon as sacrificial layer.** *IEEE Sens. J.* 2006, **6**:548–556.

127. Flubacher P, Leadbetter AJ, Morrison JA: **The heat capacity of pure silicon and germanium and properties of their vibrational frequency spectra.** *Philos. Mag.* 1959, **4**:273–294.

128. Rankin D: *CRC Handbook of Chemistry and Physics.* 2009, **15**.

129. Chung JD, Kaviani M: **Effects of phonon pore scattering and pore randomness on effective conductivity of porous silicon.** *Int. J. Heat Mass Transf.* 2000, **43**:521–538.

130. Kim K, Murphy TE: **Strong anisotropic thermal conductivity of nanoporous silicon.** *J. Appl. Phys.* 2015, **118**:154304.

131. Behzad K, Mat Yunus WM, Talib ZA, Zakaria A, Bahrami A, Shahriari E: **Effect of Etching Time on Optical and Thermal Properties of p-Type Porous Silicon Prepared by Electrical Anodisation Method.** *Adv. Opt. Technol.* 2012, **2012**:1–9.

132. Lee YH, Biswas R, Soukoulis CM, Wang CZ, Chan CT, Ho KM: **Molecular-dynamics simulation of thermal conductivity in amorphous silicon.** *Phys. Rev. B* 1991, **43**:6573.

133. Cahill DG, Fischer HE, Klitsner T, Swartz ET, Pohl RO: **Thermal conductivity of thin films: Measurements and understanding.** *J. Vac. Sci. Technol. A Vacuum, Surfaces, Film.* 1989, **7**:1259.

134. Shin S, Cho HN, Kim BS, Cho HH: **Influence of upper layer on measuring thermal conductivity of multilayer thin films using differential 3- ω method.** *Thin Solid Films* 2008, **517**:933–936.

135. Smith TL, Anthony PJ, Anderson AC: **Effect of neutron irradiation on the density of low-energy excitations in vitreous silica.** *Phys. Rev. B* 1978, **17**:4997.

136. Lee S-M, Cahill DG: **Heat transport in thin dielectric films.** *J. Appl. Phys.* 1997, **81**:2590.

137. Fang J, Pilon L: **Scaling laws for thermal conductivity of crystalline nanoporous**

- silicon based on molecular dynamics simulations. *J. Appl. Phys.* 2011, **110**:064305.
138. Alvarez FX, Jou D, Sellitto A: **Pore-size dependence of the thermal conductivity of porous silicon: A phonon hydrodynamic approach.** *Appl. Phys. Lett.* 2010, **97**:033103.
139. Millikan RA: **The General Law of Fall of a Small Spherical Body through a Gas, and its Bearing upon the Nature of Molecular Reflection from Surfaces.** *Phys. Rev.* 1923, **22**:1–23.
140. Carslaw HS, Jaeger JC: *Conduction of Heat in Solids*. second ed. 1986.
141. Abramowitz M, Stegun IA: *Handbook of Mathematical Functions: With Formulas, Graphs, and Mathematical Tables*. 1964.
142. *Tables of Integral Transforms*. McGraw- Hill, New York: 1954.
143. Moon IK, Jeong YH, Kwun SI: **The 3ω technique for measuring dynamic specific heat and thermal conductivity of a liquid or solid.** *Rev. Sci. Instrum.* 1996, **67**:29.
144. Shenoy S, Bayazitoglu Y: **3-Omega Method for Thin Films with the Non-Fourier Boundary Condition.** *Numer. Heat Transf. Part B Fundam.* 2015, **67**:363–375.
145. Wang H, Sen M: **Analysis of the 3-omega method for thermal conductivity measurement.** *Int. J. Heat Mass Transf.* 2009, **52**:2102–2109.
146. Tong T, Majumdar A: **Reexamining the 3-omega technique for thin film thermal characterization.** *Rev. Sci. Instrum.* 2006, **77**:104902.
147. Borca-Tasciuc T, Kumar AR, Chen G: **Data reduction in 3ω method for thin-film thermal conductivity determination.** *Rev. Sci. Instrum.* 2001, **72**:2139.
148. Ding T, Jannot Y, Degiovanni A: **Theoretical study of the limits of the 3ω method using a new complete quadrupole model.** *Int. J. Therm. Sci.* 2014, **86**:314–324.
149. Slack GA: **Thermal Conductivity of Pure and Impure Silicon, Silicon Carbide, and Diamond.** *J. Appl. Phys.* 1964, **35**:3460.
150. G. Holland, Neuringer L: **Proceedings of the International Conference on the Physics of Semiconductors.** In London: 1962:474.
151. Asheghi M, Kurabayashi K, Kasnavi R, Goodson KE: **Thermal conduction in doped single-crystal silicon films.** *J. Appl. Phys.* 2002, **91**:5079–5088.
152. Cahill DG, Pohl RO: **Thermal conductivity of amorphous solids above the plateau.** *Phys. Rev. B* 1987, **35**:4067–4073.
153. Bhatta RP, Annamalai S, Mohr RK, Brandys M, Pegg IL, Dutta B: **High temperature thermal conductivity of platinum microwire by 3ω method.** *Rev. Sci. Instrum.* 2010, **81**:114904.
154. Duquesne JY, Fournier D, Frétiigny C: **Analytical solutions of the heat diffusion equation for 3ω method geometry.** *J. Appl. Phys.* 2010, **108**.
155. Yu J-K, Mitrovic S, Tham D, Varghese J, Heath JR: **Reduction of thermal conductivity in phononic nanomesh structures.** *Nat. Nanotechnol.* 2010, **5**:718–21.
156. Valalaki K, Nassiopoulou AG: **Thermal conductivity of highly porous Si in the temperature range 4.2 to 20 K.** *Nanoscale Res. Lett.* 2014, **9**:318.
157. Bunde A, Havlin S: *Fractals and Disordered Systems*. Berlin, Heidelberg: Springer Berlin Heidelberg; 1996.
158. Ben-Avraham D, Havlin S: *Diffusion and Reactions in Fractals and Disordered Systems*. Cambridge, United Kingdom: Cambridge University Press; 2000.
159. Renner U, Schütz GM, Vojta G: **Diffusion on Fractals.** In *Diffus. Condens. Matter*. edited by Heitjans P, Kärger J Berlin/Heidelberg: Springer-Verlag; 2005:793–811.
160. Karperien, A., FracLac for ImageJ

<http://rsb.info.nih.gov/ij/plugins/fraclac/FLHelp/Introduction.htm>. 1999-2013.

161. Li J, Du Q, Sun C: **An improved box-counting method for image fractal dimension estimation.** *Pattern Recognit.* 2009, **42**:2460–2469.
162. Alexander, S, Orbach R: **Density of states on fractals: “fractons.”** *Le J. Phys. - Lettres* 1982, **43**:L–625.
163. Alexander S, Laermans C, Orbach R, Rosenberg HM: **Fracton interpretation of vibrational properties of cross-linked polymers, glasses, and irradiated quartz.** *Phys. Rev. B* 1983, **28**:4615–4619.
164. Alexander S, Entin-Wohlman O, Orbach R: **Phonon-fracton anharmonic interactions: The thermal conductivity of amorphous materials.** *Phys. Rev. B* 1986, **34**:2726–2734.
165. Ben-Chorin M, Moller F, Koch F, Schirmacher W, Eberhard M: **Hopping Transport On A Fractal - Ac Conductivity of Porous Silicon.** *Phys. Rev. B* 1995, **51**:2199–2213.
166. Nychyporuk T, Lysenko V, Barbier D: **Fractal nature of porous silicon nanocrystallites.** *Phys. Rev. B* 2005, **71**:115402.
167. Chantrenne P, Barrat JL, Blase X, Gale JD: **An analytical model for the thermal conductivity of silicon nanostructures.** *J. Appl. Phys.* 2005, **97**:104318.
168. Zhigunov DM, Emelyanov AV, Timoshenko VY, Sokolov VI, Seminogov VN: **Percolation effect in structures with amorphous and crystalline silicon nanoclusters.** *Phys. Status Solidi* 2012, **9**:1474–1476.
169. Kumar S, Alam MA, Murthy JY: **Effect of percolation on thermal transport in nanotube composites.** *Appl. Phys. Lett.* 2007, **90**:104105.
170. Ono Y, Mayama H, Furó I, Sagidullin AI, Matsushima K, Ura H, Uchiyama T, Tsujii K: **Characterization and structural investigation of fractal porous-silica over an extremely wide scale range of pore size.** *J. Colloid Interface Sci.* 2009, **336**:215–25.
171. Smytyna VA, Kulinich OA, Iatsunskyi IR, Marchuk IA, Pavlenko NN: **Investigation of nanostructured silicon surfaces using fractal analysis.** 2011:753–754.
172. Agboola O, Mokrani T, Sadiku R: **Porous and fractal analysis on the permeability of nanofiltration membranes for the removal of metal ions.** *J. Mater. Sci.* 2016, **51**:2499–2511.
173. **Rasband, W.S., ImageJ, U. S. National Institutes of Health, Bethesda, Maryland, USA, <http://imagej.nih.gov/ij/>, 1997-2016.**
174. Tang HP, Wang JZ, Zhu JL, Ao QB, Wang JY, Yang BJ, Li YN: **Fractal dimension of pore-structure of porous metal materials made by stainless steel powder.** *Powder Technol.* 2012, **217**:383–387.
175. Rammal R, Toulouse G: **Random walks on fractal structures and percolation clusters.** *J. Phys.* 1983, **44**:L13 – L22.
176. Nakayama T, Yakubo K, Orbach R: **Dynamical properties of fractal networks: Scaling, numerical simulations, and physical realizations.** *Rev. Mod. Phys.* 1994, **66**.
177. Courtens E, Pelous J: **Brillouin-scattering measurements of phonon-fracton crossover in silica aerogels.** *Phys. Rev. Lett.* 1987, **58**:128–131.
178. Shintani H, Tanaka H: **Universal link between the boson peak and transverse phonons in glass.** *Nat. Mater.* 2008, **7**:870–7.
179. Graebner J, Golding B, Allen L: **Phonon localization in glasses.** *Phys. Rev. B* 1986, **34**.
180. Foret M, Courtens E, Vacher R, Suck J: **Scattering Investigation of Acoustic Localization in Fused Silica.** *Phys. Rev. Lett.* 1996, **77**:3831–3834.
181. Gregora I, Champagnon B, Halimaoui A: **Raman investigation of light-emitting porous silicon layers: Estimate of characteristic crystallite dimensions.** *J. Appl. Phys.*

1994, **75**:3034.

182. Liu F, Liao L, Wang G, Cheng G, Bao X: **Experimental observation of surface modes of quasifree clusters.** *Phys. Rev. Lett.* 1996, **76**:604–607.

183. Fujii M, Kanzawa Y, Hayashi S, Yamamoto K: **Raman scattering from acoustic phonons confined in Si nanocrystals.** *Phys. Rev. B* 1996, **54**:R8373–R8376.

184. Ovsyuk NN, Novikov VN: **Influence of the degree of disorder of amorphous solids on the intensity of light scattering by acoustic phonons.** *J. Exp. Theor. Phys.* 1998, **87**:175–178.

185. Claudio T, Schierning G, Theissmann R, Wiggers H, Schober H, Koza MM, Hermann RP: **Effects of impurities on the lattice dynamics of nanocrystalline silicon for thermoelectric application.** *J. Mater. Sci.* 2012, **48**:2836–2845.

186. Lockwood D, Kuok M, Ng S, Rang Z: **Surface and guided acoustic phonons in porous silicon.** *Phys. Rev. B* 1999, **60**:8878–8882.

187. Fan H, Kuok M, Ng S, Boukherroub R, Baribeau J-M, Fraser J, Lockwood D: **Brillouin spectroscopy of acoustic modes in porous silicon films.** *Phys. Rev. B* 2002, **65**:165330.

188. Polomska-Harlick AM, Andrews GT: **Systematic Brillouin light scattering study of the elastic properties of porous silicon superlattices.** *J. Phys. D. Appl. Phys.* 2012, **45**:075302.

189. Posselt D, Kjems J, Bernasconi A, Sleator T, Ott H: **The thermal conductivity of silica aerogel in the phonon, the fracton and the particle-mode regime.** *EPL (Europhysics Lett.)* 1991, **16**:59–65.

190. de Oliveira JE, Page JN, Rosenberg HM: **Heat Transport by Fracton Hopping in Amorphous Materials.** *Phys. Rev. Lett.* 1989, **62**:780–783.

191. Donadio D, Galli G: **Temperature dependence of the thermal conductivity of thin silicon nanowires.** *Nano Lett.* 2010, **10**:847–51.

192. Nassiopoulou AG: **Thermal Isolation with Porous Silicon.** In *Handb. Porous Silicon*, edited by Canham LT Cham: Springer International Publishing; 2014:1–12.

193. Lysenko V, Périchon S, Remaki B, Barbier D: **Thermal isolation in microsystems with porous silicon.** *Sensors Actuators A Phys.* 2002, **99**:13–24.

194. Leadley, D., Shah, V., Ahopelto, J., Alzina, F., Chávez-Ángel, E., Muhonen, J., Myronov, M., Nassiopoulou, A.G., Nguyen, H., Parker, E., Pekola, J., Prest, M., Prunnila, M., Reparaz, H., Shchepetov, A., Sotomayor-Torres, C., Valalaki, K., and Whall T: **Thermal Isolation Through Nanostructuring.** In *Beyond C. Nanodevices 1*, edited by Balestra F2014.

195. Valalaki K, Nassiopoulou AG: **Porous silicon as an efficient local thermal isolation platform on the Si wafer in the temperature range 5-350K.** In *2014 11th Int. Work. Low Temp. Electron.* IEEE; 2014:61–64.

196. Schierning G: **Silicon nanostructures for thermoelectric devices: A review of the current state of the art.** *Phys. Status Solidi* 2014, **211**:1235–1249.

197. Pichanusakorn P, Bandaru P: **Nanostructured thermoelectrics.** *Mater. Sci. Eng. R Reports* 2010, **67**:19–63.

198. Mouis, M., Chávez-Ángel, E., Sotomayor-Torres, C., Alzina, F., Costache, M.V., Nassiopoulou, A.G., Valalaki, K., Hourdakakis, E., Valenzuela, S.O., Viala, B., Zakharov, D., Shchepetov, A., Ahopelt J: **Thermal Energy Harvesting.** In *Beyond C. Nanodevices 1*, edited by Balestra F2014.

199. de Boor J, Kim DS, Ao X, Becker M, Hinsche NF, Mertig I, Zahn P, Schmidt V: **Thermoelectric properties of porous silicon.** *Appl. Phys. A* 2012, **107**:789–794.

200. Lee J-H, Galli GA, Grossman JC: **Nanoporous Si as an efficient thermoelectric material.** *Nano Lett.* 2008, **8**:3750–4.

201. Lee H, Vashaee D, Wang DZ, Dresselhaus MS, Ren ZF, Chen G: **Effects of nanoscale porosity on thermoelectric properties of SiGe.** *J. Appl. Phys.* 2010, **107**:094308.
202. Tarkhanyan RH, Niarchos DG: **Seebeck coefficient of graded porous composites.** *J. Mater. Res.* 2013, **28**:2316–2324.
203. Mathur RG, Mehra RM, Mathur PC: **Thermoelectric power in porous silicon.** *J. Appl. Phys.* 1998, **83**:5855.
204. Yamamoto A, Takazawa H, Ohta T: **Thermoelectric transport properties of porous silicon nanostructure.** In *Eighteenth Int. Conf. Thermoelectr. Proceedings, ICT'99 (Cat. No.99TH8407)*. IEEE; 1999, **107**:428–431.
205. Valalaki K, Benech P, Nassiopoulou AG: **High Seebeck Coefficient of Porous Silicon: Study of the Porosity Dependence.** *Nanoscale Res. Lett.* 2016, **11**:201.
206. Loni A: **Porous Silicon Formation by Anodization.** In *Hanb. Porous Silicon*. edited by Canham L Springer International Publishing; 2014:11–22.
207. Martin J, Wong-Ng W, Green ML: **Seebeck Coefficient Metrology: Do Contemporary Protocols Measure Up?** *J. Electron. Mater.* 2015, **44**:1998–2006.
208. Freemer G: **Measuring Temperature by Direct Contact.** *Chem. Eng. Prog.* 2011, **107**:26–30.
209. Geballe G.W., Hull TH: **Seebeck Effect in Silicon.** *Phys. Rev.* 1955, **98**.
210. Yamashita O: **Effect of metal electrode on Seebeck coefficient of p- and n-type Si thermoelectrics.** *J. Appl. Phys.* 2004, **95**:178–183.
211. Yamamoto A, Takimoto M, Ohta T, Whitlow L, Miki K, Sakamoto K, Kamisako K: **Two dimensional quantum net of heavily doped porous silicon.** *Seventeenth Int. Conf. Thermoelectr. Proc. ICT98 (Cat. No.98TH8365)* 1998:198–201.
212. Sadhu J, Tian H, Ma J, Azeredo B, Kim J, Balasundaram K, Zhang C, Li X, Ferreira PM, Sinha S: **Quenched Phonon Drag in Silicon Nanowires Reveals Significant Effect in the Bulk at Room Temperature.** *Nano Lett.* 2015, **15**:3159–3165.
213. Li H, Yu Y, Li G: **Computational modeling and analysis of thermoelectric properties of nanoporous silicon.** *J. Appl. Phys.* 2014, **115**:124316.
214. Singh V, Yu Y, Sun Q-C, Korgel B, Nagpal P: **Pseudo-direct bandgap transitions in silicon nanocrystals: effects on optoelectronics and thermoelectrics.** *Nanoscale* 2014, **6**:14643–14647.
215. Michelakaki E, Valalaki K, Nassiopoulou AG: **Mesoscopic Ni particles and nanowires by pulsed electrodeposition into porous Si.** *J. Nanoparticle Res.* 2013, **15**:1499.
216. Neophytou N, Zianni X, Kosina H, Frabboni S, Lorenzi B, Narducci D: **Simultaneous increase in electrical conductivity and Seebeck coefficient in highly boron-doped nanocrystalline Si.** *Nanotechnology* 2013, **24**:205402.
217. Wang Z, Alaniz JE, Jang W, Garay JE, Dames C: **Thermal conductivity of nanocrystalline silicon: importance of grain size and frequency-dependent mean free paths.** *Nano Lett.* 2011, **11**:2206–13.
218. Neophytou N: **Prospects of low-dimensional and nanostructured silicon-based thermoelectric materials: findings from theory and simulation.** *Eur. Phys. J. B* 2015, **88**:86.
219. Strasser M, Aigner R, Lauterbach C, Sturm TF, Franosch M, Wachutka GKM: **Micromachined CMOS thermoelectric generators as on-chip power supply.** *Sensors Actuators, A Phys.* 2004, **114**:362–370.
220. Volklein F, Balles H: **A microstructure for measurement of thermal conductivity of polysilicon thin films.** *J. Microelectromechanical Syst.* 1992, **1**:193–196.
221. Moser D, Ilkaya D, Kopp D, Paul O: **Determination of the thermoelectric figure of**

- merit of doped polysilicon thin films by micromachined test structures. *2012 IEEE Sensors* 2012:1–4.
222. Xie J, Lee C, Wang M-F, Liu Y, Feng H: **Characterization of heavily doped polysilicon films for CMOS-MEMS thermoelectric power generators.** *J. Micromechanics Microengineering* 2009, **19**:125029.
223. Maldovan M: **Thermal energy transport model for macro-to-nanograin polycrystalline semiconductors.** *J. Appl. Phys.* 2011, **110**:114310.
224. Dong H, Wen B, Melnik R: **Relative importance of grain boundaries and size effects in thermal conductivity of nanocrystalline materials.** *Sci. Rep.* 2014, **4**:7037.
225. Cho J, Francis D, Chao PC, Asheghi M, Goodson KE: **Cross-Plane Phonon Conduction in Polycrystalline Silicon Films.** *J. Heat Transfer* 2015, **137**:071303.
226. Plummer JD, Deal MD, Griffin PB: *Silicon VLSI Technology: Fundamentals, Practice and Modeling.* Prentice Hall; 2000.
227. Cerva H, Oppolzer H: **Microstructure and interfaces of polysilicon in Integrated Circuits.** In *Polycryst. Semicond. Springer Proc. Physics, Vol.35.* edited by Werner J, Moller H, Strunk H Heidelberg: Springer-Verlag Berlin; 1989:354.
228. Harbeke G, Krausbauer L, Steigmeier EF, Widmer AE, Kappert HF, Neugebauer G: **Growth and Physical Properties of LPCVD Polycrystalline Silicon Films.** *J. Electrochem. Soc.* 1984, **131**:675.
229. Kamins TI: **Structure and Properties of LPCVD Silicon Films.** *J. Electrochem. Soc.* 1980, **127**:686.
230. Puchner H: **Advanced Process Modeling for VLSI Technology.** 1996.
231. Nakhodkin NG, Rodionova T V: **The mechanism of secondary grain growth in polysilicon films.** *J. Cryst. Growth* 1997, **171**:50–55.
232. Cohen M: **Progress and prospects in metallurgical research.** In *Adv. Mater. Res.* edited by Psaras PA, Dale Langford H Washington, D.C.: National Academies Press; 1987:90.
233. Lu NCC: **The Effect of Film Thickness on the Electrical Properties of LPCVD Polysilicon Films.** *J. Electrochem. Soc.* 1984, **131**:897.
234. Learn AJ, Foster DW: **Deposition and electrical properties of in situ phosphorus-doped silicon films formed by low-pressure chemical vapor deposition.** *J. Appl. Phys.* 1987, **61**:1898.
235. Valalaki K, Vouroutzis N, Nassiopoulou AG: **Significant enhancement of thermoelectric figure of merit of boron doped polycrystalline Si films by reducing grain size.** *J. Phys. D. Appl. Phys.* 2016, **Submitted**.
236. Raman MS, Kifle T, Bhattacharya E, Bhat KN: **Physical Model for the Resistivity and Temperature Coefficient of Resistivity in Heavily Doped Polysilicon.** *IEEE Trans. Electron Devices* 2006, **53**:1885–1892.
237. Spessot A, Molteni M, Ventrice D, Fantini P: **A Physics-Based Compact Model for Polysilicon Resistors.** *Electron Device Lett. IEEE* 2010, **31**:1251–1253.
238. Seto JYW: **The electrical properties of polycrystalline silicon films.** *J. Appl. Phys.* 1975, **46**:5247–5254.
239. A.F. Ioffe: *Physics of semiconductors.* New York: Publishing House of the U.S.S.R. Academy of Sciences, Moscow-Leningrad; 1960.
240. Anderson B, Anderson R: *Fundamentals of Semiconductor Devices.* New York: McGraw-Hill, Inc.; 2005.
241. Okumura F, Sera K, Tanabe H, Yuda K, Okumura H: **Excimer Laser Annealed Poly-Si TFT Technologies.** *MRS Proc.* 2011, **377**:877.

242. Kamins TI: **Hall mobility in chemically deposited polycrystalline silicon.** *J. Appl. Phys.* 1971, **42**:4357–4365.
243. McConnell A, Uma S, Goodson KE: **Thermal conductivity of doped polysilicon layers.** *J. Microelectromechanical Syst.* 2001, **10**:360–369.
244. von Arx M, Paul O, Baltes H: **Process-dependent thin-film thermal conductivities for thermal CMOS MEMS.** *J. Microelectromechanical Syst.* 2000, **9**:136–145.
245. Nan C-W, Birringer R: **Determining the Kapitza resistance and the thermal conductivity of polycrystals: A simple model.** *Phys. Rev. B* 1998, **57**:8264–8268.
246. Regner KT, Sellan DP, Su Z, Amon CH, McGaughey AJH, Malen J: **Broadband phonon mean free path contributions to thermal conductivity measured using frequency domain thermorefectance.** *Nat. Commun.* 2013, **4**:1640.
247. Nomura M, Kage Y, Müller D, Moser D, Paul O: **Electrical and thermal properties of polycrystalline Si thin films with phononic crystal nanopatterning for thermoelectric applications.** *Appl. Phys. Lett.* 2015, **106**:223106.
248. Xie J, Lee C, Wang M-F, Tsai JM: **Microstructures for characterization of seebeck coefficient of doped polysilicon films.** *Microsyst. Technol.* 2010, **17**:77–83.
249. Nassiopoulou AG, Kaltsas G: **Porous Silicon as an Effective Material for Thermal Isolation on Bulk Crystalline Silicon.** *Phys. status solidi* 2000, **182**:307–311.